306319900V

Gravity Anomalies, Flexure and the Thermo-Mechanical Evolution of the West Iberia Margin and its Conjugate of Newfoundland

by

Tiago Cunha



Thesis submitted for the Degree of Doctor of Philosophy, University of Oxford



Wolfson College &
Department of Earth Sciences

Trinity Term 2008

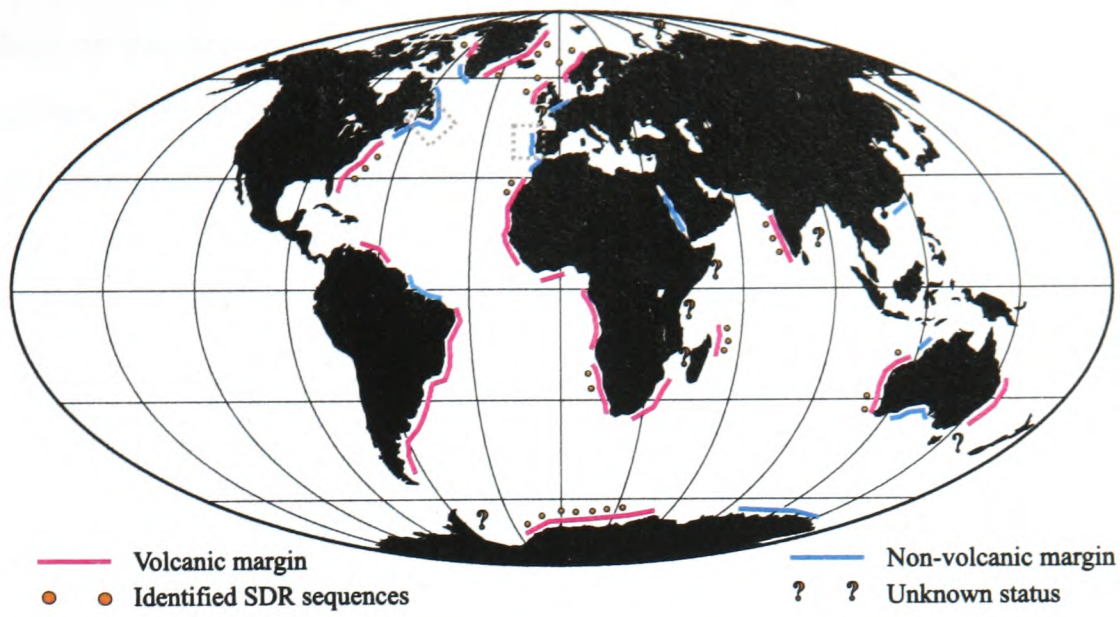

Figure 1.1: Worldwide distribution of volcanic (pink) and magma-poor (blue) passive continental margins. Modified from Menzies *et al.* [2002]. Volcanic passive margins where sequences of intrabasement seaward dipping reflectors (SDR's) have been identified are marked by orange dots (according to Coffin & Eldholm [1994]). The dashed grey rectangles highlight the margins studied in this thesis, namely, the magma-poor passive margins of West Iberia and Newfoundland, in the eastern and western central North Atlantic, respectively.

with the activity of mantle plumes (Hill [1994]; Courtillot *et al.* [1999]; Skogseid [2001] and references therein). Globally, volcanic margins may represent up to 90% of the oceans rifted margins (pink lines in Figure 1.1; Menzies *et al.* [2002]).

One of the most distinctive features of these margins is the existence of a thick (> 3 km) zone of extrusive basaltic complexes, characterized by a smooth opaque surface and internal wedges of seaward dipping reflectors (e.g. Eldholm *et al.* [1995]; the SDR's in Figure 1.2a). These complexes resulted from the emplacement of multiple sub-aerial basalt flows interbedded with thin sediment layers, that were subsequently rotated and tilted as the margin subsided (Skogseid & Eldholm [1987]). This type of sequence was first identified by Hinz [1981]), and later confirmed by drilling in a number of North Atlantic margins (Coffin & Eldholm [1994]; Eldholm *et al.* [1995]; Menzies *et al.* [2002] and references therein). Other geological features commonly observed at rifted volcanic margins include (e.g. White *et al.* [1987]; Coffin & Eldholm [1994]; Geoffrey [2005]): (1) a thick, wedge shape, underplated lower crustal body (up to 15 km thick) of high P-wave velocities (> 7.3 km s^{-1}; Figure 1.2a); (2) sills and low-angle dikes within pre-rift sediments; (3) thicker than normal oceanic crust adjacent to the ocean-continent boundary (OCB); (4) and, in some cases, onshore continental flood basalts.

Magma-poor passive continental margins, on the other hand, form away from the influence of hotspot activity. Due to the lack of significant magmatism, either extruded

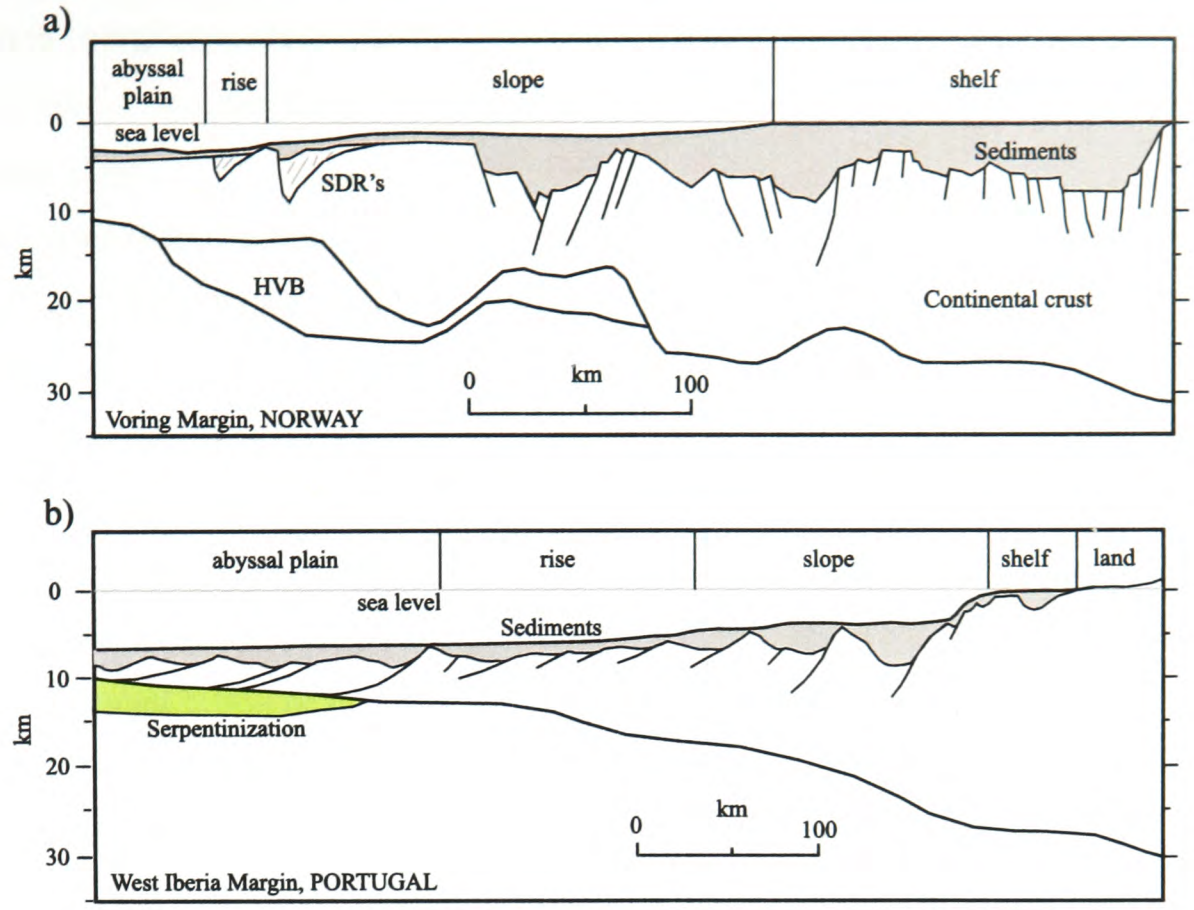

Figure 1.2: Typical structure of volcanic (a) and magma-poor (b) rift margins. a) The Vøring volcanic margin, off Norway (modified from Skogseid & Eldholm [1995]), shows the typical SDR sequences and the High-Velocity lower crustal Body (HVB). b) The non-volcanic margin example is from NW Portugal (modified from Alves *et al.* [2006]). It shows the typical rotated faulted blocks sequence (Montadert *et al.* [1977]) and the serpentinization of the lithosphere mantle peridotites under highly thinned continental crust, which will eventually become exhumed as extension proceeds (e.g. Boillot *et al.* [1988a]; Sibuet [1992]). Also indicated are the distinct morphological sectors which characterize passive continental margins in general (i.e. the continental shelf, slope, rise and abyssal plain; see text).

et al. [2006a]; Sibuet *et al.* [2007]). Under the currently accepted rift models, however, the existence of such a wide region of exhumed mantle without significant magmatism is paradoxal (see discussion in Section 1.1.4). Buck [2004], for example, referred to this as the "No Magma" paradox.

Despite the large differences in the amount of magmatism and in the structure of the break-up zone, most passive continental margins can be described in terms of similar conventional morphological features (Figure 1.2). These include (after Heezen [1974]):

- The continental shelf, characterized by a gently dipping slope between the coast line and the shelf break. The depth of the shelf break in passive continental margins varies in function of the latitude. In the West Iberia Margin, for example, the shelf break varies narrowly between $\sim$ 160 and 200 m (Vanney & Mougenot [1981]). In some passive

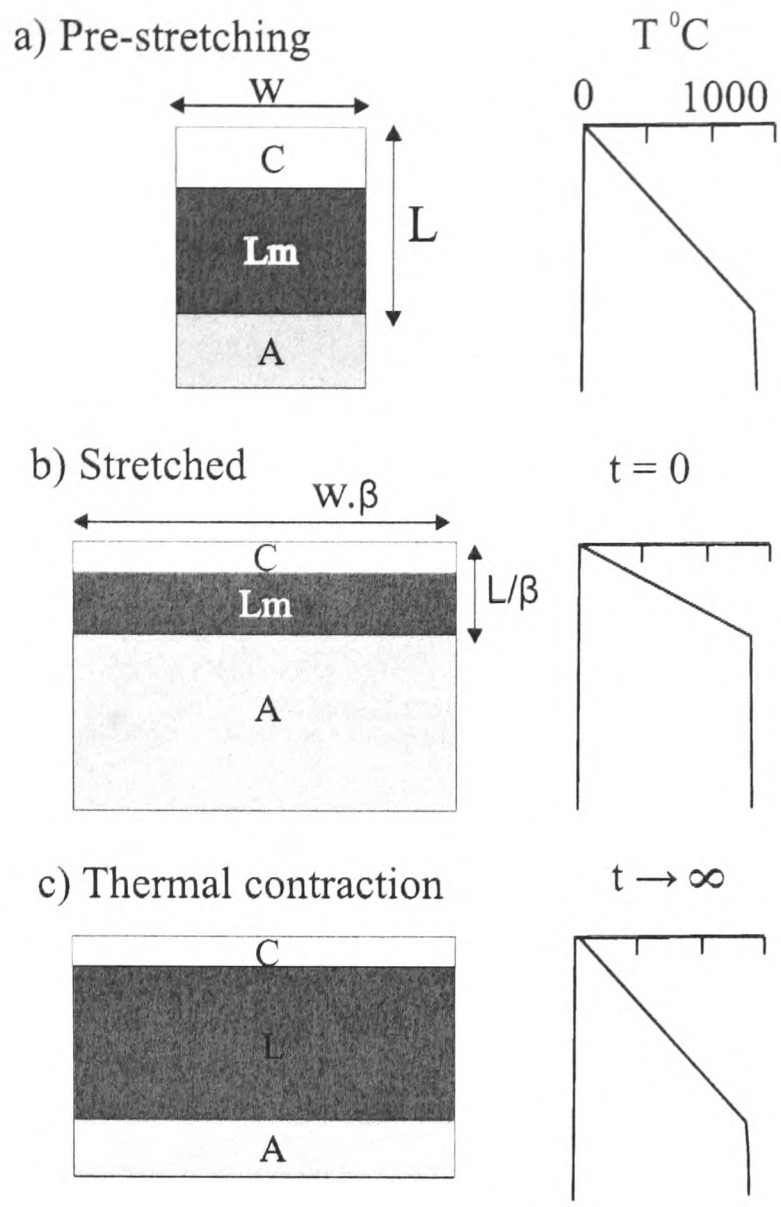

Figure 1.3: Illustration of the McKenzie [1978] "pure shear" model of lithospheric extension and thermal evolution for the formation of rift type basins. β is the stretching factor, by which the lithospheric mantle (Lm) and crust (C) are initially stretched. A is the asthenosphere, w is the initial width of the basin, L is the initial thickness of the lithosphere and t is the time since rifting.

Cochran [1983]) can explain, in broad terms, the subsidence/uplift history and heat-flow record, as well as the geometry and thickness of the sediment strata in many rift type basins, both in passive continental margins and intracontinental rift settings.

One limitation of the McKenzie type pure shear kinematic models is that they predict highly symmetric rift basins (Figure 1.4a), whilst rifts are often asymmetric (e.g. Wernicke [1981]; Ebinger *et al.* [1991]; Lister *et al.* [1991]). Wernicke [1981], and later Wernicke & Burchfiel [1982] and Wernicke [1985], proposed a different conceptual model of rifting, where large amounts of lithospheric extension are accommodated along low-angle normal faults (or detachment faults) which cut through the crust and mantle lithosphere (Figure 1.4b). They invoked the model to explain the formation of metamorphic core complexes, where low and high grade metamorphic rocks are juxtaposed near the surface, as observed in the Basin and Range Province, Western U.S.A. (e.g. Wernicke [1981]; Armstrong [1982]). This model, commonly known as the "simple shear", Wernicke or the Lithospheric Wedge stretching model (e.g. Lister *et al.* [1991]), is associated with lateral variations in the amount of crust and lithospheric stretching and the formation of an "upper plate" margin, in the hangingwall of the detachment surface, and a lower plate margin in the footwall. The subsidence and uplift history of the upper and lower

plate margins predicted by such models will be fundamentally different, with more initial (i.e. isostatic) subsidence in the lower plate and greater thermal subsidence in the upper plate margin (Wernicke [1985]).

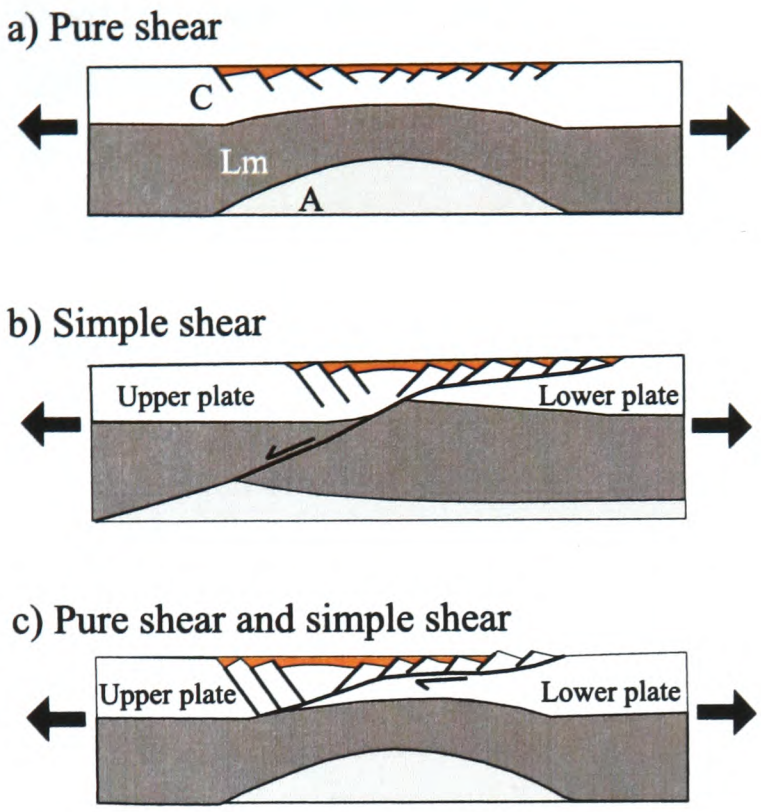

Figure 1.4: Different models of lithospheric extension proposed to explain the formation of rift basins and passive continental margins. a) Pure shear. b) Simple shear. c) Combination of lithospheric-scale pure shear and simple shear stretching within the crust. Modified from Keen *et al.* [1989].

A number of rift models which combine the effects of large displacements along lithospheric and/or crustal scale penetrative major shear zones, symmetrical extension on the ductile lower crust and mantle lithosphere, and the isostatic response of the lithosphere to the asymmetric redistribution of loads during stretching, have been since proposed (e.g. Coward [1986]; Lister *et al.* [1986]; Weissel & Karner [1989]; Lister *et al.* [1991]). The importance of these models is that they can predict not only the asymmetry of the rift basins, but also a great variety of features observed in Atlantic type margins and intracontinental rifts, such as: (1) permanently uplifted rift flanks (e.g. Weissel & Karner [1989]; Ebinger *et al.* [1991]); (2) large post-rift regional subsidence, in relation to that predicted from the amount of stretching measured from faulting in the upper-middle crust (Boillot *et al.* [1988a]; Driscoll & Karner [1998]; Davis & Kusznir [2004]); and (3) marginal plateaus (Etheridge *et al.* [1989]; Lister *et al.* [1991]).

1.1.3 Mechanics of Rifting and "Modes" of Lithospheric Extension

The models discussed above provide an essential kinematic framework that explains the formation and, to a certain extent, the diversity and geometry of rift type basins, based on simple principles of isostasy and heat conduction. They are, however, limited in the sense that they do not take into consideration the rheological structure and the strain distribution within the lithosphere during stretching.

A number of studies into the dynamics of rifting show that different styles, or "modes",

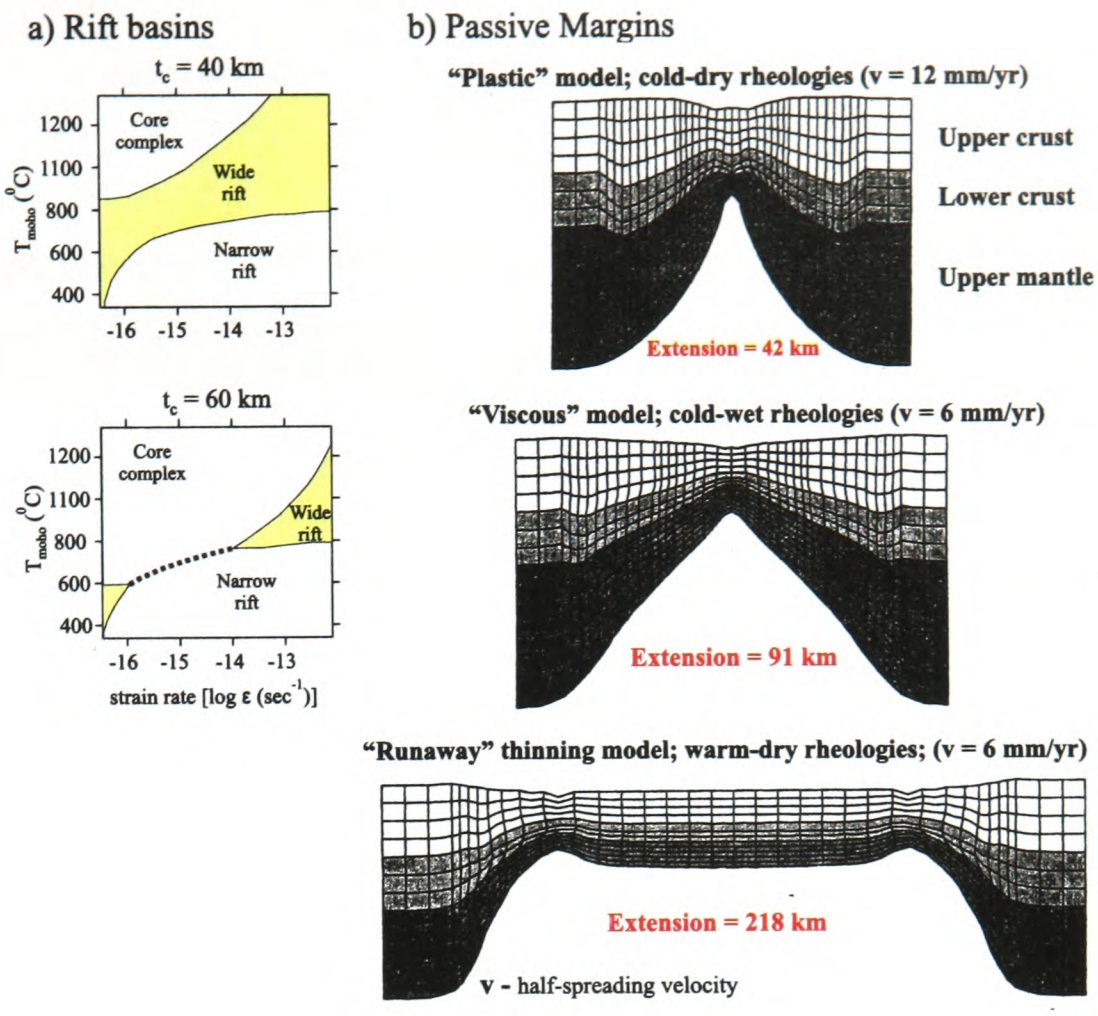

Figure 1.5: Numerical modelling predictions on the style, or mode, of continental rifting. a) Results from numerical models which use a thin sheet approximation to determine the evolution of the lithospheric intrinsic strength and gravitational buoyancy forces during rifting (after Buck [1991]). b) Finite element models developed to investigate the style of rifting at passive continental margin settings (after Bassi *et al.* [1993]).

Lin & Parmentier [1990]), the lithosphere becomes mechanically unstable for stretching factors (β) > 3-4 (i.e. 150-200% of extension). This leads to rapid necking and continental rupture, thus preventing the formation of a very wide region of highly stretched continental and/or transitional basement.

Over the past decade, both numerical (e.g. Hopper & Buck [1996]; ter Voorde *et al.* [1998]; Govers & Wortel [1999]; Burov & Poliakov [2001]; Behn *et al.* [2002]; Davis & Kusznir [2002]) and analogue (Brun & Beslier [1996]; Michon & Merle [1998]) models of rift basin evolution have become increasingly more complex, integrating multi-layer crustal and mantle rheologies. Of particular interest for this thesis are those studies which focus on the mechanical effects of coupling-decoupling between crust and mantle competent layers (ter Voorde *et al.* [1998]; Burov & Poliakov [2001]), and on the development of necking instabilities, which control both the subsidence/uplift history and the overall style of lithospheric thinning of rift basins (Braun & Beaumont [1989]; Brun & Beslier [1996]; Govers & Wortel [1999]).

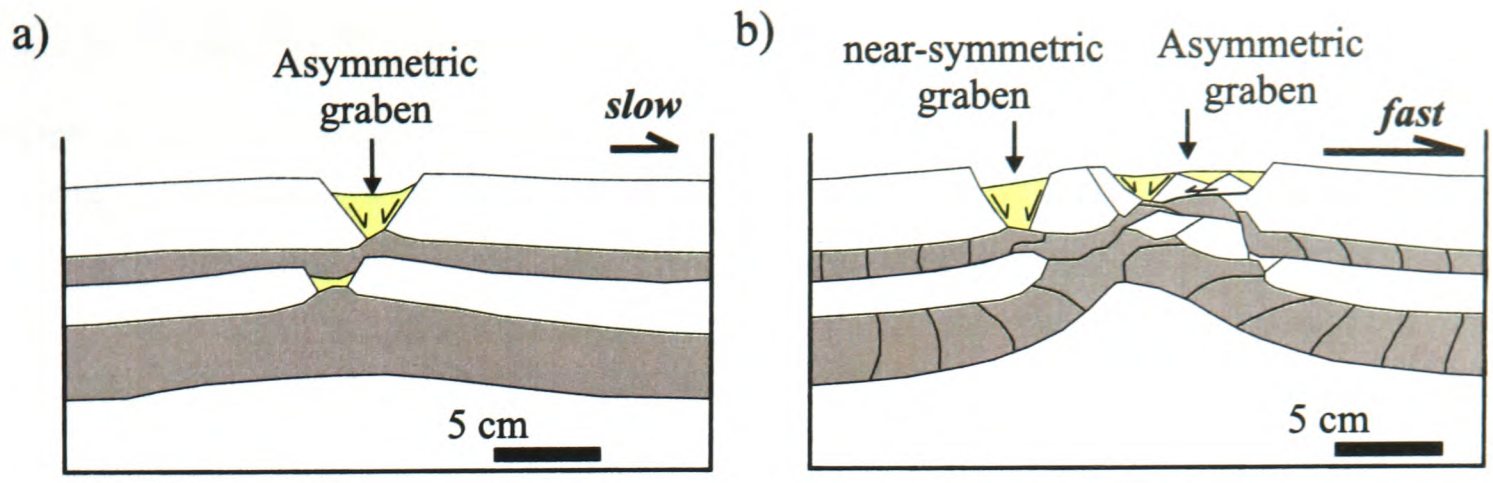

Figure 1.6: Comparison of rift geometries obtained from analogue sandbox modelling. The experiments predict the formation of two main shear zones, in the ductile portions of the crust and mantle (dark grey areas). In experiment (a) the extension rates are small, and the model predicts a narrow, essentially asymmetric rift, with the development of a lithospheric-scale detachment structure; Experiment (b) uses higher extension rates, which results in a wider rift basin and the development of crustal-scale detachments faults, superimposed on a lithospheric-scale symmetric rift.

Brun & Beslier [1996], for example, using a sandbox analogue modelling apparatus, showed that by applying a constant rate of deformation at the edges of the model, a combination of pure (regional necking) and simple shear (grabens and half-grabens) related structures would be generated within the same rift system. Brun & Beslier [1996], and later Michon & Merle [1998], further suggest that both the geometry and width of the rift vary as a function of the extension rate, with higher extension rates favouring the development of wider and more symmetric rifts (Figure 1.6). These results are, therefore, at odds with the predictions from the numerical modelling experiments of Bassi *et al.* [1993] discussed above.

Govers & Wortel [1999], on the other hand, using finite element modelling techniques, argued that the depth at which lithospheric necking occurs (Z_{neck}), which corresponds to levels of maximum strength in the crust and mantle (e.g. Braun & Beaumont [1989]), is not fixed, as commonly assumed in kinematical models of rift basin formation (e.g. Weissel & Karner [1989]; Watts & Stewart [1998]), but evolves both in time and space. However, according to their modelling predictions Z_{neck} becomes stationary after relatively small amounts of extension, $\beta < 1.5$. In most passive continental margins, this amount of stretching is typical for the upper continental slope, and reached within the early stages of rifting. Therefore, the Z_{neck}'s inferred from the kinematic models, based on the stratigraphy, subsidence and gravity anomaly data, probably reflect an average mechanical structure of the lithosphere during the rifting process, as suggested by Keen & Dehler [1997].

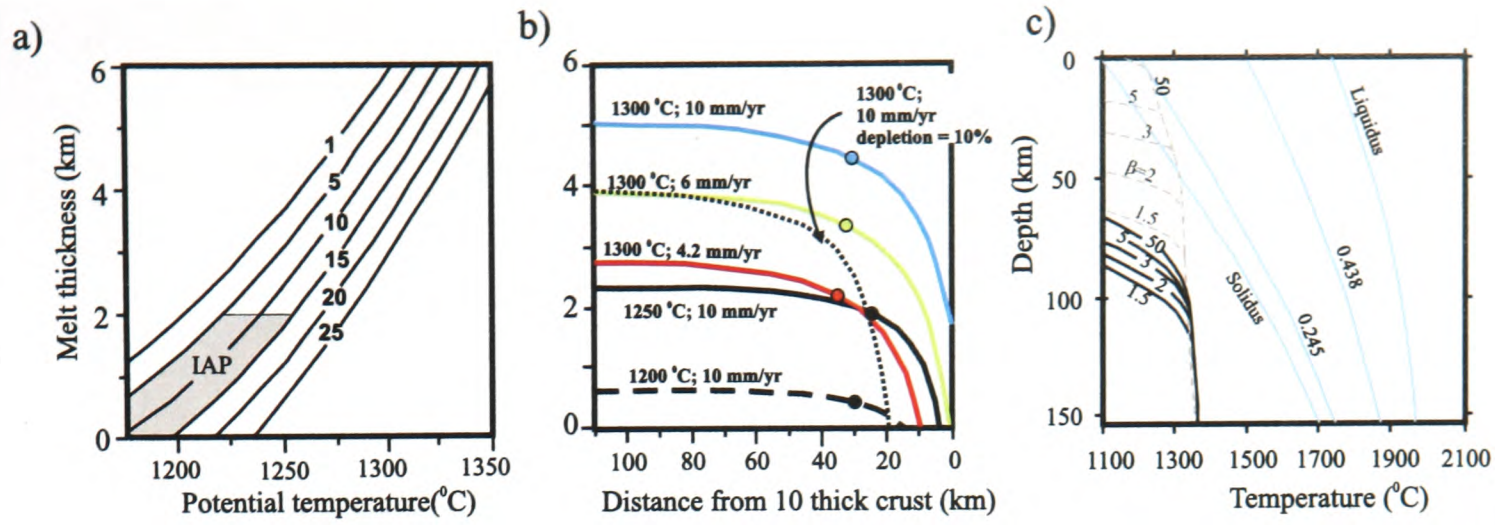

Figure 1.7: The No Magma Paradox in passive continental margins: Predictions from thermal numerical models. a) Predicted melt thicknesses assuming depth uniform stretching. Results are shown in function of mantle potential temperature and rift duration (indicated in the curves). For a rift duration of 5-15 m.y., mantle potential temperatures < 1250°C would be needed to justify the estimated melt thicknesses (< 2 km) in the Iberia Abyssal Plain (IAP). Modified from Minshull *et al.* [2001]. b) Results from numerical models which also take into account the heat losses and gains associated with melting and serpentinization, respectively (Pérez-Gussinyé *et al.* [2006]). According to these authors, a slow rifting velocity (red and green lines) and/or high mantle depletions (> 10%; dotted line) could explain the low melt productions at the OCTZ. c) Predictions from simple thermal models showing the effectiveness of a simple shear model of rifting (solid black lines; labels give the amount of stretching, β) in reducing the amount of melt predicted from a pure shear model (dashed grey lines). Mantle potential temperature is 1280°C. The blue lines between the liquidus and solidus show the melt fraction by weight (McKenzie & Bickle [1988]). After Latin & White [1990].

mid eighteenth century. His remarks concerned the observations of Pierre Bouguer a few years earlier, who suggested that the gravitational attraction of the Andes was "much smaller than expected from the mass of matter represented in the mountains". According to Boscovich, the mountains were supported by the " ... thermal expansion of the material in depth ... ".

The first models of isostasy, however, were only formally conceptualised approximately one century later (Pratt [1855]; Airy [1855]), to explain a difference of more than 5" between the positions determined using geodetic and astronomical methods in northern India (i.e. just south of the Himalayas mountain range). According to the model of Pratt, the differences in height of the mountains were compensated by lateral variations in the average density of the rocks, in a way that the lithostatic pressure would be maintained at a certain reference level (i.e. the compensation depth; D_c in Figure

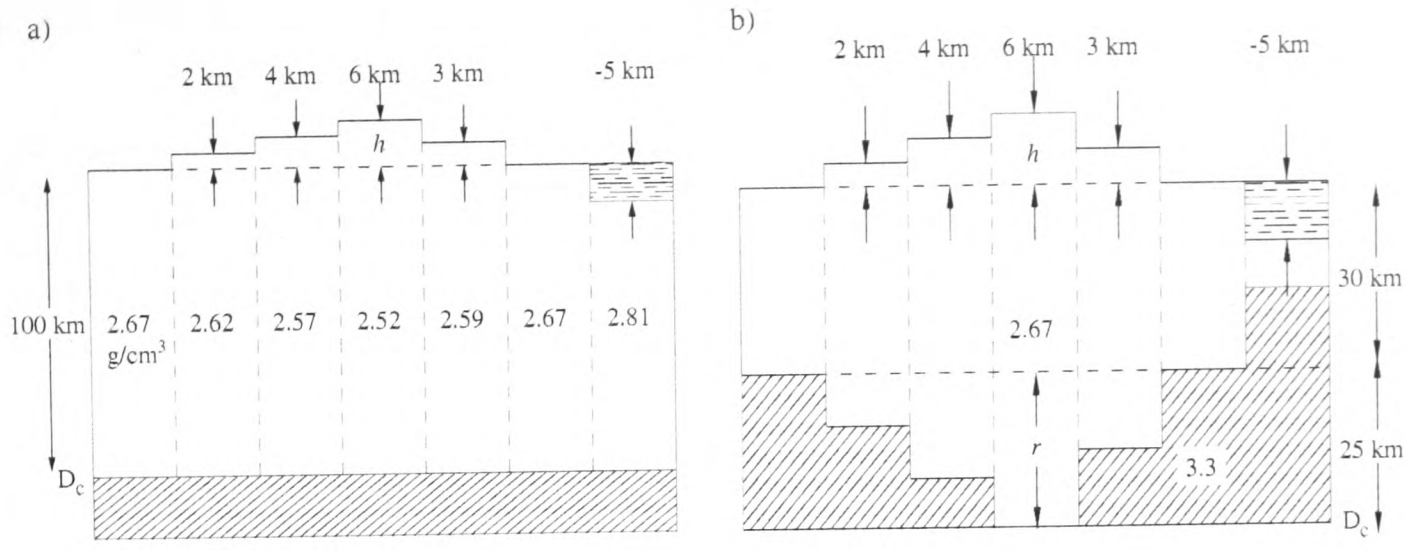

Figure 1.8: Pratt (a) and Airy (b) models of isostasy. In Pratt's model, topography (h) is supported by density contrasts above a compensation depth (D_c). Airy's model of isostasy involves a lower density root (r) underneath an excess of mass due to topography.

1.8a). Pratt's calculations, however, predicted discrepancies between the geodetic and astronomical methods approximately three times greater than observed.

Airy, on the other hand, believed that the outermost rigid layer of the Earth overlies a fluid of greater density, and that the excess in mass caused by the mountains was compensated in depth by an equivalent mass deficiency, or a root, as represented in Figure 1.8b. A concise historical record on the developments of the concept and models of isostasy is given in Watts [2001b].

1.2.2 Flexure and T_e

The Pratt and Airy models of isostasy, although based on contrasting assumptions, are similar in that they assume that an excess in mass due to topography is locally compensated. This view was later contested in a series of papers by J. Barrell in 1914 (see Watts [2001b] for summary) who, based on relief and gravity considerations, argued that the Earth's outermost solid crust, or the lithosphere as he referred to it, was capable of rigidly supporting loads associated with prominent geological features, such as mountain ranges and river deltas. Barrell also predicted the existence of an underlying week, viscous layer, which accommodates the bending of the lithosphere by lateral flow. He called this layer the asthenosphere.

Although the concept of regional, rather then local compensation, had already been suggested in previous works (e.g. Gilbert [1889]), it was Vening Meinesz [1931] who first proposed a model to quantitatively account for the effects of regional isostasy, where the radius of compensation, R, is proportional to the strength of the crust (Figure 1.9a). Throughout the late 30's and the 40's, R. Gunn published a series of papers where he

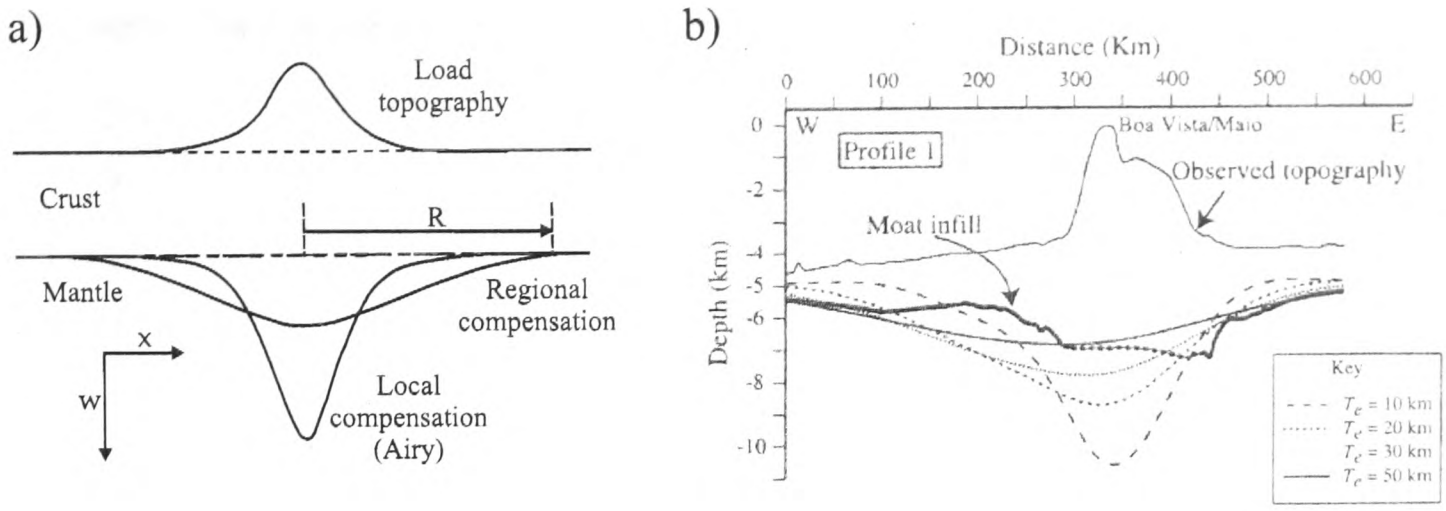

Figure 1.9: Local versus regional (i.e. flexural) models of isostasy. a) Schematic diagram showing a comparison between the local and regional models of isostasy. R represents the radius of regional compensation according to Vening Meinesz [1931] (modified from Watts [2001b]). b) Calculated versus observed flexural deformation under the Island of Boa Vista (Cape Verde) for different values of the plate's flexural rigidity, T_e. The observed flexural deformation corresponds to the moat infill. From Ali *et al.* [2003].

studied the role of lithospheric strength in explaining the departures from local models of isostasy (see Watts [2001b] for summary). Importantly, he showed that the major gravity anomalies associated with different types of geological loads (e.g. mountain ranges, seamounts, passive margins and island arcs-trenches systems) could be explained assuming that the lithosphere behaves as a thin elastic plate overlying a weak, inviscid fluid. According to Gunn [1943],

$$D\frac{d^4w}{dx^4} + (\rho_m - \rho_{infill})gw = 0 \tag{1.1}$$

where D is the plate's flexural rigidity, ρ_m is the density of the underlying fluid, ρ_{infill} is the density of the material infilling the deflection (w), and g is the acceleration due to gravity.

The flexural rigidity of the plate can then be expressed in terms of an equivalent elastic thickness, T_e,

$$D = \frac{ET_e^3}{12(1-\nu^2)} \tag{1.2}$$

where E and ν are the Young's modulus and the Poisson's ratio, respectively, which reflect intrinsic mechanical properties of the materials.

As shown in Figure 1.9b, by varying the T_e associated with the emplacement of a load, both the amplitude and wavelength of the flexural deformation will change considerably. The resulting gravity anomaly (i.e. load+flexure) will thus be a consequence of T_e.

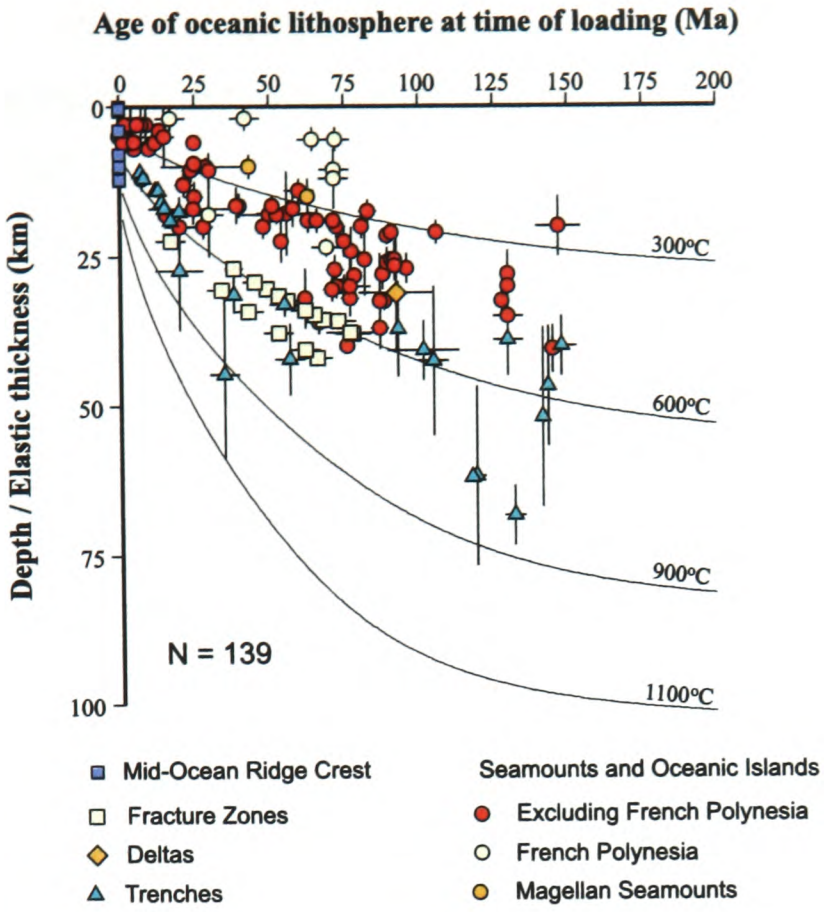

Figure 1.10: T_e versus age of the oceanic lithosphere at the time loading. Although T_e estimates from distinct tectonic environments are compared, the values appear to cluster between the depths of the 300 and 600°C isotherms, as predicted by Watts [1978]. N is the number of plotted estimates. After Watts [2001b].

A great number of studies have since been published with estimates of T_e in distinct tectonic environments, such as seamounts (Watts [1978]; Calmant [1987]), foreland basins (Karner & Watts [1983]), passive continental margins and intracontinental rift basins (Stewart [1998] and references therein), trenches (McNutt [1984]) and cratonic terranes Forsyth [1985]. These estimates are based either on purely elastic models (i.e. Equation 1.1), or on more or less complex viscoelastic plate models, which account for the rheological stratification of the lithosphere (e.g. McNutt [1984]; McNutt *et al.* [1988]; Watts & Zhong [2000]). The general equation for the flexure of a viscoelastic plate overlying an inviscid substrate is given by (e.g. Nadai [1963]),

$$D\frac{d^4\dot{w}}{dx^4} + (\rho_m - \rho_{infill})g(\dot{w}\tau + w) = 0 \tag{1.3}$$

where $\dot{w}$ is the first derivative of w with respect to time and τ is the Maxwell relaxation time; i.e. when the accumulated elastic strain equals the viscous strain.

In the oceans, a strong correlation has been found between the age of the lithosphere at the time of loading and the T_e's calculated using a simple elastic plate model. This was first noticed by Watts [1978], using cross-spectral modelling techniques to analyse the relationship between gravity and bathymetry along the Hawaiian-Emperor Seamount Chain. According to Watts [1978], the T_e of the Pacific Plate follows a predictable pattern, and corresponds to the depth of the 450°C ± 150°C isotherm. As shown in Figure 1.10, the predictions of Watts [1978] have been confirmed over both recent and old oceanic lithosphere, and in distinct tectonic settings, throughout the world's ocean basins (see Watts [2001b] for references).

Watts *et al.* [1982] compared the stratigraphy and gravity anomalies observed at a number of intracratonic rift basins to the predictions from both elastic and viscoelastic plate models. The modelling results suggest that, overall, an elastic plate model where the T_e increases with age since rifting explains better the observations. As depicted in Figure 1.11a, this model is characterized by a widening of the basin depocentre with time and the onlap of the younger sediment units onto the basin flanks (the steer's head basin model; Watts *et al.* [1982]). In contrast, the viscoelastic plate model predicts that the younger sediments are confined to the basin centre, due to the increasing stress relaxation with the age of the load, and show more subsidence than older units (Figure 1.11c).

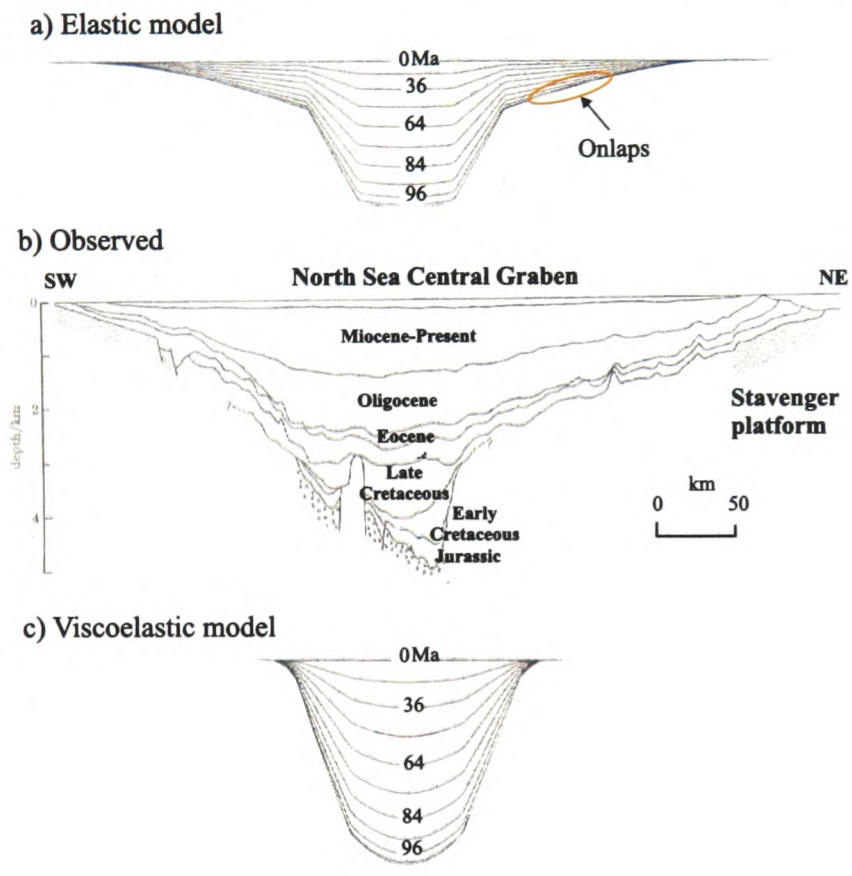

Figure 1.11: Predicted and observed stratigraphy at intracontinental rift settings: elastic versus viscoelastic plate models (from Watts *et al.* [1982]). a) Elastic plate model. b) Cross section from the North Sea Central Graben. c) Viscoelastic plate model.

The example shown in Figure 1.11b is a cross section from the North Sea Basin (see Watts *et al.* [1982] for references), where the maximum subsidence occurred initially over a narrow, fault controlled central graben and then extended over the basin flanks during the Tertiary. The overall Mesozoic-Tertiary basin development therefore follows the pattern predicted by the elastic model. Despite this, some offlap is noticed at the basin edges, with the sediments age decreasing towards the basin centre, particularly in the eastern flank. It appears, however, that this flank has been truncated by late Pleistocene uplift and erosion associated with the ice loading of the Fenoscandian shield (Holtedahl & Bjerkji [1975]). Sloss & Scherer [1975], for example, also invoked basin-wide erosional events to explain offlap patterns and the apparent decrease in width of some basins with time, such as the Michigan Basin, U.S.A. and the Moscow Basin, in the former Soviet Union.

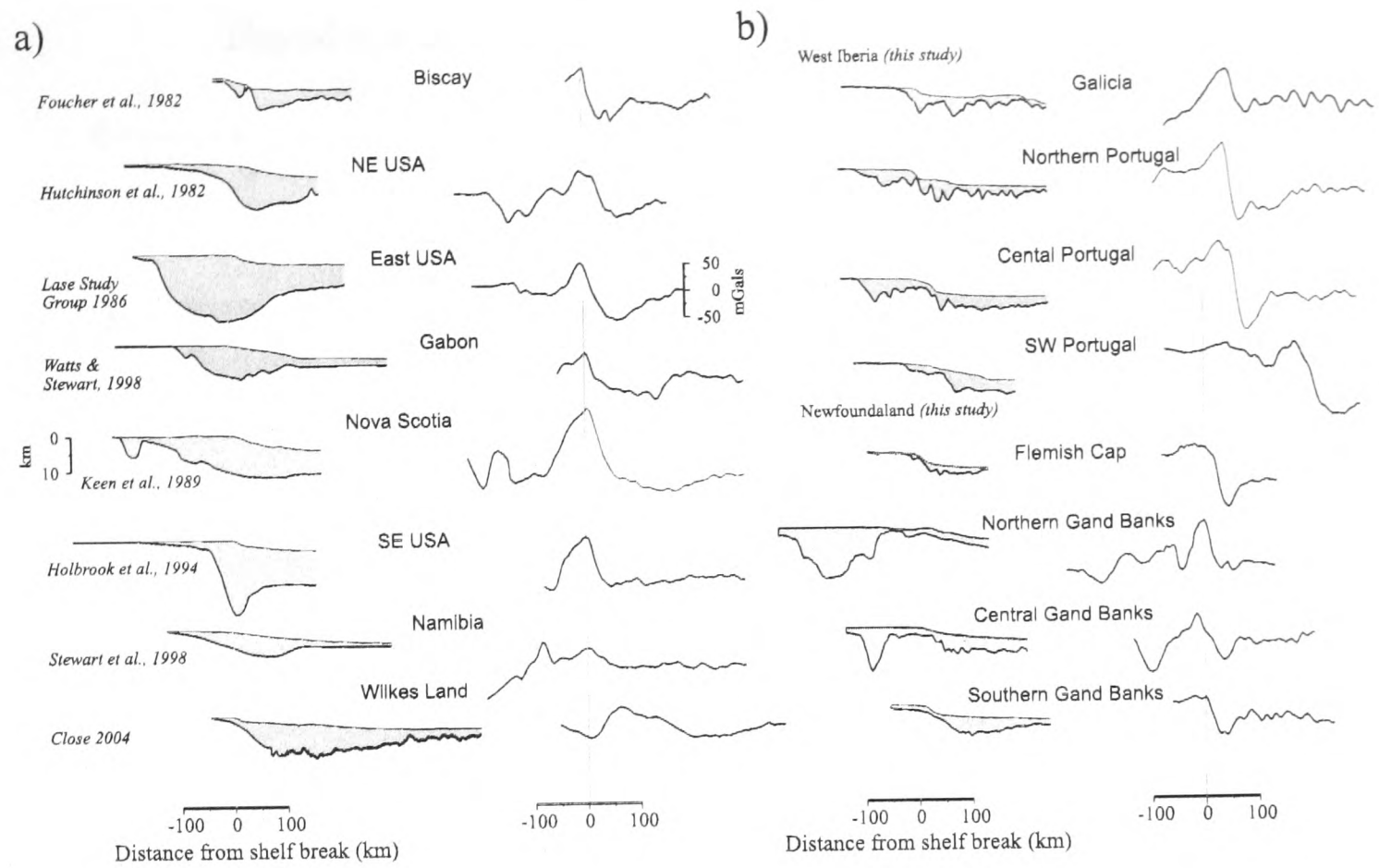

Figure 1.12: a) Compilation of previously published profiles showing the sediments and free-air gravity anomalies (FAA) at a number passive continental margins. Profiles are stacked at the shelf edge, where a distinctive FAA high is observed in most of the margins, flanked by a low over the continental slope and rise. Modified from Stewart *et al.* [2000]. b) Profiles from West Iberia and Newfoundland margins (this study) showing important along strike variations in the amplitude and wavelength of the edge-effect anomaly.

sedimentation, to the observed gravity field. This technique, dubbed Process-Oriented Gravity Modelling (POGM, Watts [1988]), has subsequently been improved to account for strength during rifting (Watts & Stewart [1998]) and underplating (Watts & Fairhead [1999]). By comparing the observed and calculated gravity anomalies and crustal geometries for different modelling assumptions, constraints can be placed on the long-term mechanical strength of the margin at different times of the rifting process (Watts [1988]; Stewart *et al.* [2000]).

This technique has been successively applied to passive continental margin segments along the East Coast, U.S.A. (Watts [1988]; Wyer & Watts [2006]), the African Continent (Watts & Marr [1995]; Stewart *et al.* [2000]; Watts [2001a]), western India (Chand & Subrahmanyam [2003]), and the southern Australia-Antarctica conjugate margins (Close [2004]), revealing important information on the long-term strength of rifted continental lithosphere, the location of the OCB, and on the mechanical segmentation of passive continental margins (e.g. Stewart *et al.* [2000]; Wyer & Watts [2006]).

Figure 1.13 shows a compilation of T_e estimates at passive continental margins, plot-

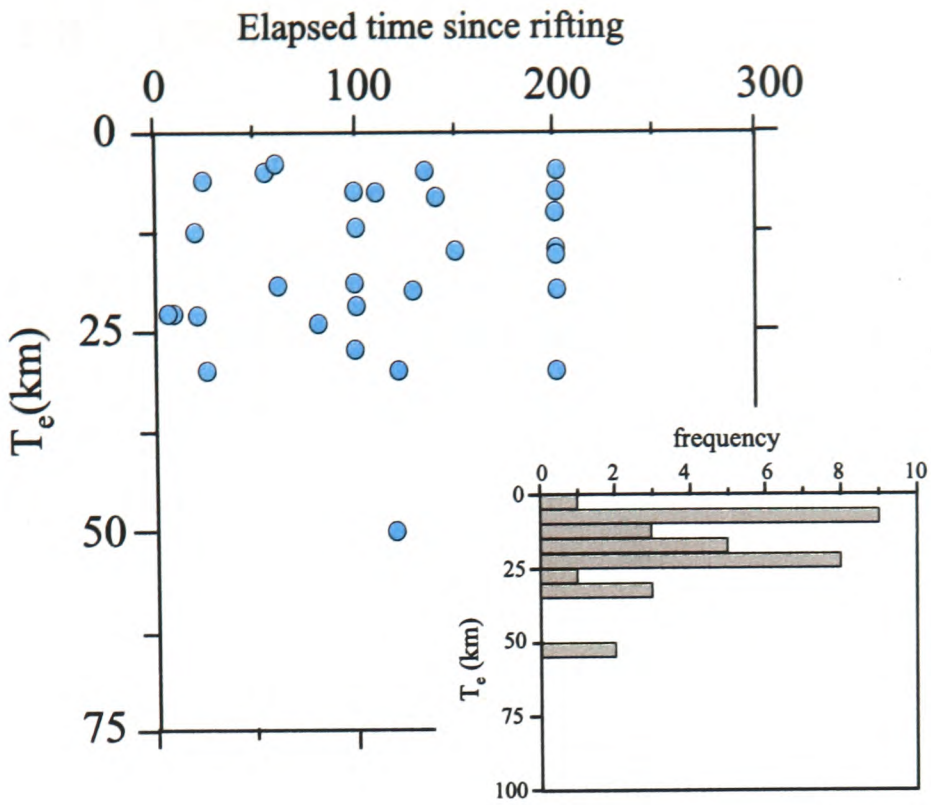

Figure 1.13: T_e estimates at passive continental margin settings (from Stewart [1998]). Values are ploted against the thermal age of the margin.

ted against the thermal age of the margin; i.e. counting from the last important rifting event. Although some correlations can be established between the bimodality of the T_e distribution (see histogram in inset) and the yield strength envelope (YSE) of stretched continental lithosphere, as highlighted by Stewart [1998], it appears that no strong correlation exists between the age of the lithosphere and T_e. It is worth noticing, however, that some of these estimates are based on the gravity signature of the entire sediment column, which has accumulated over tens or hundreds of millions years. Therefore, they reflect an average T_e over the time the margin has formed, and not at a particular time since rifting. Recent studies in a number of passive continental margin settings, which use large discrete loads deposited at different times following rifting suggest that the long-term strength of the thinned continental lithosphere may, in fact, increase with age since rifting (Rodger *et al.* [2006]; Close *et al.* [in Press] and references therein), in agreement with the predictions from both kinematical (Watts *et al.* [1982]) and dynamical (Burov & Poliakov [2001]) models of rifting.

The T_e's plotted in Figure 1.13 also indicate a weakened lithosphere at passive continental margins (> 80% of the values below 25 km), in relation to that found in other continental settings (Watts [2001b]). This suggests that factors such as widespread normal faulting (Ebinger *et al.* [1989]; Spadini & Podladchikov [1996]), thinning and heating of the continental lithosphere (Fowler & McKenzie [1989]; Burov & Poliakov [2001]), sediment thermal blanketing (Karner [1991]; Zhang [1993]; Lavier & Steckler [1997]) and yielding due to increased basement curvature under large sediment and/or magmatic loads (Watts [2001b]; Wyer & Watts [2006]) might effectively contribute to reduce the long-term flexural strength of rifted continental lithosphere.

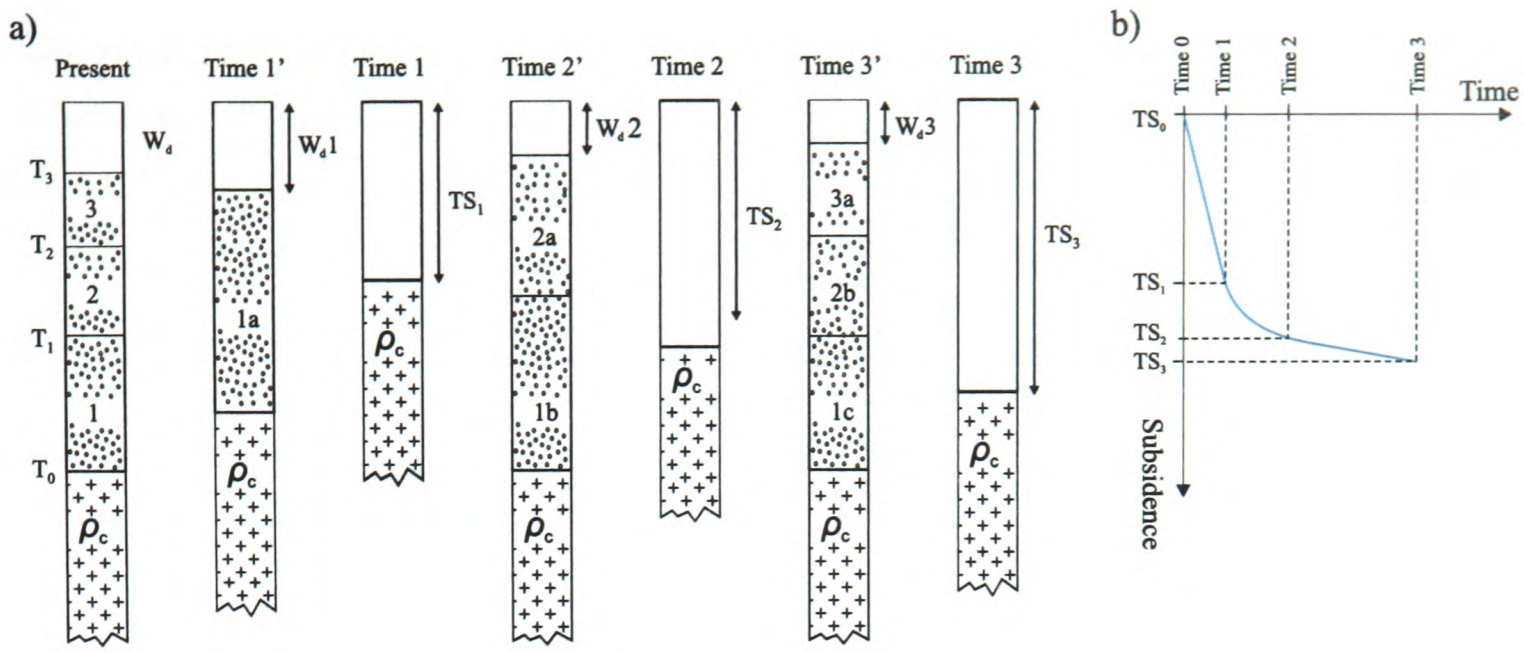

Figure 2.2: Multilayer 1-D backstripping. In a), the first column represents an observed (present day), fully lithified, stratigraphic sequence that comprises 3 compacted units. At Time 1', Unit 1 is decompacted to its original thickness and density (see equations 2.1 and 2.2). At Time 1, the basement depth in the absence of Unit 1 is isostatically restored (backstrip; Equation 2.5), recovering the TS at time-step 1. At Time 2' the initial thickness of Unit 2 is restored and Unit 1 compacted according to its new depth. At Time 2, the fully uncompacted Unit 2 and the partially compacted Unit 1 are backstripped, recovering the TS at time-step 2. This procedure is then repeated for sediment layer 3. In b), the corresponding TS curve is plotted. Modified from Bond & Kominz [1984].

$\bar{\rho}_s$ can then be substituted in Equation 2.5 and the tectonic subsidence/uplift calculated at a particular time (i.e. TS_i in Figure 2.2b). Figure 2.2b shows a typical backstrip from a rift-type basin, commonly referred to as the tectonic subsidence curve (e.g. (Steckler & Watts [1978])). It shows an initial, rapid subsidence event (syn-rift), followed by a long period ($\sim$ 50 to 100 m.y.) of exponential-like subsidence (post-rift).

2.2.2 Flexural Methods

A widely accepted model to determine the deformation of the lithosphere associated with long-term ($>$ 1 m.y.) geological loads (e.g. sediments, volcanics) is that of a thin elastic plate overlying an inviscid substrate; i.e. which acts at every point along the base of the plate with a force that is proportional to the deflection produced by the load (Watts [2001b] and references therein). This is a classical problem in engineering know as the Winkler foundation (Hetényi [1979]).

The thin plate approximation model assumes that the thickness of the deformed plate is small in relation to its width, and that only the stresses in the plane of the plate are significant (Timoshenko & Woinowsky-Krieger [1959]). Furthermore, by considering

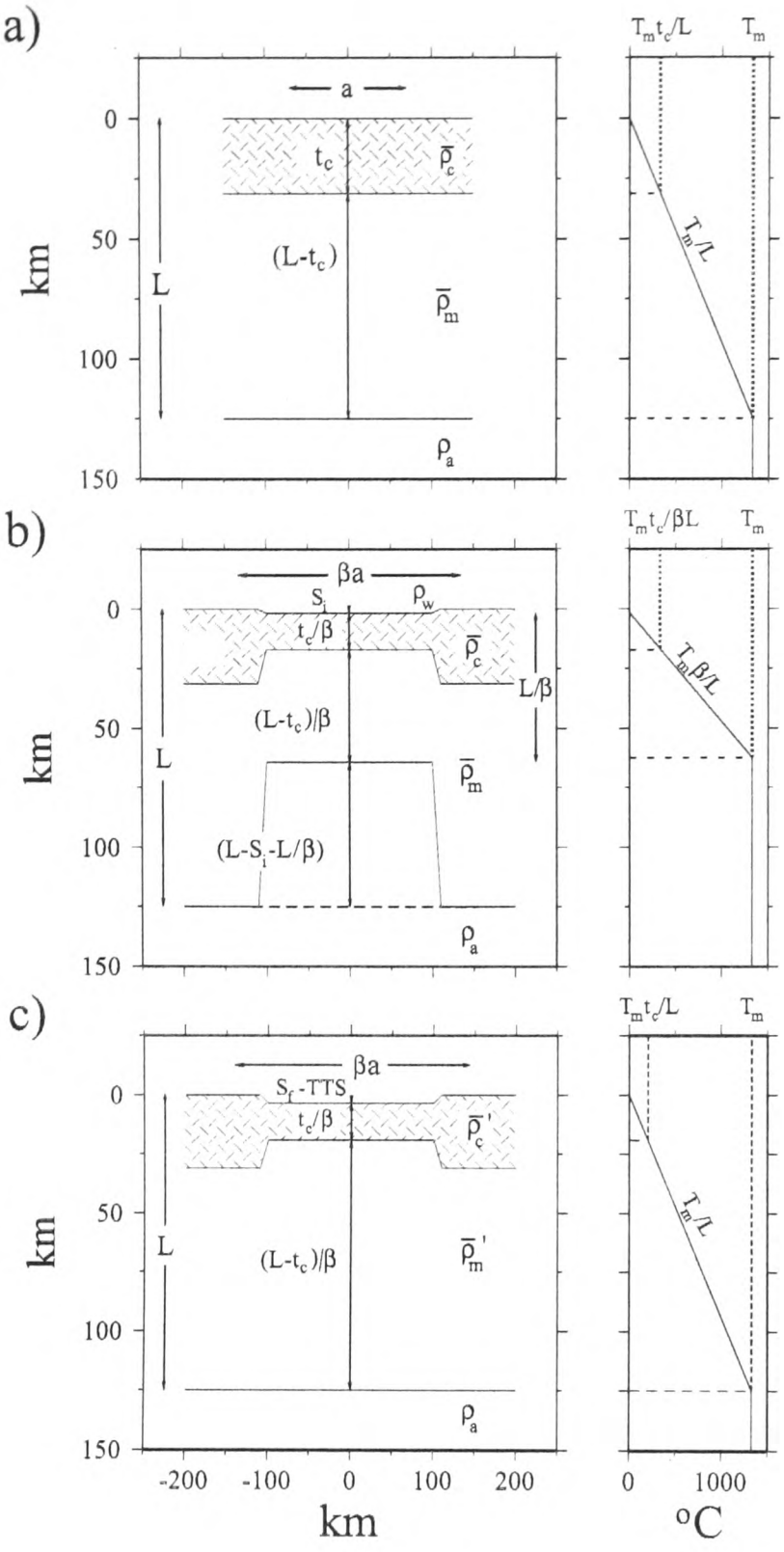

Figure 2.4: Two-stage rift model proposed by McKenzie [1978] to explain the formation and evolution of rift basins: subsidence (left) and thermal structure of the lithosphere (right). a) Pre-stretched lithosphere. b) After instantaneous rifting event. c) After thermal relaxation of the lithosphere and recovery of the initial temperature gradient. All the symbols are described in the text, together with the equations used to compute the margin's thermal and subsidence evolution (see also Appendix A).

$$P_{eq} = S_f \rho_w g + \frac{t_c}{\beta} \bar{\rho_c}' g + \left(L - S_f - \frac{t_c}{\beta} \right) \bar{\rho_m}' g \tag{2.18}$$

where S_f is the final basin subsidence, or the total tectonic subsidence (TTS), which results from both the thinning and the thermal relaxation.

From Figure 2.4c it is also evident that the initial geotherm (before stretching has occurred) is restored. However, the relative proportions of crust and mantle in the lithosphere are now different and, consequently, the expressions for the average densities of the crust and mantle have been altered.

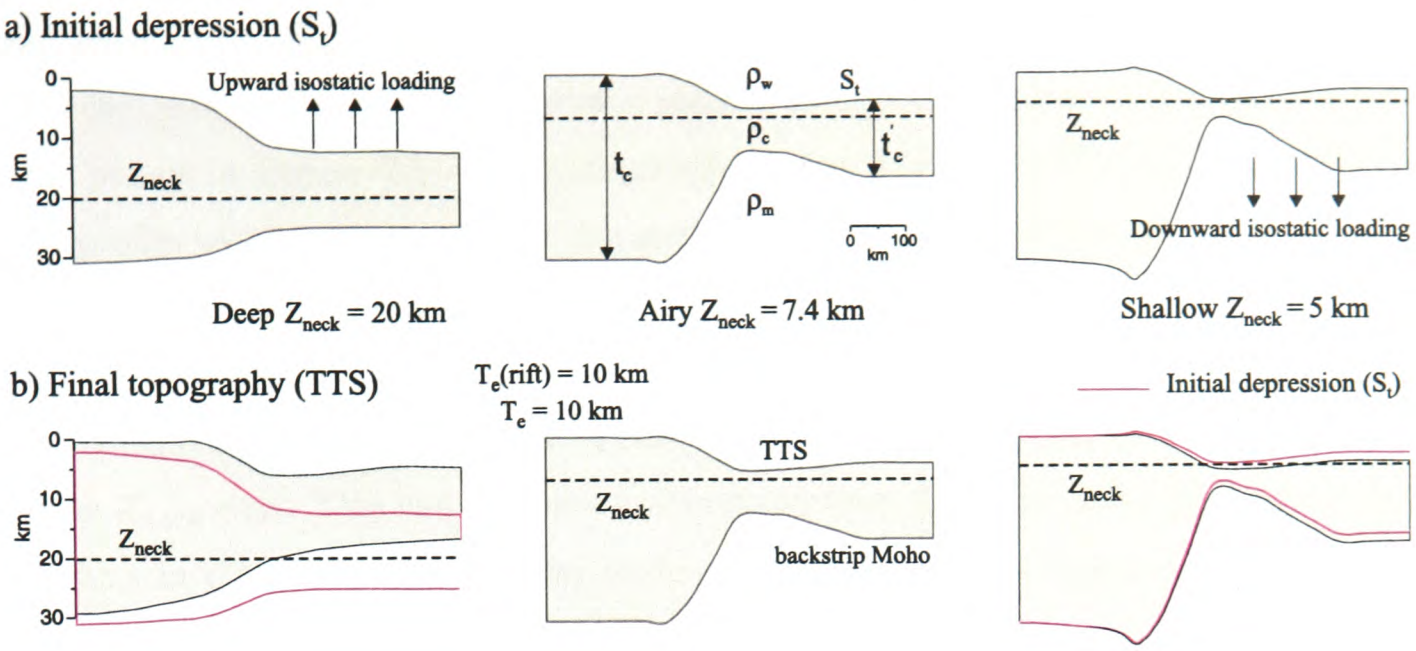

Figure 2.5: Introduction to the concept of lithospheric necking in extensional settings. According to Braun & Beaumont [1989], departures from an Airy-type model of extension will produce: Left - a net upward vertical force, if necking occurs at greater depths than predicted by the Airy model; Right - a downward vertical force, if necking is shallower than Airy predicted. The central panel shows the reference Airy rift model which, for the parameters given in Table 2.1 corresponds to a depth of necking, Z_{neck}, of 7.4 km (Watts & Stewart [1998]). The solid pink lines in the bottom panels show the initial basin geometry and calculated Moho for comparison. The Z_{neck} is represented in all the panels by the dashed black line. t_c' the thickness of the thinned crust.

plate, T_e(rift). For a given T_e(rift) and Z_{neck}, the formulation of Watts & Stewart [1998] predicts that,

$$\beta = \frac{Z_{neck}\zeta(k) + q_0}{\boldsymbol{Q_0}(k) - \boldsymbol{TTS^*}(k)\zeta} \tag{2.25}$$

where the bold upper case variables represent the Fourier transform of the lower case variables and k is the wavenumber; $TTS^* = TTS - Z_{neck}$; $q_0 = Z_{neck}(\rho_w - \rho_m) + t_c(\rho_m - \rho_c)$; $\zeta = Dk^4 + (\rho_m - \rho_w)g$.

Figure 2.5 illustrates the concept of Z_{neck} and associated syn-rift isostatic loads. In the central panel, an Airy-type rift margin (reference model) is generated, which for the parameters described in Table 2.1 (in Section 2.3.3) corresponds to a "neutral" Z_{neck} at 7.4 km (see Watts & Stewart [1998] for derivation). For a deeper value of Z_{neck} (left panel) the margin will subside more than predicted by the Airy model, and the isostatic loads will act upwards in the centre of the basin (i.e. the margin is in an upward state of flexure; Weissel & Karner [1989]; Kooi *et al.* [1992]). This results in the uplift of the rift flanks and downward bulging at the base of the slope (bottom left panel). On the

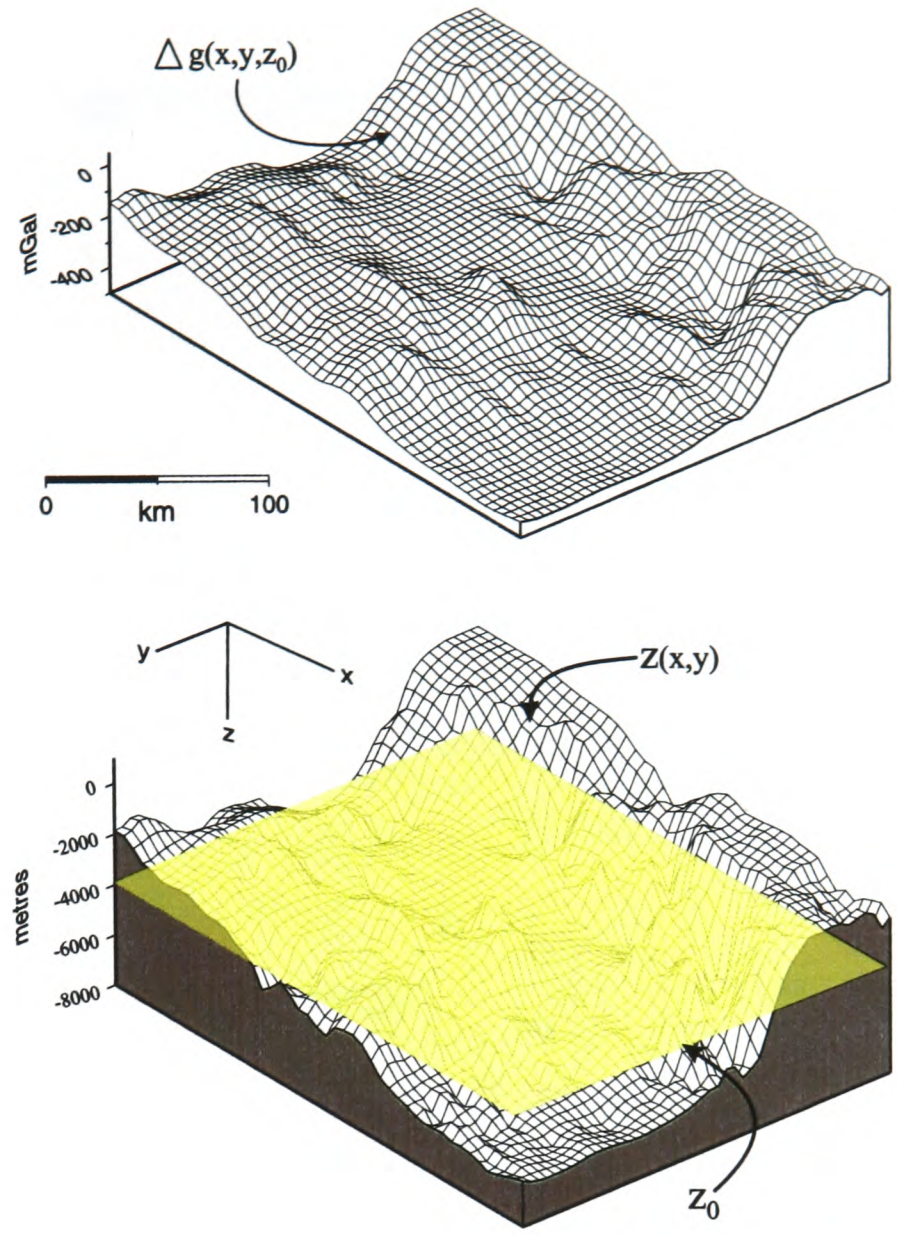

Figure 2.7: 3-D gravity anomaly calculation for an uneven, uniform layer $[Z(x,y)]$ of mean depth Z_0 (shaded yellow). Modified from Blakely [1996].

1. Backstrip the observed sediment loads to determine the basement TTS (dashed line in Figure 2.8a), assuming either a fixed or laterally varying T_e structure;

2. Calculate the β's and recover the geometry of the Moho at the time of rifting (i.e. the backstrip Moho), assuming either an Airy or finite strength model of rifting (Figure 2.8a), and compute the rift anomaly (water-crust + mantle-crust). This resulting anomaly shows a characteristic edge-effect, with a high over the shelf break and a low in the region of the continental slope and/or rise (Figure 2.8b);

3. Restore the sediment load to the margin and compute the flexure for the T_e structure used in step 1 (Figure 2.8c). The gravity anomaly associated with the sedimentation process can thus be obtained from the sum of loading (sediment-water) and flexural (sediment-crust + crust-mantle) effects (Figure 2.8d);

4. Add the rift and sedimentation anomalies and compare the "sum" to the observed gravity field. By varying the T_e structure used to backstrip the sediment loads

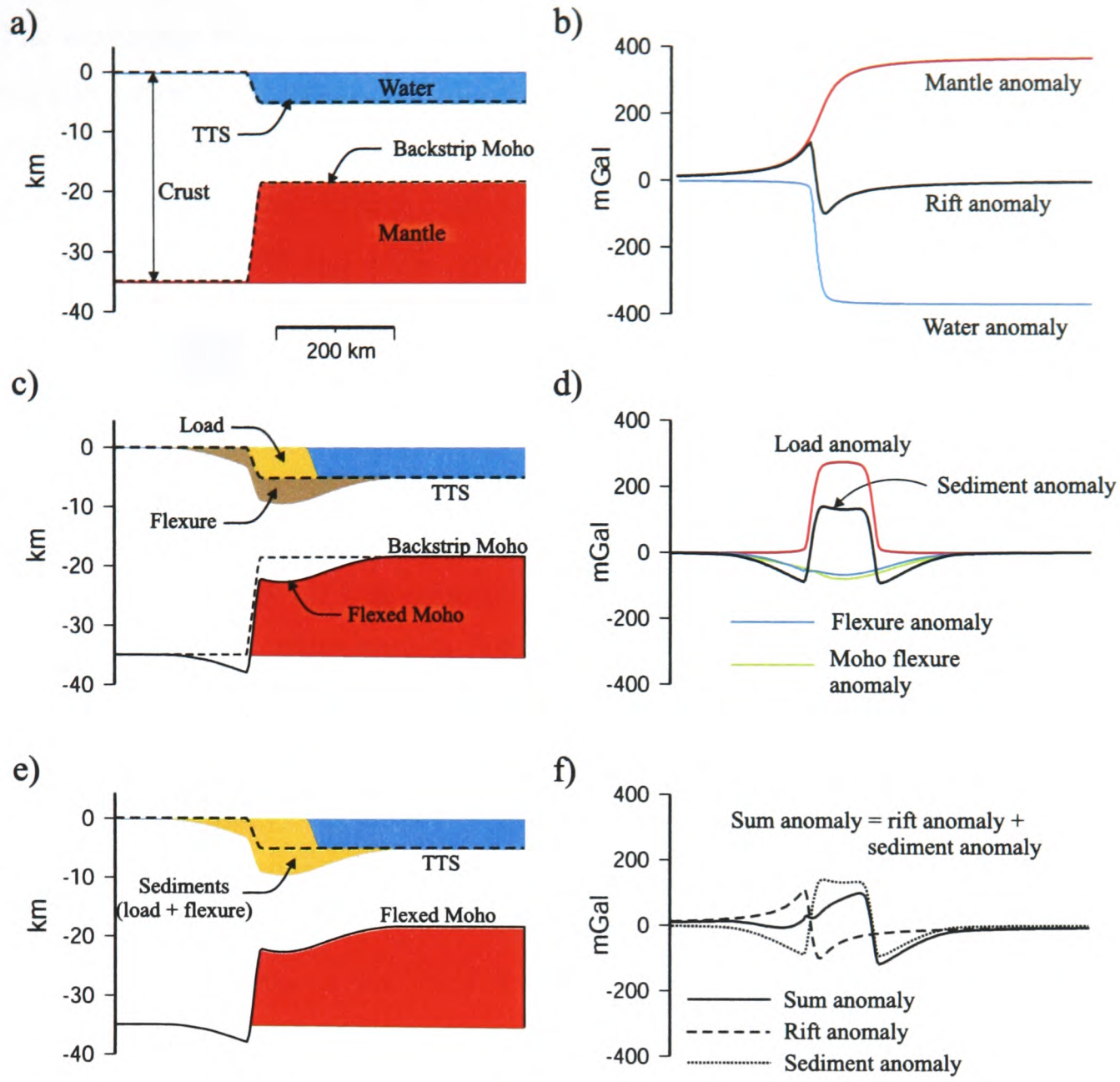

Figure 2.8: Illustration of the POGM methodology.

different sum anomalies will be computed, and constraints can be placed on the long-term mechanical structure across the margin transect (Figure 2.8f). Additional constraints can be obtained by comparing the final geometry of the gravity Moho (i.e. the flexed Moho in Figure 2.8e) to the seismic Moho constrained from wide-angle and refraction data.

In this thesis, POGM techniques will be applied to closely space profiles orthogonal to the local trend of the WIM (Chapter 5). The results from POGM will provide the basis to investigate the mechanical segmentation of the margin along strike, and its relationship with the structure of the Variscan orogen onshore, as well as the effects of rifting on the long-term ($>$ 1 m.y.) strength of the continental lithosphere. A number of conjugate transects along the West Iberia and Newfoundland margins will also be modelled (Chapter 7), to study the symmetry of the rift system, in terms of the margins thermal and mechanical structure, and how it relates to observations such as the unstretched crustal structure, the amount of basement subsidence and the width of the rift.

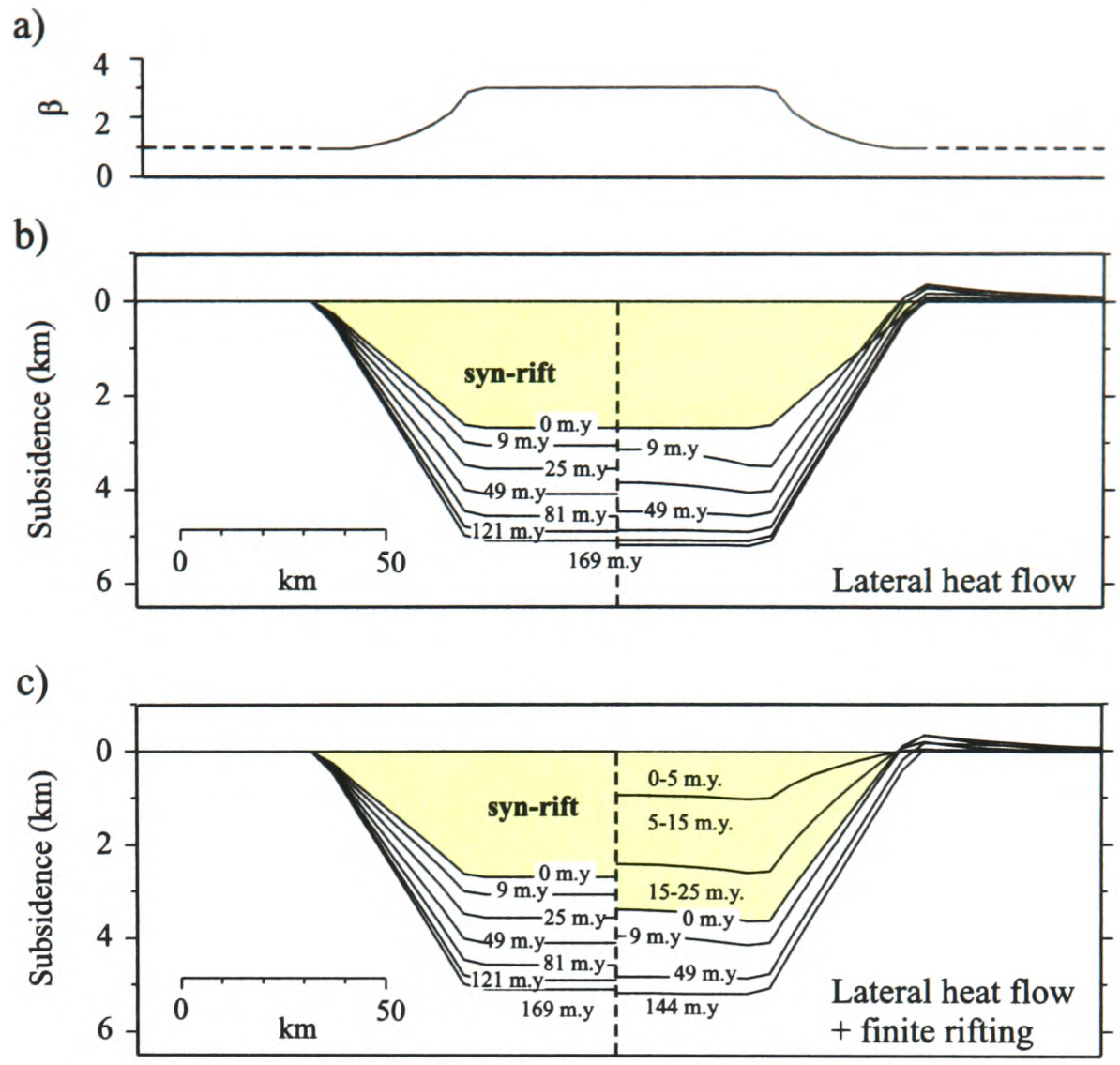

Figure 2.9: Predicted subsidence in a simple rift basin geometry. Effects of lateral heat flow (a) and finite rifting (b). During the post-rift stages, the subsidence was calculated at n^2 m.y. since rifting, where n = 0, 1 ,2 ,3 ,4... 13. During the syn-rift, the subsidence was determined at 5 m.y. intervals.

good agreement with those of Cochran [1983], who also noticed that the effects of finite rifting are particularly relevant when lateral as well as vertical heat flow is considered, even for rift durations < 20 m.y.

In the kinematic models which allow for finite rift durations, some important aspects of basin's evolution and thermal structure need to be taken into account. The *Mrift* code compiled in this study follows the model proposed by Cochran [1983], in that the total amount of stretching associated with a rifting event is first discretised into small increments of extension. The amount of thinning at each block of the basin profile, and correspondent horizontal stretching, is then computed for each time step assuming a particular β distribution throughout the syn-rift period (e.g. linear or exponential, see Section 2.3.3). Finally, at the end of each step the temperature structure is computed from Equation 2.27, and used as the new temperature structure in the next rift pulse.

As noticed by Cochran [1983], however, this poses a problem when calculating the Fourier coefficients which determine the vertical component of the temperature structure

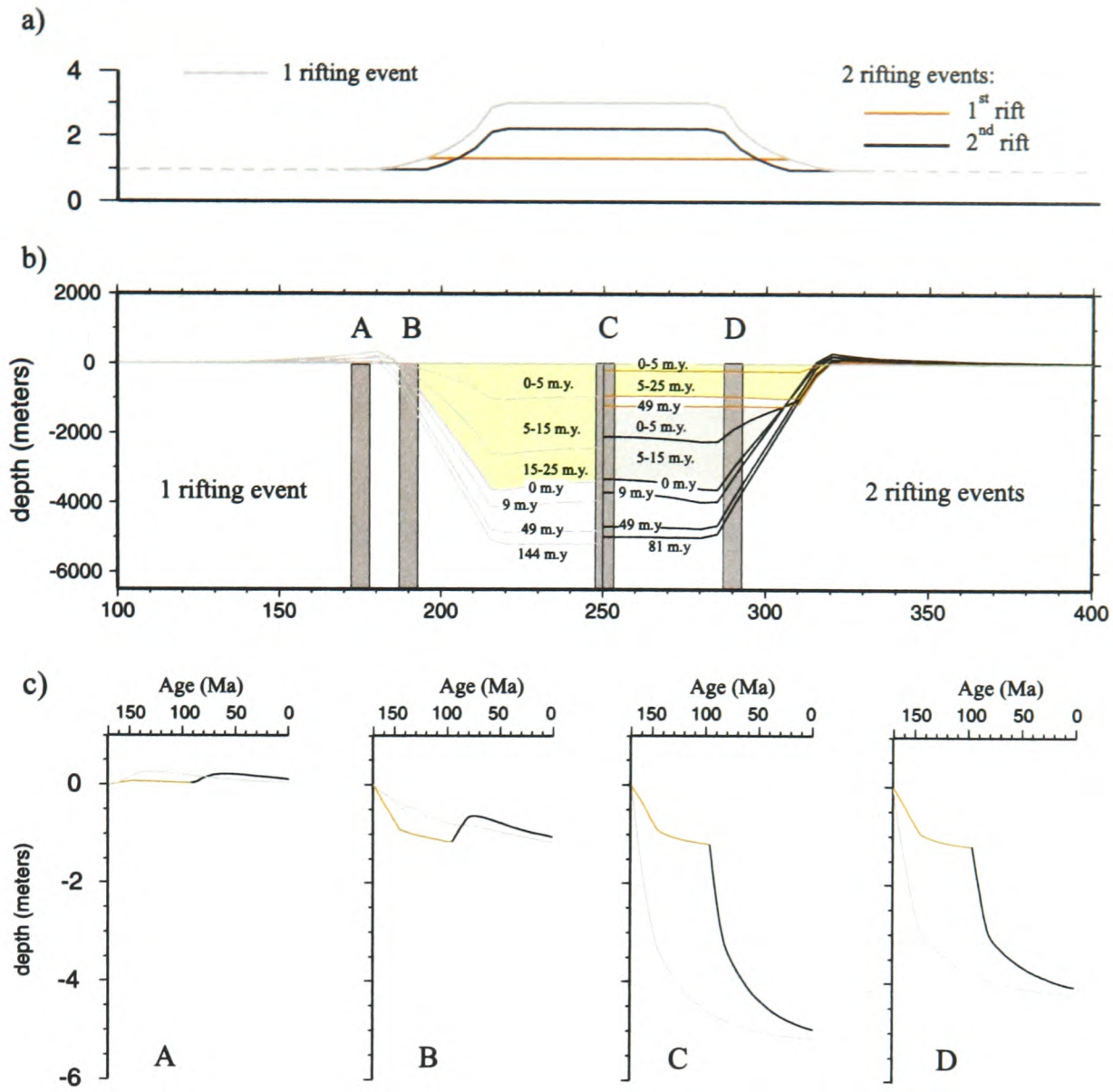

Figure 2.10: Predicted subsidence for single and multi-stage, finite duration continental rift scenarios. a) Shows the β's utilized to compute the basin subsidence. The grey lines correspond to the single rift scenario, which starts at 169 Ma and lasts for 25 m.y. The orange and black lines correspond to the first and second events in the multi-rift scenario, respectively. The first rift starts at 169 Ma and last for 25 m.y., and the second episode starts at 95 Ma and lasts for 15 m.y. The total amount of stretching is kept constant throughout the basin in both cases. b) Shows the subsidence history for the β's and rift times and durations described above. In c), the tectonic subsidence curves are shown at for 4 distinct locations.

upper slope (B), the lower slope (C) and the basin centre (D). The β's used to simulate the single and multi-stage rifting cases are shown in Figure 2.10a, where the total amount of stretching is kept constant between the 2 scenarios.

In the two-rift scenario, a 130 km wide, relatively shallow basin is initially formed. The β's corresponding to this event are relatively small (< 1.2, orange lines in Figure 2.10a). The lithosphere is then allowed to cool for a period of 49 m.y., before being subjected to a second stretching pulse (black lines). This second rift stage is more localized, with the β's increasing abruptly from 1 to > 2 in less than 25 km width. As a consequence,

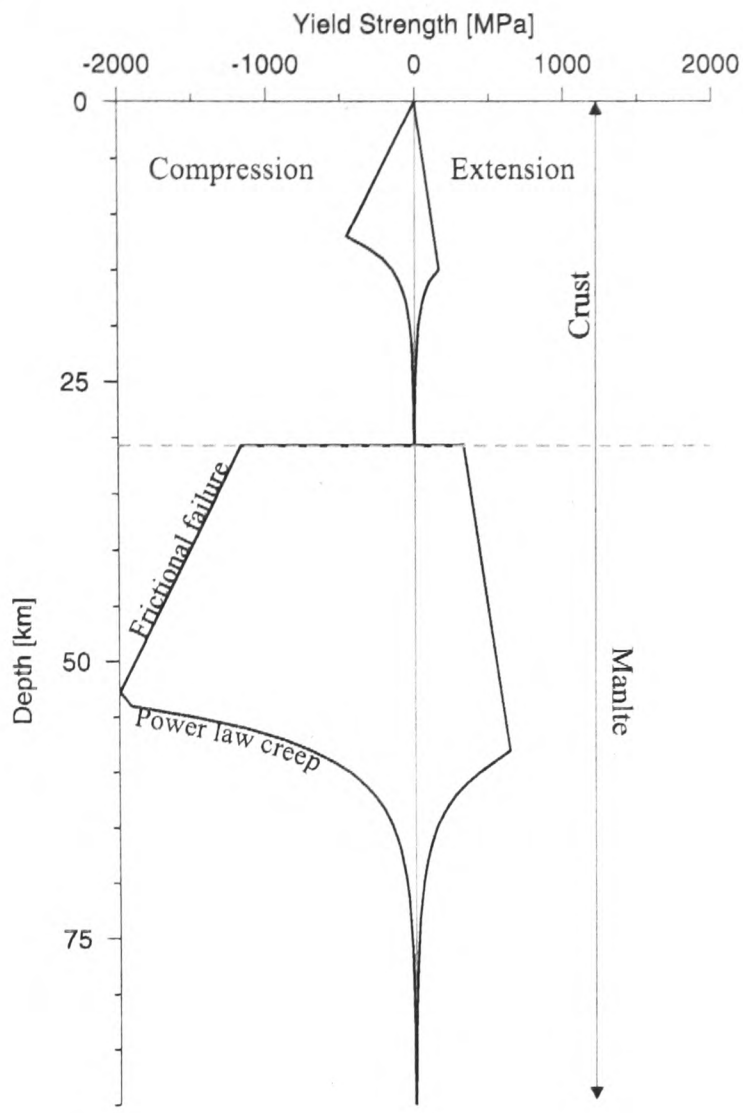

Figure 2.11: The yield strength envelope (YSE) derived from equations 2.28 to 2.30 an using typical continental crust and lithospheric mantle rheologies (see text).

Assuming linear elasticity, the fibre stresses generated due to flexure are directly related to the curvature of the plate by,

$$\sigma_f = -\frac{E}{1-\nu^2}\left(\frac{\partial^2 z}{\partial x^2}\right)(z - z_n)dz \tag{2.34}$$

where E and ν are the Young's modulus and Poisson's ratio, respectively.

If the entire thickness of the lithosphere behaves elastically, then T_e corresponds to the mechanical thickness (h) in Equation 2.33. This is the situation illustrated in Figure 2.12a, where the vertically integrated fibre stresses are calculated within the grey shaded area. However, if the plate bending stresses overcome those determined by the frictional resistance and dislocation creep properties of the materials failure will occur, with the consequent reduction in the thickness of the plate responding elastically (Figure 2.12b).

The examples shown in Figure 2.12 were built using a single rheology for the entire crust. As shown by Burov & Watts [2006], however, the presence of a strong lower crustal layer might result in a drastic increase of the overall rigidity of the lithosphere. This is mainly due to the effects of coupling/decoupling between the mechanically strong upper crust and upper olivine mantle layers (Figure 2.13). As demonstrated by Burov & Diament [1992], the T_e of a lithosphere composed of three mechanically decoupled layers (i.e. upper-middle crust, lower crust and mantle) can be approximated by the following expression,

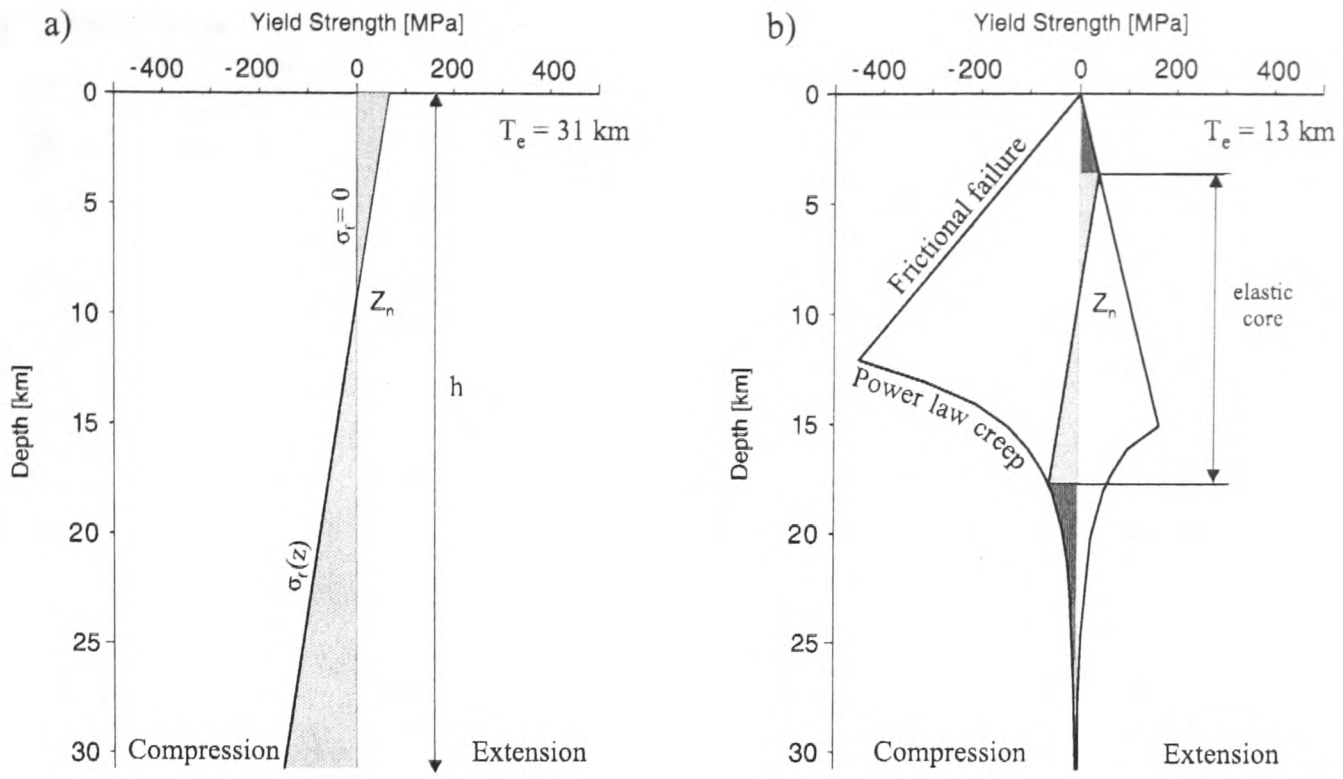

Figure 2.12: Relationship between the fibre stresses calculated in a thin bending plate a), and the YSE failure criterion for a crustal type rheology b). The light grey shaded areas show the region where the plate behaves elastically. In b), the dark shaded areas represent areas of the YSE where the elastic stresses exceed the strength of the material as determined by its frictional resistance (above) and dislocation creep properties (below). Consequently, the plate effective elastic thickness, T_e, will be reduced. z_n is the depth of the neutral surface (see text). Modified from Lowry & Smith [1995].

$$T_e = \left(Te_1^3 + Te_2^3 + Te_3^3\right)^{\frac{1}{3}} \tag{2.35}$$

This results in a significantly lower T_e then when vertically integrating the bending moment along the entire thickness of the lithosphere (i.e. Equation 2.33). In the *Mrift* code, the criterion for mechanical decoupling was established for the dislocation creep power law (which asymptotically approaches zero) when $\Delta\sigma < 20$MPa.

Figure 2.13 shows the sensitivity of the T_e calculated based on the YSE to variations in the rheology of the lower crust, strain rate and amount heat generated by the decaying of radioactive isotopes in the upper crustal layers. In Figure 2.13a, for example, changing from an aggregate lower crust (50% dry quartz and 50% anorthosite) to stronger, more mafic, anorthosite and mafic granulite compositions (see Table 2.2 for parameterisation and references) results in a progressive increase in the T_e, with a total variation of less than 10 km. This variation, obtained for a crustal thickness of 31 km and a lower crust of 10 km (see Table 2.1) is relatively small when compared to that estimated by Burov & Watts [2006] for a considerably thicker lower crust layer (15 km) in a 40 km thick crust.

The effects of mechanical coupling and decoupling are well noticed in Figure 2.13b

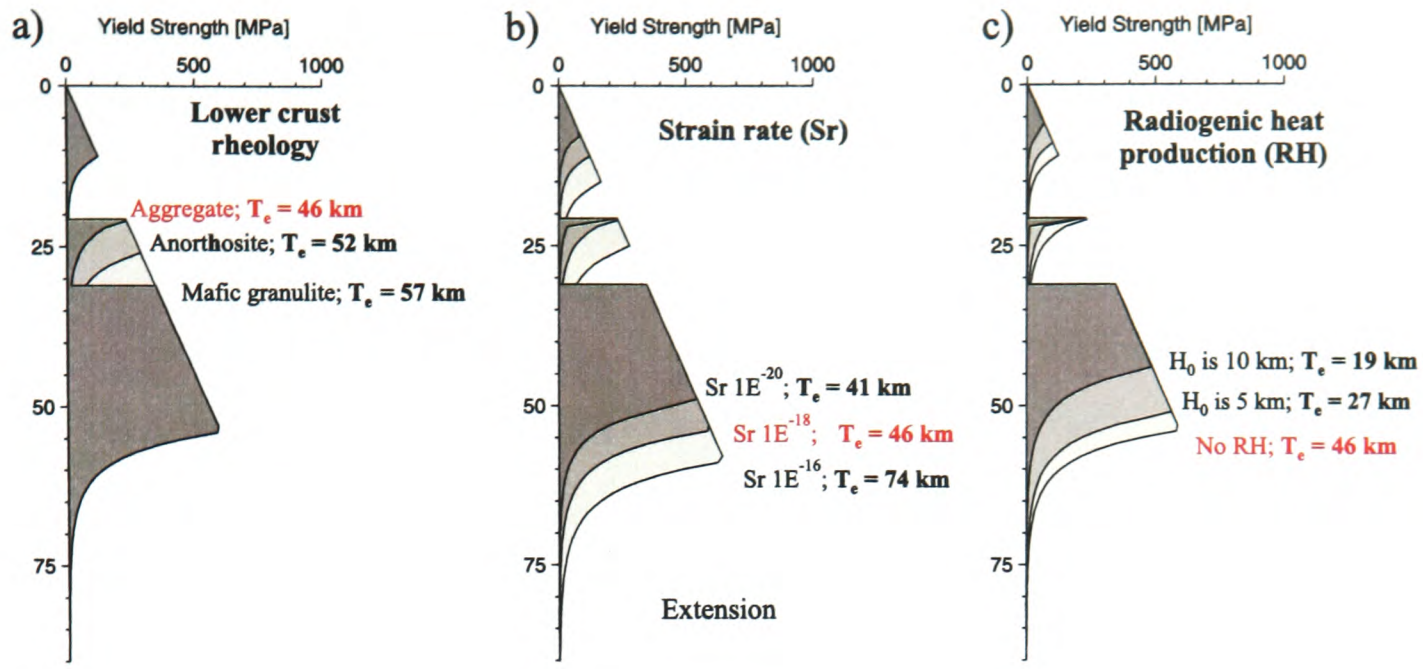

Figure 2.13: Sensitivity of the calculated T_e's to variations in the lower crust rheology (a), strain rates (b) and radiogenic heat production (c). For each YSE envelope the reference model (see Section 2.3.3) is highlighted in red. The lithospheric thermal parameterisation and rheologies are described in Tables 2.1 and 2.2, respectively. The dashed grey vertical line at 20MPa represents the limit for mechanical decoupling (see text). The greater oscillations in the calculated T_e's occur when coupling/decoupling between distinct rheological layers occurs.

and 2.13c, respectively. The strain rates control the thickness of a given rheological layer that deforms by dislocation creep (Equation 2.30). For the values tested in Figure 2.13b, which are within the range predicted for relatively small amounts of extension in rift basins ($\beta < 1.2$, e.g. White [1994]; Newman & White [1999]), significant variations in the calculated T_e's are obtained, especially for the higher strain rates, due to the mechanical coupling between the upper-middle and lower crust and the mantle.

The heat generated by the decaying of radioactive isotopes (mainly uranium, thorium and potassium) in crustal rocks has long since been recognised as an important contribution of the net heat flux measure at the surface of the continents (Roy *et al.* [1968]; Lachenbruch [1970]). The considered heat production follows an exponential decrease with depth (z), which according to Lachenbruch [1970] is given by,

$$A(z) = A_0 e^{(-z/D_0)} \tag{2.36}$$

where A_0 is the surface radiogenic heat production and D_0 is the length scale parameter that describes the depth-dependent decrease.

If the contribution from heat produced in the crust is taken into account an increase in the Moho temperature between 50^0 and 100^0C is expected (Morgan & Sass [1984]). Pasquale *et al.* [1997], for example, estimated an increase of $\sim 80^0$C for a 28 km thick

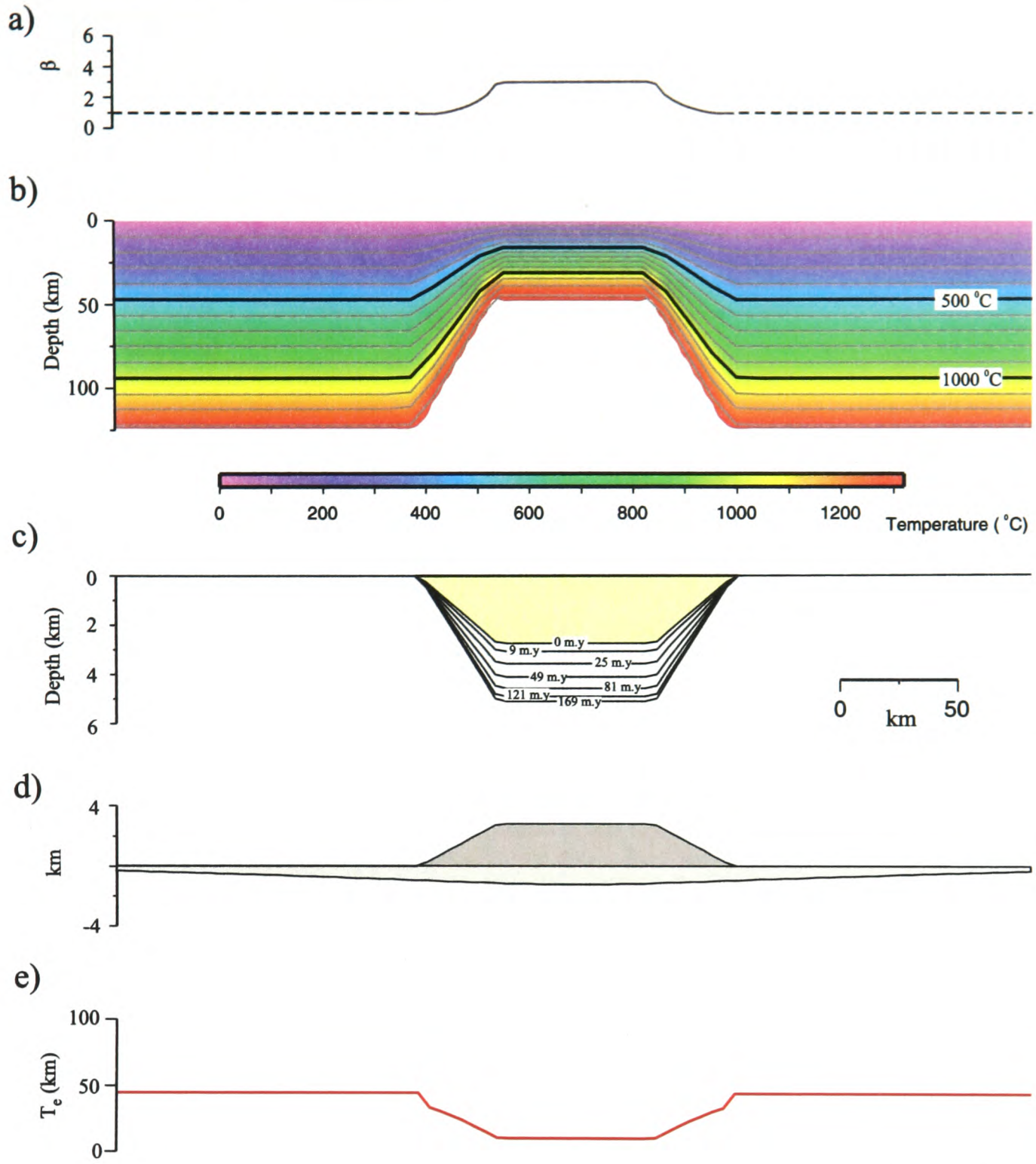

Figure 2.14: Temperature structure, subsidence, T_e and flexure at rift basins. a) Stretching factors, β's, used to generated the basin profile. b) Temperature structure at the end of rifting, calculated from the β's shown in (a), and assuming an instantaneous rifting event. The effects of lateral heat flow and radioactive heat production in the crust have not been taken into account. The model parameters are shown in Table 2.1. c) Predicted margin subsidence at n^2 m.y. since rifting, where n = 0, 1 ,2 ,3 ,4... 13. d) Sedimentary load corresponding to the syn-rift stage (dark grey shading), defined between the initial subsidence (yellow area in c) and the paleowater depths (assumed at the pre-deformation surface), and calculated flexural deformation (light grey shading), from the T_e structure shown in (e). e) T_e's calculated at the end of rifting from the thermal structure of the margin and YSE considerations (see text).

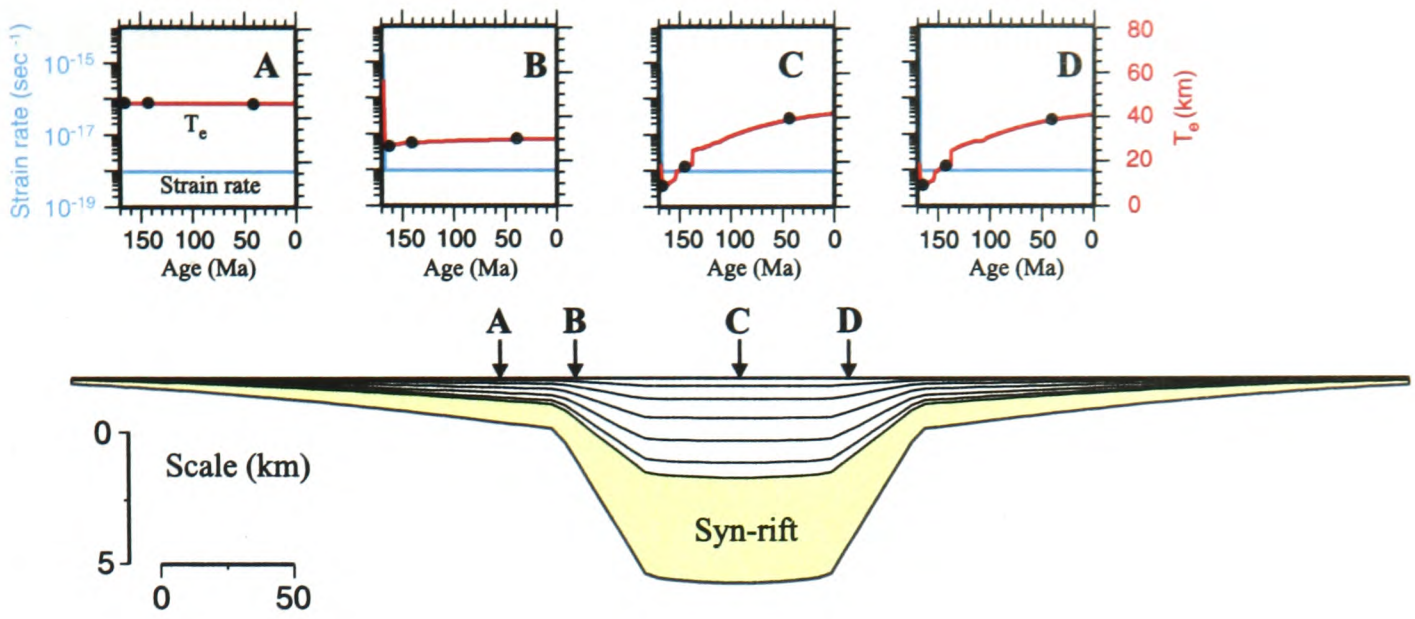

Figure 2.15: The steer's head basin: T_e's, strain rates and predicted stratigraphy.

depicted in locations B, C and D (see Figure 2.13 for the relationship between the strain rates, the T_e's and the YSE).

For the case presented here, a minimum T_e of $\sim$ 10 km is obtained in the centre of the basin (Location C) at the end of rifting. As it cools, the lithosphere progressively recovers its strength, in agreement with the predictions from dynamical models of rifting (Burov & Poliakov [2001]). However, the T_e's do not increase in a continuous way. Instead, some major steps are observed, which are due to the mechanical coupling between distinct rheological layers as the thermal gradients are attenuated (e.g. at 155 and 135 Ma in locations C and D in Figure 2.15). At the basin edges, where the thermal structure has not been significantly perturbed (Figure 2.14b), the effects of stretching predominate, and the T_e's remain relatively constant between the end of the stretching event and the Present (Location B).

Variations to this reference case, in terms of the computed stratigraphy and T_e evolution, are shown in Figure 2.16; the reference model of Figure 2.15 is shown is Figure 2.16a. In all the examples the rift occurs instantaneously, and zero paleowater depths are assumed. When lateral heat flow is included in the model, the flanks of the basin will be uplifted and the post-rift subsidence in the centre of the basin increases, as depicted in Figure 2.9b. This results in the thinning of the post-rift sediment units near the basin edges and their thickenning towards the centre (Figure 2.16b).

In Figure 2.16c, the thermal structure of the lithosphere was calculated taking into account the combined effects of lateral heat flow and radiogenic heat production. As depicted in Figure 2.13c, including the amount heat produced by the decay of radioactive elements in the crust results in the weakening of the lithosphere. This is observed particularly near the basin flanks, where the crust remains thick (e.g. Location B). As a consequence, the width of the basin is reduced, with the flexural bulge moving inwards by

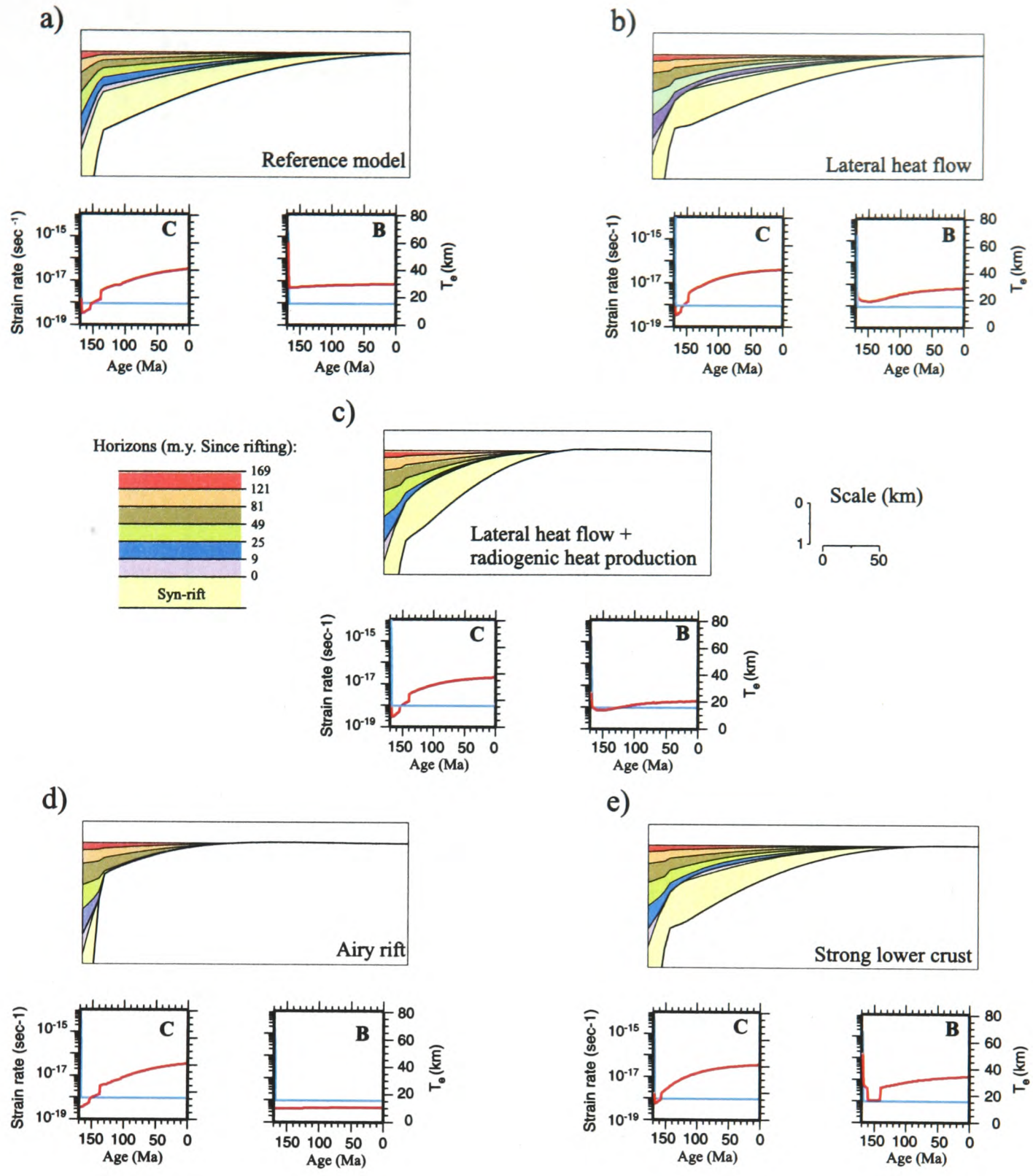

Figure 2.16: The steer's head basin: predicted stratigraphy (detail on the basin flanks) and calculated T_e's for different thermal and rheological modelling settings. In all cases an instantaneous rift event is assumed and the paleowater depths correspond to the pre-deformation surface (i.e. zero paleowater depths). The reference model in a) is that of Figure 2.15. In b), the effects of lateral heat flow have been included. In c) both lateral heat flow and radiogenic heat production in the crust are accounted for. d) and e) are variations to the model in c), where zero strength during rifting , i.e. $T_e = 0$, or a strong lower crust rheology (mafic granulite; see Table 2.2) was assumed, respectively. The the T_e-strain rate graphics correspond to the locations B (upper slope) and C (basin centre) of Figure 2.15.

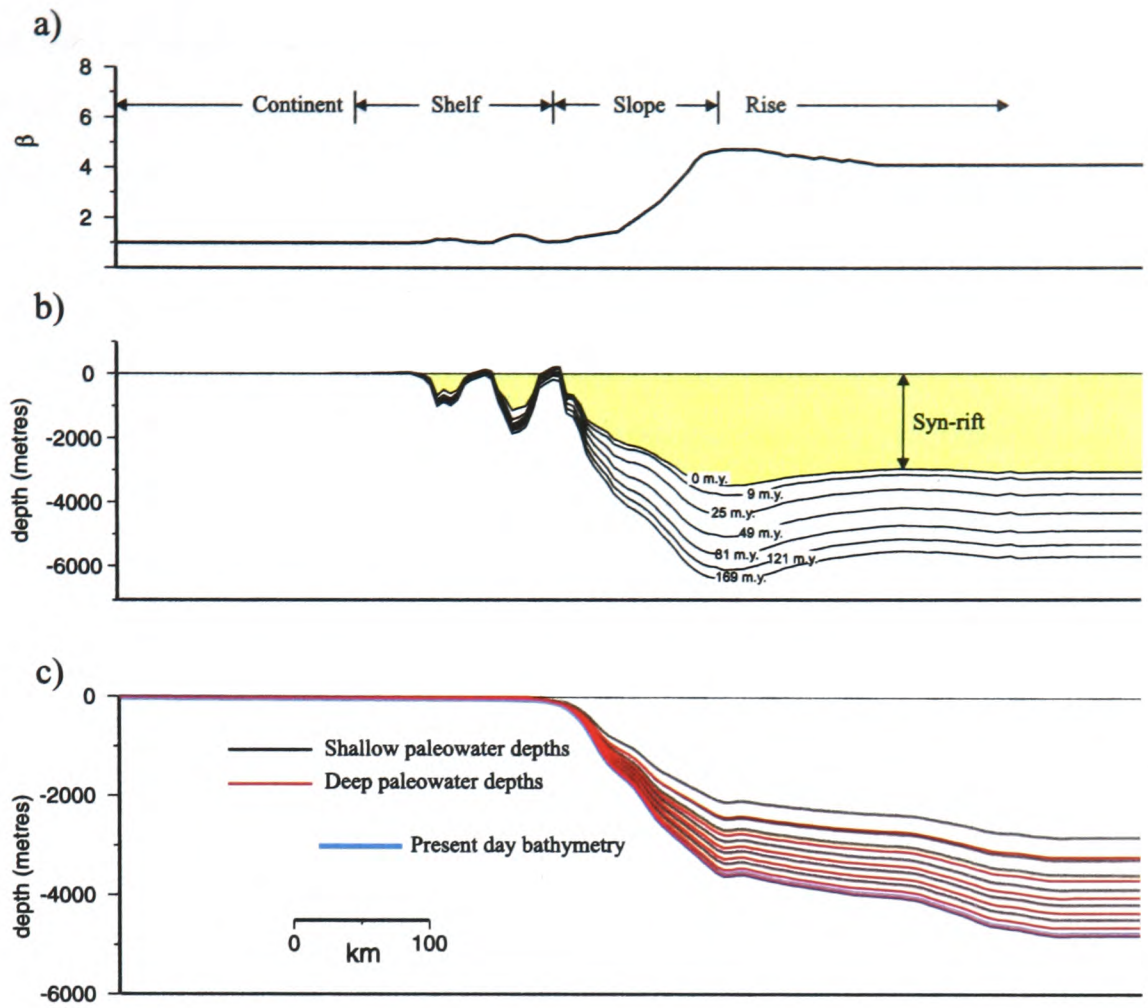

Figure 2.17: Synthetic passive continental margin transect: a) Stretching factors (β's); b) Subsidence; c) Paleowater depths. The subsidence was calculated for an instantaneous rifting event and accounting for both vertical and lateral heat flow at n^2 m.y. since rifting, where n = 0, 1 ,2 ,3 ,4... 13. The paleobathymetries are imaged from an hypothetical present day bathymetry (thick blue line) and calculated in proportion to the amount of syn-rift margin subsidence (see text).

m (Figure 2.17a; see also Figure 1.2). The assumption of zero paleowater depths, or the pre-deformation surface, is therefore not valid to model the stratigraphy at these settings.

The paleobathymetries at passive continental margins are, in most cases, largely unknown, or estimated with a large degree of uncertainty, particularly in the distal margin (i.e. outer slope and rise). First, because most commercial drilling in the past focused along the continental shelf and onshore basins, and DSDP and ODP drill sites are sparse and often located over basement highs, where the stratigraphic sections are incomplete. And second, because the gravity and current driven (e.g. turbidites, debris flows and slides, contourites, etc), and the pelagic/hemi-pelagic deposits, which dominate the sedimentation in continental slope and rise environments (e.g. Winterer [1980]), are poor in fossil benthic communities, or other sensitive paleowater depth indicators.

Figure 2.17a and 2.17b show the stretching factors (β's) and predicted subsidence along a synthetic passive continental margin transect, respectively. The profile comprises two narrow basin depressions bordering the continent (up to 50 km width), a relatively

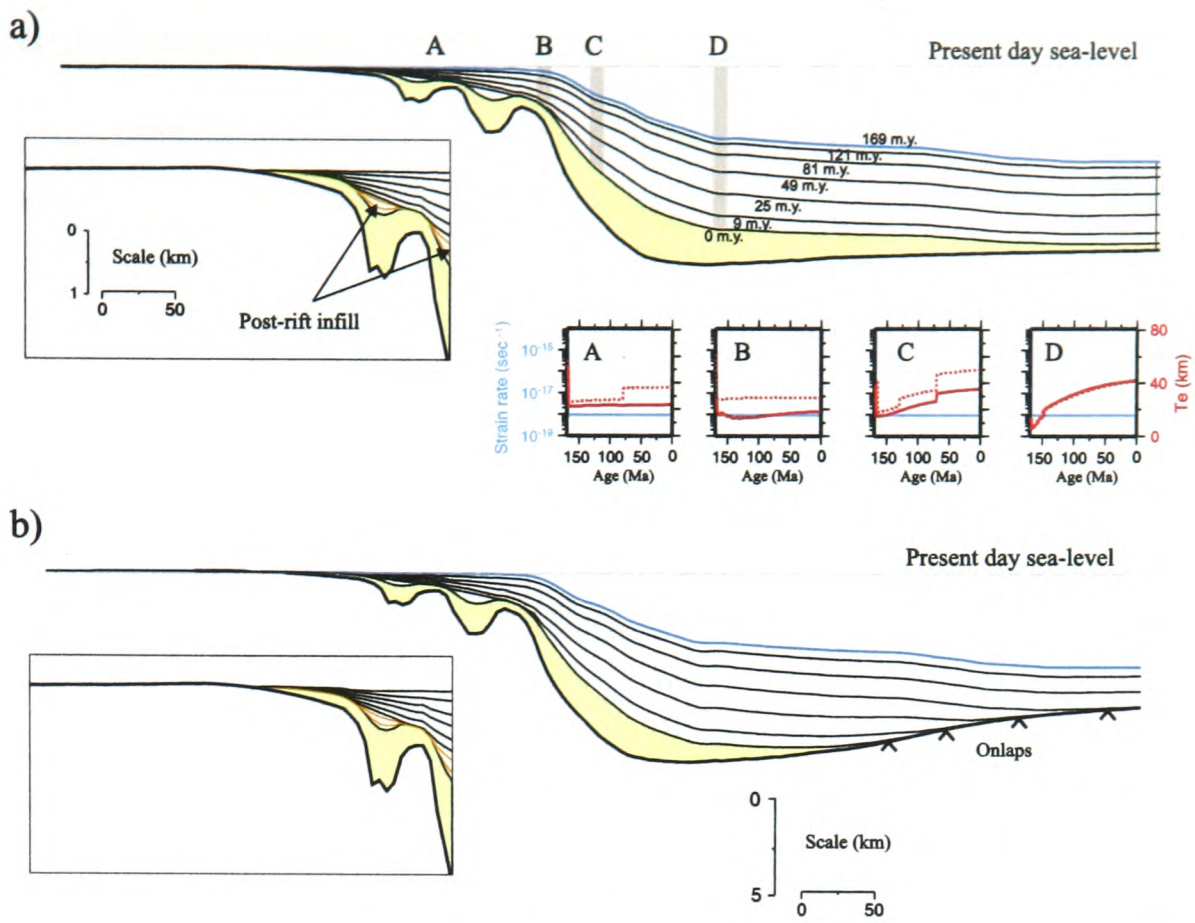

Figure 2.18: Predicted stratigraphy, T_e's and strain rates in a synthetic passive continental margin transect. The β's and subsidence history are shown in Figure 2.17a and 2.17b, respectively. In a) and b) the stratigraphy is calculated using the shallow and deep paleobathymetries shown in Figure 2.18, respectively. In the T_e-strain rate graphics the dotted lines are obtained without the contributions from lateral heat flow.

The calculated T_e's along this hypothetical margin transect (red lines in the T_e-strain rate graphics shown in Figure 2.18) are similar for the shallow and deep paleobathymetry cases, indicating that the differences in the basement curvature caused by the variations in the size of the sediment loads are not relevant for the overall strength of the lithosphere. Over the shelf and upper slope, locations A and B in Figure 2.18, respectively, the T_e's vary between 15 and 25 km, and remain relatively low throughout the margin's post-rift evolution. This is due to the effects of radiogenic heat production in the upper-middle crust, as described for the steer's head basin (see Figure 2.16c). In the lower continental slope and rise, locations C and D in Figure 2.18, respectively, T_e increases following rifting, as a result of cooling and lithospheric thickening, where the step-like increments are caused by mechanical coupling between strong crust and mantle layers.

The dashed red lines in the T_e-strain rate graphics correspond to the T_e's calculated when lateral heat flow is not included in the thermal model. These show a significant increase in the rigidity of the basement along the shelf and slope which, during post-rift times reaches up to 38 km. As discussed for the steer's head basin, this would result in thinner post-rift sediment units and the widening of the basin flanks.

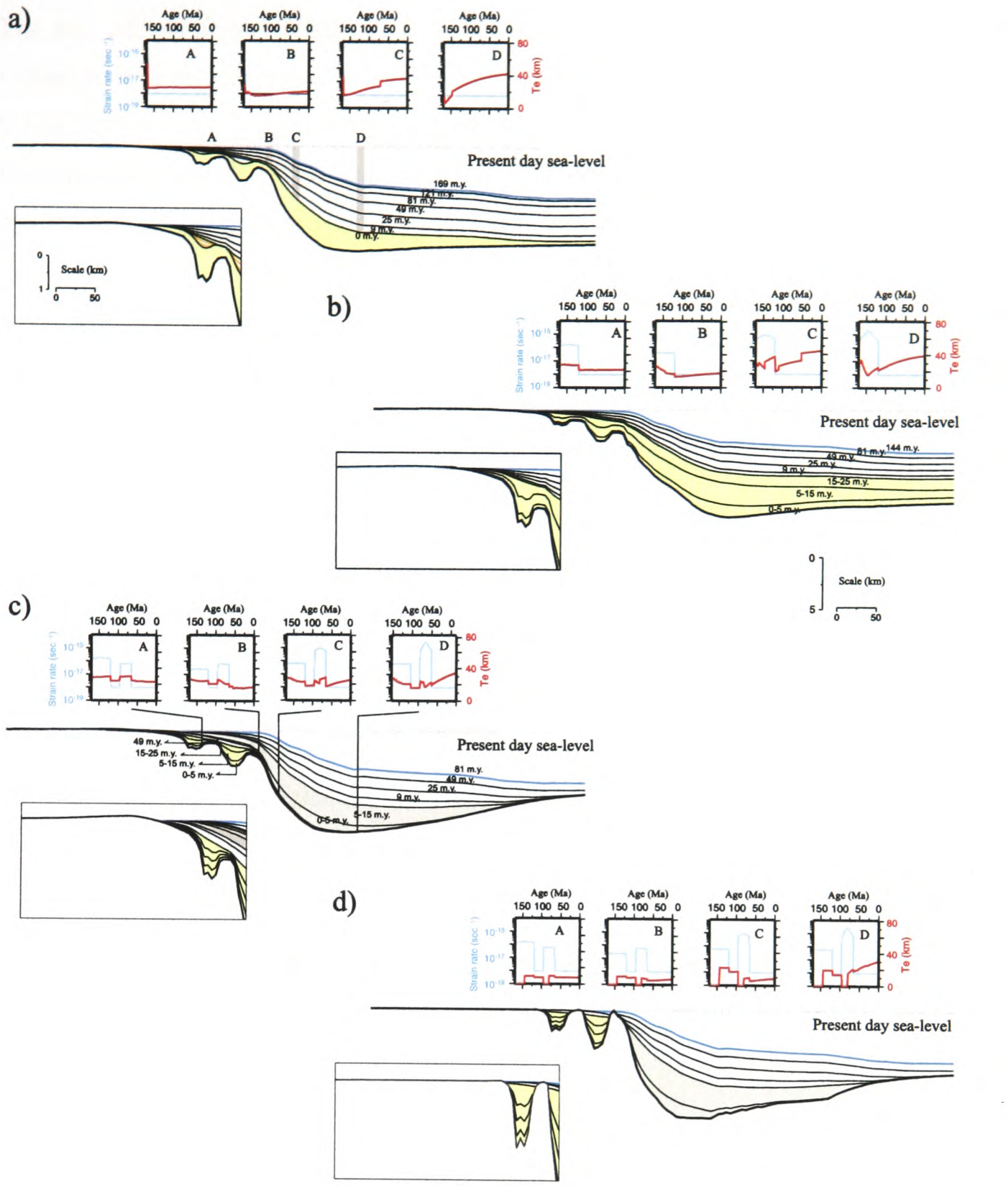

Figure 2.19: Finite rifting and multi-stage continental rifting passive margin scenarios: predicted stratigraphy, T_e's and strain rates. a) Single, instantaneous, rifting episode. b) Single, finite duration (25 m.y.) rifting episode. c) Two finite duration (25 m.y. and 15 m.y.) rifting episodes; d) As in c) but assuming zero lithospheric strength during rifting. In all the cases, both the effects of lateral heat flow and radiogenic heat production have been taken into account. The total amount of extension along the basin is the same between the single and the two-rift scenarios (see total β's in Figure 2.17a). The yellow and grey shaded areas highlight the syn-rift sediment packages deposited during the first and second rift events, respectively. The syn-rift periods and ages of the post-rift horizons in relation to the end of the last rifting event are indicated, as in figures 2.9 and 2.10.

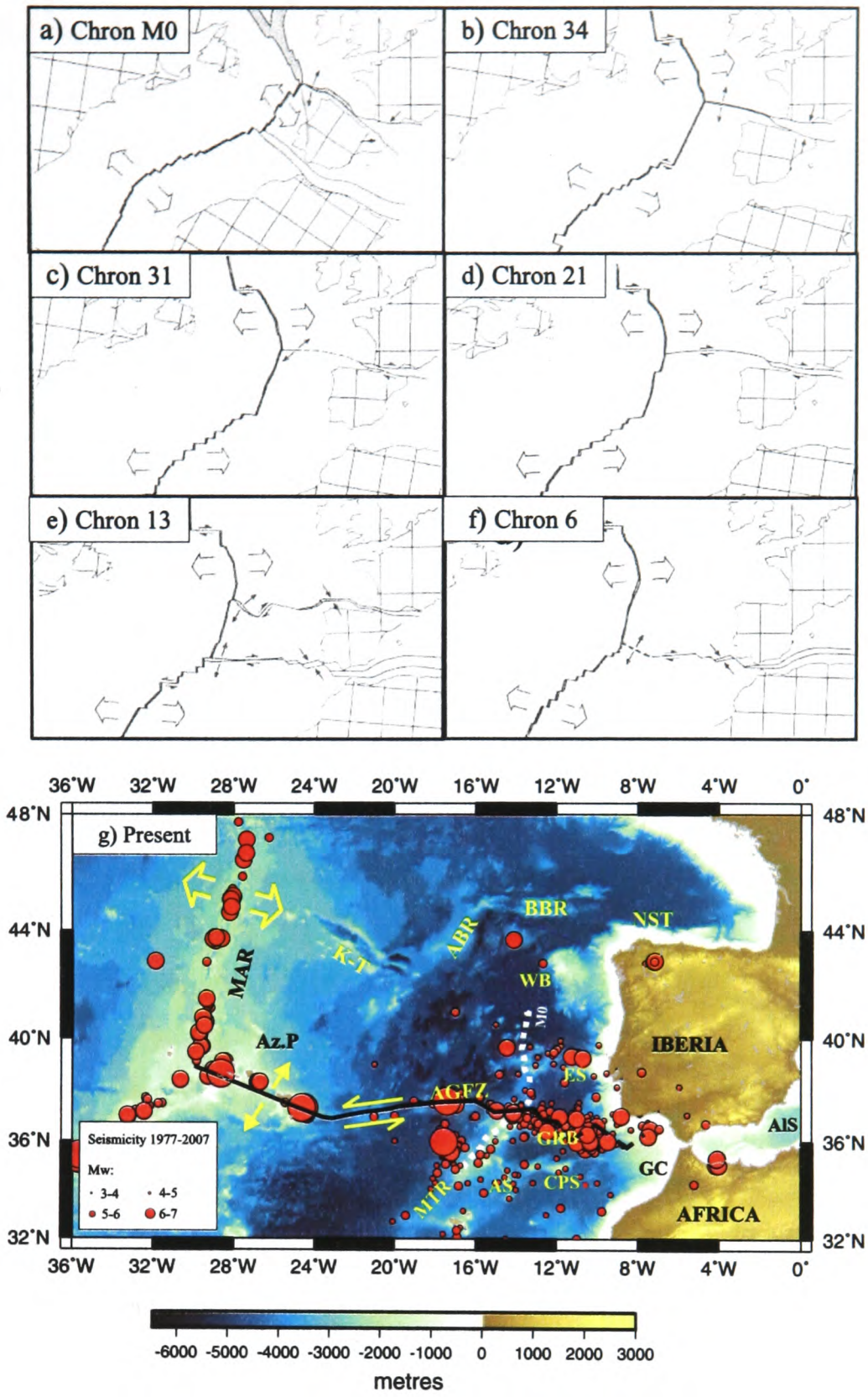

Figure 3.1: Plate tectonic setting of the Iberian microplate since continental break-up in the Early Cretaceous. The arrows in the figures indicate the relative plate motion. Dark grey areas in (a) to (f) represent regions of overlaps between plates (modified from Srivastava *et al.* [1990b]). In g), the present day instrumental seismicity is represented by the red dots (extracted from the IRIS network; *http://www.iris.edu*), where size is proportional to magnitude. The bathymetry is extracted from GEBCO [2003]. Acronyms are as follows: ABR, Azores-Biscay Rise; AGFZ, Azores Gibraltar Fracture Zone; AS, Ampere Seamount; AlS, Alboran Sea; AzP, Azores Plateau; BBR, Bay of Biscay Ridge; CPS, Coral-Patch Seamount; ES, Estremadura Spur; GC, Gulf of Cadiz; GRB, Gorringe Bank; KT, Kings Trough; MAR, Mid-Atlantic Ridge; MTR, Madeira Tore Rise; NST, North Spanish Trough; WB, Western Banks.

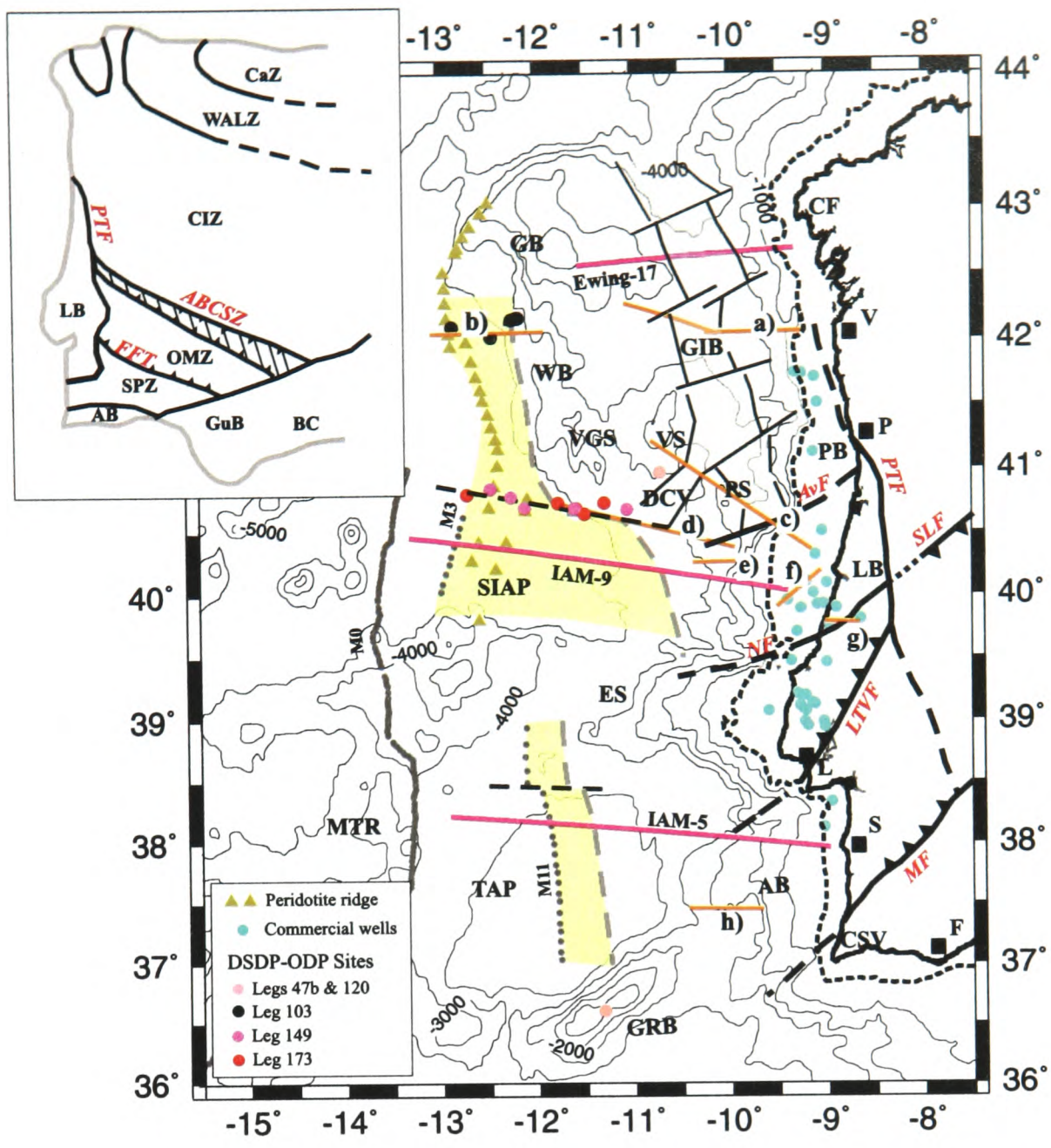

This segmentation is controlled by both the structure and zonation of the Variscan orogen (inset of Figure 3.2) and by variations in the style of rifting, amount of magmatism and compressional deformation from the latest Cretaceous onwards (e.g. Pinheiro *et al.* [1996] and references therein).

Between Cape Finisterra and the Aveiro Fault ($\sim$ 40.7-43°N), the continental shelf is 30-40 km wide, and an $\sim$ 300 km long interior basin (the Galicia Interior Basin) separates the slope from a marginal plateau (the Western Banks region; Murillas *et al.* [1990]) which comprises the Galicia Bank and a number of other prominent seamounts (the Porto, Vigo and Vasco da Gama seamounts; Figure 3.2). The seismic data shows that these features are mainly associated with NNW-SSE trending horsts which formed during the Mesozoic rifting and were reactivated under compression during the Cenozoic (Boillot *et al.* [1979]; Mougenot [1988]; (Figure 3.3a-c). The southeastern limit of the Western Banks is marked by a prominent submarine canyon, the D. Carlos Valley, which is probably one of the main conduits of sediments from the shelf and the Western Banks plateau into the Southern Iberia Abyssal Plain (Gardner & Kidd [1987]).

The structure of the Galicia Interior Basin is controlled by NW-SE to NNW-SSE and

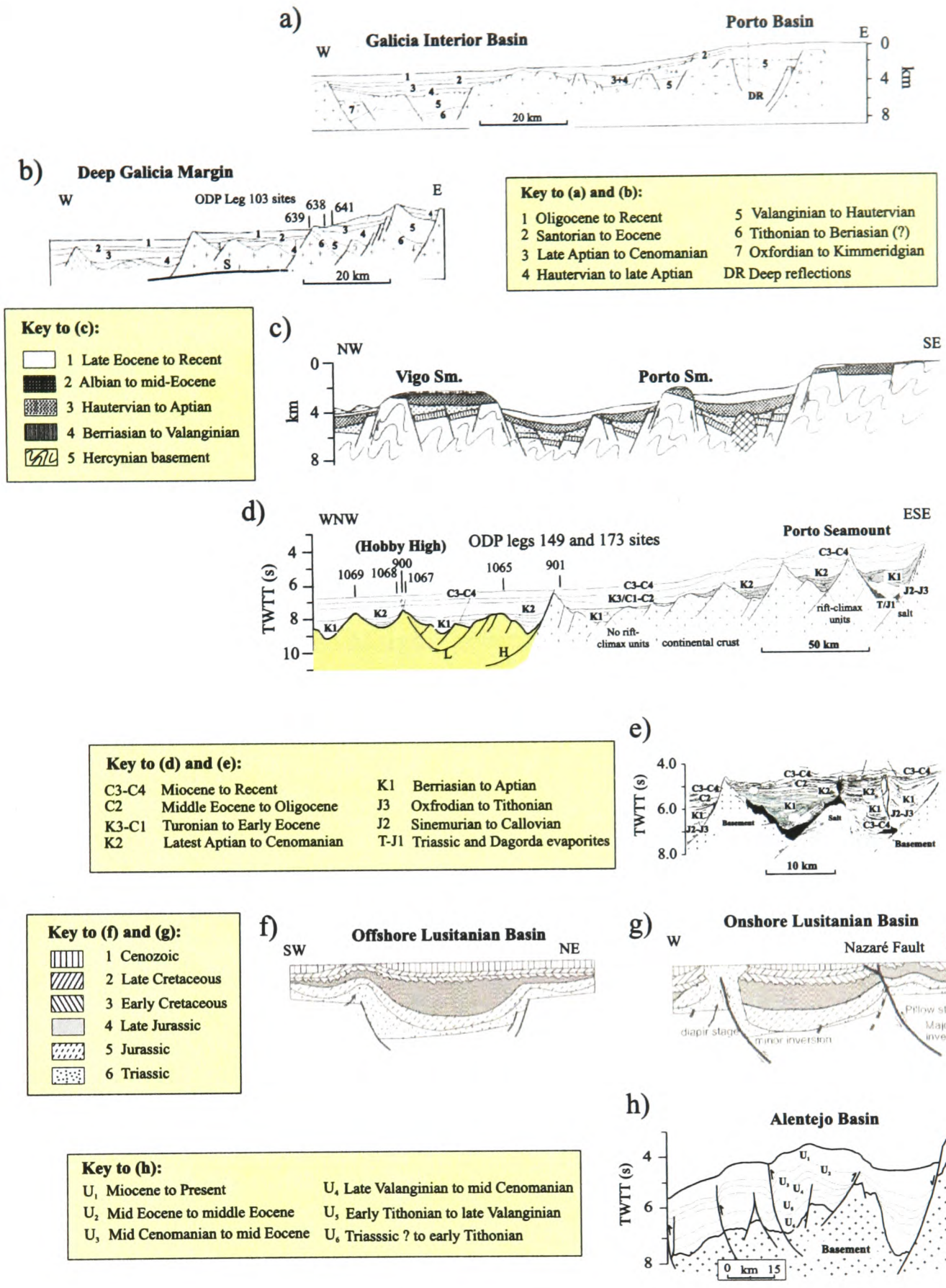

Figure 3.3: Schematic stratigraphic sections along the West Iberia Margin. The profiles are located in Figure 3.2. References for the sections are as follows: a) and b) Murillas *et al.* [1990]; c) Wilson *et al.* [1989]; d) Alves *et al.* [2006] and Krawczyk *et al.* [1996]; e) Alves *et al.* [2006]; f) and g) Rasmussen *et al.* [1998]; h) this study (see Section 5.6). Region's acronyms are as in figures 3.1 and 3.2. Note that both horizontal and vertical scales are given for each section, and the vertical scale may be in km or in seconds of two-way travel time (TWTT).

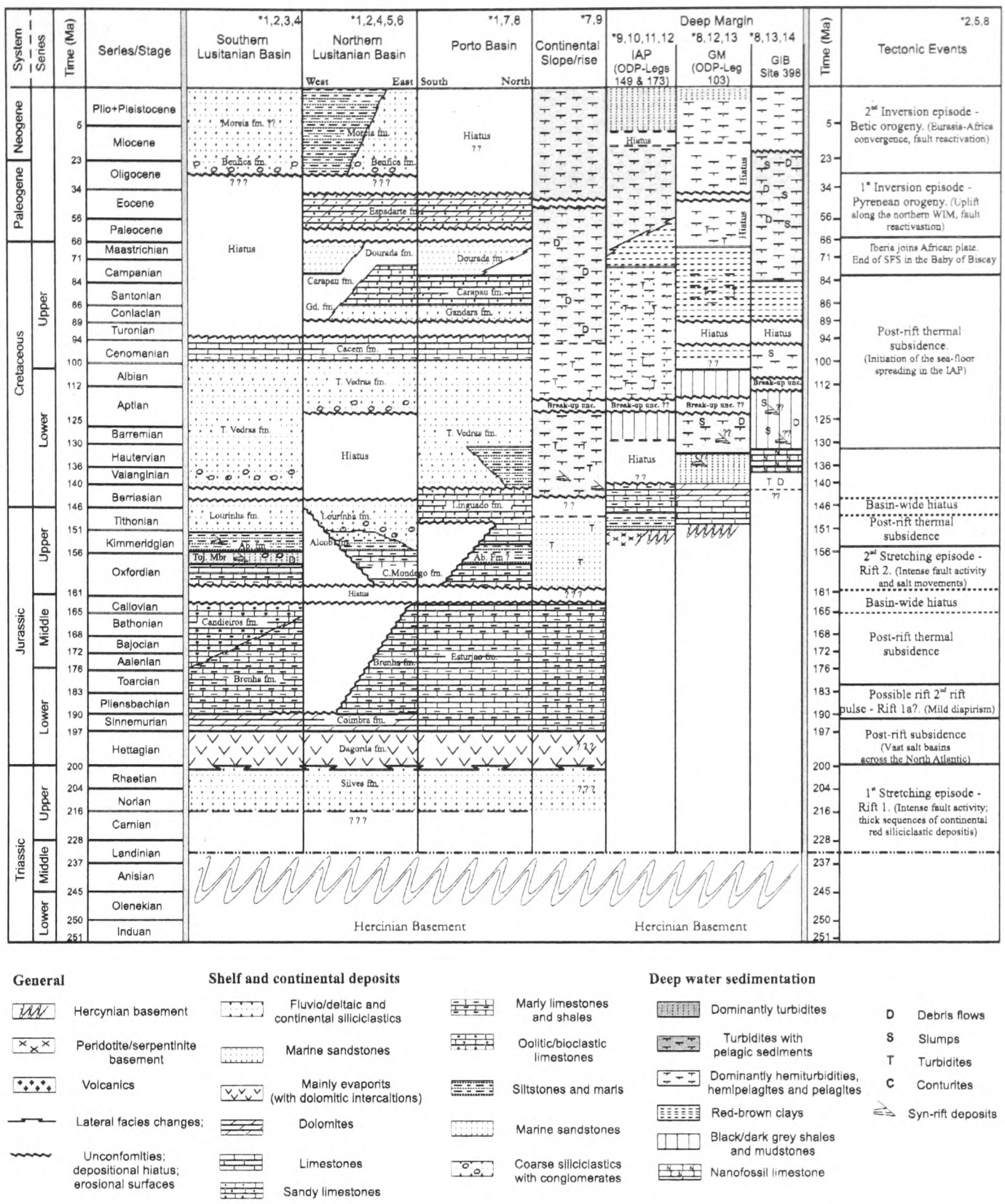

Figure 3.4: Stratigraphy summary of the main sedimentary basins in the West Iberia proximal and distal margins (Modified from Pinheiro *et al.* [1996]; see Figure 3.2 for location of the basins). The simplified tectonic history is shown in the right column. References used are: 1, Witt [1977]; 2, Wilson *et al.* [1989]; 3, Leinfelder & Wilson [1998]; 4, Rasmussen *et al.* [1998]; 5, Alves *et al.* [2002b]; 6, Cunha & Reis [1995]; 7, Moita *et al.* [1996]; 8, Murillas *et al.* [1990]; 9, Alves *et al.* [2006]; 10, Concherio & Wise [2001]; 11, Milkert *et al.* [1996]; 12, Wilson *et al.* [1996] and Wilson *et al.* [2001]; 13, Mauffret & Montadert [1988]; 14, Groupe-Galice [1979]. The utilized timescale is that of Gradstein *et al.* [2004]. GM stands Galicia Margin. Other acronyms are as in figures 3.1 and 3.2.

shear stretching model initially put forward by de Charpal *et al.* [1978], the models of Boillot *et al.* [1988a] and Winterer *et al.* [1988] (in Figure 3.5b and c, respectively) assume lithospheric-scale simple shear, where S is the master detachment fault separating crustal rocks in the upper plate from mantle rocks (possibly serpentinized peridotite, Boillot *et al.* [1989]) in the lower plate. In the model of Boillot *et al.* [1988a], S dips to the east, and continued lithospheric stretching leads to the exposure of the so-called peridotie ridge to the west, immediately before the onset of seafloor spreading.

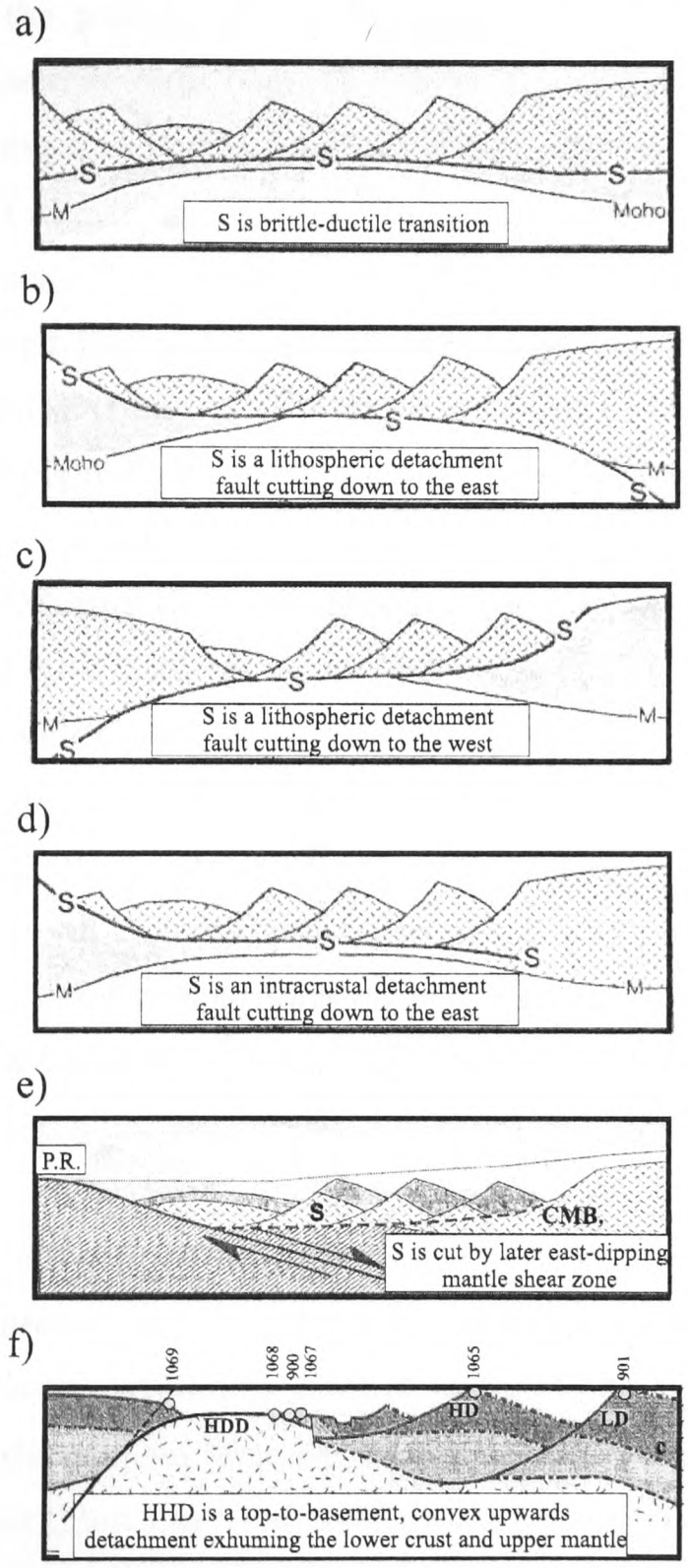

Figure 3.5: Schematic representation of some of the proposed rift models for the late stages of rifting and continental break-up along the WIM. The top five models refer to the Galicia Margin and differ in the relative position of the S detachment in the crust, its sense of dipping and in the overall style and geometry of rifting: a) Pure shear, de Charpal *et al.* [1978]; b) East dipping simple shear, Boillot *et al.* [1988a]; c) West dipping simple shear, Winterer *et al.* [1988]; d) Combined pure and simple shear, Sibuet [1992]; e) S is anthitetic or cut by a master east dipping shear zone, Reston *et al.* [1995]. Modified from Reston *et al.* [1995]. The model shown in f) has been proposed for the Southern Iberia Abyssal Plain, Manatschal *et al.* [2001] and Whitmarsh *et al.* [2001a]. It suggests three generations of detachment faults and the exhumation of the lower crust and upper mantle along a top-to-basement detachment, HDD.

Boillot *et al.* [1988a], and later Sibuet [1992] (Figure 3.5d), were particularly concerned with the discrepancies between the amount of stretching measured from the normal faulting in the upper crust and that inferred from the subsidence. In the model proposed by Sibuet [1992], S is interpreted as a major dipping to the east detachment, cutting through the upper-middle crust, and separating the less stretched upper brittle

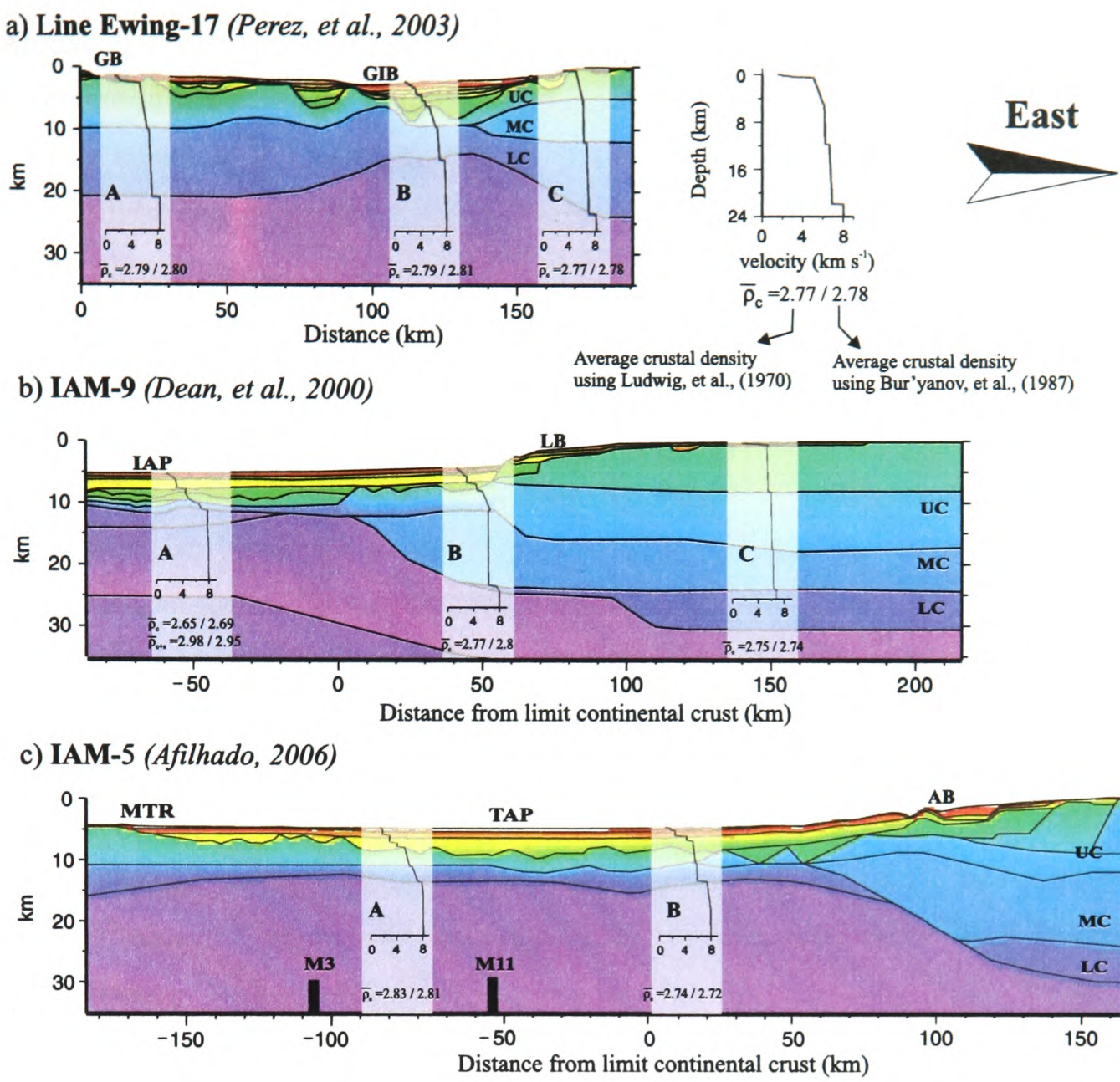

Figure 3.6: Velocity models along three wide-angle/refraction seismic sections in the WIM (thick pink lines in Figure 3.2). Along each model, three P-wave velocity (V_p)-depth profiles are displayed (A, B and C). Two average crustal densities were also calculated, using either the V_p-density conversion function of Zelt [1994] or that of Bur'yanov *et al.* [1987] (see text). For the OCTZ in line IAM-9 (V_p-depth Profile A) two average densities were calculated, depending on the depth of the Moho (see text).

on rock samples from dredge hauls and cores. According to these authors, the tonalites and granodiorites recovered from the Galicia Bank region are a strong indicator that the basement is a fragment of the Ossa Morena terrane from continental Iberia.

Oceanwards of the continental rise, the velocity structure of the basement in the Southern Iberia and Tagus abyssal plains is distinct from that observed in typical continental or oceanic crust. In the Southern Iberia Abyssal Plain, for example, it consists of an upper, high velocity gradient layer, $\sim$ 3 km thick, where V_p ranges from 4.5 to 7.0 km s^{-1}, overlying an up to 4 km thick, low gradient, high velocity layer, where V_p varies between 7.3 and 7.9 km s^{-1} (the "high velocity" layer of Chian *et al.* [1999] and Dean *et al.* [2000]); see V_p-depth profile A in Figure 3.6b). In the eastern Tagus Abyssal Plain,

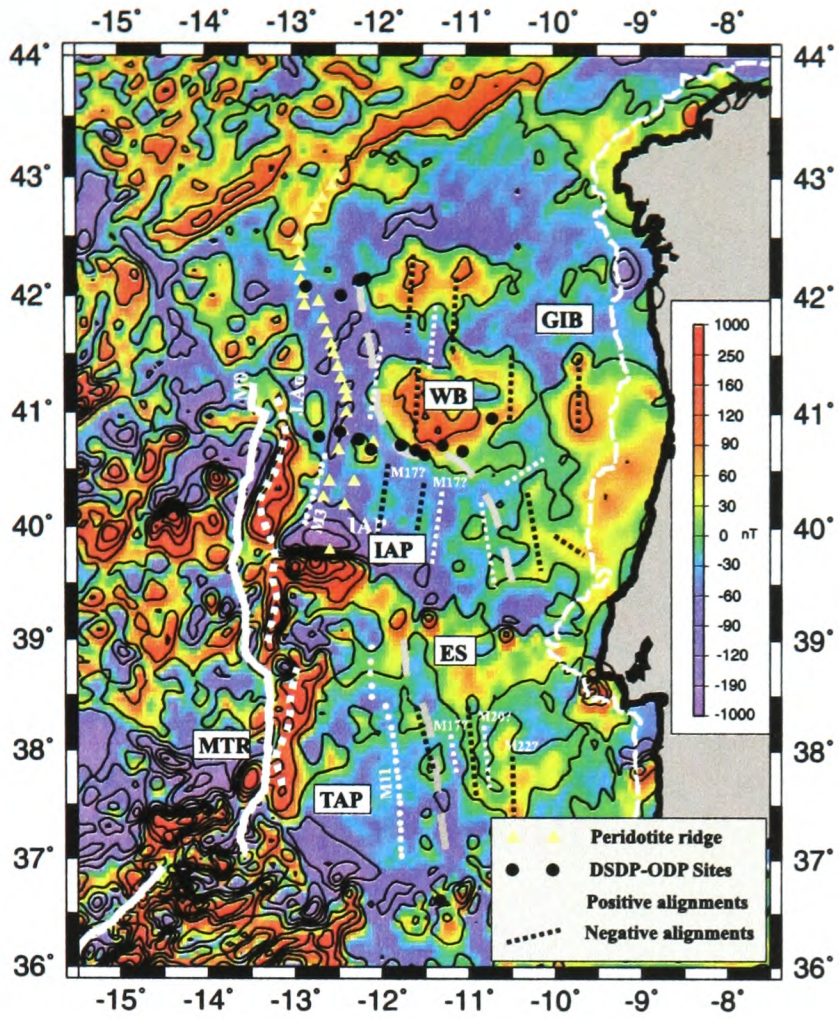

Figure 3.7: Magnetic anomalies off West Iberia compiled from ship-track data (Miles *et al.* [1994]). Positive and negative weak magnetic alignments are highlighted by the black and white dotted lines (re-interpreted from Whitmarsh & Miles [1995]). Also shown, for reference, is the western limit of thinned continental crust (thick, grey dashed line) and the shelf edge (dashed white line).

The hypothesis of thinned and disrupted continental crust is consistent with the existence of rotated faulted blocks and Early Cretaceous, possible syn-rift, sedimentary units as far west as ODP Site 1069, at the latitude of the ODP legs 149 and 173 (i.e. $\sim$ 40.70°N; Figure 3.2). Further south, however, there is a marked contrast in the basement relief and crustal velocity structure between the continental slope and rise and the OCTZ (Pickup *et al.* [1996]; Dean *et al.* [2000]). Namely, the low V_p's of the upper basement layer (Figure 3.6b) are not compatible with highly intruded, thinned continental crust (Dean *et al.* [2000]).

Figure 3.7 shows the magnetic anomaly map of the WIM compiled from ship-track data (Miles *et al.* [1994]). In the Southern Iberia Abyssal Plain, Whitmarsh & Miles [1995] identified two distinct patterns in the relatively low amplitude magnetic anomaly lineations observed to the east of the peridotite ridges (black and white dotted lines in Figure 3.7). Between the peridotite ridges and approximately 11.25°W, the magnetic lineations trend NNE-SSW ($\sim$ 14°) and parallel the SFS magnetic anomalies observed further to the west (e.g. the J and M0 anomalies in Figure 3.7). According to Whitmarsh & Miles [1995], these anomalies are caused by syn-rift intrusions in the lower continental crust under the same stress regime that controlled the early stages of oceanic accretion. East of 11.25°W, the more elongate lineations strike NNW-SSE (roughly 165°), but there are other shorter features showing a variety of trends.

The observed change in the trend of the magnetic lineations has been interpreted by

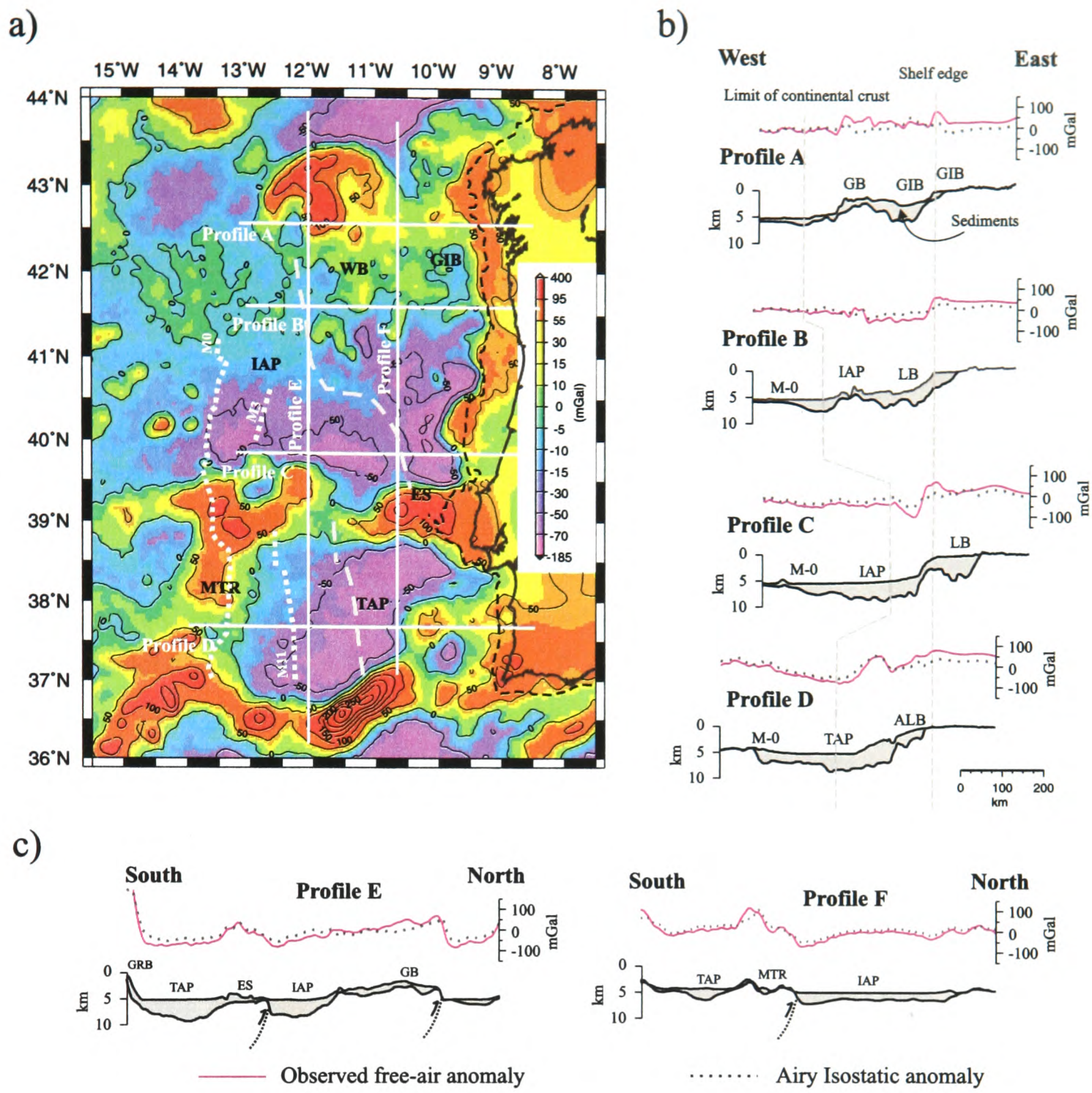

Figure 3.8: Free-air gravity and isostatic anomalies at the WIM. a) Satellite-derived free-air gravity anomaly (FAA) map of the West Iberia margin and adjacent continental areas (extracted from Sandwell & Smith [1997]). Contour interval is 50 mGal. Also shown are: the coastline (solid black line); the shelf edge (dashed black line); the limit of continental crust (thick dashed grey line); and magnetic anomalies M0, M3 and M11 (dotted white lines). Solid white lines show the location of 4 E-W and 2 N-S transects. Acronyms are as in figures 3.1 and 3.2. b) and c) show the observed FAA (pink lines), Airy isostatic anomaly (dotted black lines; see text) and the sediments (shaded areas) along the E-W and N-S profiles, respectively.

of the upper mantle peridotites (e.g. Horen *et al.* [1996]; Miller & Christensen [1997]). If not isostatically compensated, the process of serpentinization can thus result in a local mass deficiency and, consequently, a negative FAA along the OCTZ, as observed. This, and other possible explanations for the FAA lows over the Tagus and Iberia abyssal plains

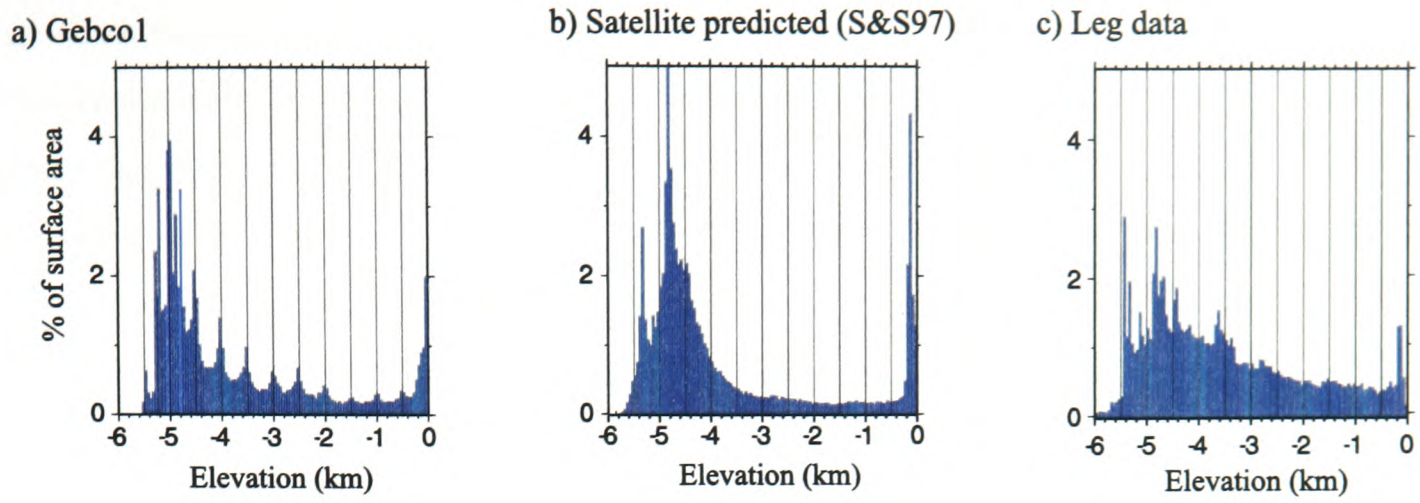

Figure 3.9: Statistical distribution of bathymetric values in the WIM region (35°-50°N; 20°-6°W), calculated from different datasets: a) GEBCO; b) Satellite-predicted (S&S); c) Shipboard data from NGDC database.

the basement relief is moderate (Smith & Sandwell [1994]). Below 15 km, the gravity signal is strongly attenuated between the seafloor and the surface, which results in a small signal-to-noise ratio (Smith & Sandwell [1994]). For wavelengths longer than ~ 160 km and up to 1000 km (i.e. the "diagnostic waveband of flexure", Watts [2001b]; see Figure 2.3), the computed seafloor topography is a function of the assumed isostatic compensation model. In order to avoid this dependence on the isostatic model the gravity data was band-pass filtered before being inverted for topography. For wavelengths greater than 160 km the S&S bathymetry relies on interpolation between conventional ship-track data.

Although the S&S 2' grid may be used together with the satellite-derived FAA grid of Sandwell & Smith [1997] in studies of regional isostasy (Smith & Sandwell [1994]; Smith [2004], written communication; Luis & Neves [2006]), in principle, however, completely independent datasets of gravity and bathymetry should be utilized, in order to avoid the possibility of circular reasoning (Smith [2004]). Furthermore, in regions of high basement topography and thick (> 200 m) sedimentary coverage, where basement highs are partially exposed, the linear inversion method utilized by Smith & Sandwell [1994] and Smith & Sandwell [1997] is not suitable for predicting the seafloor topography from the gravity measured at the surface. As shown in Figure 3.3a-e, this setting is typical of the continental shelf, slope and rise along the WIM.

Other recently compiled global bathymetric charts are either based on the S&S 2' grid, at least in the region of interest for this study (the ETOPO2 and the DBDB2 grids, ETOPO2 [2001]; DBDB2 [2002]), or result from a combination of the S&S (equatorward of 72° and below 1000 m) and the GEBCO (polarward of 72 ° and above 200 m) grids (see Marks & Smith [2004] and references therein). By compiling a new bathymetry for

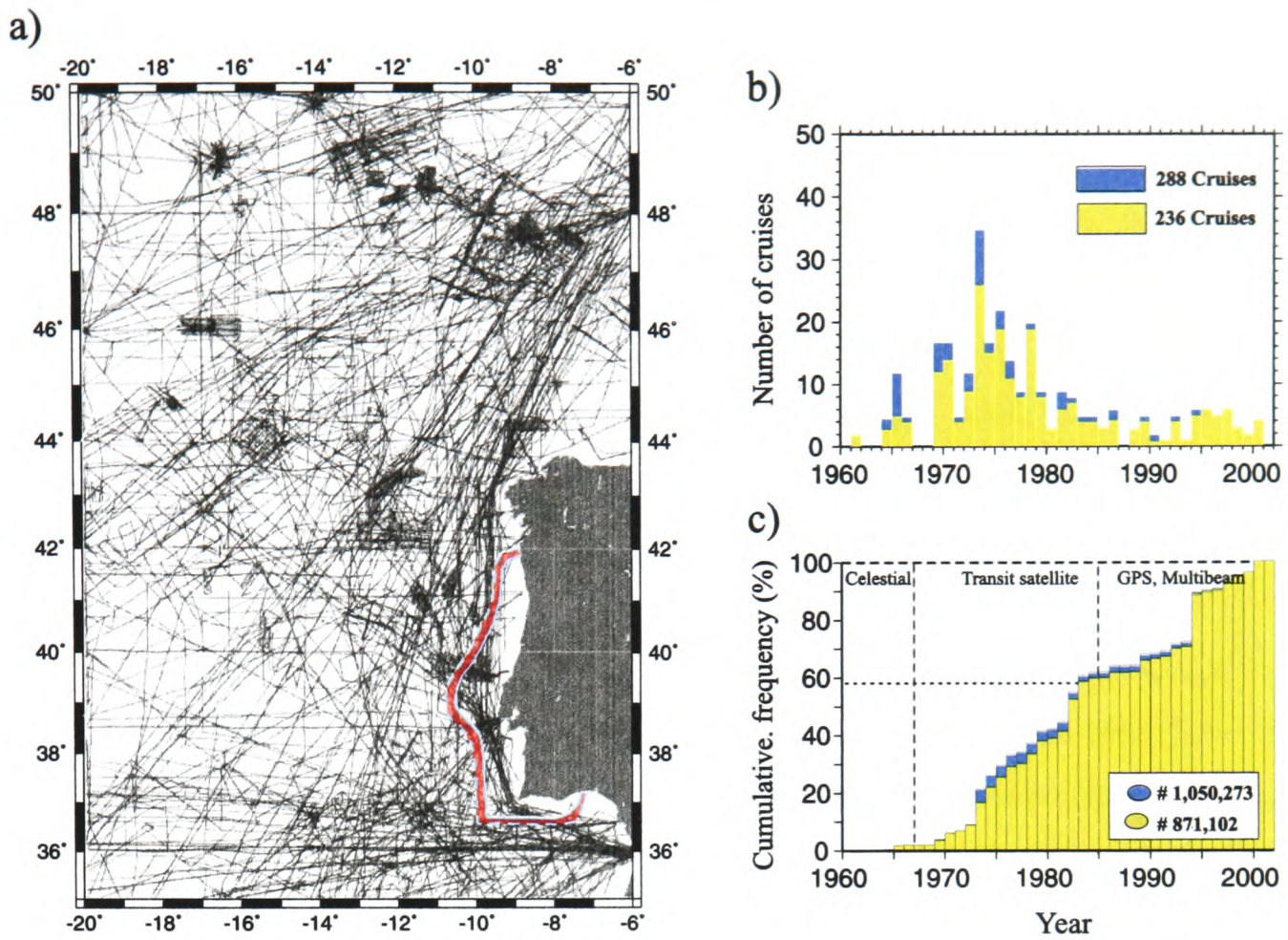

Figure 3.10: Shipboard bathymetric data from the NGDC worldwide marine geophysical data catalogue; CD-ROM updated to 2002. a) Shows the location of the ship-tracks. Solid blue line follows the -2000 isobath offshore Portugal, landwards of which the Ingmar99 bathymetry, from the Portuguese Geological Survey, has been used. The orange shaded area is a buffer zone created to merge the NGDC data with the Ingmar99 bathymetry (see text). b) Number of cruises per year which acquired bathymetric data in the region of interest. From a total of 314 cruises found in the area, 288 cruises were investigated for data quality and 236 were utilized in the new bathymetric compilation, in a total of 871,102 data points (see text). c) Cumulative distribution of bathymetric data points, referring to the 288 and 236 cruises shown in b). Approximately 60% of the data was acquired using transit satellite navigation, and 30% was acquired from 1994 onwards, using GPS navigation and, in some cases, SWATH bathymetry.

4.4% of the total).

Figure 3.10b and 3.10c show how the NGDC ship-track data is distributed in time. In the region of interest, almost no continuous shipboard depth measurements were made before the late 60's ($\sim$ 2% of the data), when only celestial navigation was available (Smith [1993] and references therein). The main peak of shipboard data acquisition occurred during the early 70's (Figure 3.10b). In this period, and until 1985, research vessels used transit satellite navigation. This data represents $\sim$ 60% of the total volume of shipboard depth soundings utilized in the WIM-Bathym (Figure 3.10c). The remaining

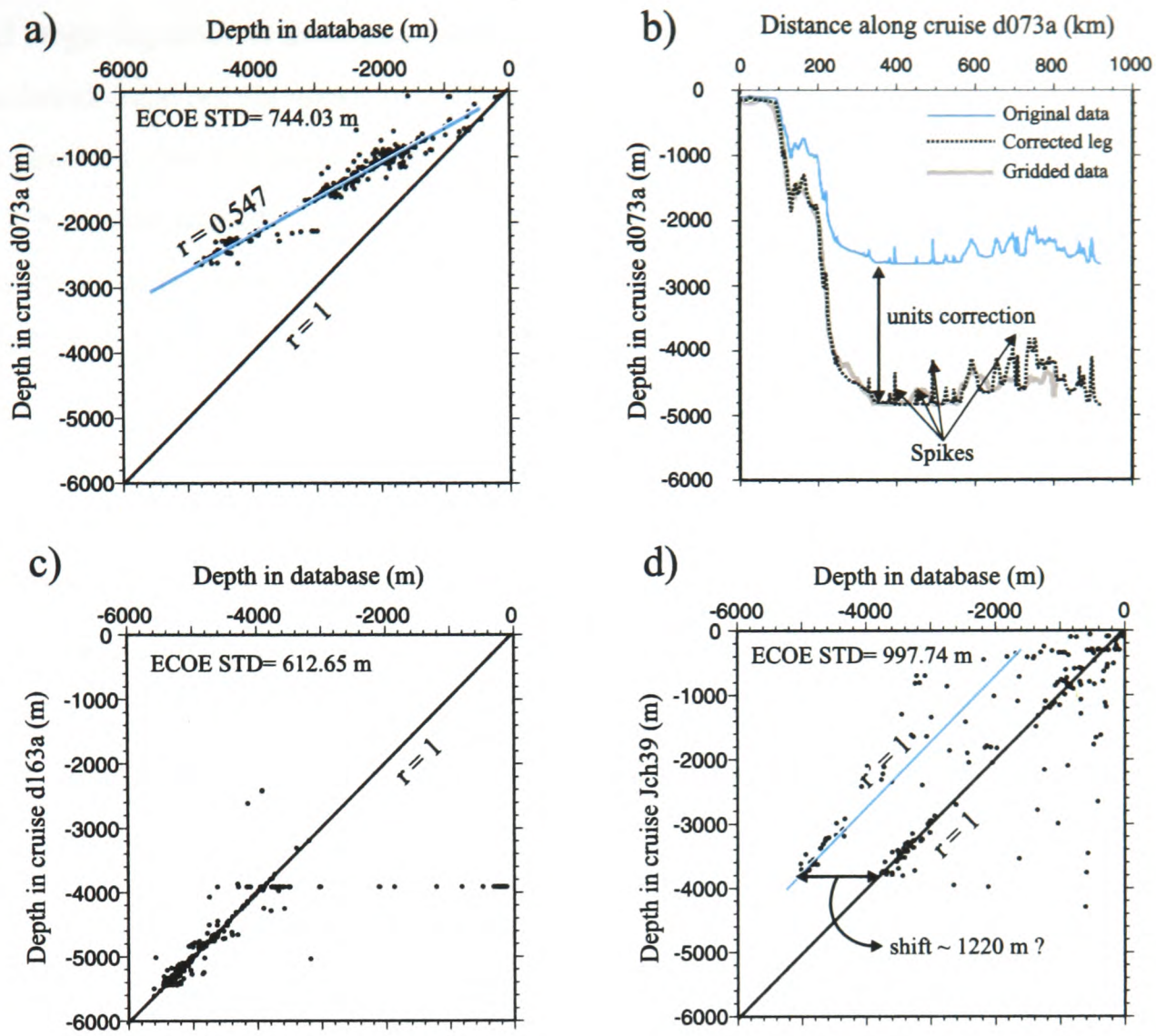

Figure 3.11: Analysis of shipboard bathymetric data and errors associated with the digitalisation of precision depth recorder (PDR) analogue charts. The panels in a), c) and d) compare the bathymetry measured in a particular cruise with that of the database (i.e. from other cruises at the intersection points). The thin, diagonal black line represents a slope (r) of 1, where good quality data should plot. a) Shows the case of a cruise where the data plots along a line with $r = 0.547$ (blue line), suggesting that depths annotated in fathoms were interpreted to be in metres (see text). In b), the data from cruise d073a is corrected, multiplying the depth soundings by the appropriate correction factor. After the units correction, the data has been de-spiked (see text). c) Shows the case where constant depths were measured during a large period of time while the ship was in transit. These cruises had to be partially deleted. In d), a large dispersion of ECOE's is observed in cruise Jch39. Some ECOE's plot along a line where $r = 1$, deviated by $\sim$ 1220 m from the reference "good quality data" line.

quality data, i.e. which after correcting the database for known errors in the bathymetry of some cruises continued to show large STD values of ECOE's ($\geq$ 500 m).

The remaining 236 cruises (288-52) were used in the WIM-Bathym compilation. Before gridding the data, however, two additional operations were performed. First, the ship-track's bathymetry was de-spiked. This consisted of removing data points which

showed large departures from the regional bathymetry (Figure 3.11b). It was established that isolated data points surrounded by slopes $\geq 25°$ should be removed. Second, a shift was applied to the bathymetric data of each cruise, based on a ECOE mode estimator, which is a robust measure of location (Rosseeuw & Leroy [1987]). The shifts were applied iteratively, with convergence in the computed STD's (< 0.2 metres improvement) being obtained after 3 iterations.

Figure 3.12 shows how the successive steps followed in the treatment of the ship-track data contributed to the reduction in the calculated ECOE's. After removing the 10 cruises which had no ECOE and the 16 cruises which showed problems of internal consistency, 29,349 ECOE's have been calculated within the area of interest, with a STD of 132.75 m (Figure 3.12a). A significant improvement ($\sim$ 30%) was achieved after removing the cruises which showed a large dispersion of high ECOE's, with a STD of 93.27 m being obtained for a total of 21,899 ECOE's.

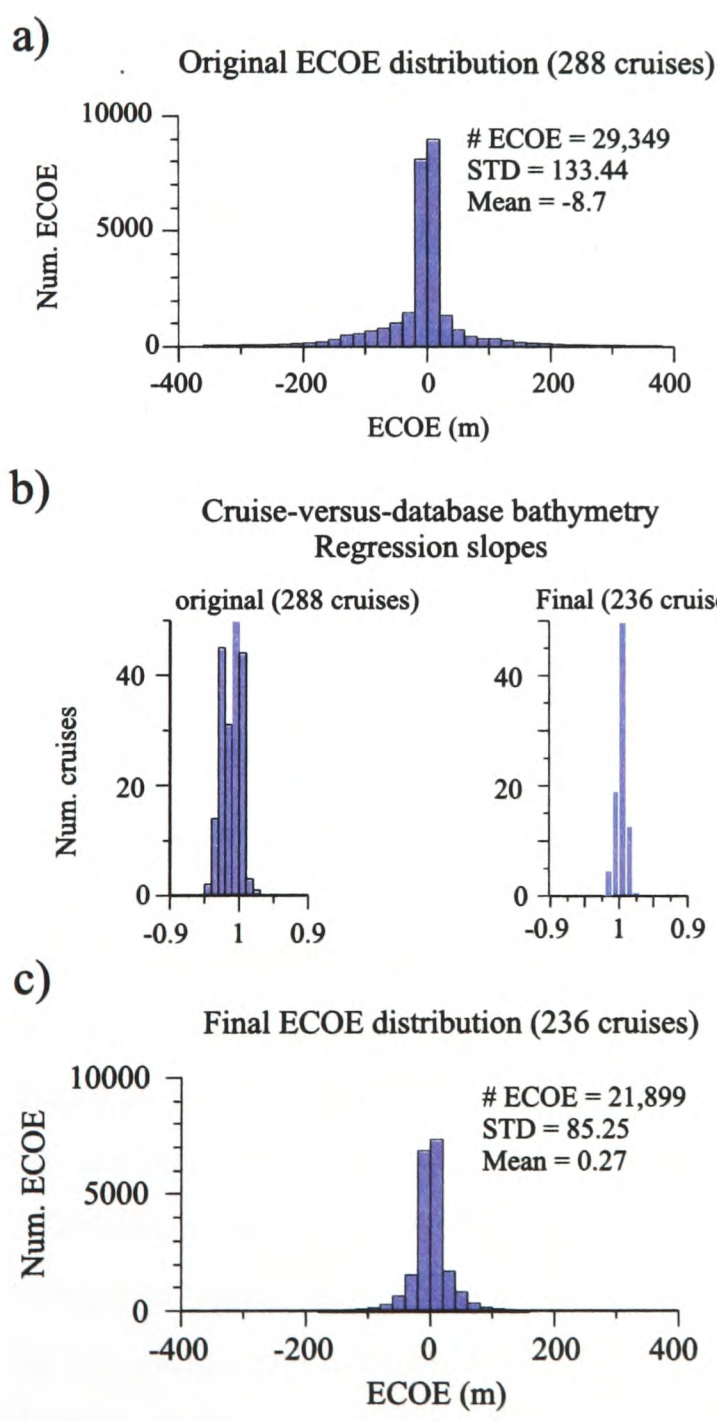

Figure 3.12: Statistics of ECOE's at different stages of the data processing. a) and c) show the distribution of ECOE's, and calculated STD and mean, before and after removing the cruises with high ECOE's, respectively. The ECOE distribution shown in a) does not include the cruises which have less than 5 ECOE and those with high ICOE's. These have been previously removed, in a total of 26 cruises (see text); b) Shows the effect of applying shifts to the cruise's data on the slope of the best-fit linear regression trend between the bathymetry in the database and that of the cruise (see Figure 3.11). The applied shifts are based on a mode estimator (see text).

Further improvement was achieved by applying the shifts to the bathymetric data of each cruise ($\sim$ 9%; Figure 3.12c). As depicted in Figure 3.12b, the slopes of the best-fit

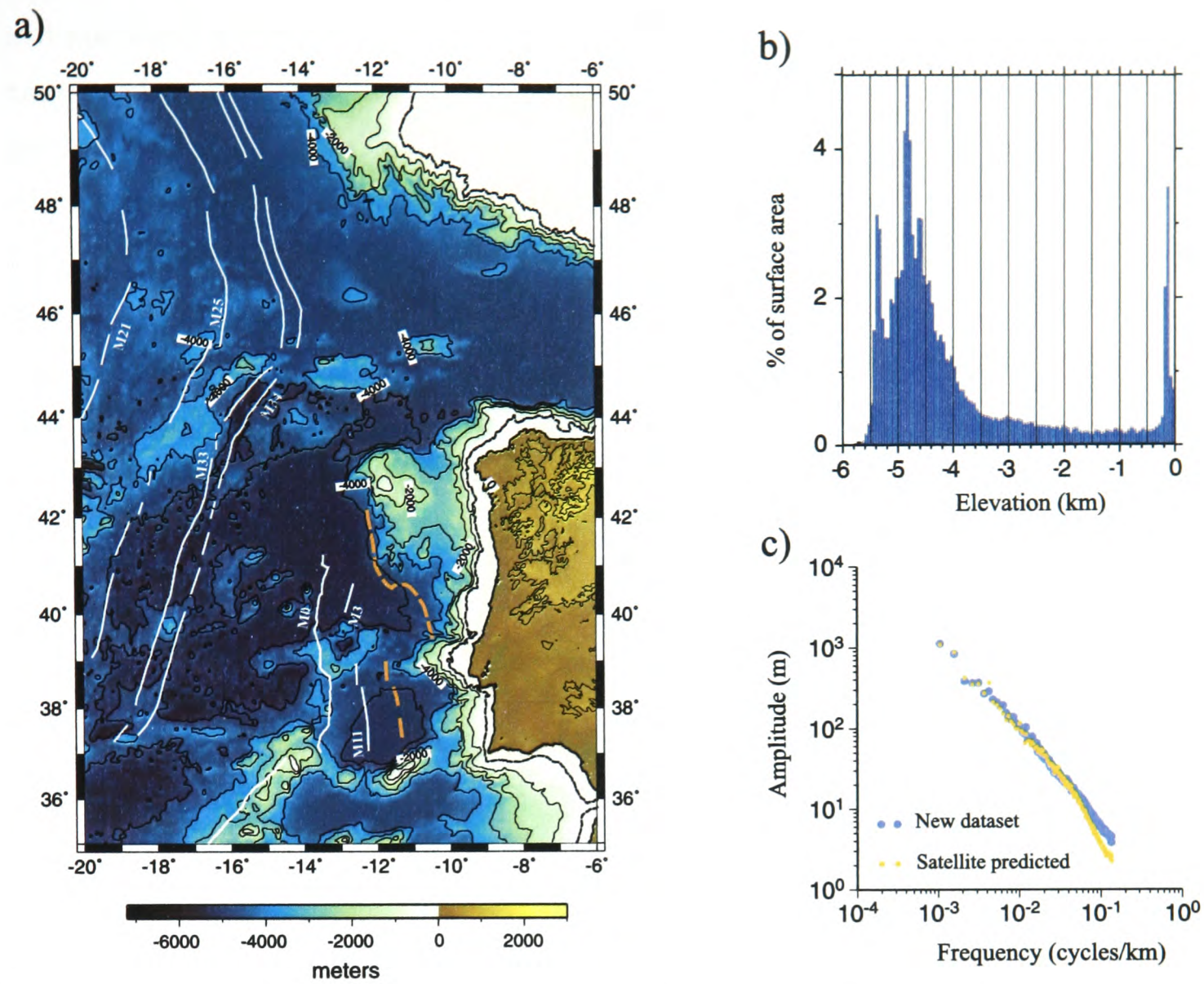

Figure 3.13: The WIM-Bathym: a) Coloured map with bathymetric contours at 1000 m intervals. Also shown are the limit of extended continental crust (dashed orange) and the magnetic anomalies (white lines) b) Statistical distribution of the bathymetric values; c) Log-plot of the amplitude spectrum (λ is the wavelength). The amplitude spectrum of the satellite-predicted bathymetry (Smith & Sandwell [1994]; Sandwell & Smith [1997]) is shown for comparison.

3.4 Sediment Thickness Compilation

3.4.1 Introduction

In this thesis, the sediment loads are used to recover the tectonic subsidence of the WIM and infer the geometry of the margin at the time of rifting, determine the contributions from rifting and sedimentation to the observed FAA gravity field, and put constraints on the long-term mechanical strength of the lithosphere, both during and following rifting (see Chapter 2 for details on the methods).

Previous sediment thickness compilations which comprise the WIM region include the global sediment thickness grid compiled by the NGDC (Holcombe & Moore [2004]), with 5' node spacing, the 2.0 Global Crustal Model of Bassin *et al.* [2000], with 2° node spacing,

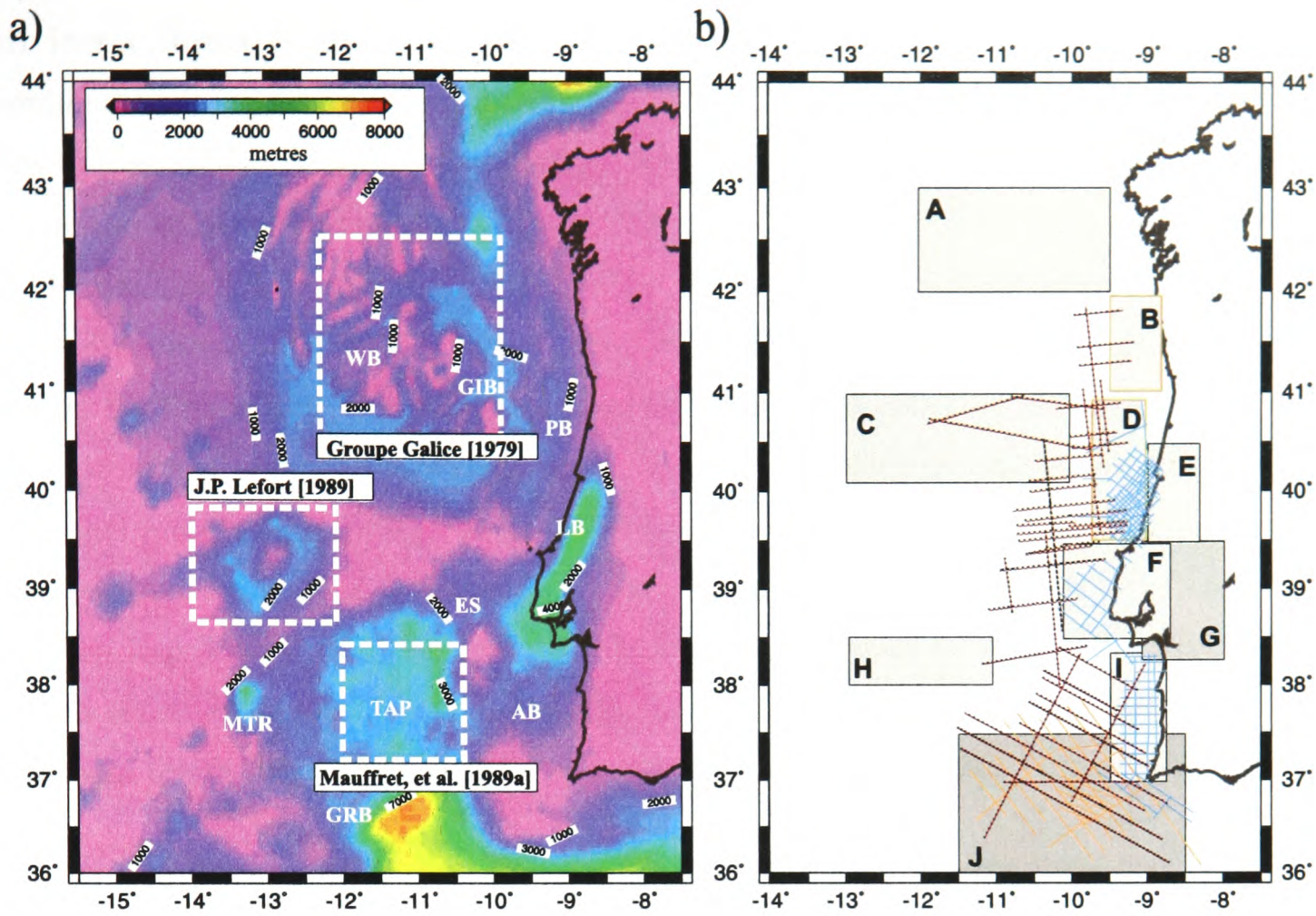

Figure 3.14: Sediment thickness data in the WIM. a) Map extracted from the North Atlantic sediment thickness compilation of Louden *et al.* [2004]. Contours are shown at 500 m intervals. The areas where there is control on the basement depths from MCS data are delimited by the dashed white rectangles (references are indicated below). b) Data sources for the new sediment thickness compilation. The description of the data and references are given in Table 3.2. The red lines with black dots show the location of the TGS-Nopec MCS profiles interpreted for this study (see text).

Atlantic. Together with the topography, these horizons define three sediment units which are designated by U_1, U_2, and U_3 (from top to bottom).

The mid Eocene-Oligocene unconformity (i.e. H_1) has been identified in the stratigraphic framework of most basin and sub-basin systems along the WIM (e.g. Mauffret & Montadert [1988]; Mauffret *et al.* [1989b]; Wilson *et al.* [1989, 1996]; Alves *et al.* [2002b, 2006]). Some diachronism in the interpreted H_2 horizon should, however, be referred here. In the Galicia Interior Basin, for example, H_2 follows the base of the Hautervian-Aptian formation of Murillas *et al.* [1990] (Figure 3.3a). Towards the east, in the Porto-Basin, H_2 is older, and corresponds approximately to the late Berriasian-early Valanginian boundary (Moita *et al.* [1996]; Alves *et al.* [2006]). Despite this, vertical variations in the relative position of this horizon in the transition between the Galicia Interior Basin and the Porto Basin are not expected to exceed 0.5 km (Alves *et al.* [2006]).

Towards the south, H_2 corresponds to the mid-late Aptian unconformity in the South-

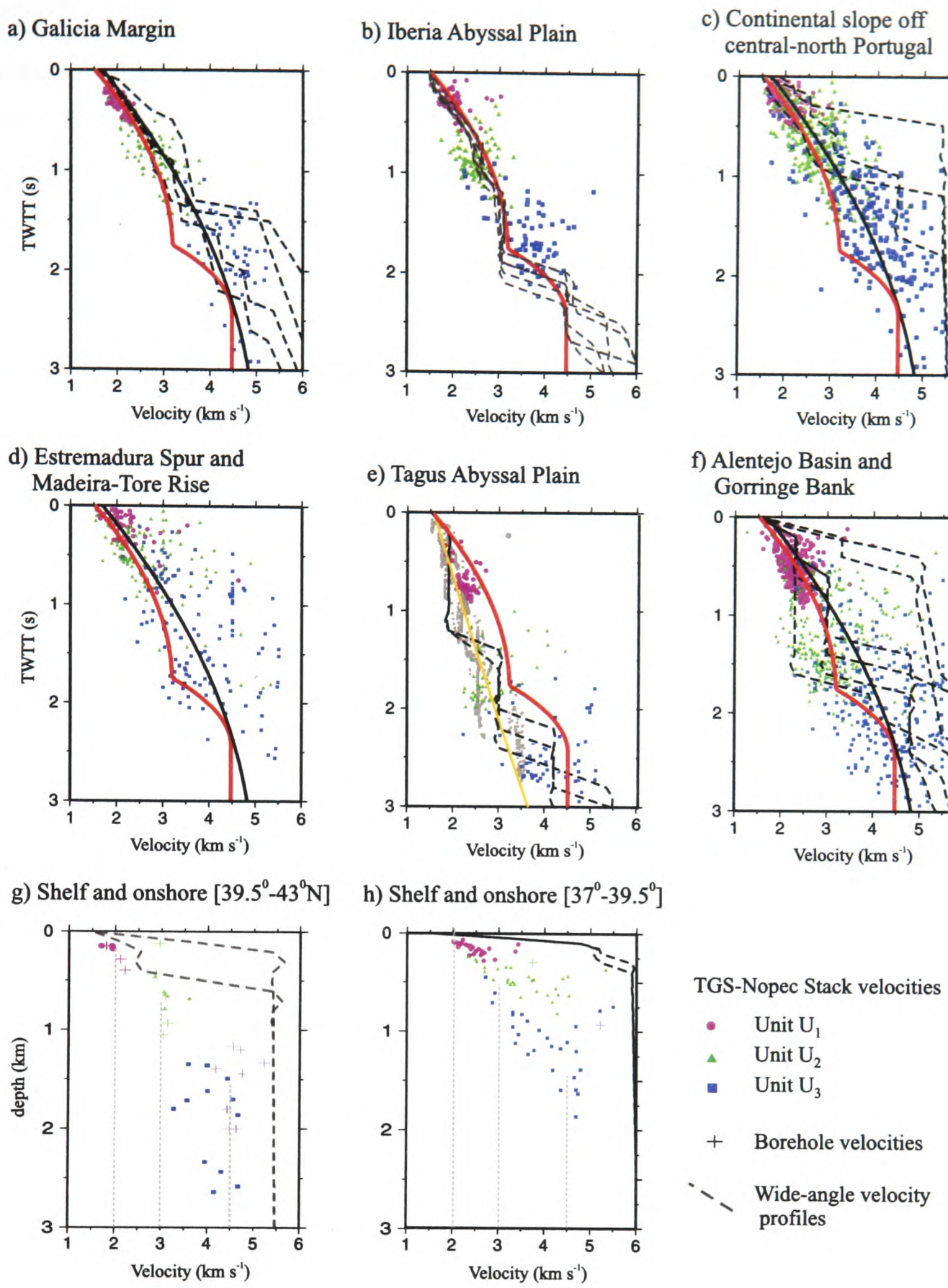

Figure 3.15: Comparison between the TGS-Nopec interval velocities in different sectors of the WIM with the velocities measured from other sources, such as wide-angle data (dashed black lines) and borehole logging (crosses in h-g). The solid black line shown in (a)-(d) and (f), and the solid yellow line in (e), correspond to the TWTT-velocity functions derived from the interval velocities in this study (see text). The solid red line shown in (a) to (f) is the TWTT-velocity function derived by Dean *et al.* [2000] for the Southern Iberia Abyssal Plain. The dashed vertical lines in (g) and (h) are the average velocities for sediment units U_1, U_2 and U_3 in the shelf (see text).

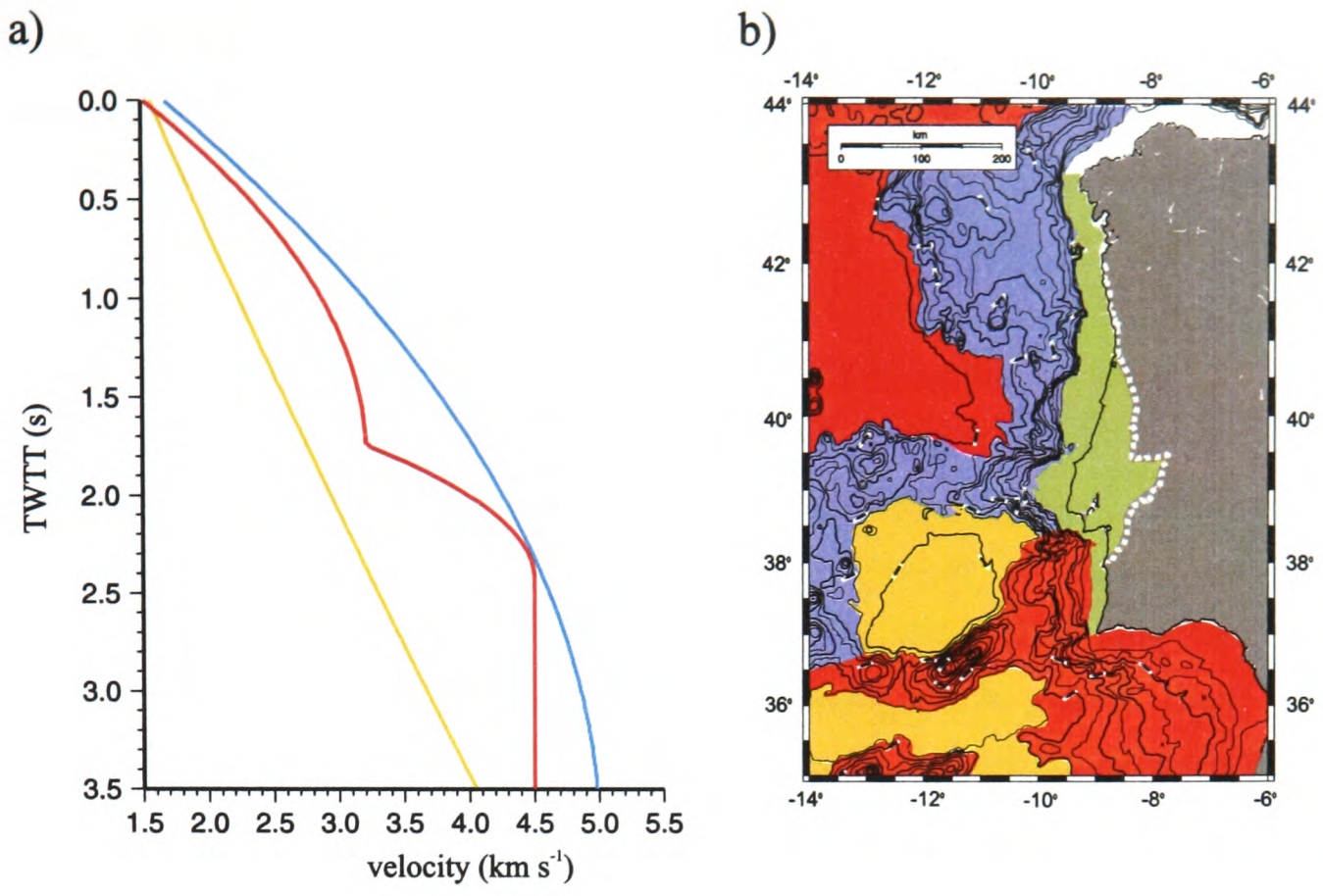

Figure 3.16: Sediment velocity structure in the WIM. a) TWTT-velocity functions used to convert the MCS data from TWTT to metres of sediment thickness. b) Areas where the different functions have been utilized. The colour schema is the same as in a). Along the shelf and onshore, fixed velocities of 2 km s^{-1}, 3 km s^{-1} and 4.5 km s^{-1} were assumed for sediment units U_1, U_2 and U_3, respectively (see Figure 3.15g-h). Bathymetric contours interval is 500 m.

$$V_p = 0.705(T) + 1.569 \qquad T < 3.5\ s$$
$$V_p = 4\ kms^{-1} \qquad T > 3.5\ s$$

Along the continental shelf and onshore, where numerous commercial wells have been drilled (see Figure 3.2 for location), borehole logging velocities have been used. In the majority of the wells analysed, the average velocities of sediment units U_1, U_2 and U_3 do not vary significantly with depth (crosses in Figure 3.15g and h). Instead, it appears that each of the defined units is characterized by a relatively narrow range of velocities, particularly U_1 and U_2. Accordingly, the conversion from TWTT to depth in the proximal margin sedimentary basins assumed a fixed velocity value for each unit. These are 2 km s^{-1} in U_1, 3 km s^{-1} in U_2 and 4.5 km s^{-1} in U_3 (dashed grey lines Figure 3.15g and h).

Figure 3.16 shows the three TWTT-velocity functions utilized to convert TWTT data to metres of sediment thickness (Figure 3.16a; excluding the shelf and onshore basins), as well as the regions of the WIM where each function has been applied (Figure

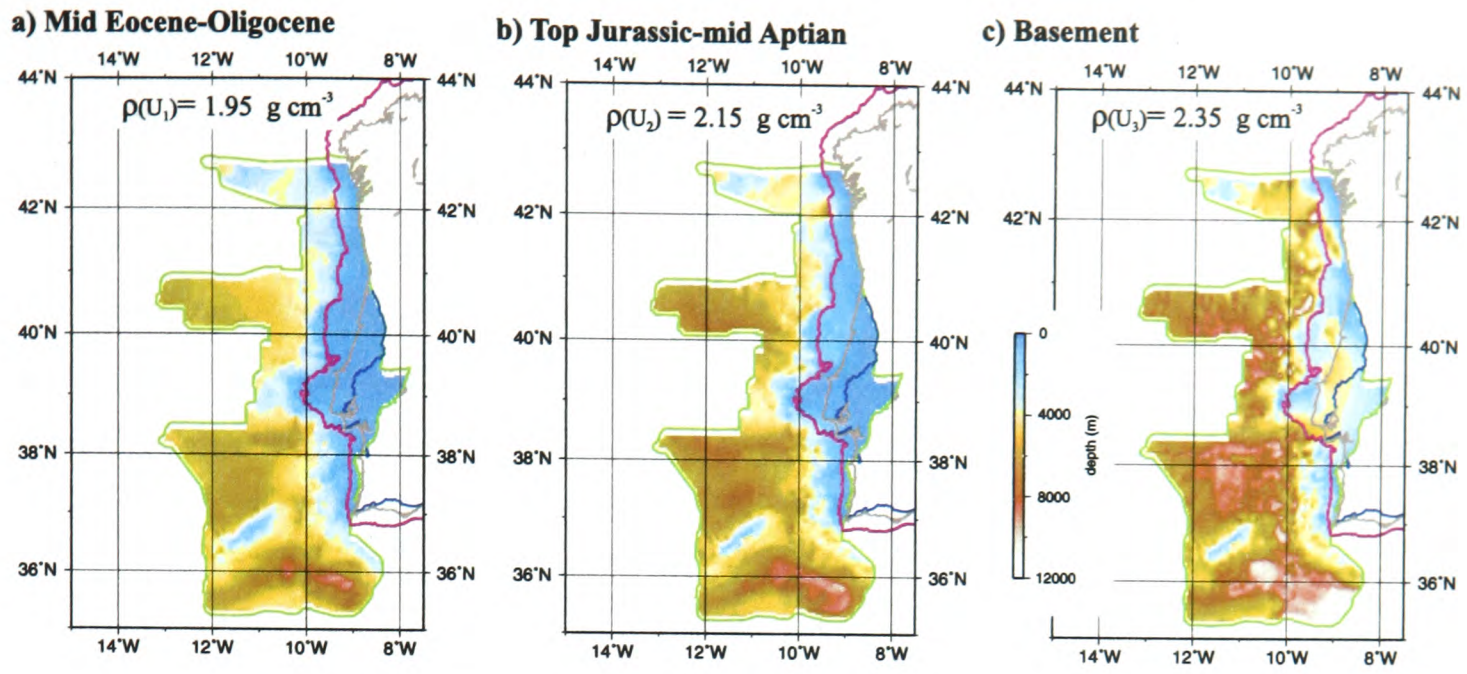

Figure 3.17: Compiled structural maps: a) H_1, mid Eocene-Oligocene unconformity; b) H_2, top Jurassic-mid Aptian; c) H_3, basement. Depths are in metres, measure in relation to the mean sea-level offshore, and to the surface topography onshore. The thick purple line highlights the limit of the continental shelf. Also depicted in each map is the average density of the sediment unit lying above (see text).

Louden *et al.* [2004] sediment thickness compilation for the North Atlantic was used, together with the bathymetry, to determine the basement depth (i.e. H_3), but H_1 and H_2 have not been compiled.

The compiled structural maps show a very irregular basement topography (H_3; Figure 3.17c), and two smoother surfaces, H_1 and H_2 (Figure 3.17a and b, respectively). This is in general good agreement with the observations from the seismic data, which show a highly disrupted stretched continental crust, both in the proximal and distal margin, and a relatively uniform Late Cretaceous-Recent sediment coverage (see Figure 3.3). Along the continental shelf and onshore, the resolution of the compiled grids is low, when compared to the density of available control data points (e.g. areas D, F and J in Figure 3.14b). Consequently, part of the intricate structure of the Lusitanian and Porto basins is not recovered in the structural maps. In the onshore Southern Lusitanian Basin (area G in Figure 3.14b), only the basement depths were known, and the data coverage is very low. This results in an essentially extrapolated grid (Figure 3.17c).

Also depicted in Figure 3.17 are the densities of the three sediment units compiled in this study, U_1, U_2 and U_3. These are average values computed from the velocity structure and using a fourth order polynomial fit to the empiric relationship between the density (ρ) and the P-wave velocity (V_p) of the rocks established by Ludwig *et al.* [1970]. According to Zelt [1994],

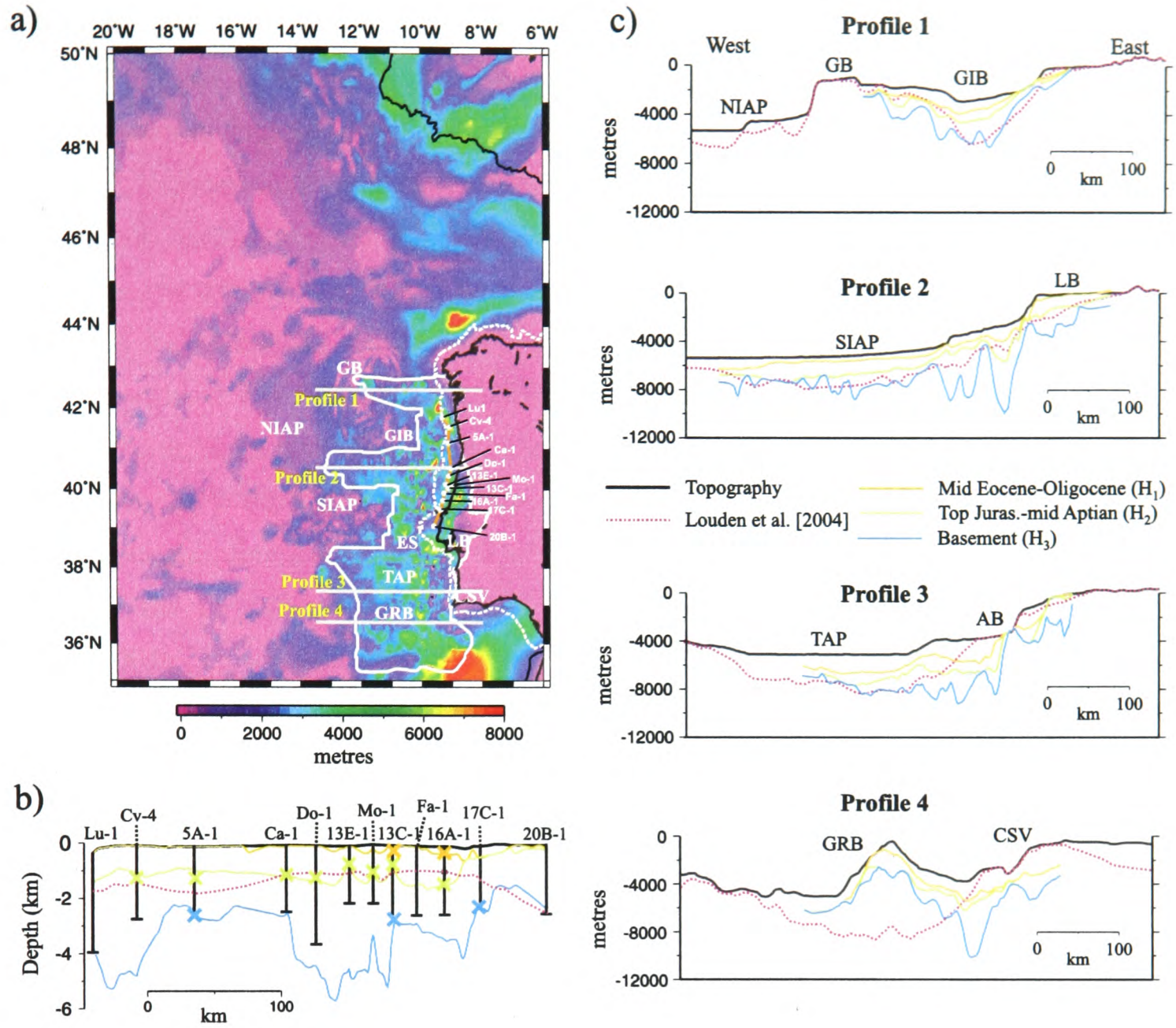

Figure 3.18: Compiled sediment thickness grid for the WIM region (35°-50°N; 20°-6°W) and comparisons with existing data. a) Compiled sediment thickness map. The thick, light grey line delimits the area where new data has been used. Outside this area, the sediment thicknesses are from the Louden *et al.* [2004] compilation for the North Atlantic. Also shown are the shelf edge (dashed white line) and the location of 4 E-W profiles (grey lines) and 1 margin parallel profile running along the Portuguese continental shelf (thick orange line). These profiles are used to make comparisons between the structural maps (H_1, H_2 and H_3) compiled in this study and other datasets. Regions acronyms are as in Figures 3.1 and 3.2. b) Compares the depth of the compiled horizons with observations in commercial boreholes along the continental shelf (crosses; the location of the boreholes is shown in a). c) Compares the basement depth from this study (blue line) with that calculated from the sediment thickness grid of Louden *et al.* [2004] and the bathymetry (dotted pink lines), along 4 E-W profiles. The depths of horizons H_1 and H_2 are also shown, in yellow and green, respectively.

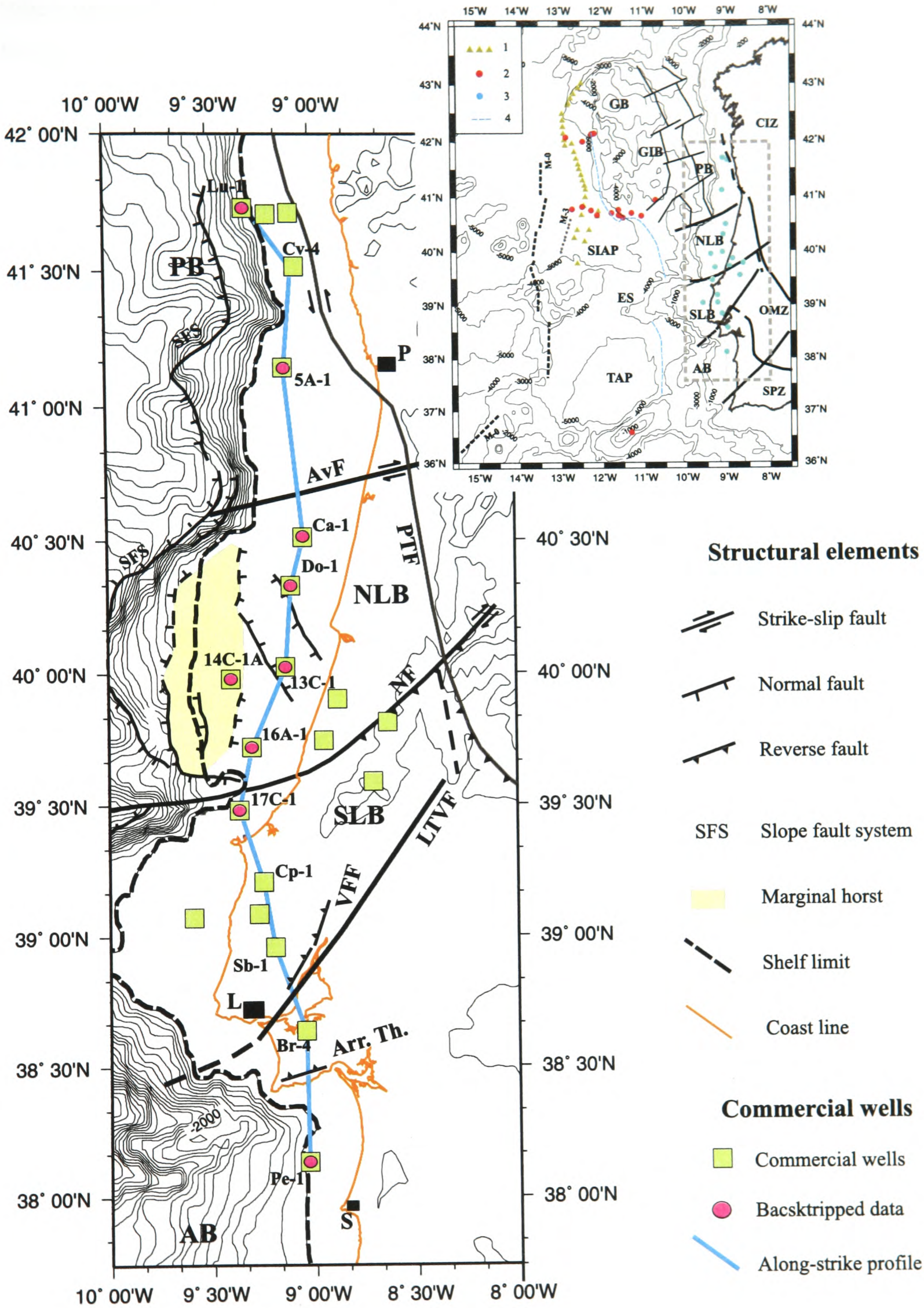
10° 00'W
9° 30'W
9° 00'W
42° 00'N
41° 30'N
41° 00'N
40° 30'N
40° 00'N
39° 30'N
39° 00'N
38° 30'N
38° 00'N
8° 00'W
PB
SFS
Lu-1
Cv-4
5A-1
P
AvF
Ca-1
Do-1
NLB
PTF
SFS
14C-1A
13C-1
16A-1
NF
17C-1
SLB
LTVF
Cp-1
VFF
Sb-1
L
Br-4
Arr. Th.
-2000
Pe-1
S
AB
15°W 14°W 13°W 12°W 11°W 10°W 9°W 8°W
44°N
43°N
42°N
41°N
40°N
39°N
38°N
37°N
36°N
1
2
3
4
GB
CIZ
GIB
PB
M-0
M-3
SIAP
NLB
ES
SLB
OMZ
TAP
AB
SPZ
Structural elements
Strike-slip fault
Normal fault
Reverse fault
SFS Slope fault system
Marginal horst
Shelf limit
Coast line
Commercial wells
Commercial wells
Bacsktripped data
Along-strike profile

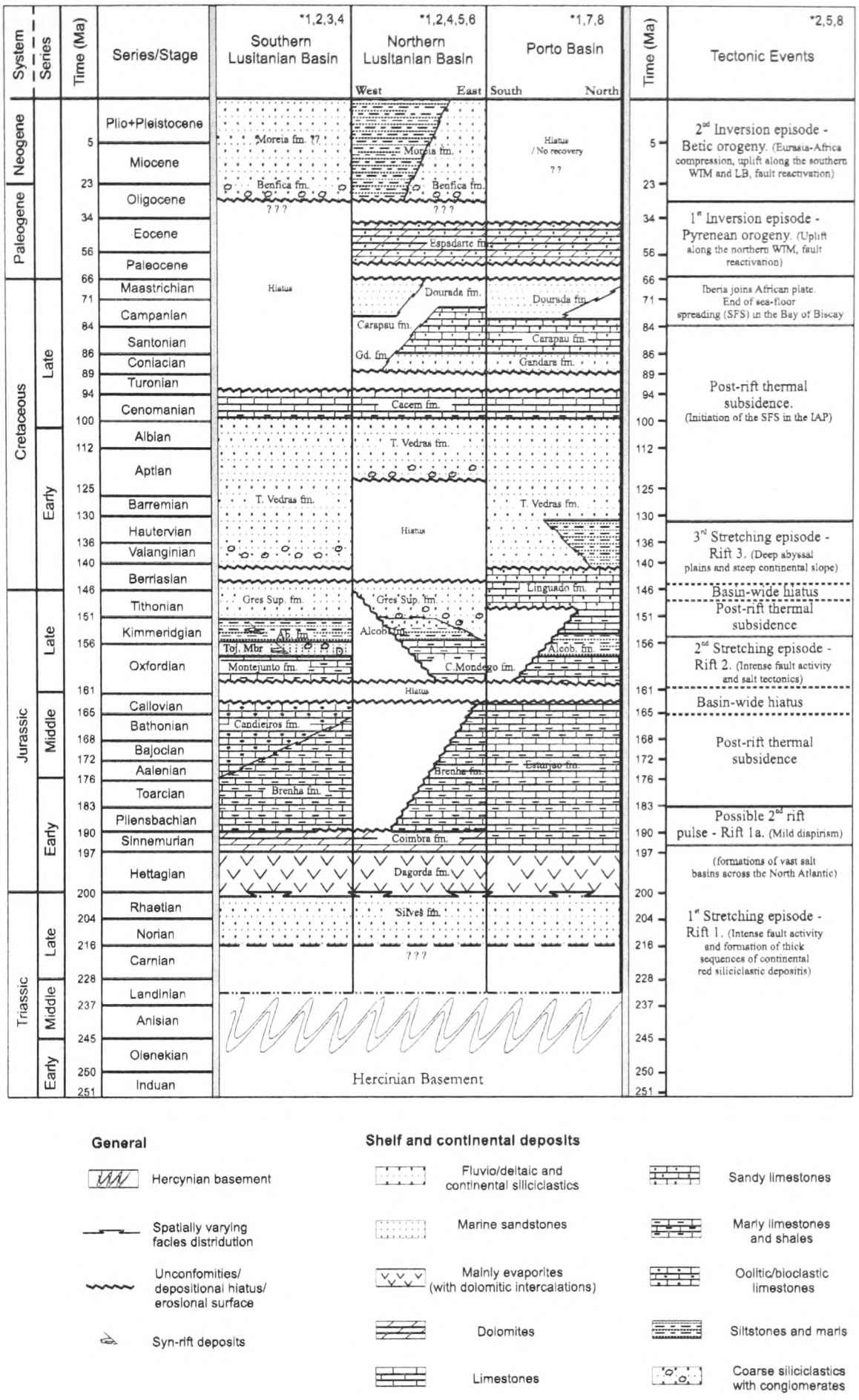

Figure 4.2: Stratigraphy of the onshore and continental shelf basins of the western Portuguese Margin (Modified from Pinheiro *et al.* [1996]). The timescale of Gradstein *et al.* [2004] is used. References used are: 1, Witt [1977]; 2, Wilson *et al.* [1989]; 3, Leinfelder & Wilson [1998]; 4, Rasmussen *et al.* [1998]; 5, Alves *et al.* [2002b]; 6, Cunha & Reis [1995]; 7, Murillas *et al.* [1990]; 8, Alves *et al.* [2006]. Regions acronyms are as in Figure 4.1

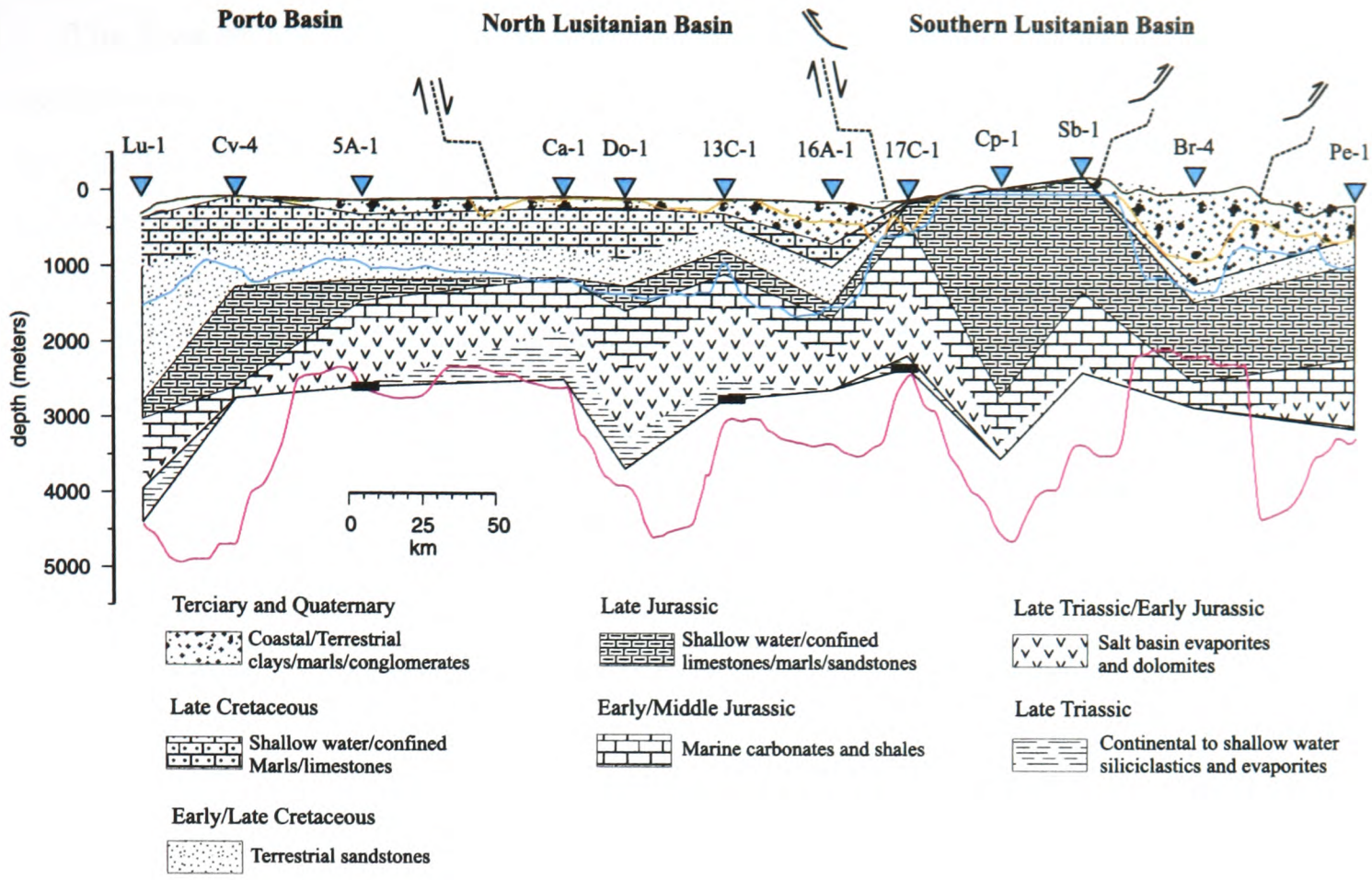

Figure 4.3: Synthetic stratigraphic profile along the Portuguese margin extrapolated from well data. The path of the profile along the Portuguese shelf and onshore is shown in Figure 4.1. Also shown by the coloured lines are the horizons sampled from the structural maps compiled for the WIM, which include: the basement (purple); the top Jurassic/mid Aptian (blue); and the mid Eocene/Oligocene (yellow). The data utilized for the compilations and ages of the horizons are discussed in Chapter 3. The black bar at the base of the stratigraphic column in wells 5A-1, 13C-1 and 17C-1 indicates that the basement was reached in these wells.

icantly reduced during this event, with low subsidence rates and relatively simple facies distribution (Wilson *et al.* [1989]; Hiscott *et al.* [1990]; Stapel *et al.* [1996]).

The Torres Vedras formation (Figure 4.2), which spans the syn-rift period and part of the post-rift (late Berriasian-mid Cenomanian; Witt [1977] and references therein), has been described in wells along the whole of the shallow Portuguese margin. It consists of an alternation of fluvial siliciclastics and carbonate lithologies with thicknesses of $\sim$ 300 to 500 m in the Northern Lusitanian Basin (Figure 4.3). In the Porto Basin, the thickness of this sequence ranges between 500 and 1500 m, in wells 5A-1 and Lu-1, respectively, and a greater carbonate component is observed. In some onshore sub-basins of the Southern Lusitanian Basin, part of the Early Cretaceous and the entire Late Cretaceous have been removed during the latest Cretaceous-Cenozoic inversion episodes (e.g. Wilson *et al.* [1989]). The wide range of thicknesses of the Early Cretaceous sediments is well illustrated in Figure 4.3.

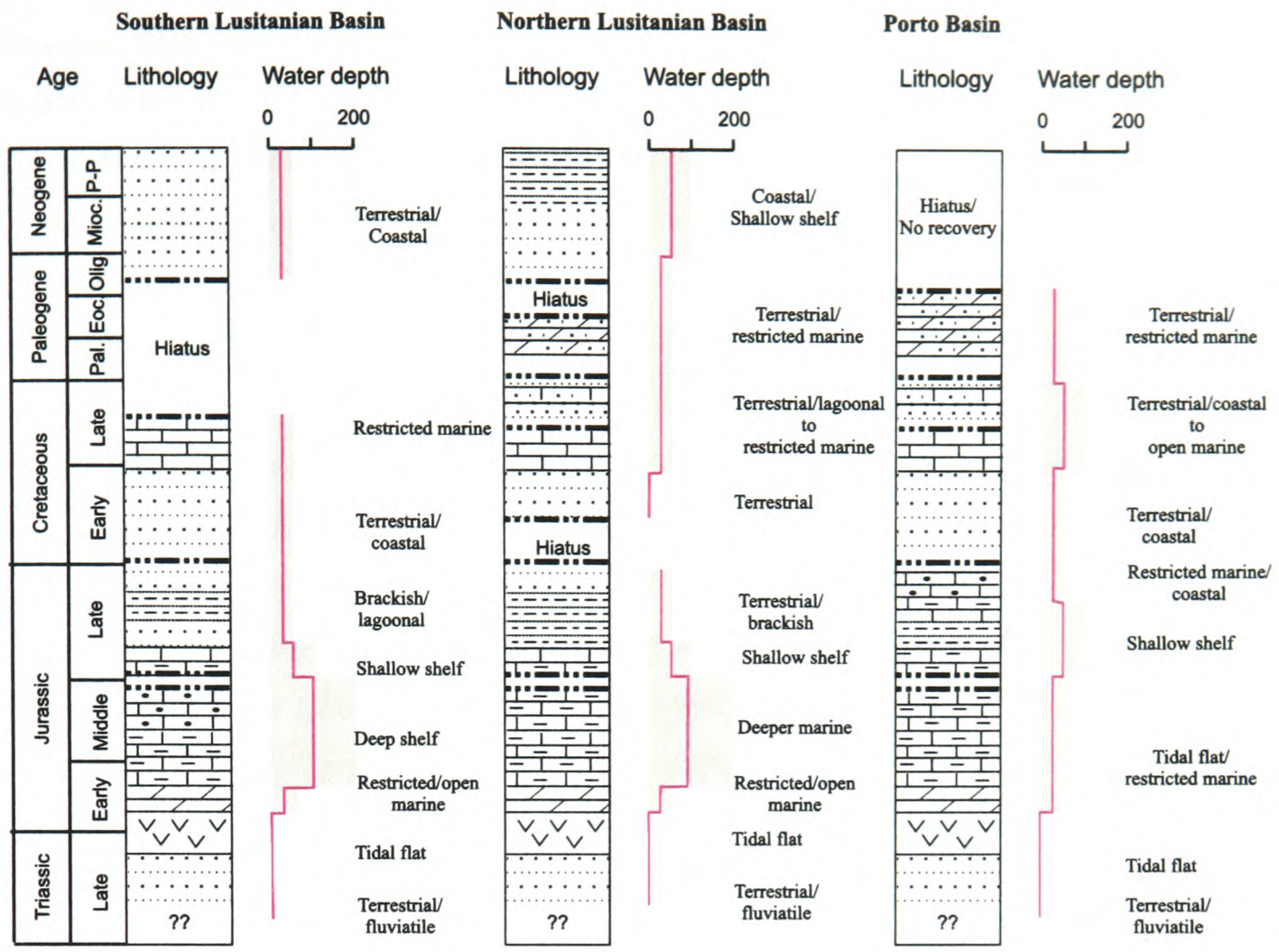

Figure 4.4: Depositional environments in the Lusitanian and Porto basins compiled from well reports and paleoenvironmental maps from GPEP [1986]. Water depths were estimated according to Ingle [1980]. Facies symbology as in Figure 4.2. Grey shading shows the range of uncertainty in the paleowater depths.

has been attributed to the base of the Oxfordian (161.2 Ma), despite the uncertainties in the age of this horizon.

The Cretaceous and Cenozoic stratigraphic record of the onshore and continental shelf basins along the WIM is also very heterogeneous. As discussed above, part of the Early Cretaceous, the Late Cretaceous and Paleogene deposits are absent in the Southern Lusitanian to the north of the Vila Franca Fault, due to uplift and erosion during the latest Cretaceous and Cenozoic compressional deformation events. To the south of this structure, however, 300-400 m of Early Cretaceous and thick Neogene sequences have been drilled (Figure 4.3, well Br-4). In well Pe-1, for example, is was possible to define 2 stratigraphic horizons, at the base of the Valanginian (140.2 Ma) and the Tortonian (11.6 Ma), respectively.

In the Northern Lusitanian and Porto basins the Cretaceous-Cenozoic record is better preserved. In most wells 5-7 horizons were identified. These correspond, in most cases, to the base (145.5-120 Ma, see below) and top (Albian-Cenomanian, 99.6 Ma) of the Torres Vedras Formation in the Early Cretaceous, the top of the Cacém (Cenomanian-

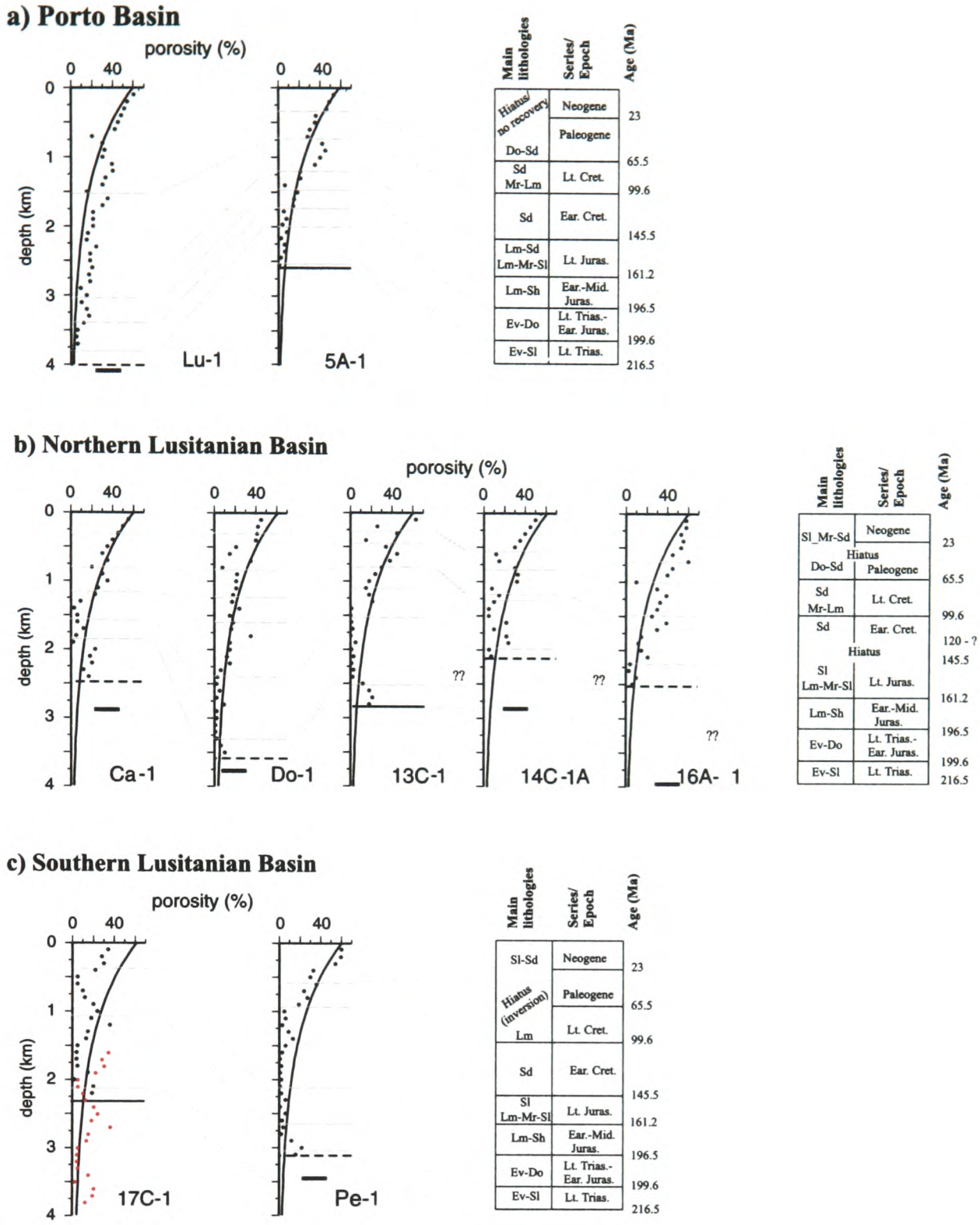

Figure 4.5: Porosity data and lithologies (right) from the 9 backstripped wells along the Portuguese continental shelf. The main stratigraphic units (thin, horizontal grey lines) are correlated across the boreholes of each basin system by the dotted lines. The drilled basement is indicated by solid black line. When the basement is not reached a dashed line is used instead, and the depth of the gridded basement (see text) is indicated by the black bar. Also shown in the graphics is the exponential-type curve (solid black) derived in this study to explain the decrease in porosity with depth in the backstripped wells (see text). The red dots in well 17C-1 were obtained by shifting the original records (black dots) by 1500 m (see text). The lithology acronyms are as follows: Cb, Carbonates; Cg, conglomerates; Cl, clays; Do, dolomites; Ev, evaporites; Lm, limestones; Mr, Marls; Sd, Sands; Sh, shales; Sl, silts.

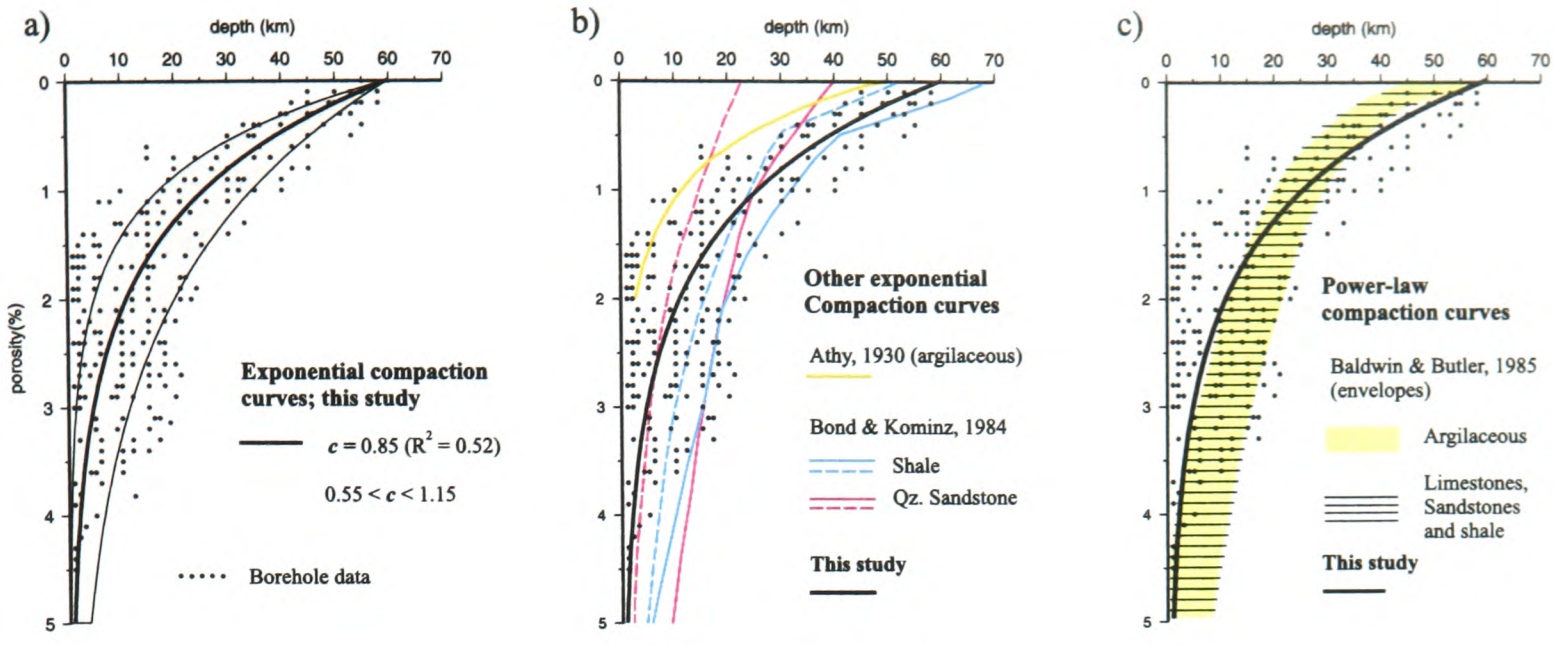

Figure 4.6: Porosity-depth compaction/decompaction curves. a) Exponential-type curve derived in this study which gives the best-fit (black line) to the data (black dots). It assumes a surface porosity of 60% and a factor of exponential decrease, c, of 0.85 (see Equation 4.4). The grey shaded area is an envelope within which $\sim$ 70% of data is predicted (see text). b) Exponential-type depth-porosity relationships proposed in previous studies. In the decompaction curves of Bond & Kominz [1984] the solid line represents the upper limit porosity and the dashed line the lower limit porosity for the indicated lithology. c) Power law-type curves put forward by Baldwin & Butler [1985].

factor of exponential decrease (c in Equation 4.4), as proposed here, it is also possible to account for the rapid decrease in the porosity observed near the surface with a single exponential-type curve.

A different type of porosity-depth curves was, almost simultaneously, put forward by Baldwin & Butler [1985]. These authors found that at depths greater than a few hundred metres most exponential-type curves predict values of porosity that are smaller than the observations, and that power-law curves should be used instead. Although some relatively high porosity values have been measured below depths of 2.5 km, which are difficult to explain with the porosity-depth curves derived in this study, the overall trend of the power-law curves proposed by Baldwin & Butler [1985] does not improve the fit to the data in the Portuguese margin (Figure 4.6c).

4.3.3 Sea-level

The last term of the backstripping equation (i.e. Equation 4.1) is a sea-level term. Its contribution to the basement subsidence is calculated from the difference in the sea-level height between the Present and the time at which the sediment units were deposited (i.e. the relative sea-level change; Δ_{sl}), multiplied by a density ratio. The density ratio

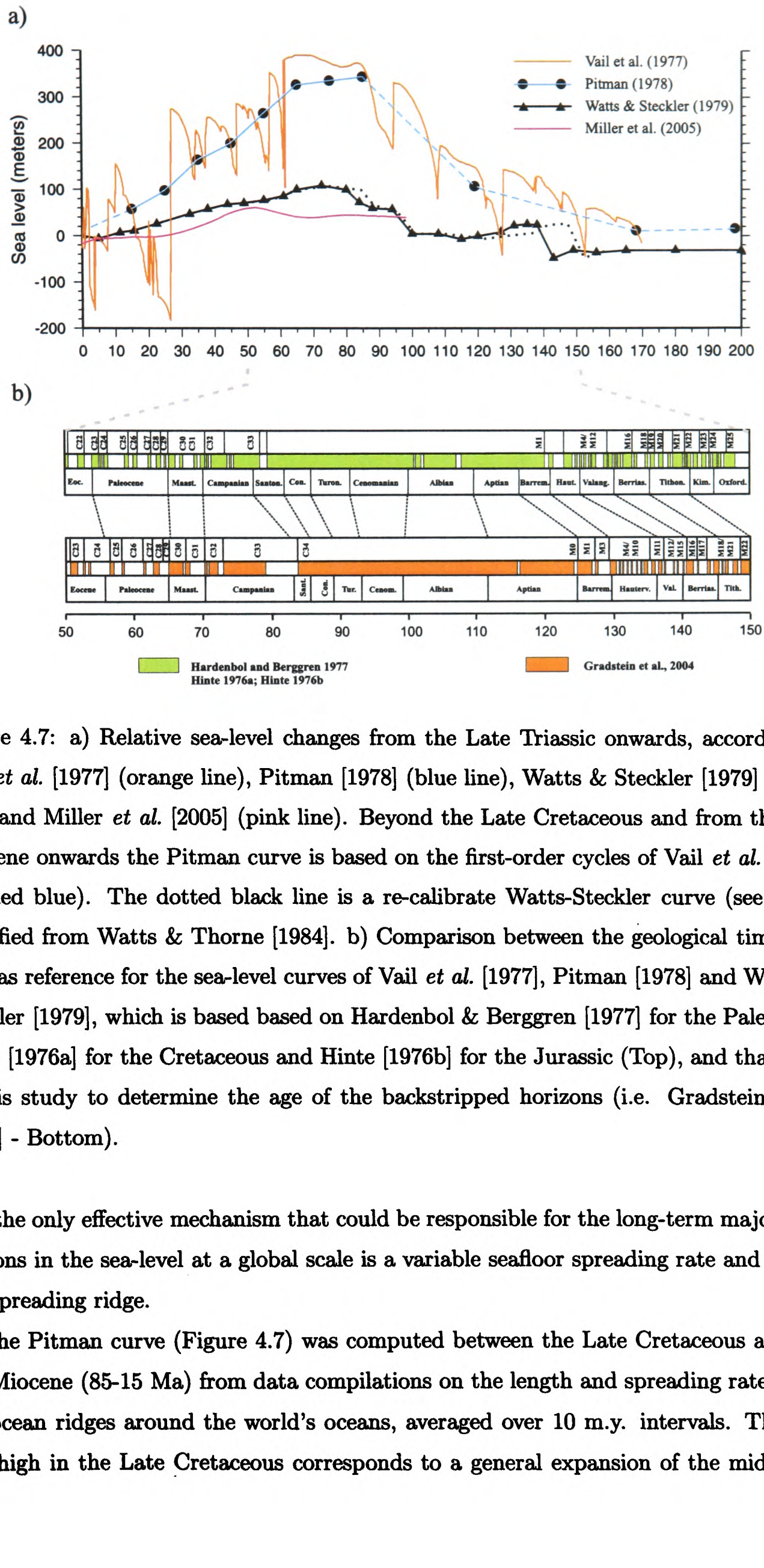

Figure 4.7: a) Relative sea-level changes from the Late Triassic onwards, according to Vail *et al.* [1977] (orange line), Pitman [1978] (blue line), Watts & Steckler [1979] (black line) and Miller *et al.* [2005] (pink line). Beyond the Late Cretaceous and from the mid Miocene onwards the Pitman curve is based on the first-order cycles of Vail *et al.* [1977] (dashed blue). The dotted black line is a re-calibrate Watts-Steckler curve (see text). Modified from Watts & Thorne [1984]. b) Comparison between the geological timescale used as reference for the sea-level curves of Vail *et al.* [1977], Pitman [1978] and Watts & Steckler [1979], which is based based on Hardenbol & Berggren [1977] for the Paleogene, Hinte [1976a] for the Cretaceous and Hinte [1976b] for the Jurassic (Top), and that used in this study to determine the age of the backstripped horizons (i.e. Gradstein *et al.* [2004] - Bottom).

that the only effective mechanism that could be responsible for the long-term major fluctuations in the sea-level at a global scale is a variable seafloor spreading rate and length of a spreading ridge.

The Pitman curve (Figure 4.7) was computed between the Late Cretaceous and the mid Miocene (85-15 Ma) from data compilations on the length and spreading rates from mid-ocean ridges around the world's oceans, averaged over 10 m.y. intervals. The sea-level high in the Late Cretaceous corresponds to a general expansion of the mid-ocean

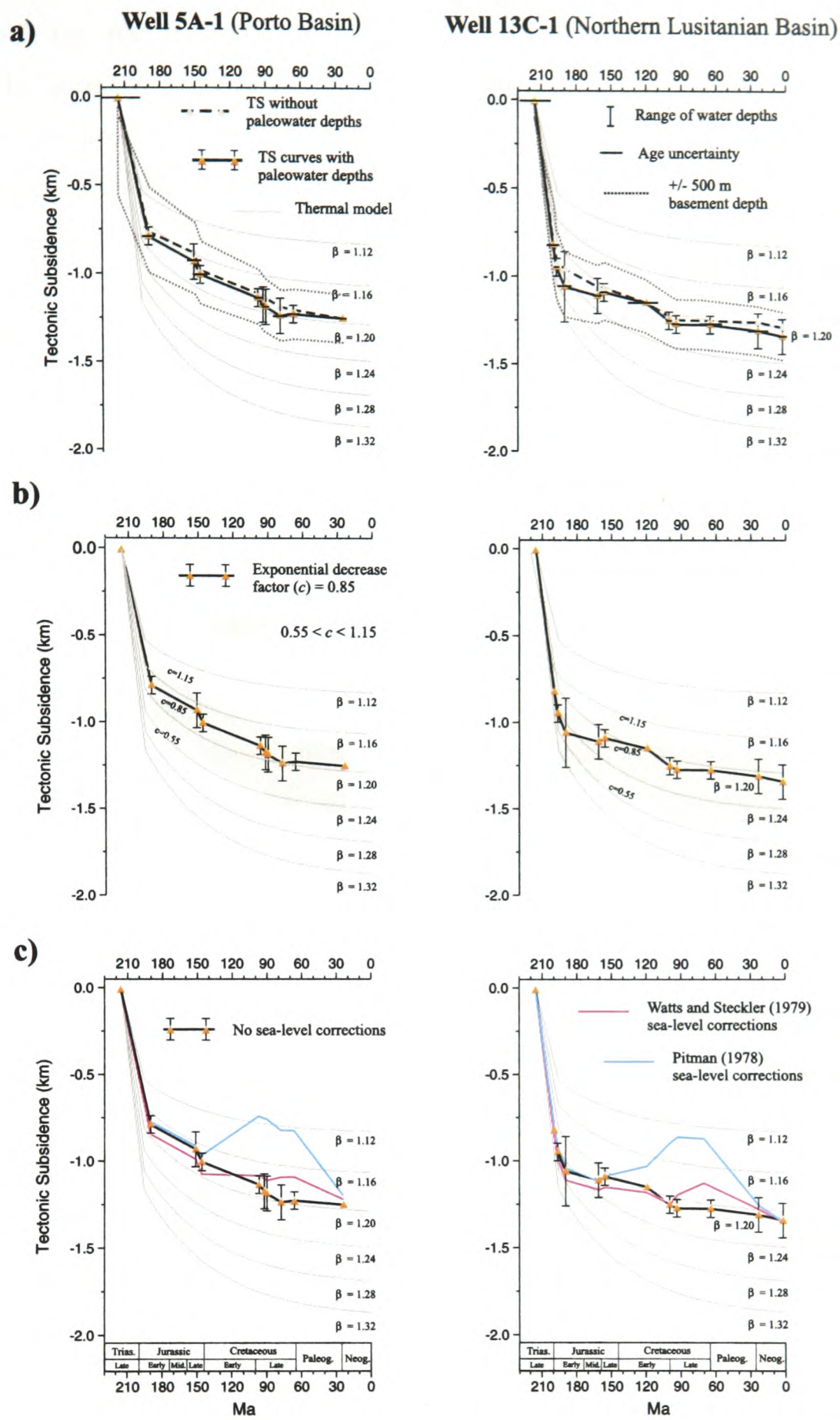

Figure 4.8: Sensitivity of the calculated backstrip curves to: a) Uncertainties in the paleowater depths, age of the stratigraphic horizons and depth to basement; b) Porosity-depth compaction/decompaction curves; c) Sea-level corrections. Orange triangles indicate the backstripped horizons. No sea-level corrections have been applied in a) and b). Thin grey lines show the subsidence predicted by the thermal model (see Table 4.1 for parameters) with different values of β for a 216.5 m.y. old rift, with a duration of 20 m.y.

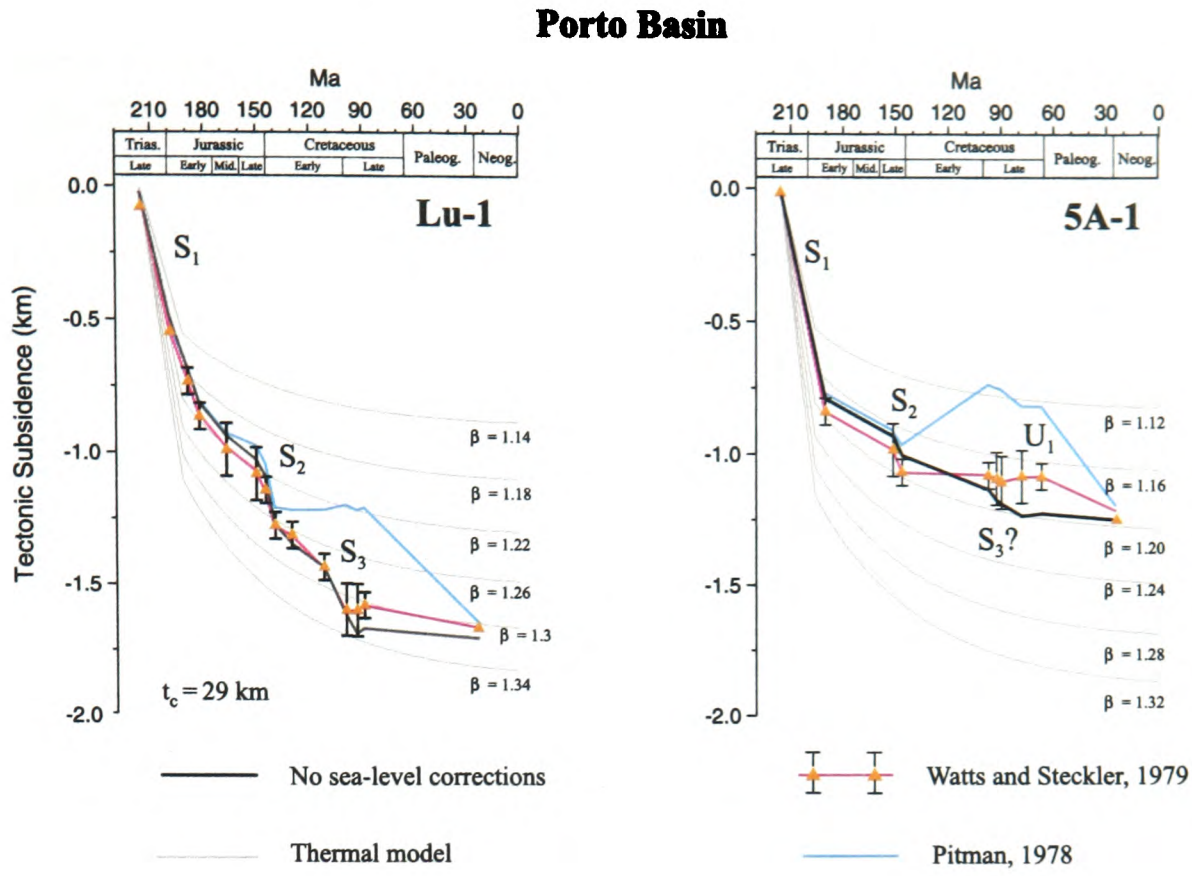

Figure 4.9: Results from well backstripping in the Porto Basin: wells Lu-1 and 5A-1 (see Figure 4.1 for location). The TS curves were calculated without eustatic corrections (black), and using the mean sea-level curves of Pitman [1978] (blue) and Watts & Steckler [1979] (pink). In the latter, the vertical bars correspond to the uncertainties in the estimated paleowater depths. The theoretical curves (thin grey lines) were obtained from a thermal model using the parameters of Table 4.1 and assuming a 216.5 m.y. old rift with a duration of 20 m.y. (see text). The β values are indicated below the curves for reference. In well Lu-1 an initial crustal thickness (t_c) of 29 km was used, in agreement with the crustal models derived from wide-angle and refraction data onshore (see Section 4.4). The main episodes of subsidence and uplift are identified by S_i and U_i, respectively.

curve), whilst the TS curve of well 5A-1 remains flat (Figure 4.9). This period of relative tectonic quietness is interrupted by a sudden increase in the subsidence rates of wells Lu-1 (Albian-Cenomanian, $\sim$ 110-100 Ma) and 5A-1 (Cenomanian-Turonian, $\sim$ 100-93 Ma; S_3 in Figure 4.9). The age of this event corresponds to that of the initial stages of seafloor spreading off the Galicia Bank (e.g. Boillot *et al.* [1989]), more than 250 km to the west, suggesting that it might be related to a regional effect of basin sagging following continental break-up. Again, this effect is more pronounced in well Lu-1.

The top 450 m of well Lu-1 are not described in the well completion report. It is likely, however, that at least part of the latest Cretaceous and Tertiary sedimentary units are still in place, since they have been recovered in well 5A-1, located over the southern flank of the Porto Basin, and in other commercial boreholes within the Porto Basin (e.g. Alves *et al.* [2006]). It was assumed, for the purposes of backstripping, that the sediments

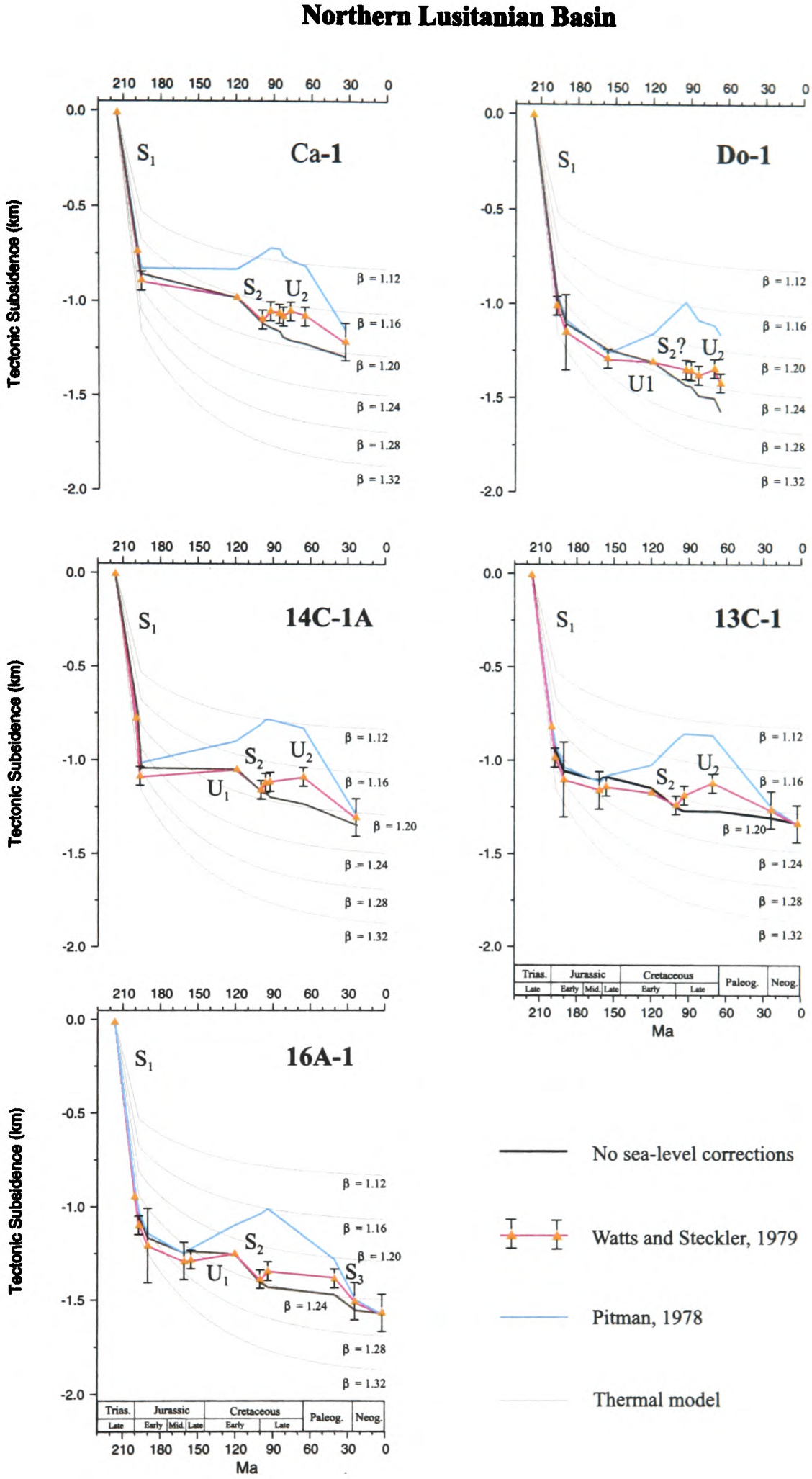

Figure 4.10: Results from well backstripping in the Northern Lusitanian Basin: wells Ca-1, Do-1, 14C-1A, 13C-1 and 16A-1 (see Figure 4.1 for location). See Figure 4.9 for legend.

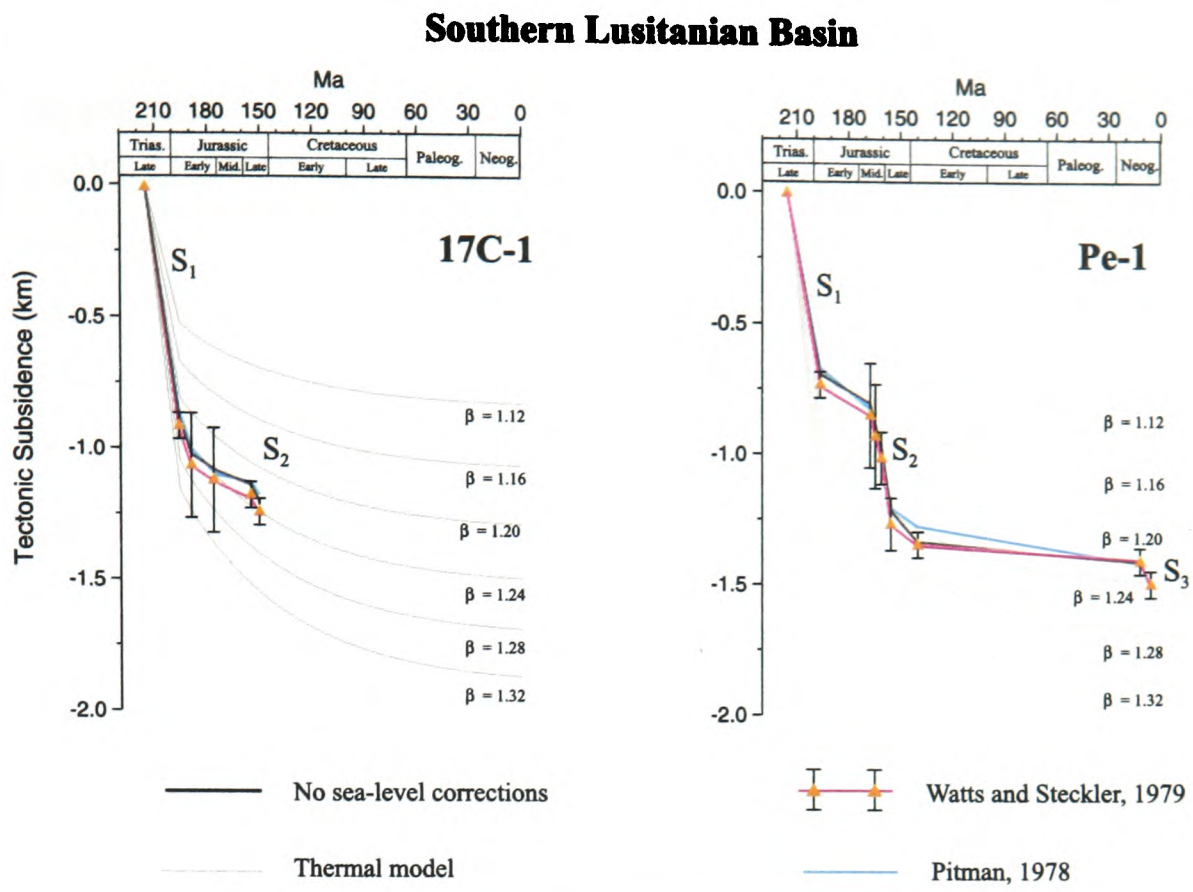

Figure 4.11: Results from well backstripping in the Southern Lusitanian Basin: wells 17C-1 and Pe-1 (see Figure 4.1 for location). See Figure 4.9 for legend.

intensities of this Middle to Late Jurassic rift event in distinct sub-basins are controlled by localized and diachronous fault movements and salt tectonics, possibly associated with a sequence of rift pulses that affected the margin between the mid Middle and the early Late Jurassic.

A similar model for the evolution of the Southern Lusitanian Basin throughout the Early and Middle Jurassic has, in fact, been suggested by Carvalho *et al.* [2005], based on the seismic stratigraphy and borehole data of some sub-basin systems. However, according the these authors the last extensional pulse which affected the margin during this period dates from the Sinemurian, and does not explain the sudden increase in the subsidence rates between the Bajocian and the Bathonian, i.e. approximately 20 m.y. later.

The latest Jurassic, Cretaceous, and Cenozoic successions are missing in well 17C-1 as in the majority of the onshore wells of the Southern Lusitanian Basin (e.g. Stapel *et al.* [1996]). As discussed in Section 4.2, this is mainly due to uplift and erosion during the latest Cretaceous and Cenozoic inversion episodes. In the light of the backstripping results from the Northern Lusitanian Basin, however, it is also arguable that some of the uplift and erosion, in the region of well 17C-1 (i.e. the proximal offshore), might have been caused by thermal uplift during the latest Jurassic-Early Cretaceous rifting episode.

From the mid Miocene onwards (15-0 Ma), the subsidence observed in well Pe-1 (S_3 in Figure 4.11) is likely to be associated with the strong compressional stresses that affected

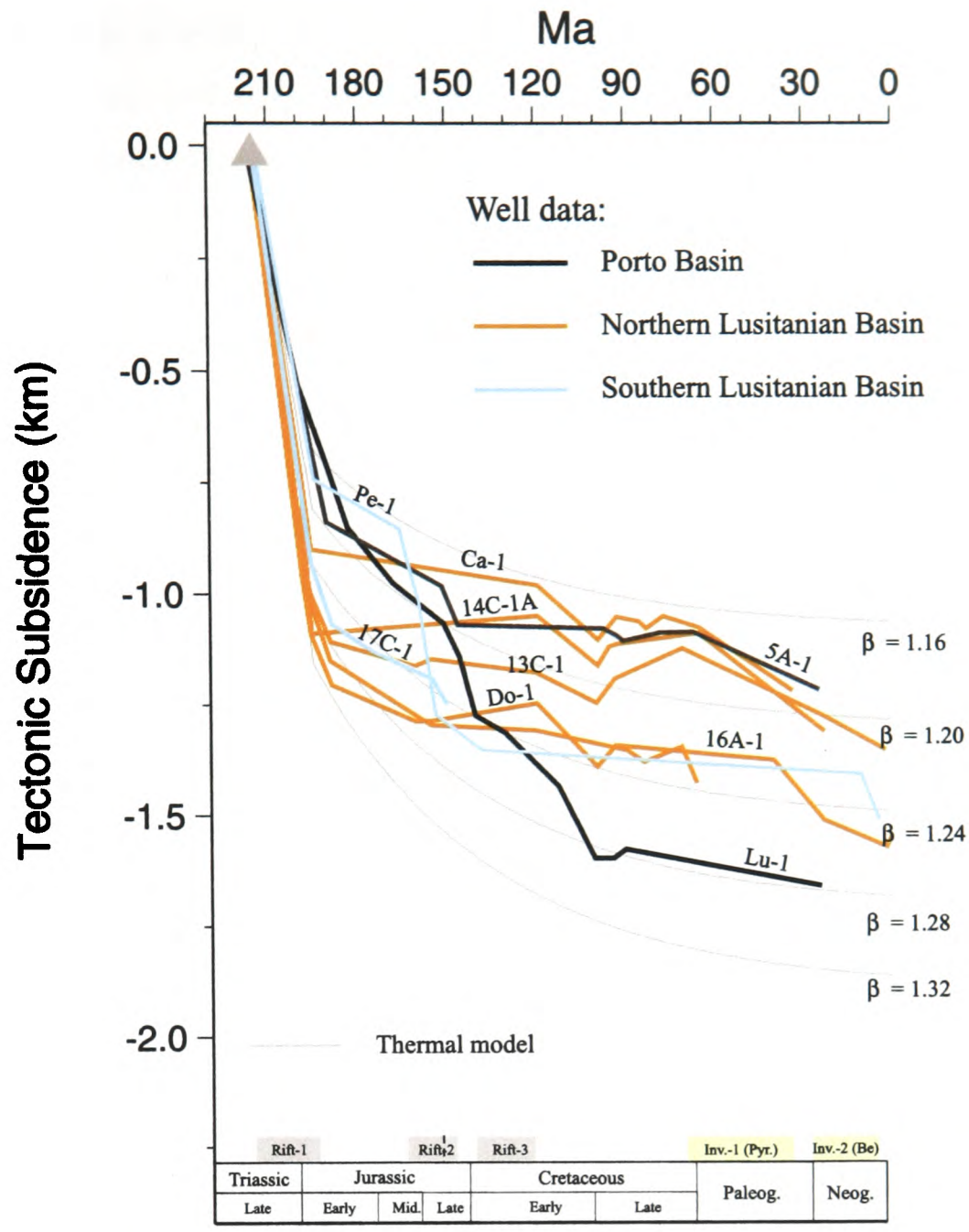

Figure 4.12: Subsidence and uplift history of the main sedimentary basins along the Portuguese margin continental shelf: summary of results from 9 backstripped wells. See figure 4.1 for location of the data. The TS curves were calculated using the sea-level corrections of Watts & Steckler [1979]. The basins are grouped by colours, and the name of the borehole is indicated for each TS curve. The main extensional (syn-rift period) and inversion (Inv.) episodes recognised in the Lusitanian and Porto basins are indicated below (see also Figure 4.2), together with a simplified stratigraphic chart. The dashed line in the shaded area of Rift 2 (bottom bar) denotes a departure from the conventionally assumed period for this event in the WIM (see text for discussion).

southern and northern sectors of the Iberian Abyssal Plain, respectively. The differential subsidence between wells Lu-1 and 5A-1, in the Porto Basin (see Figure 4.1 for location), suggest a continued NNW-SSE to NW-SE transtensional deformation along the Porto-Tomar and sub-parallel faults between the Late Jurassic and the Late Cretaceous.

During the remaining of the Late Cretaceous the TS curves in the Northern Lusitanian and southernmost Porto (well 5A-1) basins show small amplitude uplifts (Figure 4.12).

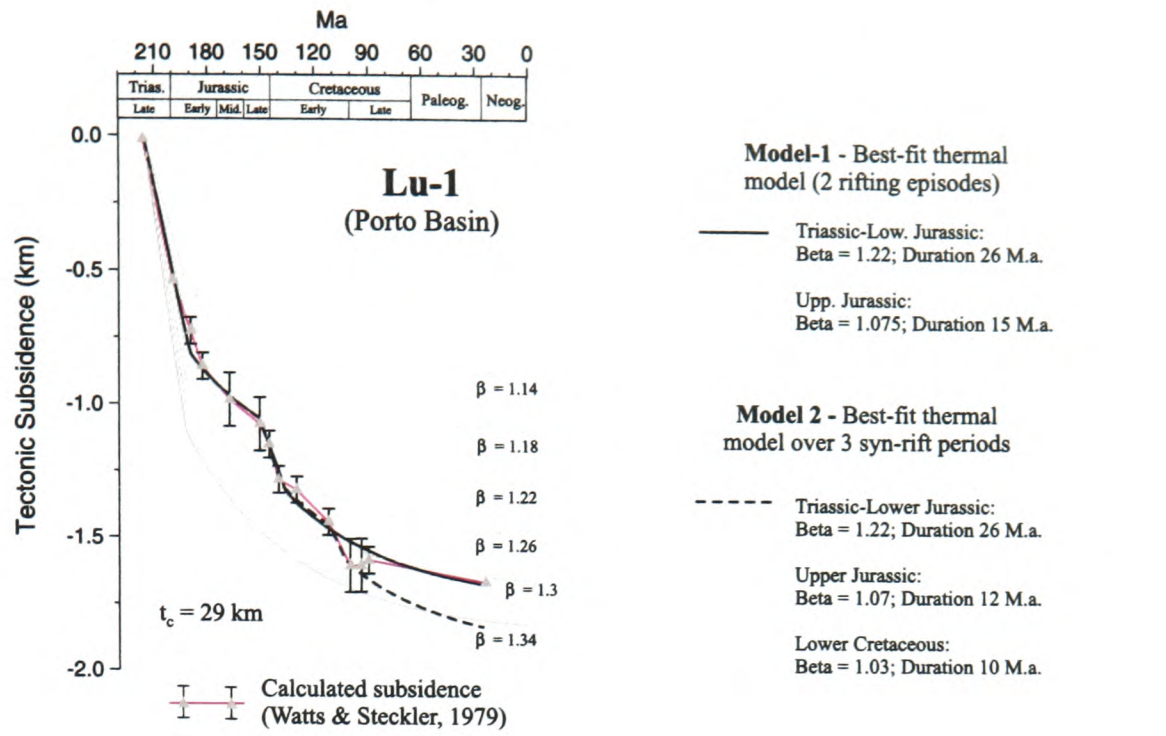

Figure 4.13: Evidence for multi-stage continental rifting from the TS curves calculated at wells Lu-1 (Porto Basin) and Pe-1 (Southern Lusitanian Basin). The TS curves (pink lines) were calculated using the sea-level corrections of Watts & Steckler [1979]. The single-rift theoretical subsidence curves (thin grey lines) are for a 216.5 m.y. old rift with a duration of 20 m.y. The multi-stage continental rifting models 1 (solid black) and 2 (dashed black) are labelled in each graphic. Both single- and multi-stage thermal models assume the parameterisation of Table 4.1.

in the late Early Cretaceous and Late Cretaceous (Albian to Coniacian, $\sim$ 112-89 Ma) could then be attributed either to: 1 - an increment of the regional subsidence during the early stages of seafloor spreading west of the Galicia Bank, which is not accounted for in the model; 2 - transtensional activity along the Porto-Tomar and sub-parallel NNW-SSE striking faults, possibly associated with intense halokinesis; 3 - some combination of both

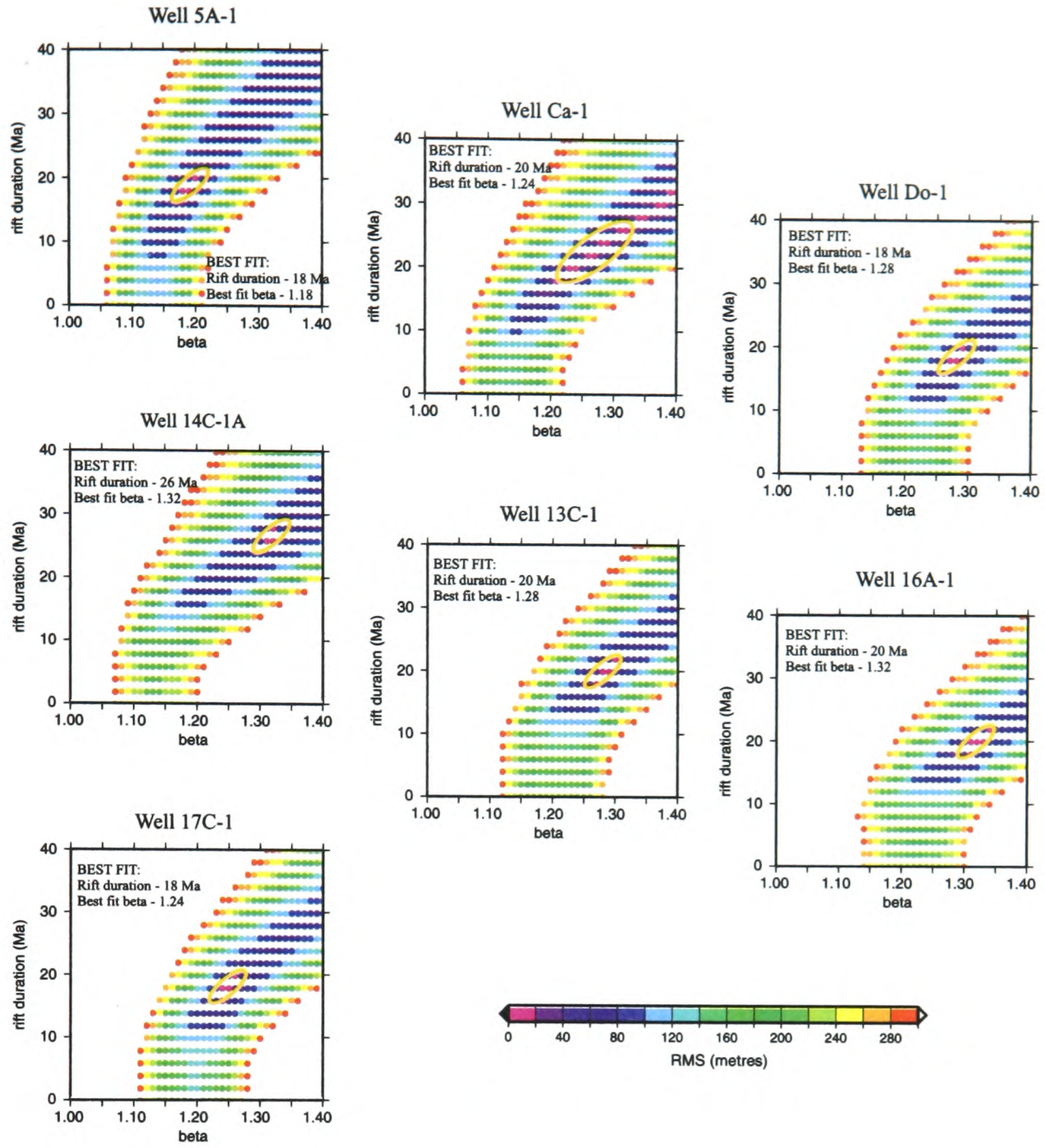

Figure 4.14: Extension factors and duration of the Late Triassic-Early Jurassic rifting event from RMS analysis in 7 boreholes. The RMS is computed between observed (i.e. backstrip) and model predicted subsidence. The thermal model assumes a single, 216.5 Ma old rift event. The parameters of the thermal model are shown in Table 4.1. The RMS is computed for the Late Triassic-Early/Middle Jurassic period, where the sediments are preserved in most of the studied wells. For each well the preferred best-fit curve is defined in terms of β and rift duration. The orange ellipses highlight the region of the graphics where the lower RMS values are located.

4.14), in comparison to that modelled for well Lu-1 (1.22; Figure 4.13). This is consistent with the relative position of these boreholes in the southern flank and centre of the Porto Basin, respectively, and could be explained by continued transtensional deformation along the Porto-Tomar fault, as discussed in Section 4.5. The discrepancies in terms of the duration of the rifting event (8 m.y. difference) are, however, more difficult to explain.

The β estimates presented above only account for the Late Triassic-Early Jurassic

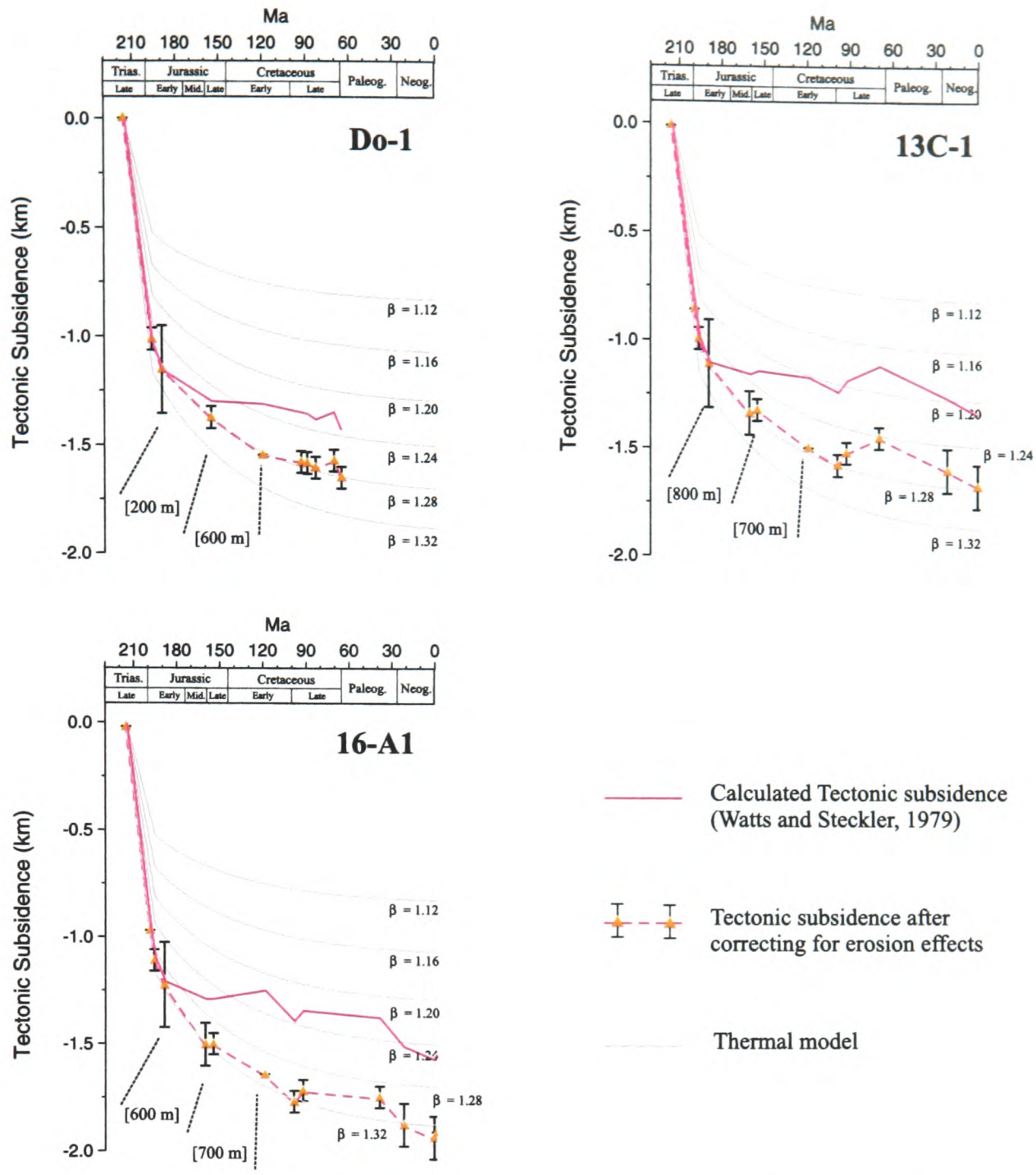

Figure 4.15: Erosion estimates in the Northern Lusitanian Basin: results from 3 wells. The amount of erosion is indicated within brackets for the late Early-Middle Jurassic and Late Jurassic-Early Cretaceous periods, and correspond to the thicknesses of sediments added to the stratigraphic column of the wells in order to obtain a god fit between the backstrip and the thermal model predictions (see text).

added to the late Early-Middle Jurassic successions in order to obtain a good-fit between the calculated TS and the thermal model. These values contrast with the 200 m of eroded material calculated for well Do-1, which is located within a depocentre. A possible explanation is that during the Middle-Late Jurassic significant amounts of salt migrated towards the flanks of the main depocentres, forming salt pillows, and causing uplift at the footwalls of the normal faults (Alves *et al.* [2002a]; Rasmussen *et al.* [1998]).

These results are relevant to understand the hydrocarbon potential of the Portuguese margin, especially because the Late Jurassic and Early Cretaceous formations have been

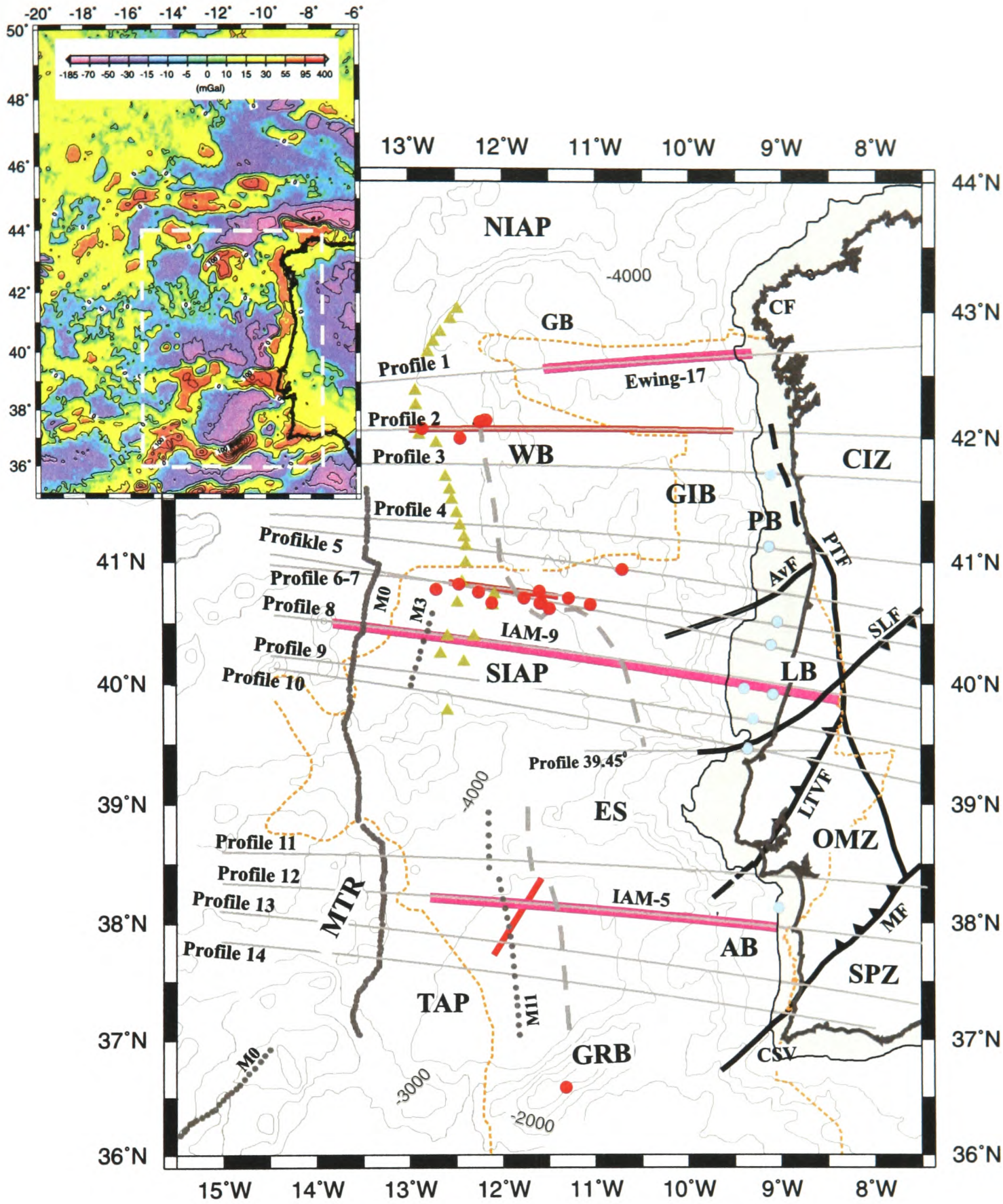

backstripping along the shelf and onshore (see Figure 5.1 for location of the backstripped wells in Chapter 4), and the seismic stratigraphy. These constraints are particularly relevant for POGM, where the anomalies are calculated in terms of the geological processes that shaped the margin, instead of a particular configuration of blocks with contrasting densities.

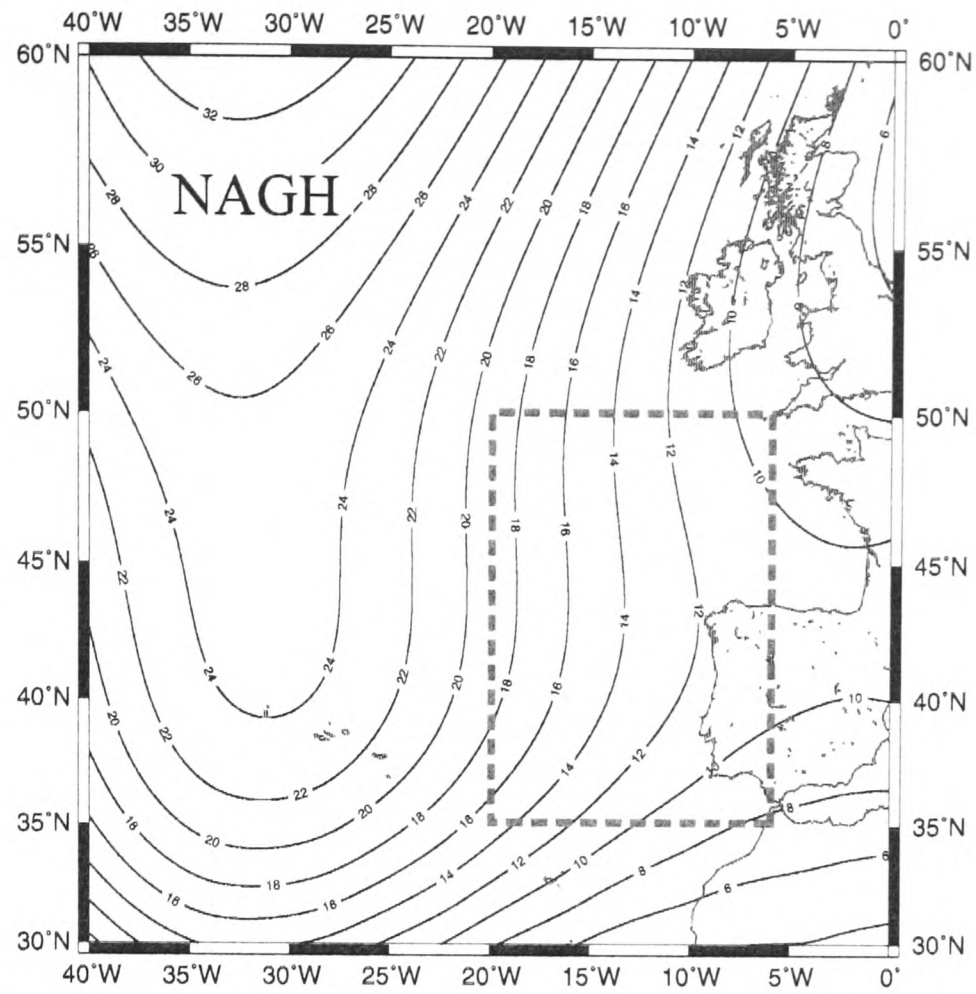

Figure 5.2: Degree and order 12 gravity field calculated from the global geopotencial coefficient model EGM96 for the central NE Atlantic. Approximate minimum included wavelength is 3330 km. Contour spacing is 2 mGal. The long wavelength gravity field of the region is dominated by the North Atlantic Gravity High, NAGH (e.g. Cochran & Talwani [1978]). The area delimited by the dashed grey line corresponds to that of the FAA map in the inset of Figure 5.1

5.3 Process-Oriented Gravity Modelling, POGM

5.3.1 Methodology

Process-Oriented Gravity Modelling, POGM, utilizes seismic constraints on the sediment structure to determine the contributions of rifting and sedimentation to the observed FAA. In the process, constraints may be placed on the long-term flexural strength of the lithosphere, hence T_e, and on the geometry of the margin at the time of rifting (Watts [1988]; Stewart *et al.* [2000]).

The POGM methodology was presented in Chapter 2, together with the mathematical background for the flexure and gravity anomaly calculations, and can be described in sequence of steps (Figure 5.3). The first step is to backstrip the sediments in order to recover the basement total tectonic subsidence (TTS). This process can be carried out assuming that the sediment load is either locally (Airy) or regionally (flexural) supported (e.g. Watts [1988]; Watts & Marr [1995]). In a second step, the geometry of the

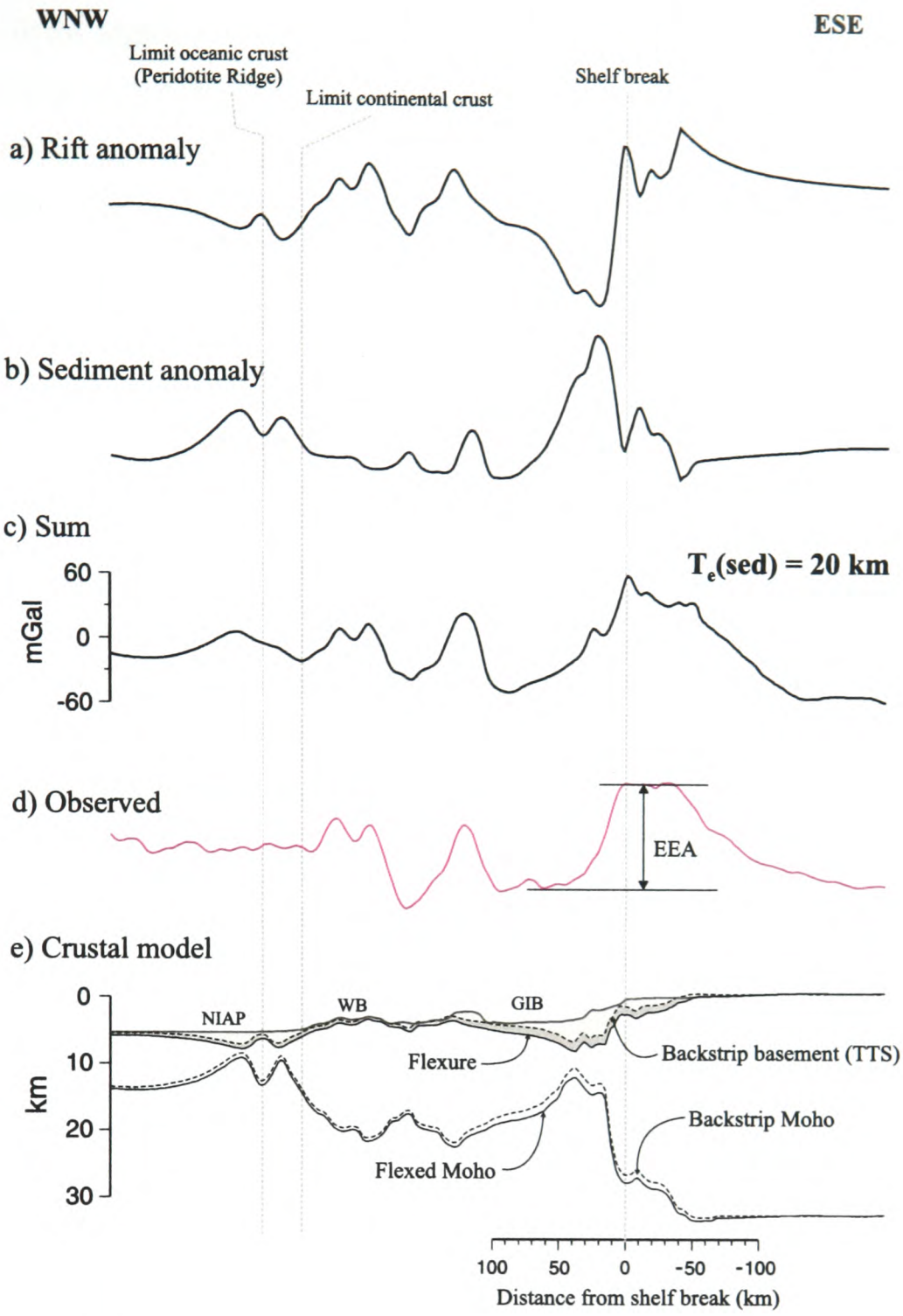

Figure 5.4: Gravity anomalies, flexure and geometry of the rift margin along a transect which crosses the southern Galicia Margin (Profile 4 in Figure 5.1). A constant T_e(sed) of 20 km was used to backstrip the sediments. a) Rifting anomaly, calculated from the total tectonic subsidence (TTS) and the backstrip Moho. b) Sedimentation anomaly, obtained from the combined effects of sediment loading and associated flexure. c) Sum anomaly, obtained by adding (a) and (b). d) Observed gravity. EEA is the edge effect anomaly which forms between the shelf break and the continental slope and rise (see text). e) Crustal structure and configuration of the margin at the time of rifting (dashed lines). The shaded areas show the sediment load (light grey) and associated flexure (dark grey). The shelf break, the limit of stretched continental crust and the peridotite ridge are indicated by the vertical dashed grey lines, separating sectors of distinct basement nature and/or structural framework (see text). Acronyms are as in Figure 5.1.

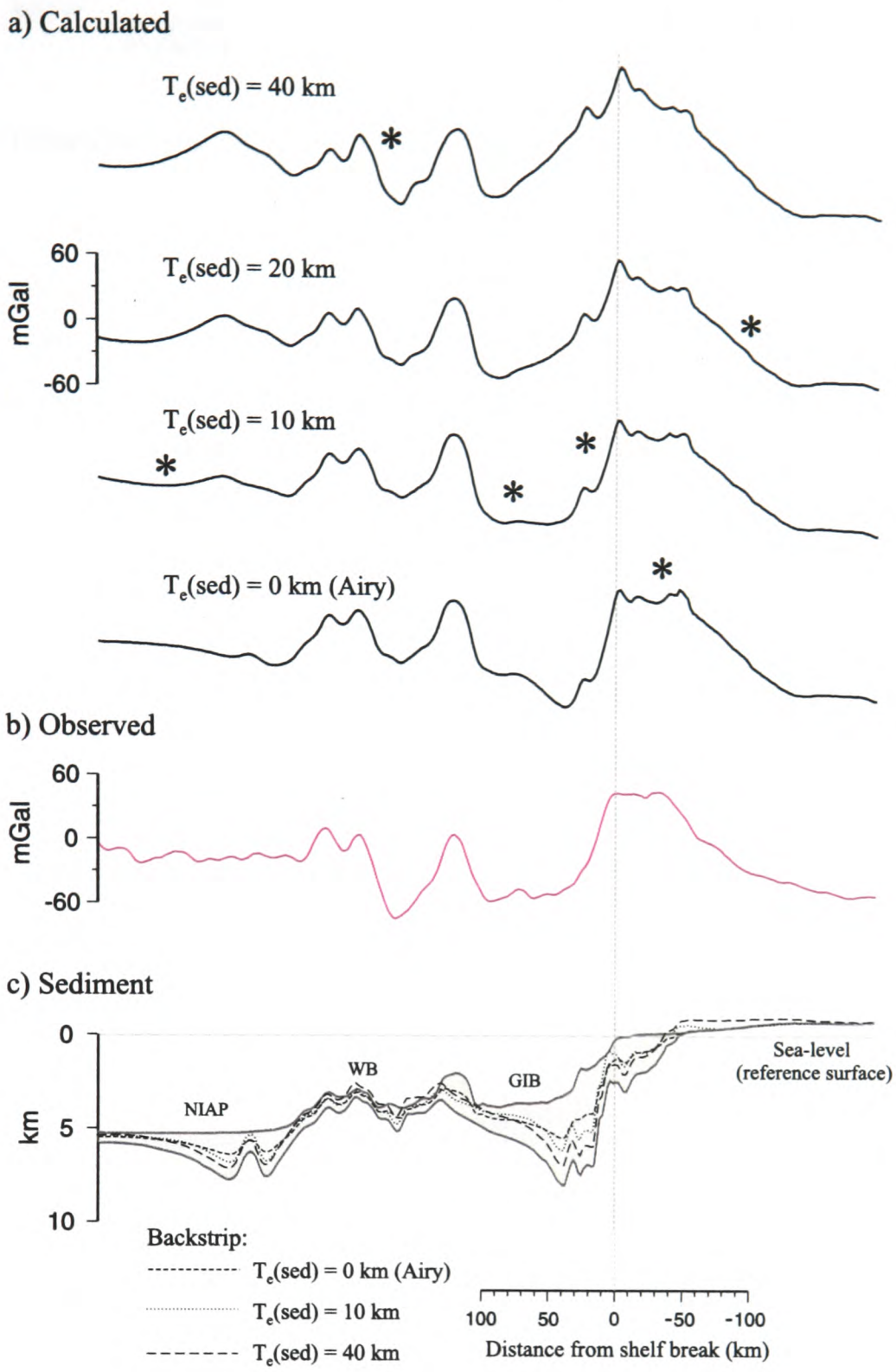

Figure 5.5: Comparison between observed and calculated gravity anomalies for various T_e(sed) scenarios along Profile 4. a) Sum anomaly (rift+sedimentation) calculated for T_e(sed) values of 0, 10, 20, and 40 km. The asterisks indicate a good-fit between observed and calculated gravity anomalies. b) Observed gravity. c) Sediments and backstrip basement for different values of T_e(sed). Regions acronyms are as in Figure 5.1.

Sensitivity Analysis

Figure 5.7 shows the model sensitivity, in terms of the computed RMS between observed and calculated gravity anomalies, to variations in ρ_s, ρ_m, and t_c as a function of T_e(sed); where T_e(sed) is assumed uniform along the profile. The vertical pattern of the RMS contours which dominates the graphics implies that the results are mostly sensitive to variations in T_e(sed), with a well defined minimum between 12 and 14 km (highlighted

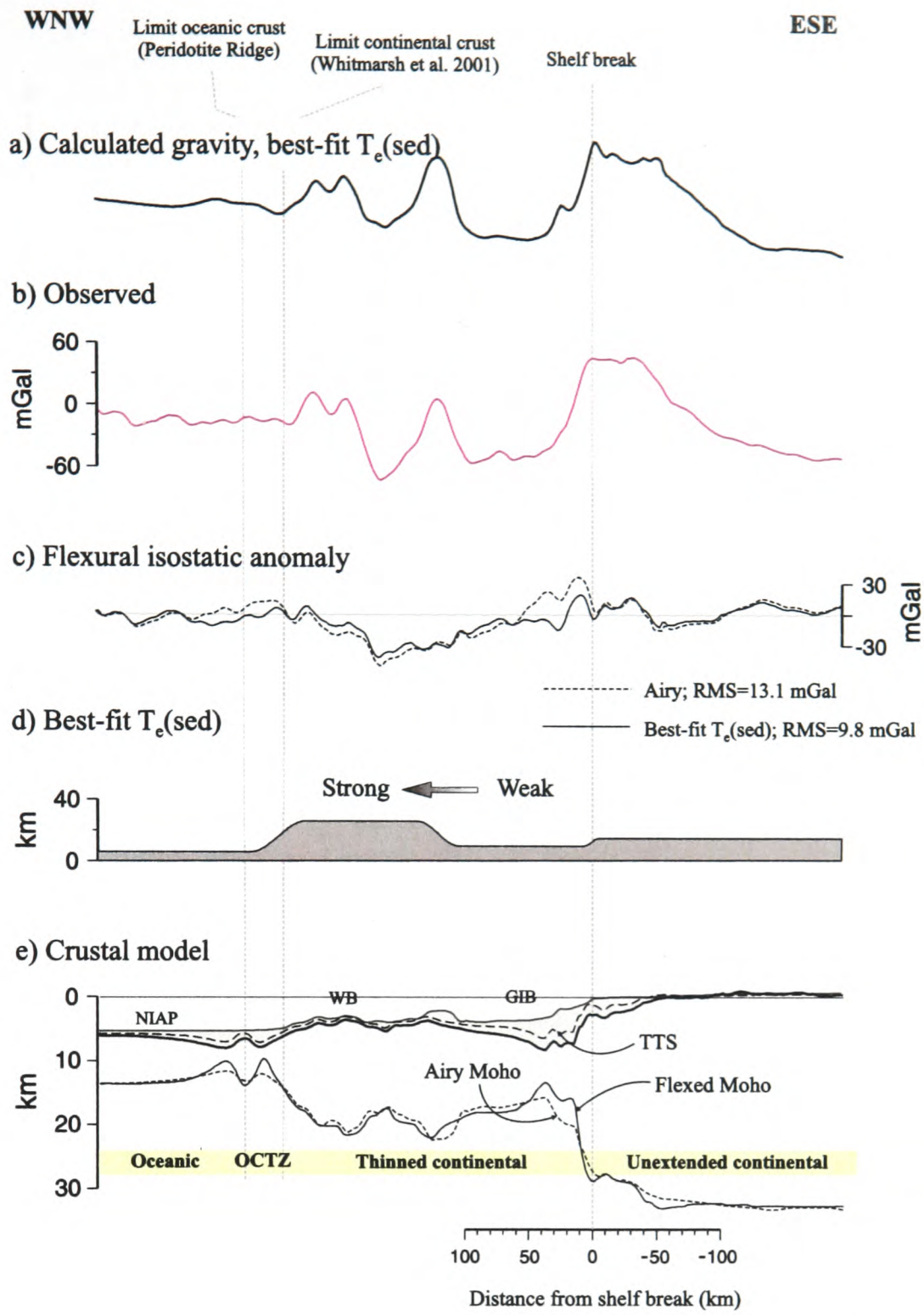

Figure 5.6: Calculated gravity anomalies, residuals and crustal model for a laterally varying T_e(sed) along Profile 4. a) Calculated gravity. b) Observed FAA. c) Flexural isostatic anomaly, obtained by subtracting (a) from (b). Also shown is the Airy isostatic anomaly, i.e. for a T_e(sed) of 0 km (dashed line). d) Best-fit T_e(sed). e) Crustal structure implied by the best-fit T_e(sed) model. Regions acronyms are as in Figure 5.1.

with a cross in each of the panels).

Around these values, variations in the RMS associated with oscillations in the other tested parameters are below 1 mGal and can be considered negligible. This observation is not valid for very low mantle densities (3200 kg m^{-3}). These, however, would imply high mantle potential temperatures, which are unlikely in the context of a magma-poor rifted margin, such as the WIM (e.g. Minshull *et al.* [2001]; Reston & Morgan [2004]).

The sensitivity of the modelling results to other parameters, such as the average

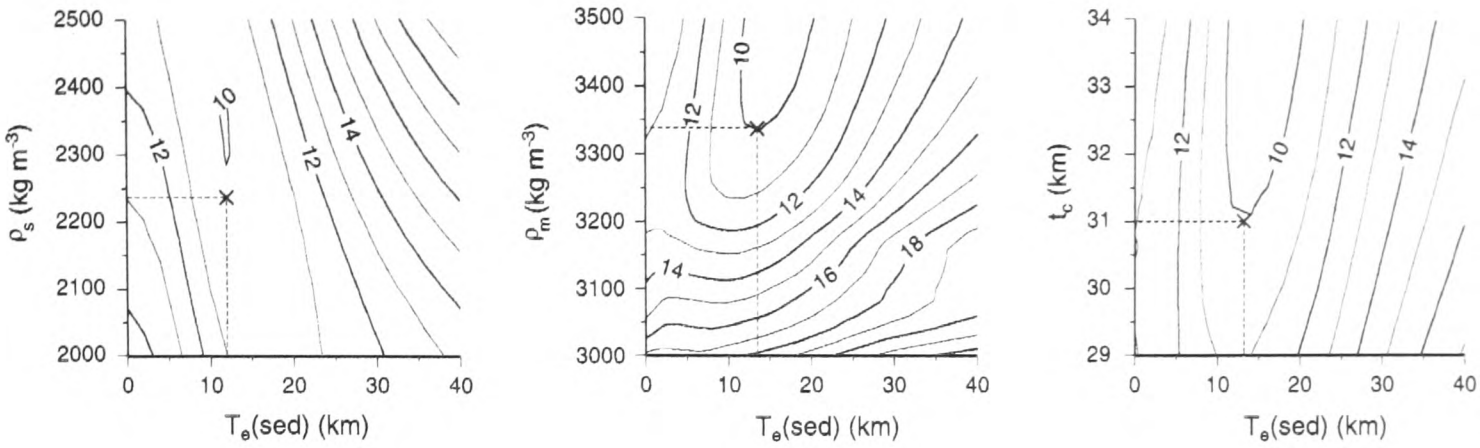

Figure 5.7: Root mean square difference (RMS) between observed and calculated gravity anomalies along Profile 4 for varying ρ_s, ρ_m, and t_c, as a function of a uniform T_e(sed). Contour interval is 1 mGal. The graphics suggest that POGM results are mostly sensitive to variations in T_e(sed). The T_e(sed) which produces the minimum RMS is plotted in each of the graphics for the value of the parameter assumed in this study (see text).

crustal density and the volumetric coefficient of thermal expansion, is not considered here, since these would affect the recovered rift basin geometry and calculated gravity anomalies in a similar way as, for example, the mantle density.

Profile 4 is located in the transition between the Galicia Margin and the Southern Iberia Abyssal Plain, in a region where both the bathymetry and the FAA signature of the margin hold resemblances with that observed to the north and south (Figure 5.1). Moreover, the range of sediment thicknesses found along this transect, between 2 to 6 km, are typical of the WIM (see Figure 3.18). Therefore, the results of the sensitivity analysis in Profile 4 are likely to be representative of the WIM.

In the introduction to the methodology and sensitivity analysis presented above, only the total sediment thickness was used, despite the 3 isopach maps compiled for the margin (see Chapter 3). The reasons for this are three-fold. First, west of the limit of the recently compiled datasets (dashed orange line in Figure 5.1) only the total sediment thickness is available. Consequently, the other horizons would have to be extrapolated along each profile. Second, the total sediment thickness in the WIM is relatively small (less than 6 km in most places). If the sediment loads were to be sub-divided into three distinct layers, with maximum amplitudes of $\sim$ 3-4 km, then the sensitivity of the method would be reduced. And third, the inclusion of three sediment layers implies possible variations on three values of ρ_s and T_e(sed). This would generate more uncertainty in the models without the necessary sensitivity to test the results.

Therefore, the one layer approach will be used throughout this chapter to determine the gravity anomalies associated with the rifting and sedimentation processes and put constraints on the long-term flexural strength of the lithosphere along the margin.

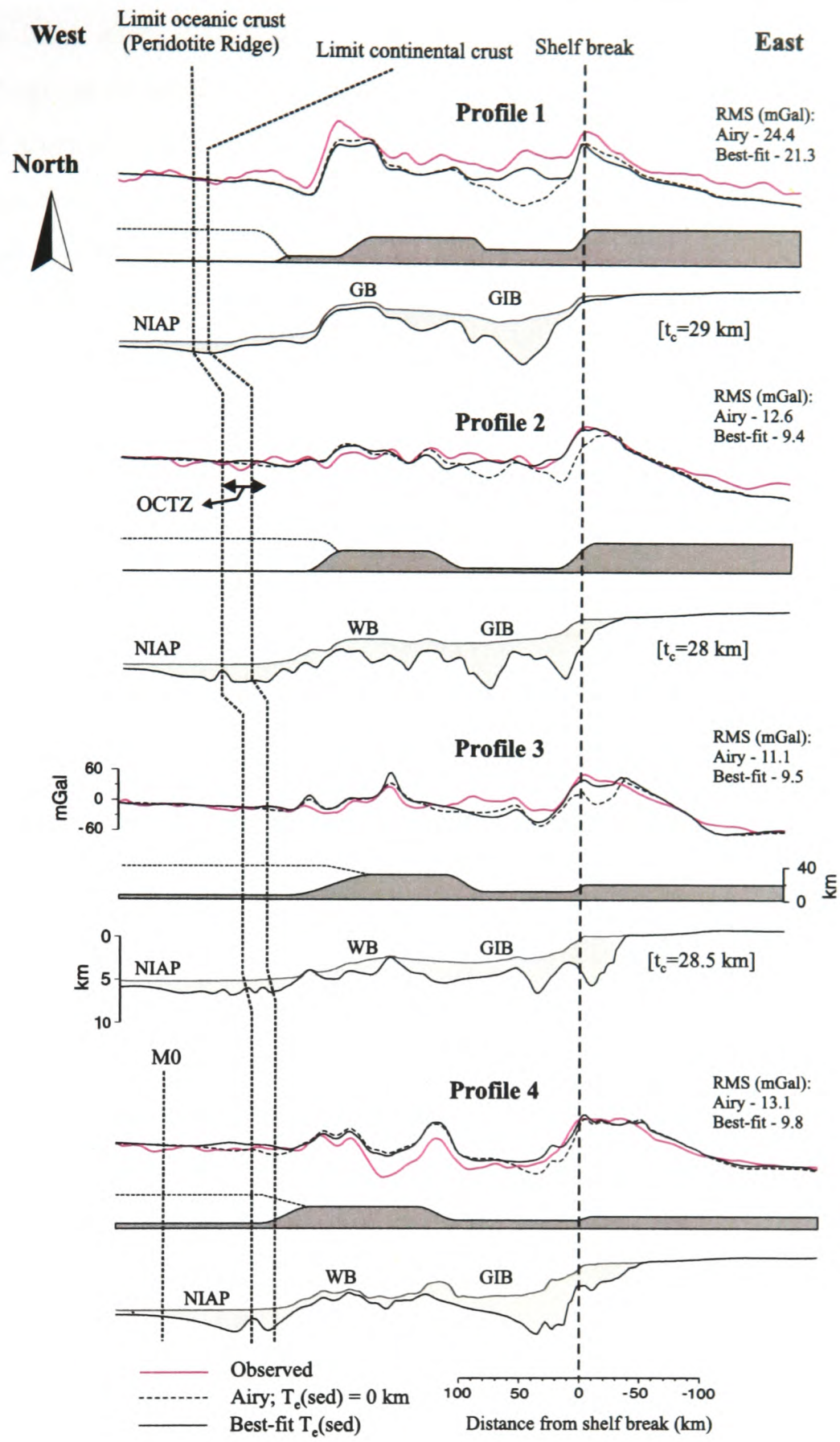

Figure 5.8: Results from POGM in the Galicia Margin, Profiles 1-4 (see Figure 5.1 for location). Along each profile we show: top - the observed FAA (pink) and calculated gravity anomalies for the Airy (T_e(sed) = 0 km; dashed black) and best-fit T_e(sed) scenarios (solid black); middle - the best-fit T_e(sed). The dashed line at 40 km represents the uncertainty of the gravity modelling results along transitional and oceanic domains (see text); bottom - the basin configuration. Profiles are stacked on the shelf break. The modelling parameters are as defined in Section 5.3.1. Variations to the initial crustal thickness (t_c) are indicated within brackets. Acronyms are as in Figure 5.1.

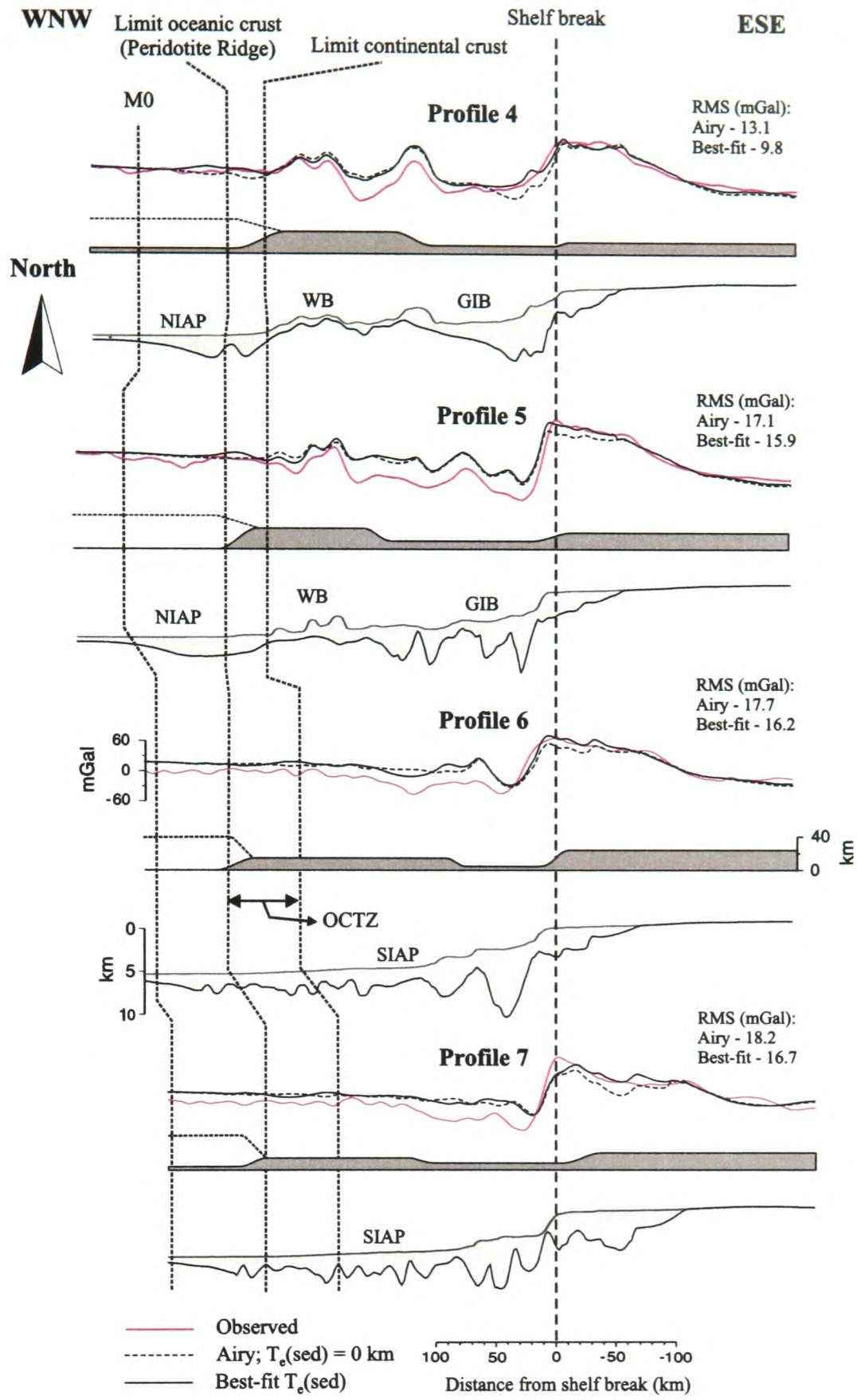

Figure 5.9: Results from POGM in the Intermediate Segment, Profiles 4-7 (see Figure 5.1 for location). See Figure 5.8 for legend.

Intermediate Segment

The Intermediate Segment extends from the southern Western Banks and Galicia Interior Basin (Profiles 4 and 5) to the northermost Southern Iberia Abyssal Plain and Lusitanian Basin (Profiles 6 and 7; see Figure 5.1). As discussed in Chapter 3, this segment of the WIM is characterized by a progressive change in the physiography and structural framework of the margin, and the widening of the OCTZ towards the south.

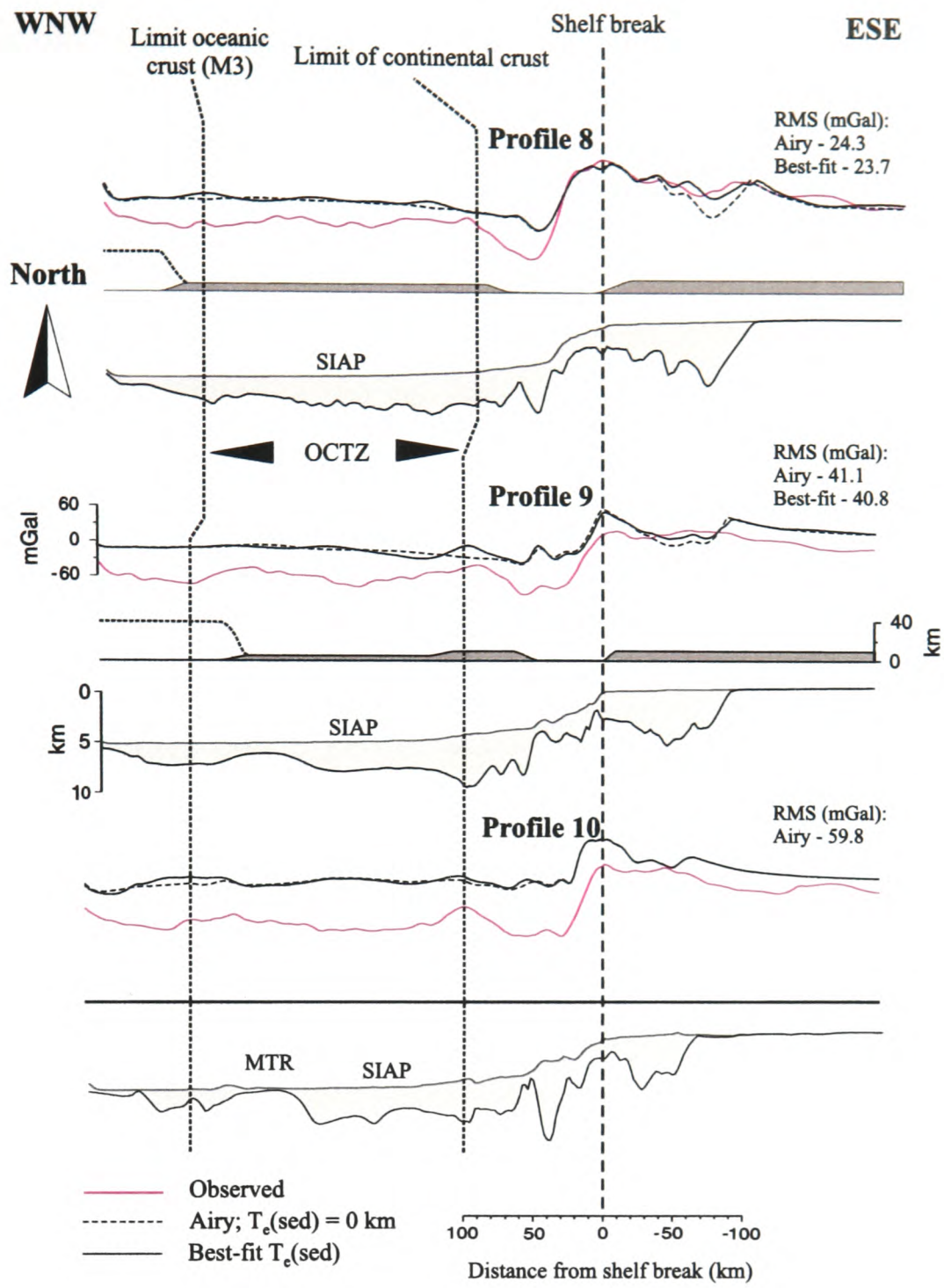

Figure 5.10: Results from POGM in the Central Portuguese Margin, Profiles 8-10 (see Figure 5.1 for location). See Figure 5.8 for legend.

less than 50 km to the west of the base of the continental slope (Figure 5.1), based on MCS and wide-angle data (Pickup *et al.* [1996]; Dean *et al.* [2000]). Consequently, the width of highly stretched continental crust is reduced and that of transitional type basement significantly increased (up to 170 km according to Dean *et al.* [2000]), in relation to that observed in the Galicia and Intermediate segments of the WIM.

In Profiles 8 and 9, the T_e(sed) estimated over relatively unstretched Variscan basement varies between 10 and 20 km (Figure 5.10). This is consistent with the results in profiles 5-7 (Figure 5.9), also located in the Ossa Morena terrane. In Profile 10, the Airy model (i.e. T_e(sed) = 0 km) gives the minimum RMS, but the calculated gravity anomalies over the continental shelf, slope and rise bear little resemblance with the observed.

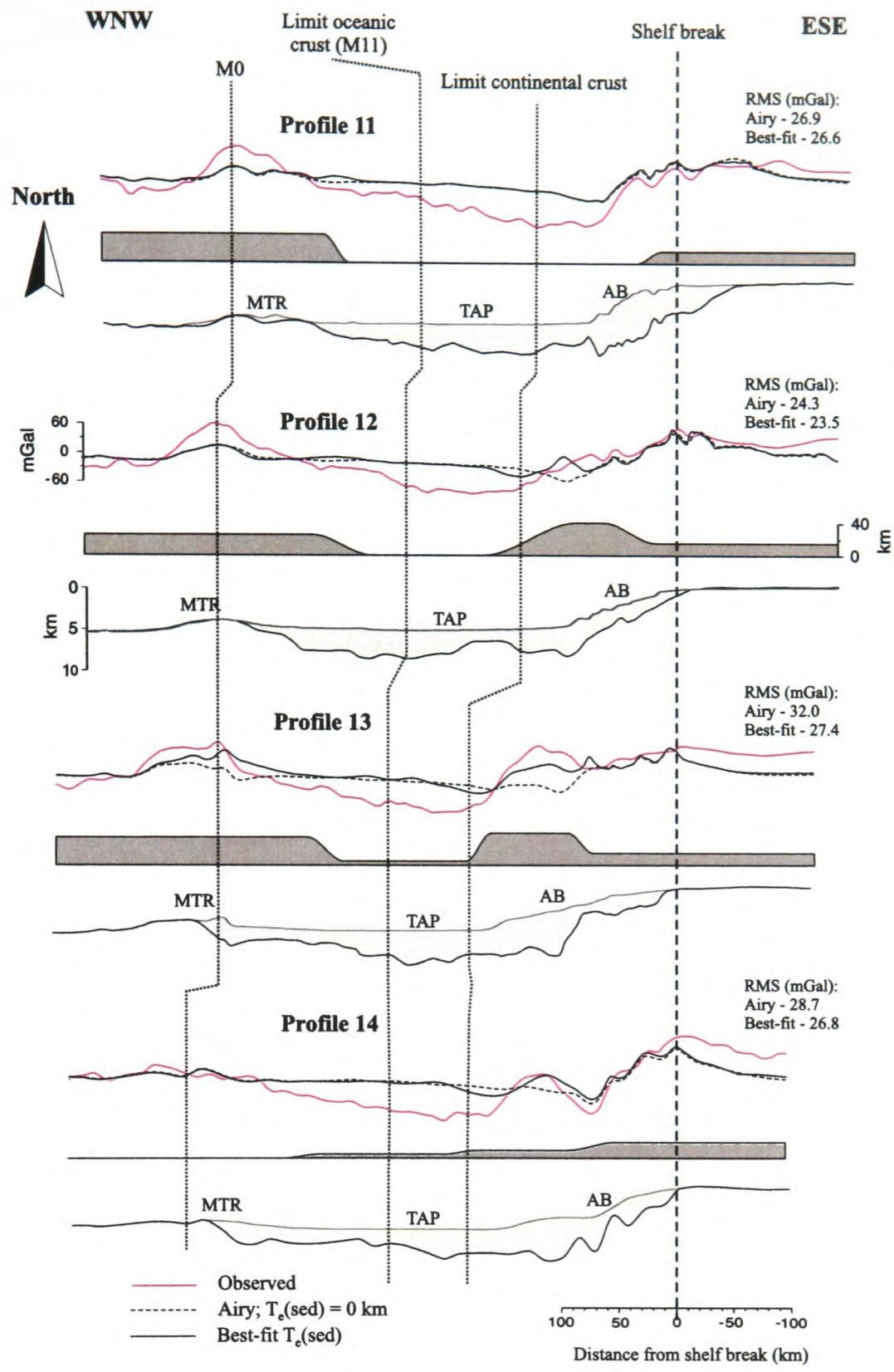

Figure 5.11: Results from POGM in the Southwest Portuguese Margin, Profiles 11-14 (see Figure 5.1 for location). See Figure 5.8 for legend.

seismic refraction and wide-angle data onshore and along the continental shelf (Matias [1996]; see also Figure 3.6).

In the central SW Portuguese Margin, along Profiles 12 and 13, it appears that lithospheric thinning between the shelf and the continental rise is associated with an increase in the flexural strength of the basement. The higher values of T_e(sed) constrained in these profiles are necessary to reduce the misfits between the observed and calculated gravity anomalies along the FAA "slope high". However, they are in marked contrast with the results obtained in Profiles 11 and 14, and with the mechanical structure of

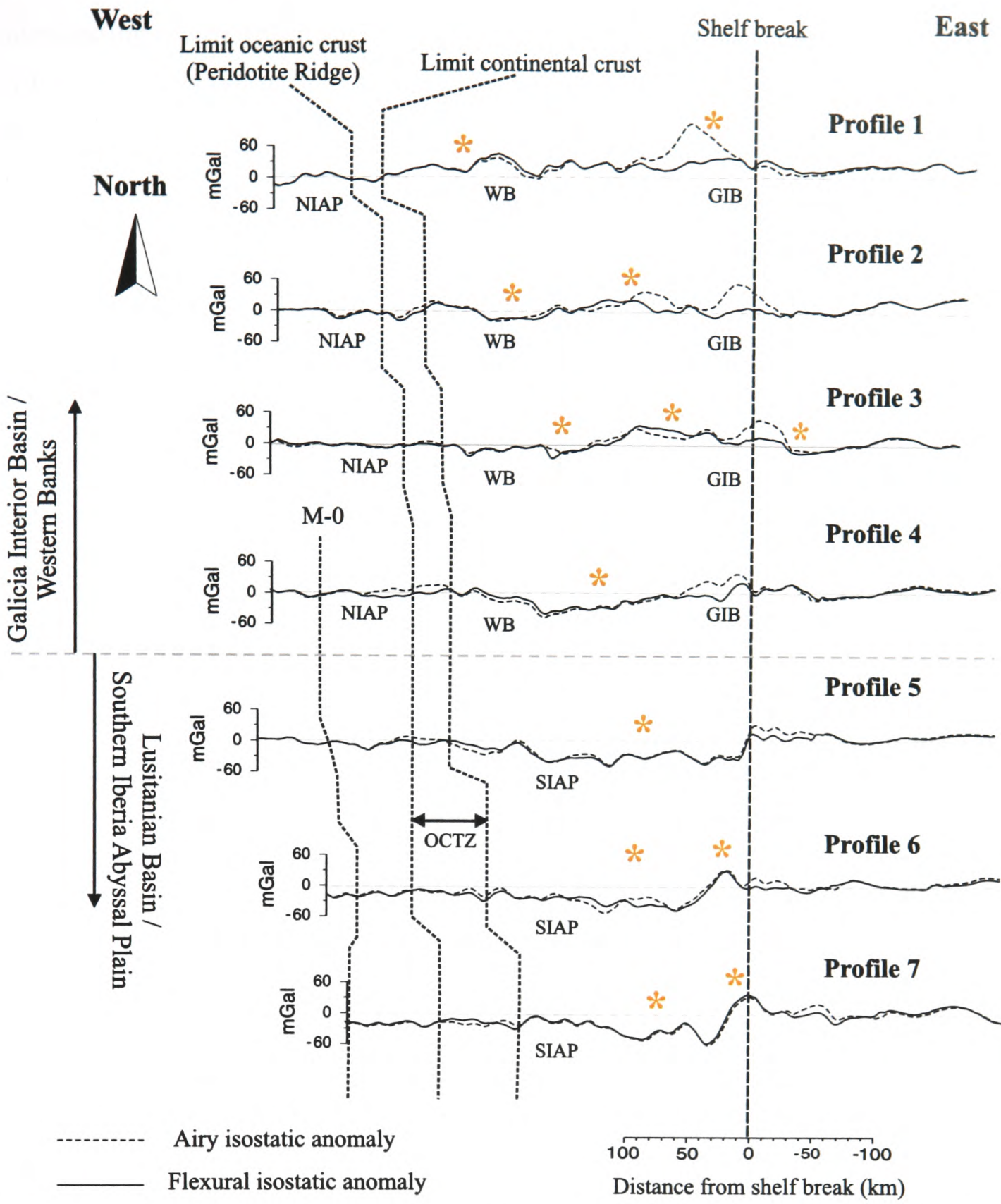

Figure 5.12: Airy and flexural, best-fit T_e(sed), isostatic anomalies in the Galicia and Intermediate segments of the WIM, Profiles 1 to 7 (see Figure 5.1 for location). The orange asterisks highlight important misfits between modelled and observed gravity anomalies, possibly related to departures from an Airy model of rifting (see text for discussion).

In the following discussion, the largest departures between observed and calculated gravity anomalies are evaluated in terms of the computed isostatic residuals (or the isostatic anomalies, IA; Figures 5.12 and 5.13); where the IA are obtained by subtracting the calculated gravity anomaly from the observed FAA. As highlighted in the work of Kooi *et al.* [1992] and Lin & Watts [2002], for example, this is a powerful means of

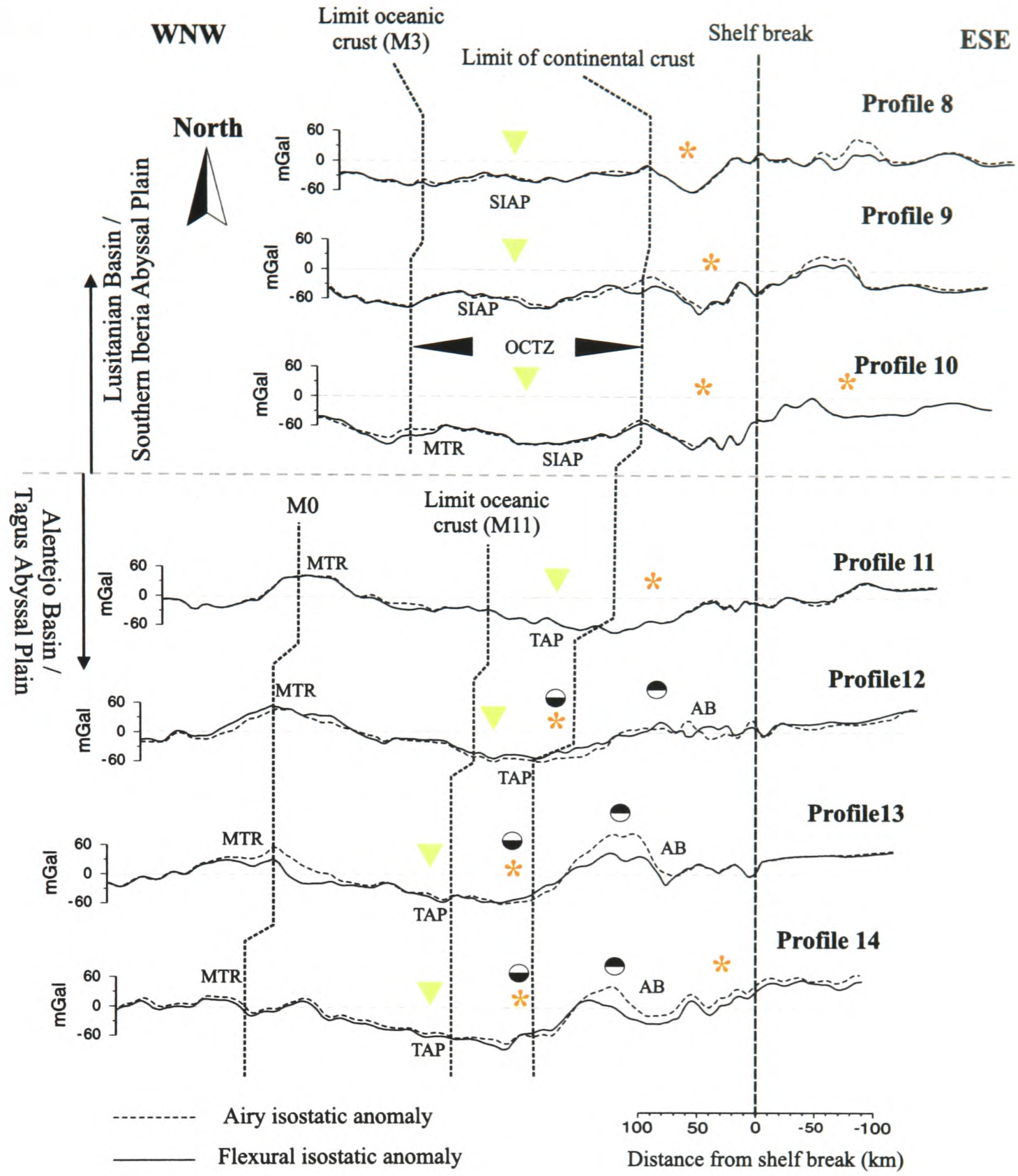

Figure 5.13: Airy and flexural, best-fit T_e(sed), isostatic anomalies in the Central and SW Portuguese segments of the WIM, Profiles 8 to 14 (see Figure 5.1 for location). The orange asterisks, black-white circles, and green triangles highlight important misfits between modelled and observed gravity anomalies possibly related to departures from an Airy model of rifting, thrust loading, and lithospheric mantle serpentinization and/or depletion, respectively (see text for discussion).

are not observed elsewhere along the WIM (see inset in Figure 5.1). In Profiles 12, 13 and 14, for example, it appears as if the EEA low had been overprinted (Figure 5.11).

The Airy IA calculated along profiles 13 and 14 (dashed lines in Figure 5.13) show a distinctive positive-negative "couple" over the lower continental slope and rise, respec-

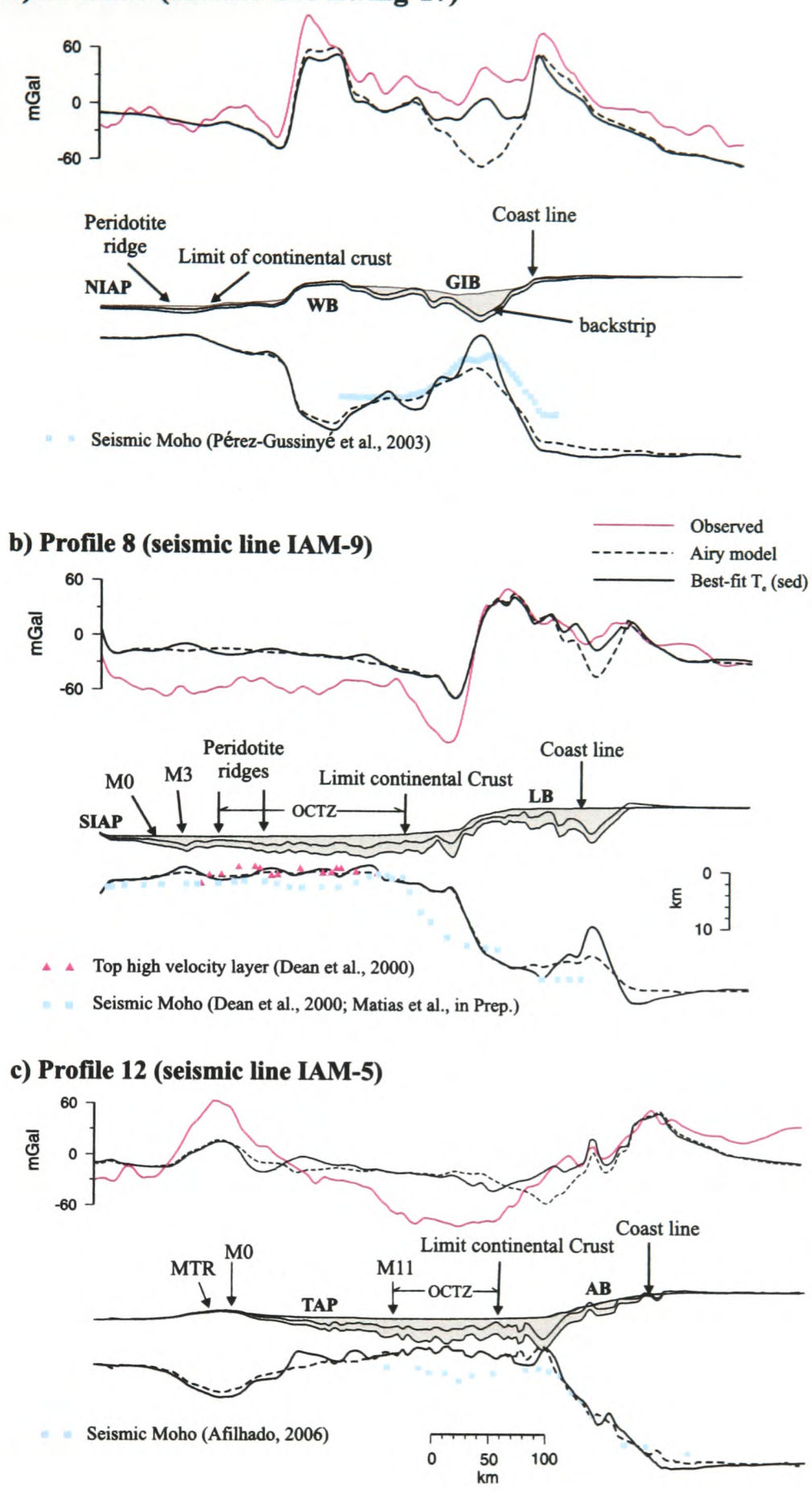

Figure 5.14: Gravity anomalies (top) and crustal structure constrained from the gravity modelling (bottom) along three wide-angle/refraction profiles (see Figure 5.1 for location of the data and modelled profiles): a) Seismic line Ewing-17 and modelled Profile 1; b) Seismic line IAM-9 and modelled Profile 8; Seismic line IAM-5 and modelled Profile 12. Along all the profiles the seismic Moho (blue squares) are shown, for comparison with the results from the gravity modelling (black lines).

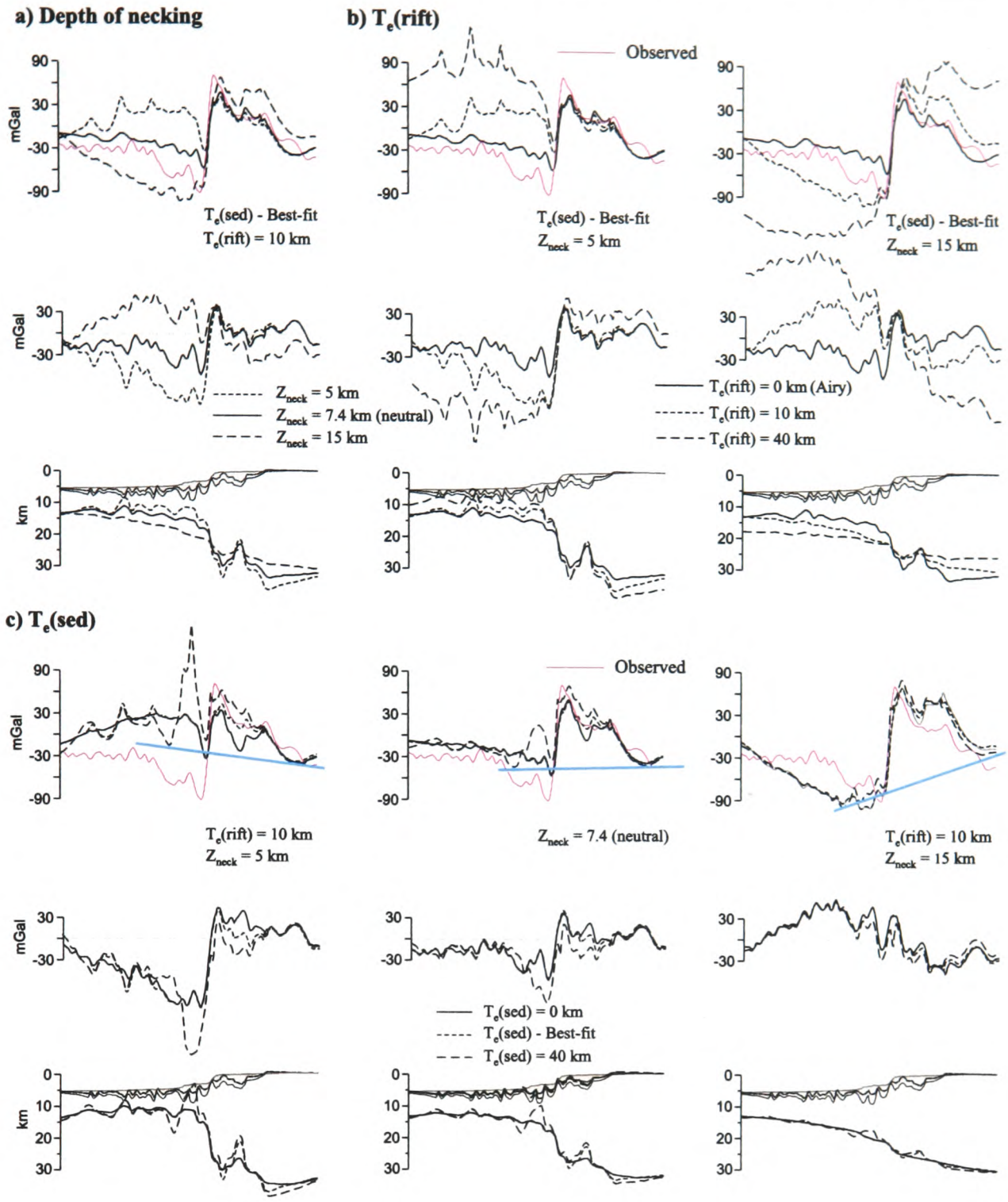

Figure 5.15: Effects of varying Z_{neck}, T_e(rift) and T_e(sed) on the calculated gravity anomalies (top), isostatic residuals (middle) and the geometry of the rifted margin (bottom) along a WIM transect. Results are from Profile 7 (see Figure 5.1 for location). a) T_e(rift) is kept constant and equal to 10 km, while Z_{neck} varies between 5, 7.4 and 15 km. For the crustal parameters used (see Section 5.3.1) a Z_{neck} = 7.4 km (solid black lines) corresponds to a balance in the forces associated with extension (i.e. Airy rifting; see text). b) T_e(rift) is varied between 0 km (Airy rift; solid black lines) 10 and 40 km, for two values of Z_{neck} (5 km and 15 km; left and right panels, respectively). c) T_e(rift) is kept constant (10 km) and three T_e(sed) scenarios are tested (0 km, 40 km and the best-fit T_e(sed) structure; see Figure 5.9) for a Z_{neck} of 5 km (left), 7.4 km (Airy rift; centre) and 15 km (right). Solid blue lines highlight the general trend of the computed EEA for each of the tested Z_{neck}'s (see text).

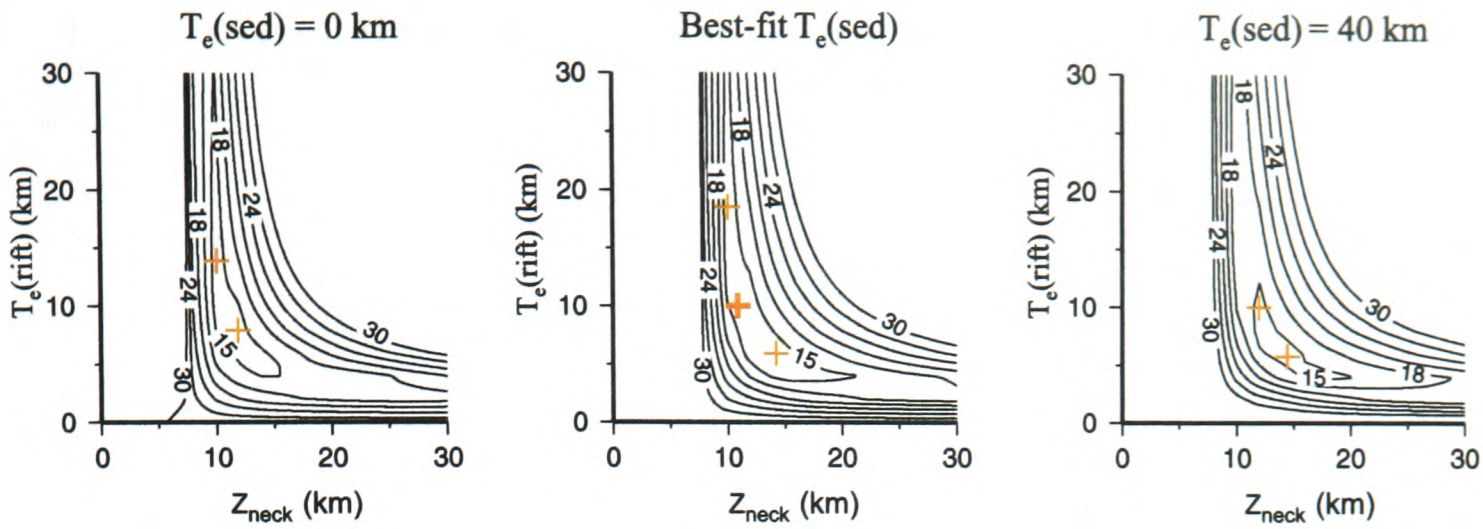

Figure 5.16: Sensitivity of the isostatic anomaly to T_e(rift) and Z_{neck} for different T_e(sed) scenarios along Profile 7. Contour interval is 3 mGal. RMS's higher than 30 mGal were not plotted. For each T_e(sed) the models that best explain the observed FAA (minimum RMS) are highlighted by the orange crosses. The results suggest an interdependence between Z_{neck} and T_e(rift) (see text). In the middle panel, the thick cross indicates the preferred model.

5.15c). Independently of T_e(sed), a shallow Z_{neck} is associated with a landward dip of the EEA (left panel), in relation to the neutral case (i.e. the Airy model, centre), and the opposite effect is observed for a deeper than Airy predicted Z_{neck} (right panel).

The models depicted in Figure 5.15 suggest that at the latitude of Profile 7 ($\sim$ 40.3°; Figure 5.1) the margin is in an upward state of flexure. It appears, however, that an improvement in the fit between observed and calculated gravity anomalies could be achieved either by assuming a Z_{neck} between 7.4 and 15 km, for a T_e(rift) of $\sim$ 10 km (Figure 5.15a), or by reducing T_e(rift) for a deeper Z_{neck} (Figure 5.15b).

This trade-off relationship between T_e(rift) and Z_{neck} is clearly exposed in the RMS graphics (computed between observed and calculated gravity anomalies) of Figure 5.16, which show at least two local minima (orange crosses) for distinct combinations of these parameters. Despite this, there are differences between the calculated gravity anomalies and geometry of the recovered rift basin that can be used to select between possible "best-fit" models. This is particularly true when the Moho depth is well constrained from wide-angle and/or refraction seismic data, as in several modelled transects along the WIM (see Figure 5.1). In the case of Profile 7, the preferred model is given by a T_e(rift) of 10 km, a Z_{neck} of 11 km and a laterally varying T_e(sed). As shown in Figure 5.17, and in Appendix C (Figure C.7), this model explains the FAA signature of the margin and is in good agreement with the seismic and well data constraints on the Moho depth. Other situations arise where different combinations of T_e(rift) and Z_{neck} values suite better distinct sections of the profile (e.g. Profile 1 in Figure 5.17).

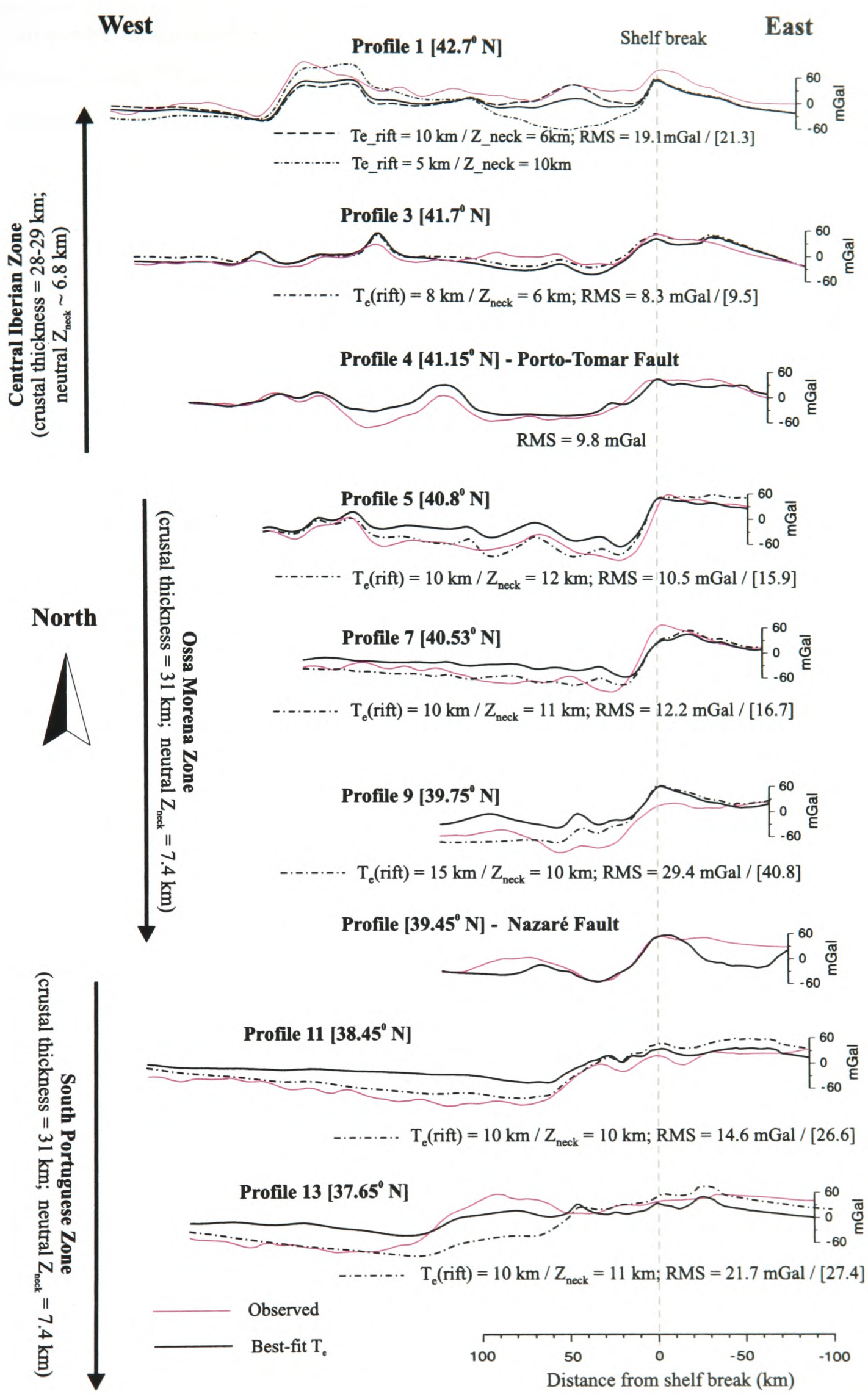
West
East
Shelf break
Profile 1 [42.7° N]
Te_rift = 10 km / Z_neck = 6km; RMS = 19.1mGal / [21.3]
Te_rift = 5 km / Z_neck = 10km
Profile 3 [41.7° N]
Te(rift) = 8 km / Zneck = 6 km; RMS = 8.3 mGal / [9.5]
Profile 4 [41.15° N] - Porto-Tomar Fault
RMS = 9.8 mGal
Profile 5 [40.8° N]
Te(rift) = 10 km / Zneck = 12 km; RMS = 10.5 mGal / [15.9]
Profile 7 [40.53° N]
Te(rift) = 10 km / Zneck = 11 km; RMS = 12.2 mGal / [16.7]
Profile 9 [39.75° N]
Te(rift) = 15 km / Zneck = 10 km; RMS = 29.4 mGal / [40.8]
Profile [39.45° N] - Nazaré Fault
Profile 11 [38.45° N]
Te(rift) = 10 km / Zneck = 10 km; RMS = 14.6 mGal / [26.6]
Profile 13 [37.65° N]
Te(rift) = 10 km / Zneck = 11 km; RMS = 21.7 mGal / [27.4]
60
0
-60
mGal
Central Iberian Zone
(crustal thickness = 28-29 km;
neutral Zneck ~ 6.8 km)
North
Ossa Morena Zone
(crustal thickness = 31 km; neutral Zneck = 7.4 km)
South Portuguese Zone
(crustal thickness = 31 km; neutral Zneck = 7.4 km)
Observed
Best-fit Te
100
50
0
-50
-100
Distance from shelf break (km)

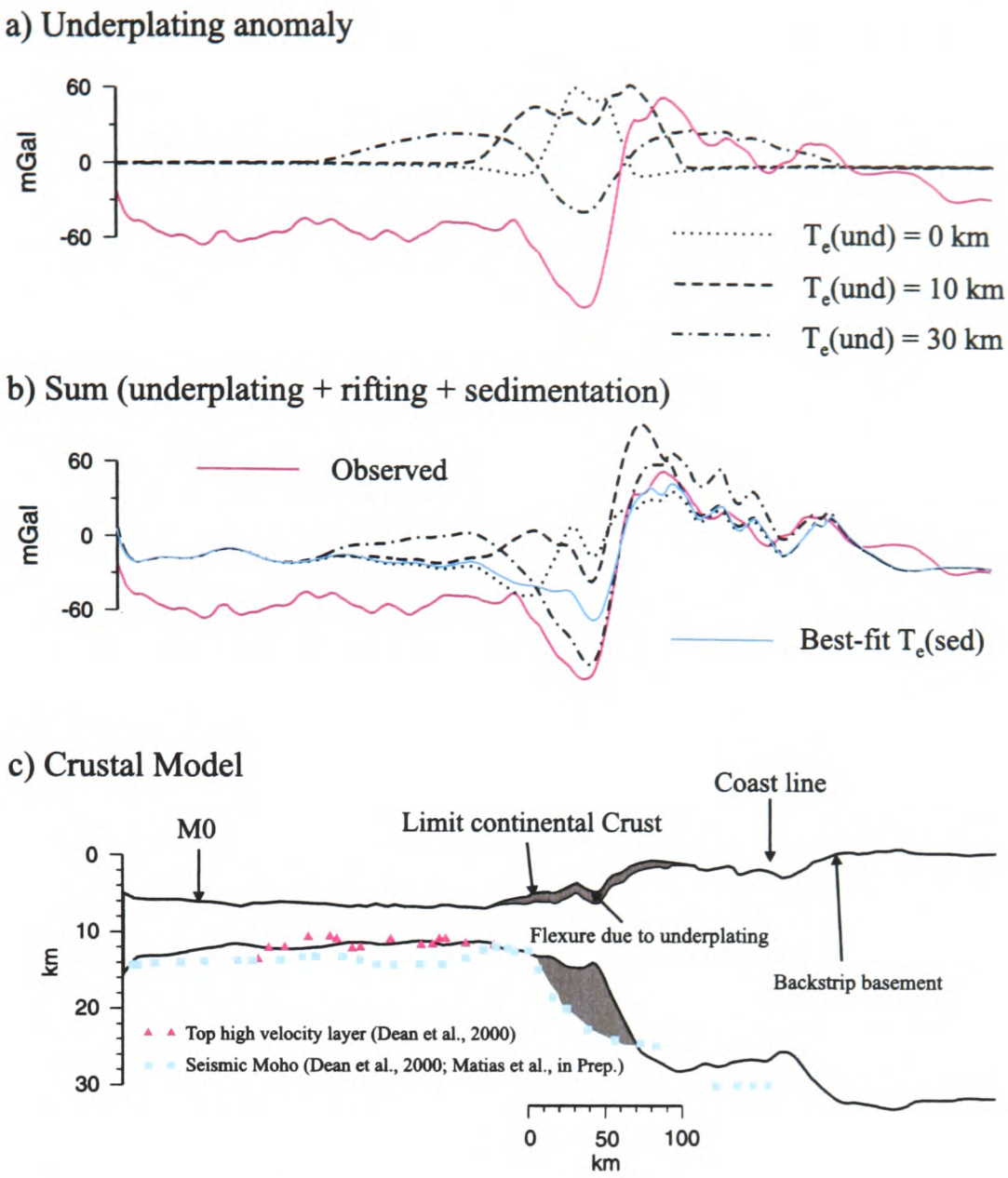

Figure 5.18: Underplating in the Central Portuguese Margin; results along Profile 8, seismic Line IAM-9 (see Figure 5.1 for location). a) Underplating gravity anomaly for different values of T_e(und). where T_e(und) is the rigidity of the margin at the time the magmatic body was emplaced. The underplating anomaly is the sum of effects of the underplated load and associated flexure (see text). A density of 2850 kg m^{-3} was assumed for the underplated body. b) Comparison between observed (pink) and calculated gravity anomalies (black), where the calculated is the total obtained by adding the underplating anomalies to those of rifting and sediment loading. The rift and sedimentation anomalies were computed assuming a laterally varying T_e(sed) (see Figure 5.10) and T_e(rift) = 0 km; blue line. c) Crustal structure, underplated load and associated flexure. The load is defined between the basckstrip and the seismic Mohos (see text).

the constrained T_e(und) is higher than that obtained from backstripping and sediment modelling over unextended Variscan basement (T_e(sed) between 10 and 25 km in Profiles 5 to 9; Figures 5.9 and 5.10), which is unlikely, since the rigidity of the margin is expected to decrease during intense lithospheric thinning (e.g. Burov & Poliakov [2001]).

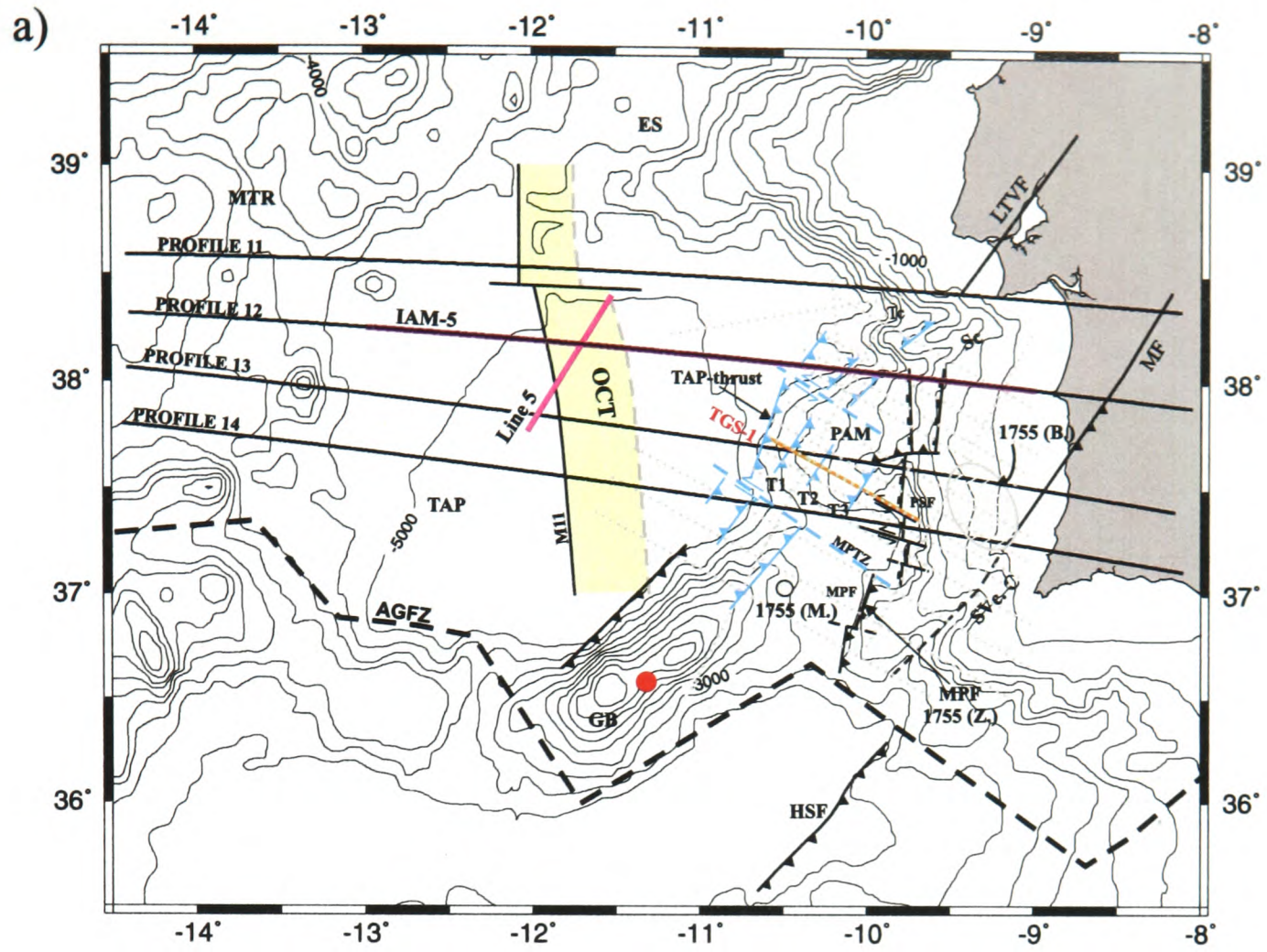

As shown in Figure 5.19a, this corresponds to the major front of compressional deformation, here designated by the Tagus Abyssal Plain-Thrust (TAP-Thrust), striking NNE-SSW along the base of the continental slope between just north of the Gorringe Bank and the Setúbal canyon (Cunha *et al.* [in Prep]).

The interpretation in depth of the major structures, although speculative in some places (dashed lines in Figure 5.19b), suggests that the Príncipes d´Avis Mountains formed as a crustal-scale pop-up structure, and that the main E to SE dipping thrusts might be soling into a common detachment surface deep in the crust. It is therefore likely that the FAA gravity high over the lower continental slope, and part of the flanking low,

a) Isolate FAA 'slope high'
Shelf break
mGal
60
0
-60
Observed
Airy model (RMS = 32.03 mGal)
Best-fit T_e(sed);
T_e(rift) = 10 km;
Z_{neck} = 10 km.
(RMS = 20.08 mGal)
b) Load and flexure (broken-plate model)
km
2
0
-2
-4
rho_{load} = 2650 kg m^{-3}
$rho_{linfill}$ = 2650 kg m^{-3}
T_e(thrust) = 50 km
T_e(thrust) = 20 km
T_e(thrust) = 0 km
c) Thrusting anomaly
mGal
60
0
-60
Flexure
Total (flexure + load)
d) Sum (thrusting + rifting + sedimentation)
mGal
60
0
-60
Observed
T_e(sed) = T_e(rift) = 0 km
T_e(thrust) = 50 km (22.67)
T_e(thrust) = 0 km (16.48)
T_e(thrust) = 20 km (15.06)
T_e(thrust) = 50 km (12.35)
e) Best-fit T_e(sed)
km
40
0
f) Crustal model
Depth (km)
0
10
20
30
MTR
M0
M11
TAP-thrust
PAM
PSF
Coast Line
Oceanic crust
OCTZ
Continental crust
Buried load
(thrusting)
Flexed Moho,
T_e(thrust) = 50 km
Seismic Moho:
Afilhado, 2006 (IAM-5, projected)
Pinheiro et al., 1992 (Line 5)
Top high vel. layer;
Pinheiro et al., 1992 (Line 5)
100
50
0
-50
-100
Distance from shelf break

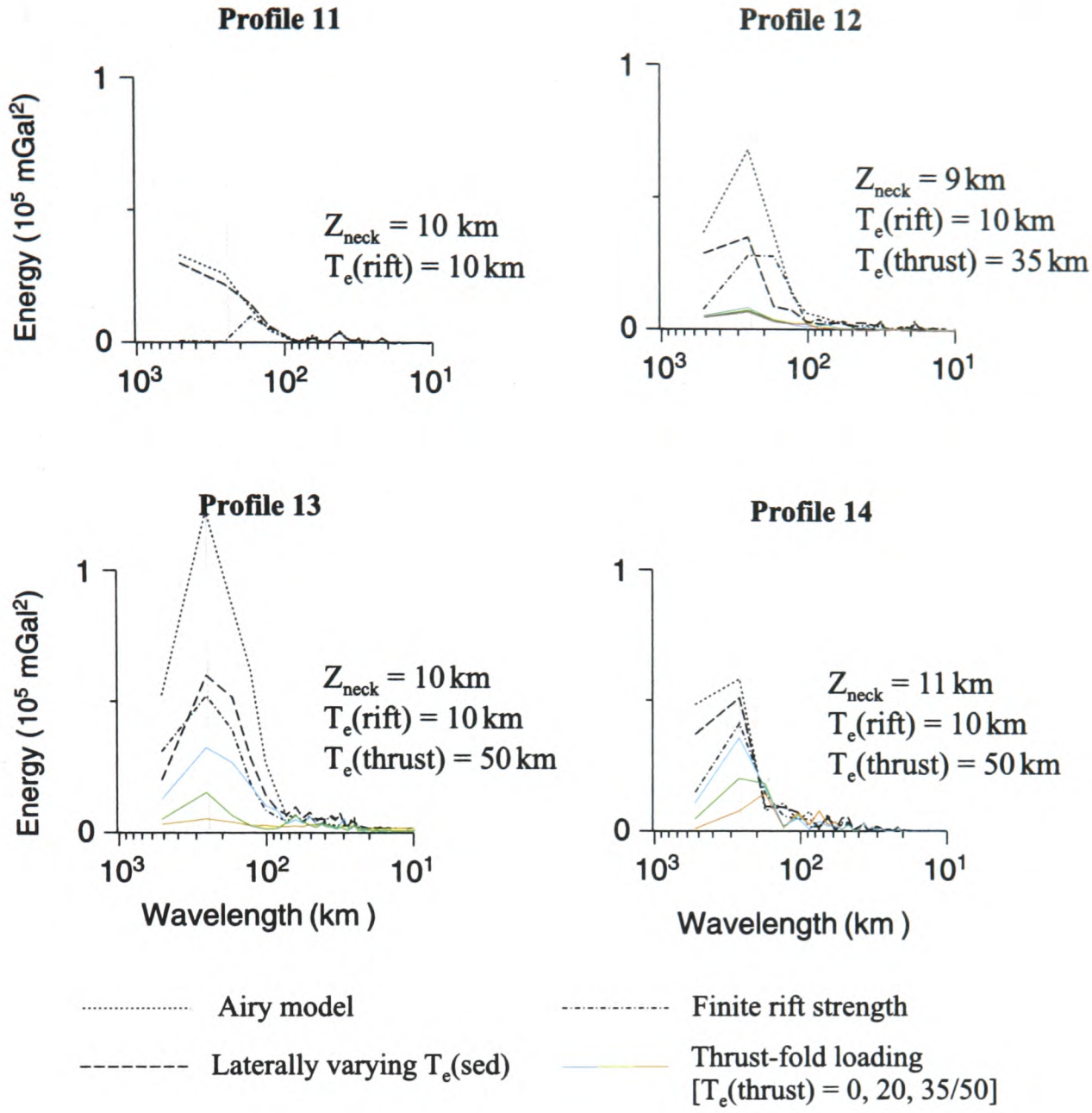

Figure 5.21: Power spectra of the isostatic anomalies calculated at different stages of the gravity modelling in Profiles 11-14 (see Figure 5.19a for location). For each profile, the T_e(rift), Z_{neck} and T_e(thrust) of the best-fit model are indicated. Note the importance of the thrust loading and the model sensitivity to T_e(thrust) in profiles 13 and 14.

bal Fault, the TAP-thrust and possibly also the Horseshoe Fault, all of which appear to be linked by major WNW-ESE transfer zones (Figure 5.19a). Baptista *et al.* [1998] showed that an L-shaped rupture, not too different from the model proposed here, could fit well the reported tsunami travel times. The new data presented here provides better constraints for the distribution of the faulting implied by such a model.

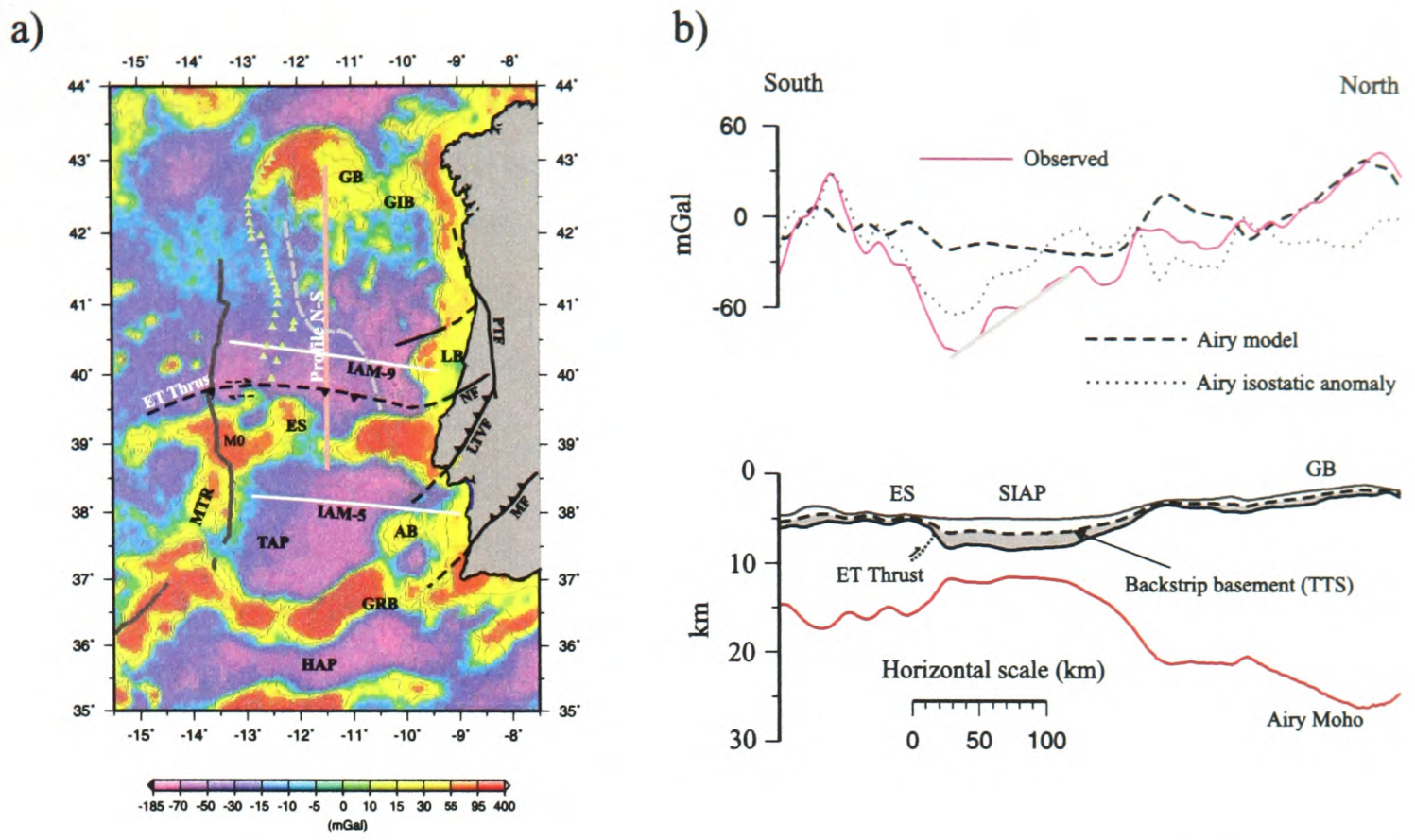

Figure 5.22: FAA and tectonic setting of the Southern Iberia Abyssal Plain. a) FAA map off West Iberia with bathymetric contours plotted at 500 m spacing. The thick pink line shows the location of a N-S profile used to model the flexure and gravity anomalies associated with the northwards thrusting of the Estremadura Spur (ES) and Madeira-Tore Rise (MTR) reliefs over the Southern Iberia Abyssal Plain. The E-W probable thrust front along the northern flank of the reliefs (the ET-Thrust) is here re-interpreted from Ribeiro *et al.* [1996] in the offshore continuation of the Nazaré Fault (NF). Other major Variscan lineaments are also shown (solid black lines), as well as the limit of stretched continental crust (thick dashed grey line), the peridotite ridge (green triangles) and magnetic anomaly M0 (black dots). Other acronyms are as in Figure 5.1. b) Top - Observed (pink), calculated (solid black; assuming an Airy rift and sediment loading) and Airy isostatic anomalies (dashed black). The thick grey line highlights the southern dip of the FAA in the Southern Iberia Abyssal Plain. Bottom - Crustal structure, sediments and topography.

decrease in the FAA values and an increase in the basement depths towards the south (Figure 5.22b), where prominent reliefs (up to 2 km high) delimit the Southern Iberia Abyssal Plain. These two features are typically associated with the flexure of the lithosphere in the regions that flank thrust and fold loads in orogenic belts (e.g. Karner & Watts [1983]; Stewart & Watts [1997]). Therefore, it is likely that at least part of the negative FAA values in the Southern Iberia Abyssal Plain might result from the flexure associated with northwards thrusting of the Estremadura Spur and Madeira-Tore Rise reliefs.

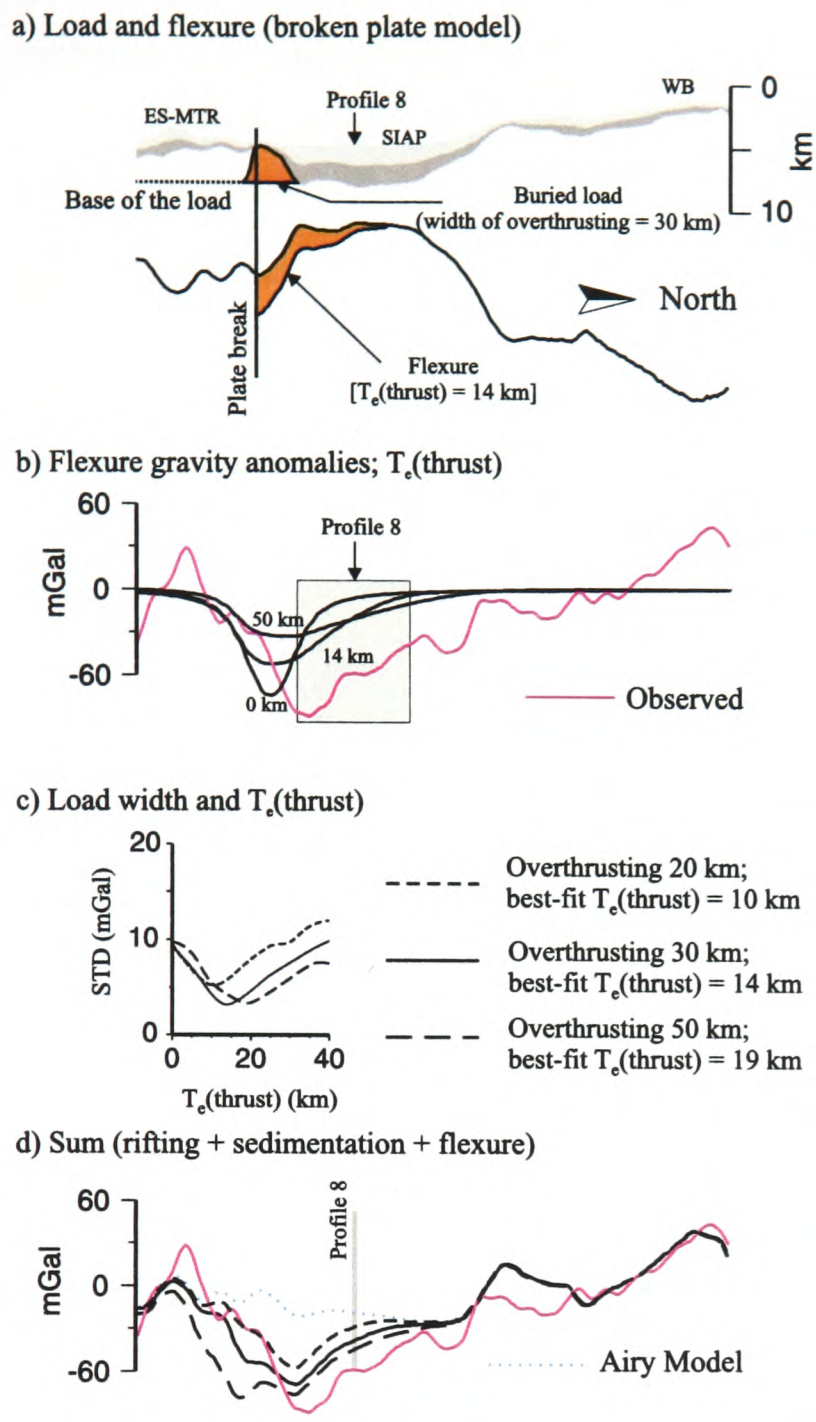

Figure 5.23: Thrust loading, flexure and gravity anomalies in the Southern Iberia Abyssal Plain: results from a POGM-approach along a N-S transect (pink line in Figure 5.22). a) Northwards thrusting of the Estremadura Spur and Madeira-Tore Rise reliefs and associated flexure (orange polygons). The dotted line at ~ 7.7 km delimits the base of the load (see text). b) Calculated gravity anomalies for three different values of T_e(thrust). c) Standard deviation (STD) between observed and modelled (flexure) gravity anomalies for three thrust loading width scenarios (20, 30 and 50 km). The STD's were calculated over the shaded grey area shown in (b). d) Sum anomalies, including the effects of rifting, sedimentation and flexure due to thrust loading, for the best-fit T_e(thrust) obtained in (c).

that although the southward dip of the observed FAA in the Southern Iberia Abyssal Plain may be explained by the thrusting of the Estremadura Spur and Madeira-Tore Rise reliefs and associate flexure, the sum anomalies are still considerably higher than the observed, independently of T_e(thrust). At the latitude of Profile 8, for example, the observed FAA is approximately -60 mGal (Figure 5.23d). After removing the effects of rifting and sediment loading (~ -20 mGal; see Figure 5.10), as well as those associated with thrust loading, assuming a 30 km wide load and a T_e(thrust) of 14 km (~ -20 mGal; Figure 5.23b), a difference of ~ -20 mGal between observed and calculated gravity anomalies remains unexplained (Figure 5.23d).

Since the contributions from the rifting and sediment loading processes to the observed FAA in the Southern Iberia Abyssal Plain are similar in the all the modelled margin orthogonal transects (see Profiles 8 and 9 in Figure 5.10), and the flexure associated with the northwards thrusting of the Estremadura Spur and Madeira Tore Seamount

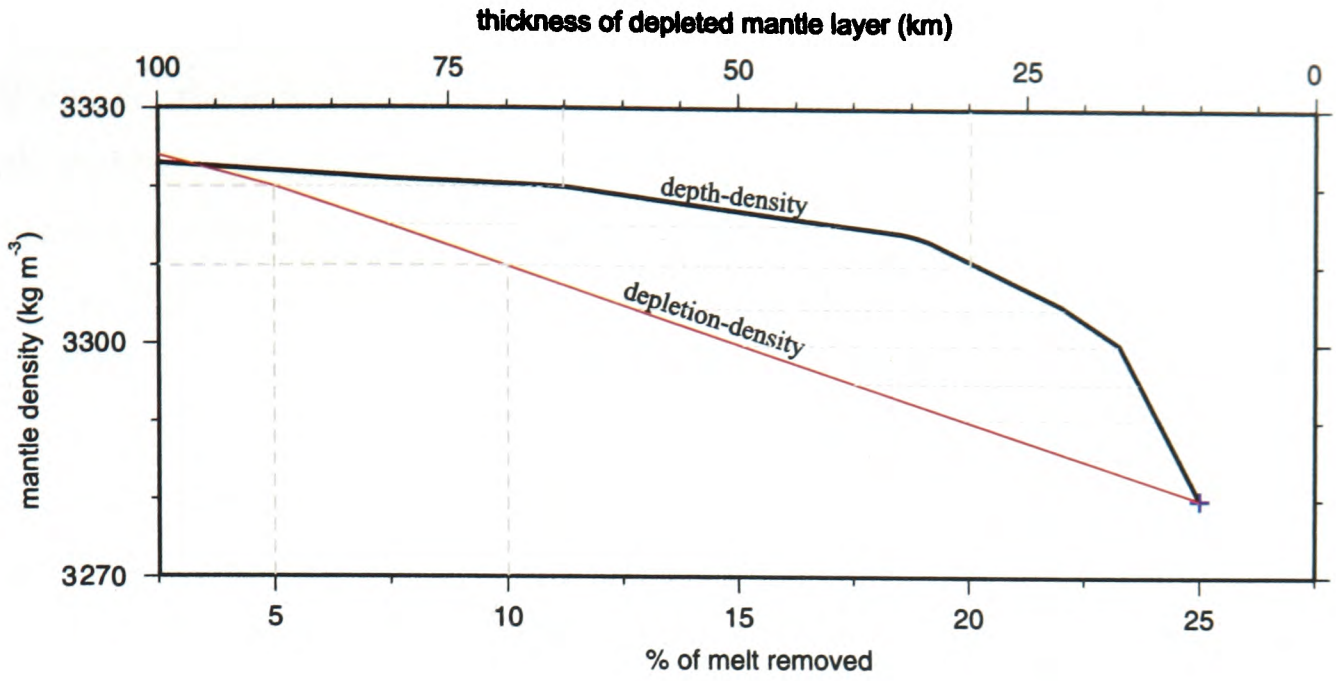

Figure 5.24: Relationships between the amounts of partial melting, mantle density and the thickness of depleted upper mantle which recovers the FAA low over the Southern Iberia Abyssal Plain. The red line shows the relationship between the percentage of partial melting (bottom axis) and the predicted reduction in the density of garnet peridotite (left axis), according to Schutt & Lesher [2006]. The black line in the graphic shows the thickness of depleted upper mantle (top axis), needed to explain a -20 mGal residual between observed and calculated gravity anomalies in the Southern Iberia Abyssal Plain (see text), for the corresponding mantle density anomalies. The thin horizontal dashed lines relate the percentage of partial melting (red line) to the thickness of depleted upper mantle (black line). The thick dashed grey lines highlight the density and thickness of depleted upper mantle predicted for 5 and 10% of partial melting, as inferred for the Southern Iberia Abyssal Plain (Cornen *et al.* [1996]).

model, is characterized by V_p's varying narrowly between 7.3 and 7.9 km s^{-1}. For this range of velocities there is a good agreement between the densities of the serpentinized peridotites calculated by Horen *et al.* [1996] and Miller & Christensen [1997], which for an average V_p of 7.6 km s^{-1} suggest a density of 3240 kg m^{-3}.

Figure 5.25a shows that, for the density structure described above the sum anomaly along the OCTZ, which includes the effects of rifting (T_e(rift) = 10 km, Z_{neck} = 12 km), sediment loading (best-fit T_e(sed); see Figure 5.10) and serpentinization, follows approximately the -40 mGal line (thick grey line). This corresponds to the residual FAA after removing the flexure associated with the northwards thrusting of Estremadura Spur and Madeira-Tore Rise (i.e. $\sim$ -20 mGal for a 30 km wide thrust load and a T_e(thrust) of 14 km; Figure 5.23b). This model, however, implies that the lower density transitional layer extends $\sim$ 75 km to west of the peridotite ridges, where the velocity model of Dean *et al.* [2000] suggests thin (between the peridotite ridges and M3) and normal thickness

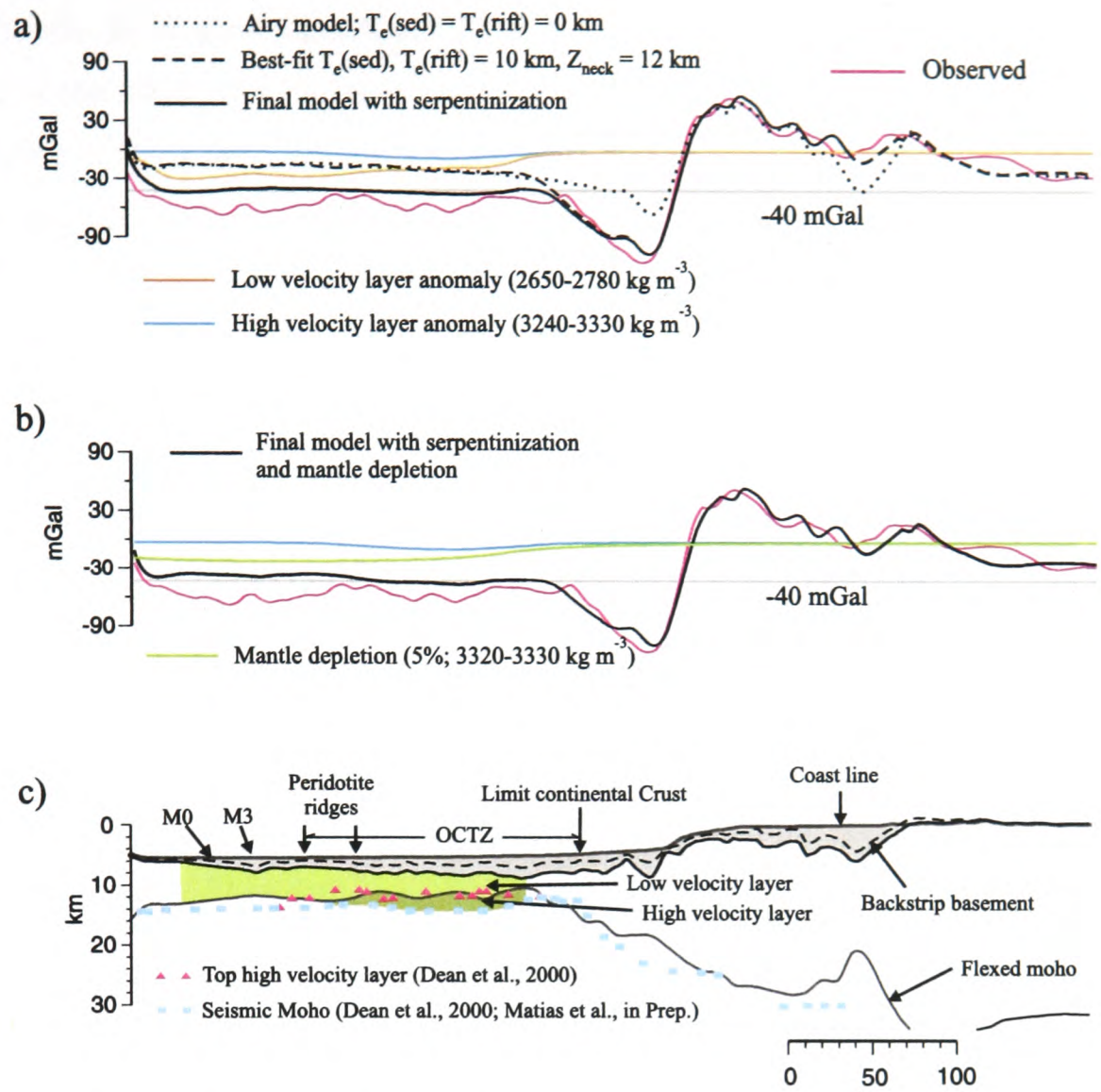

Figure 5.25: Gravity signature from upper mantle serpentinization and mantle depletion in the Southern Iberia Abyssal Plain: modelling results along Profile 8, seismic Line IAM-9 (see Figure 5.1 for location). a) Comparison between observed (pink) and calculated (black lines) gravity anomalies for 3 distinct models: Airy model, dotted line; laterally varying T_e(sed) and finite strength during rifting, with a T_e(rift) = 10 km and Z_{neck} = 12 km, dashed line; as the previous model but accounting for the effects of upper mantle serpentinization, solid line. The contributions from the low density serpentinized layers (green polygons represented in *c*), are shown in orange and blue, for the indicated density anomalies. The thin grey line at -40 mGal represents the approximate residual anomaly along the OCTZ after removing the effects of flexure associated with thrust loading (see text). b) Shows a model which accounts for a laterally varying T_e(sed), finite strength during rifting (T_e(rift) and Z_{neck} as in *a*), serpentinization of the high velocity layer (dark green body in *c*), and 5% mantle depletion in the top 55 km (see text); the individual contributions from mantle serpentinization and depletion are shown in blue and green, respectively. c) Crustal structure and serpentinized mantle layers (green). The pink triangles and blue squares correspond to the top of the high velocity layer and the Moho constrained from wide-angle and refraction seismic data, respectively.

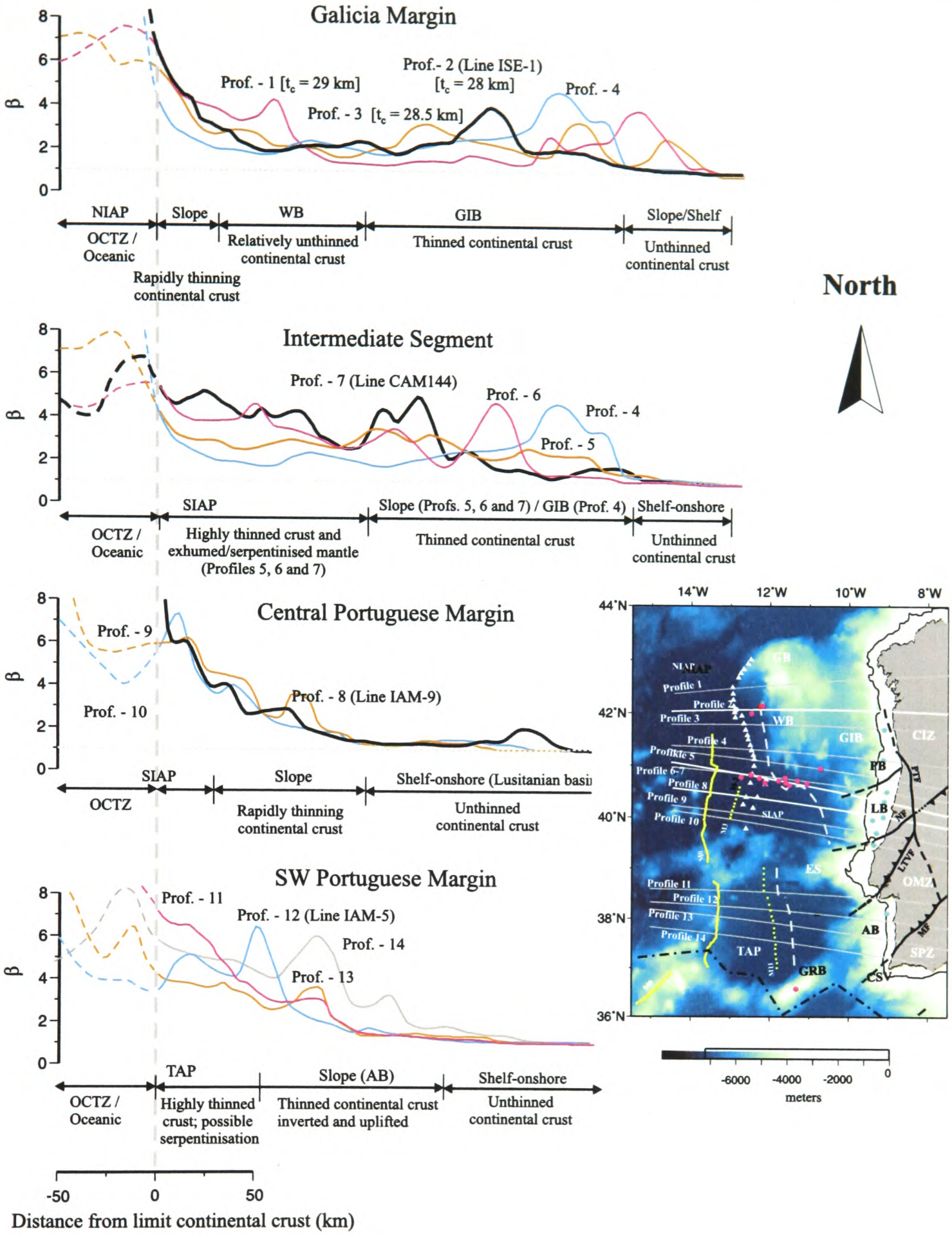

In the Central Portuguese Margin, a distinct pattern of β's is identified, characterized by well developed rift basins onshore ($1.5 < \beta < 2$), little extension in the region of the continental shelf ($\beta < 1.3$) and a steep continental slope, where the crust tapers from a thickness of more than 25 km to less 5 km over a width of < 100 km (e.g. Minshull *et al.* [2001]; Matias [Personal com.]).

In Profile 8, where the crustal structure is better constrained, this transition is clearly stepwise, associated with the location of rift-related normal faults, mainly trending NNE-

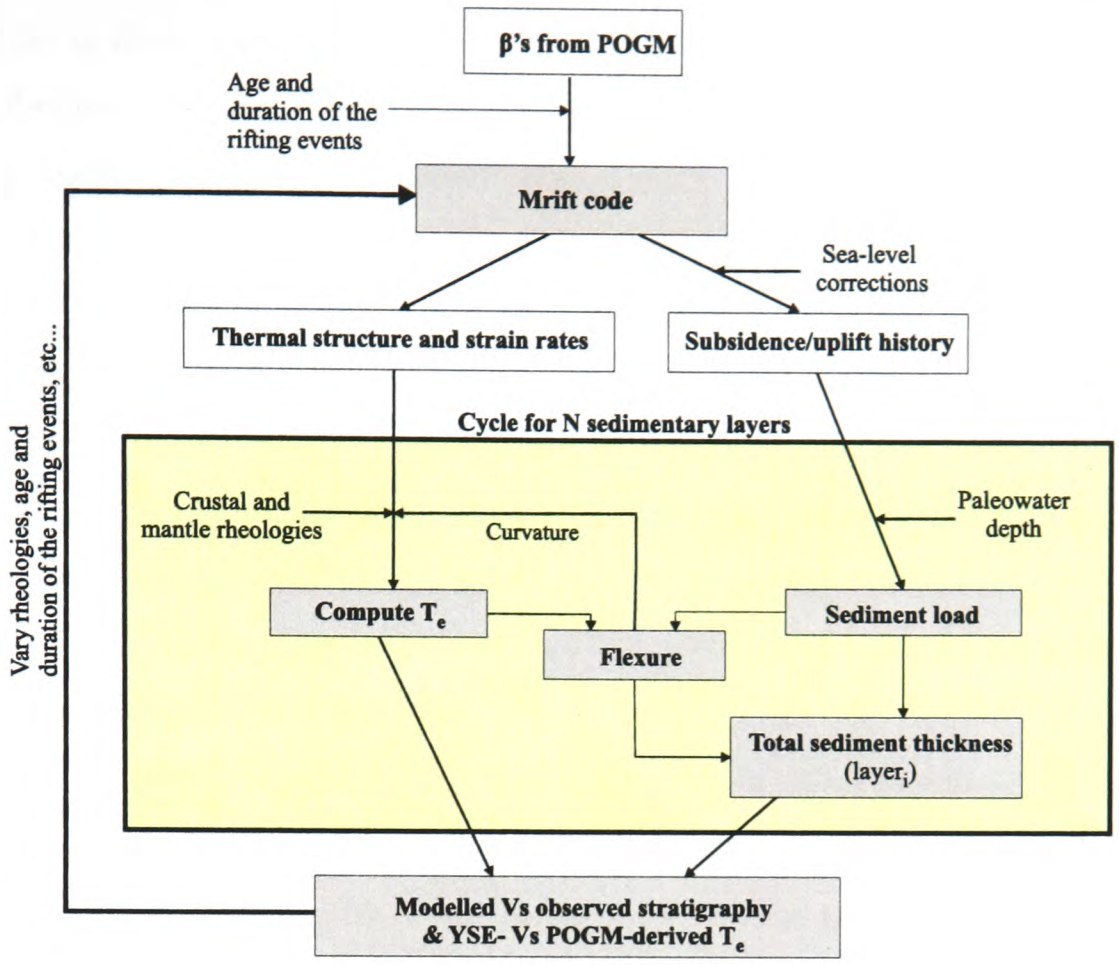

Figure 6.2: Flow chart of the multi-stage continental rifting thermo-mechanical rheological modelling procedure.

culate the T_e for a given temperature and rheological profile (Burov & Diament [1992]; Lowry & Smith [1995]). A detailed description of the software, routines used, and the mathematical treatment of the thermal and mechanical structure of the lithosphere is given in Chapter 2 and in appendixes A (thermal structure of extended continental lithosphere) and B (Mrift code user guide).

6.3.1 Modelling Strategy and Parameterisation

The modelling procedure is schematically represented in Figure 6.2. The main input are the β profiles constrained from POGM techniques. From these, and the age and duration of the main rifting events, the thermal structure and subsidence/uplift history of the margin are computed analytically, assuming lateral and vertical heat conduction and depth-uniform (pure shear) stretching (e.g. Watts *et al.* [1982]; Cochran [1983]). The calculations are performed at discrete time intervals, which need to be short enough to approximate a continuous model of rifting yet long enough to account for the effects of lateral heat diffusion between adjacent modelling blocks. As highlighted in Chapter 2, time steps of 0.5 m.y and 1 m.y., during syn- and post-rift periods, respectively, are acceptable for block widths of 5 km (Cochran [1983]), as assumed in the models presented in this chapter.

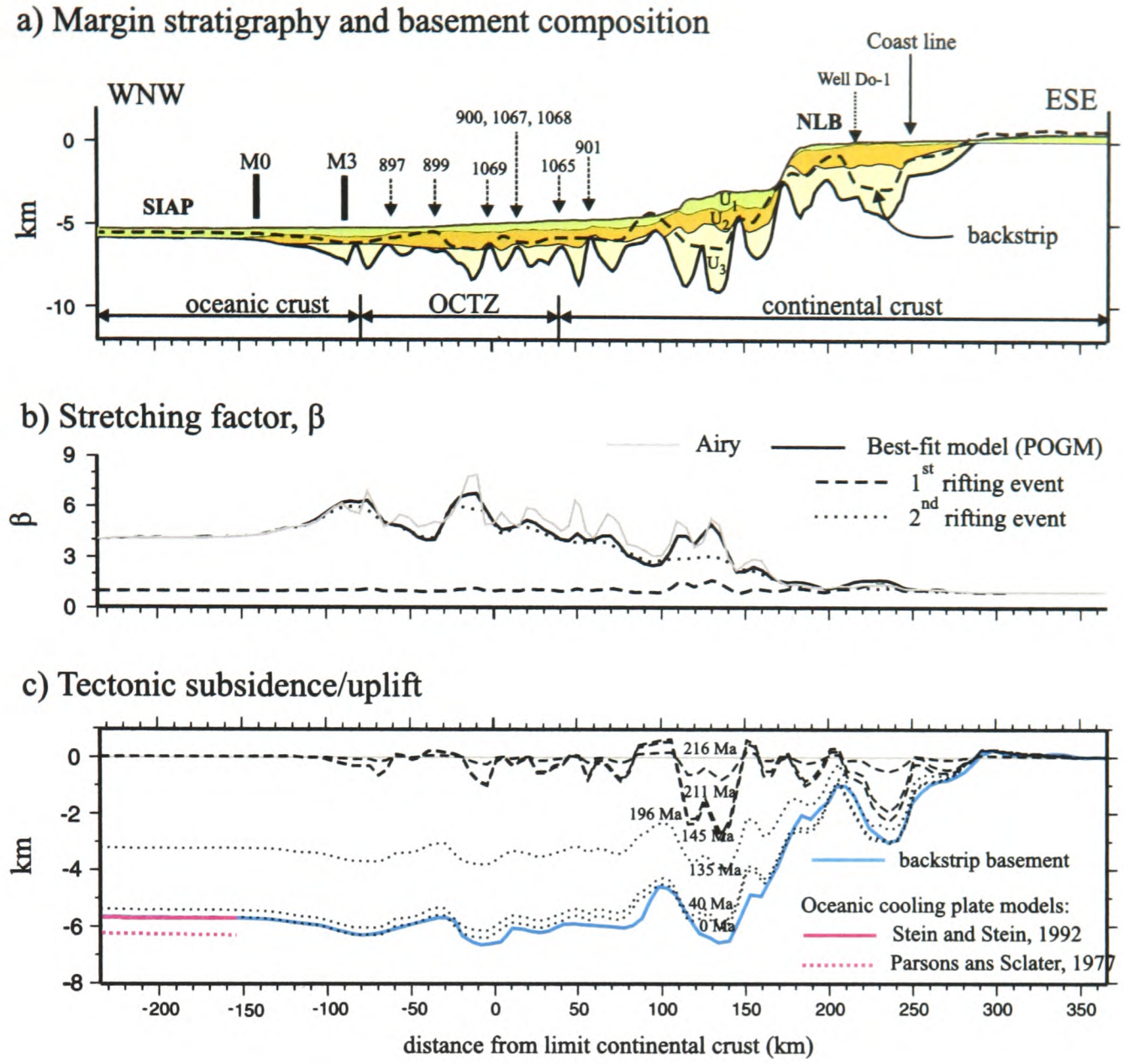

Figure 6.3: Margin stratigraphy, stretching factors and predicted subsidence along Profile 7 (see Figure 6.1 for location). a) Simplified stratigraphy of the margin and nature of the basement along Profile 7. Sedimentary units U_1, U_2 and U_3 where compiled for the whole of the WIM from the available seismic and well data (see Chapter 3 for details). Dashed line shows the backstrip basement for the best-fit gravity model. Also indicated are the locations of the commercial well Do-1, several ODP drilling sites from legs 149 and 173 and seafloor spreading magnetic anomalies M0 and M3 (see inset map of Figure 6.1). b) Stretching factors (β's). The total amount of stretching implied by the Airy and best-fit gravity models are represented by the solid grey and black lines, respectively. The dashed and dotted lines show the β's inferred for the first and second rifting stages in the best-fit gravity model, respectively (see text). All the β profiles have been filtered and resampled at 5 km spacing for input in the thermo-mechanical rheological modelling software. c) Subsidence predicted by the thermal model for a two-stage rift model. The ages and duration of the events are inferred from the available stratigraphic and thermochronological data (see text for details).

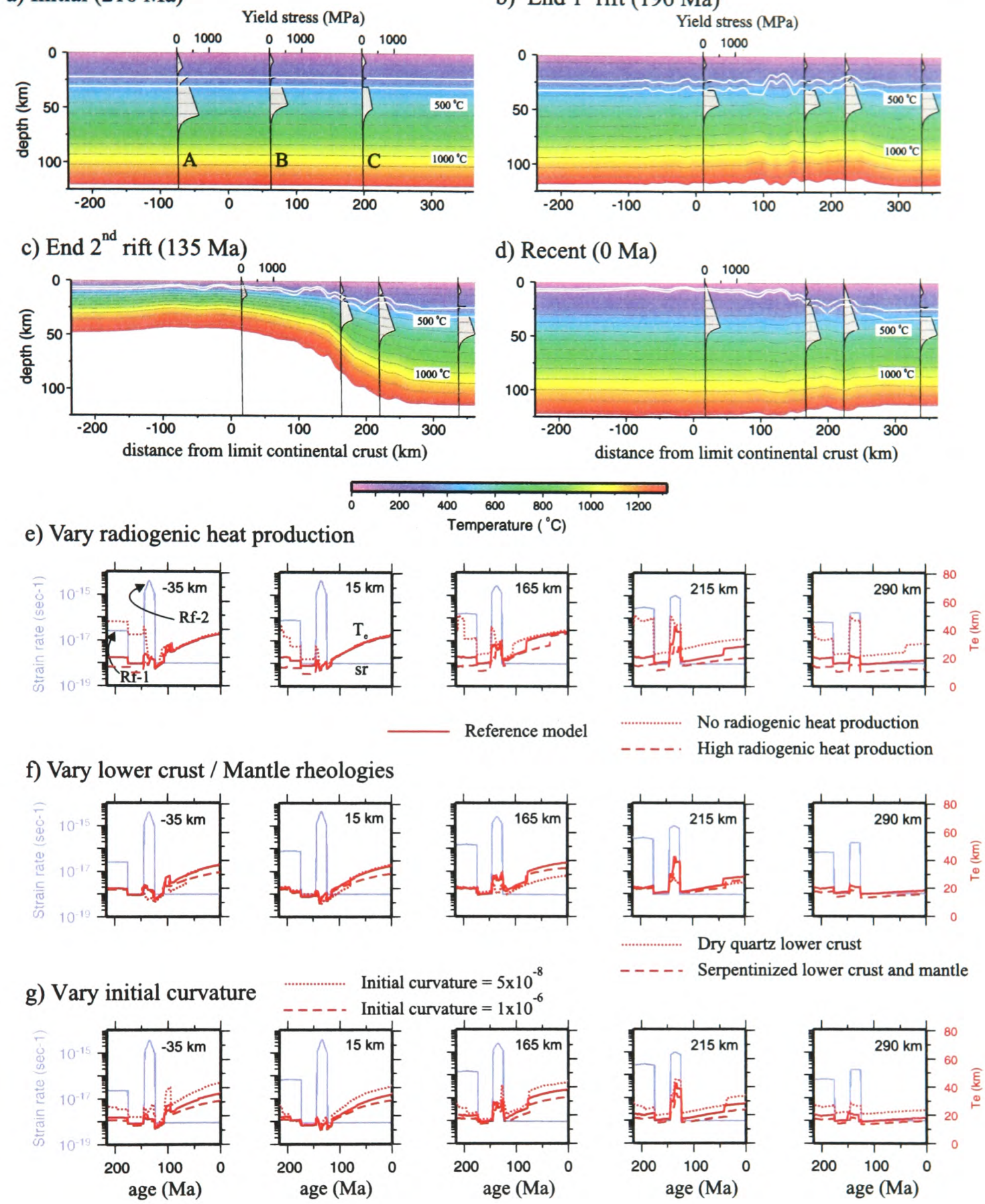

For the geothermal gradients calculated here, and assuming a dry quartz rheology for the upper-middle crust, an aggregate rheology for the lower crust and a dry olivine rheology for the lithospheric mantle (see Table 6.1 for parameterisation), the computed yield strength envelope (YSE-B in Figure 6.4a) suggests a weak lower crust, which is fully decoupled from the strong upper crust and mantle. For this reference model, the calculated vertically integrated strength of the unstretched lithosphere, T_e, is $\sim$ 20 km (solid red line in Figure 6.4e-g), which middles the range of T_e's commonly found in passive continental margin settings (Stewart [1998] and references therein). This value is

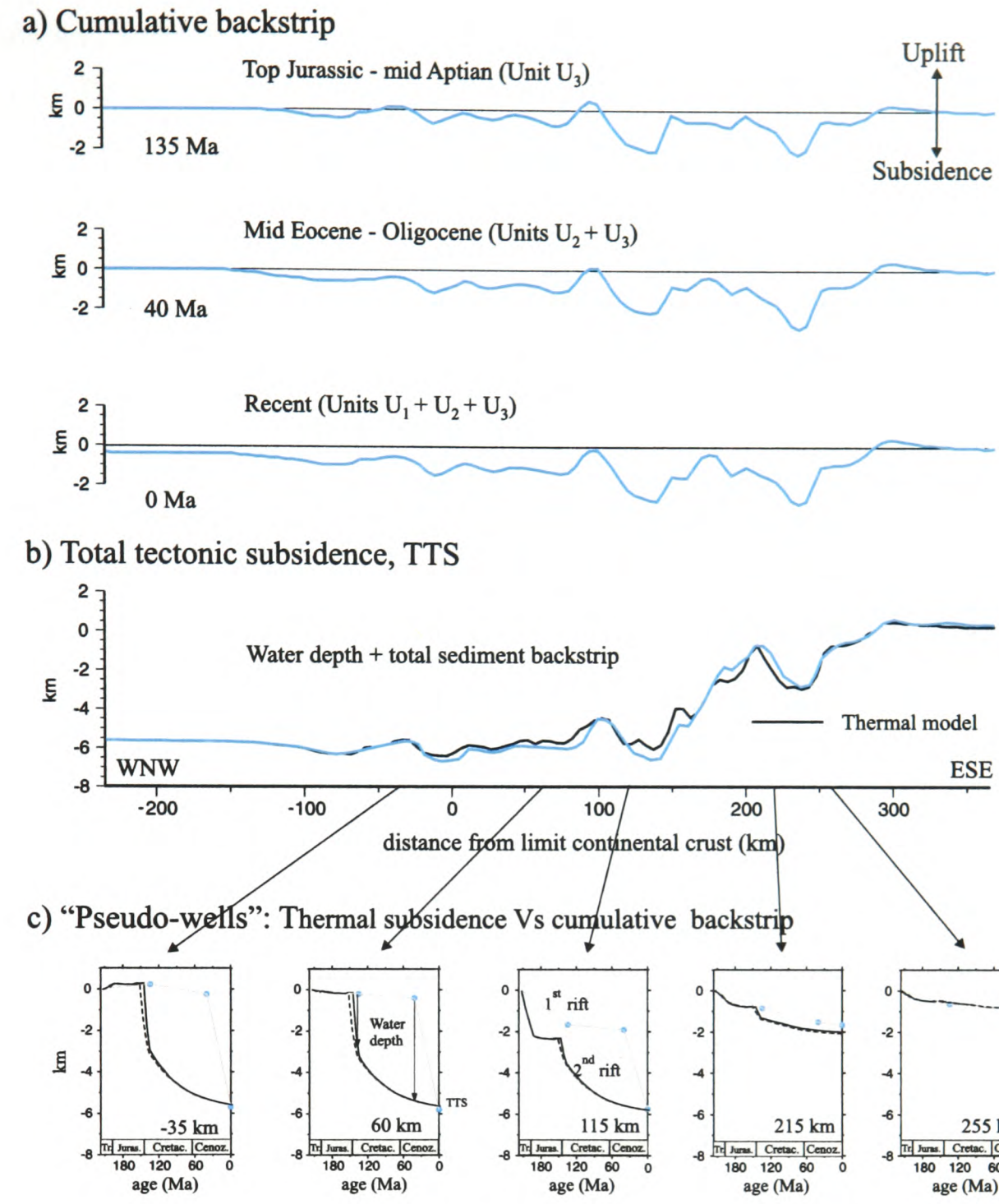

Figure 6.5: Cumulative backstrip, total tectonic subsidence and paleowater depths. a) Cumulative backstrip at the top Jurassic-mid Aptian (top; Unit U_3), mid Eocene-Oligocene (middle; units U_2+U_3) and Recent (bottom; U_1+U_2+U_3). The age of backstripping is indicated for each layer. b) Total tectonic subsidence (TTS) obtained by adding the total backstripping shown in (a-bottom) to the present day water depth. The solid black line shows the subsidence predicted by the thermal model. c) Illustration of the method used to estimate the paleowater depths at 5 distinct locations along the profile. According to Stewart *et al.* [2000], these can be inferred from the difference between the subsidence calculated from the sediment record (i.e. the cumulative backstrip; blue dots) and the subsidence predicted by the thermal model (black line). The thermal model is here corrected for past oscillations in the global sea-level (Watts & Steckler [1979]). Dashed lines simulate a second rifting event starting at 150 Ma and lasting for 15 m.y.

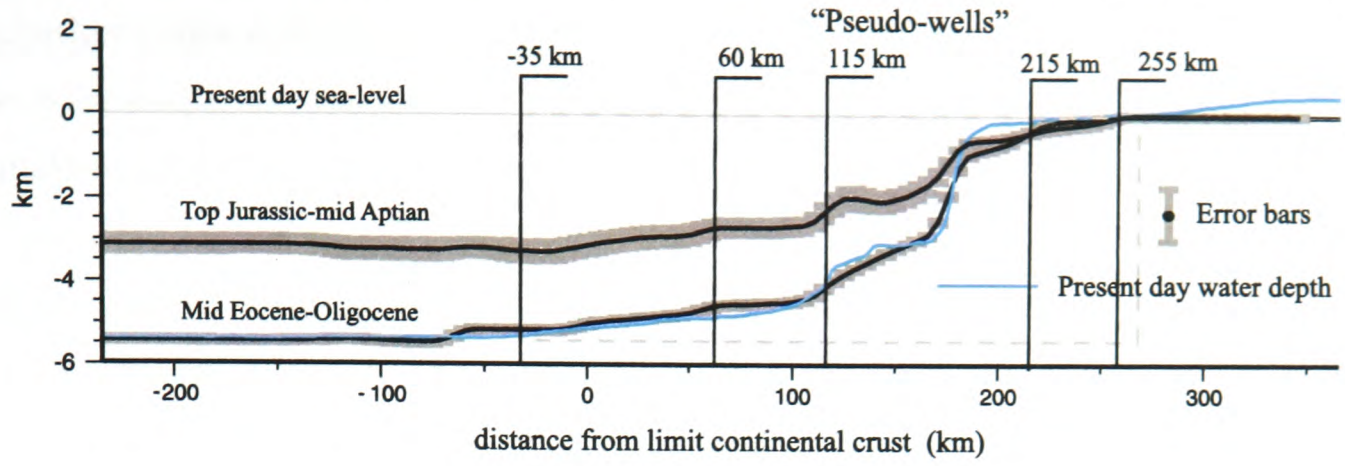

Figure 6.6: Paleowater depths estimated along Profile 7, at 5 km intervals, for the Early Cretaceous and the Paleogene periods. The paleowater depths are obtained from the difference between the subsidence predicted by the thermal model and the sediment backstrip; see Figure 6.5c for results at -35, 60, 115, 215 and 255 km along the profile. The error bars (dark grey) were calculated assuming uncertainties in the age and duration of the latest Jurassic-Early Cretaceous rifting event of ± 5 m.y. (see Figure 6.5).

6.3.5 Predicted Stratigraphy and Mechanical Structure

Figure 6.7 shows the predicted stratigraphy and mechanical structure along Profile 7 for the two-stage continental rifting margin evolution described in Section 6.3.2. The input β's are those of Figure 6.3b, the modelling parameters are given in Table 2.1, and dry quartz, aggregate and dry olivine rheologies are assumed for the upper-middle crust, lower crust and lithospheric mantle, respectively (see Table 6.1). In addition to the stratigraphic horizons that mark the start and ending of the rifting episodes (i.e. 216-196 Ma and 145-135 Ma) and the present day seafloor (0 Ma), two other surfaces are calculated by the model, at 40 and 211 Ma (Figure 6.7b). The first corresponds to the top of sediment unit U_2 and the latter is of relevance to determine the paleowater depths during the early stages of rifting, as it will be discussed ahead in this section.

For a given time interval, the model assumes that the maximum variation in the paleowater depths is determined by the amount of subsidence predicted by the thermal model. Consequently, in places where the variation in the estimated paleowater depths exceed that of the thermal subsidence a correction is applied (dashed lines in Figure 6.7a).

In the stratigraphic model presented in Figure 6.7b, zero paleowater depths (i.e. the pre-deformation surface) are assumed along the margin prior to the second rifting stage, i.e. at 211, 196 and 145 Ma. Over the shelf and onshore, the early Cretaceous and Paleogene corrected water depths (dashed lines in Figure 6.7a) correspond to the present day bathymetry, between 0 and 200 m. These are in better agreement with the

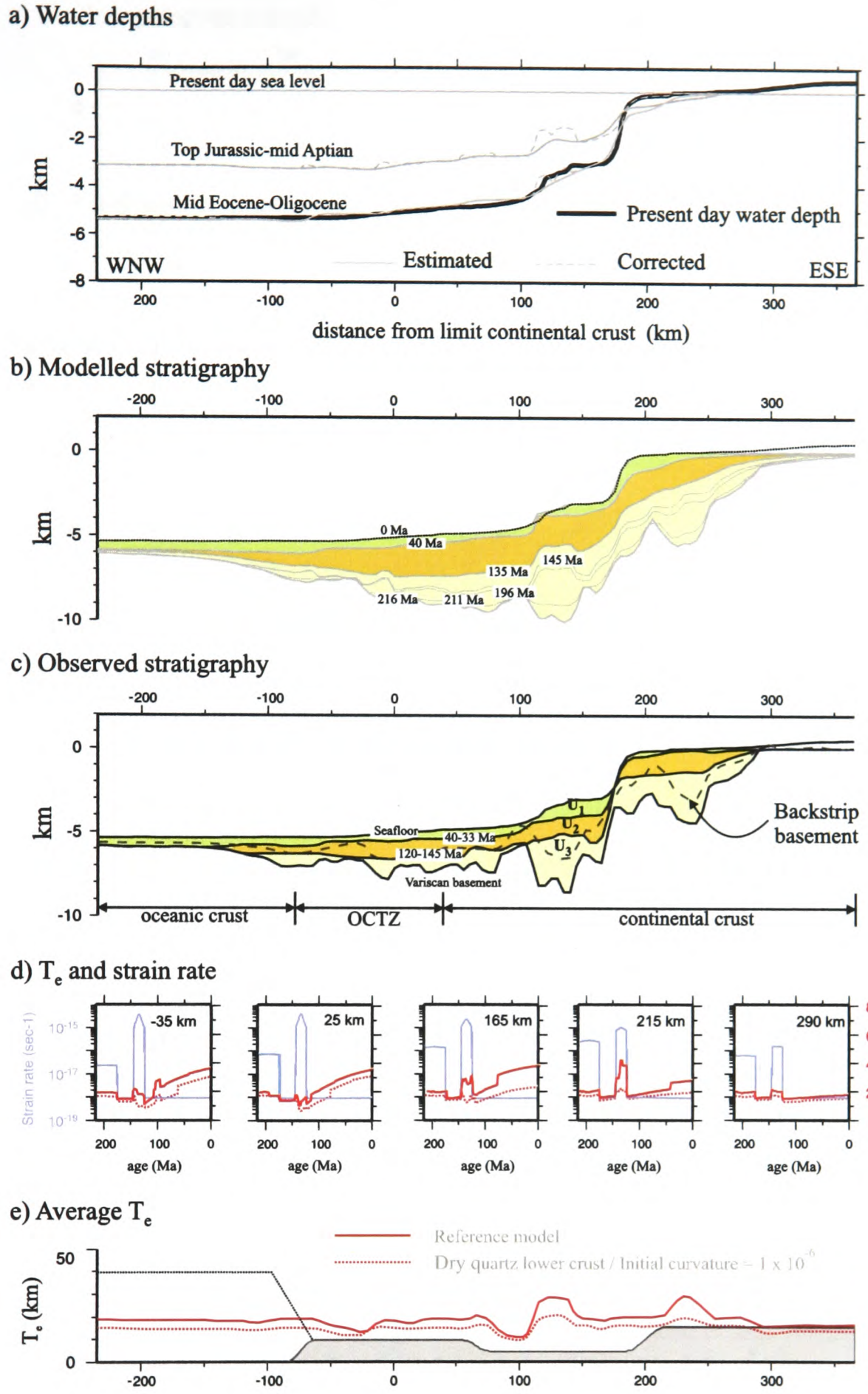

margin stratigraphy is most sensitive to variations in the different parameters.

The Airy rift model shown in Figure 6.9c may explain the high basement relief near the flanks of the main depocentres, where important normal fault activity has been described from the seismic data between the continental rise and onshore (e.g. Wilson *et al.* [1989]; Rasmussen *et al.* [1998]; Alves *et al.* [2006]), but grossly overestimates the thicknesses of sediment units U_2 and U_3. Furthermore, although a low basement rigidity may characterize the margin during intense crust and mantle stretching, associated with

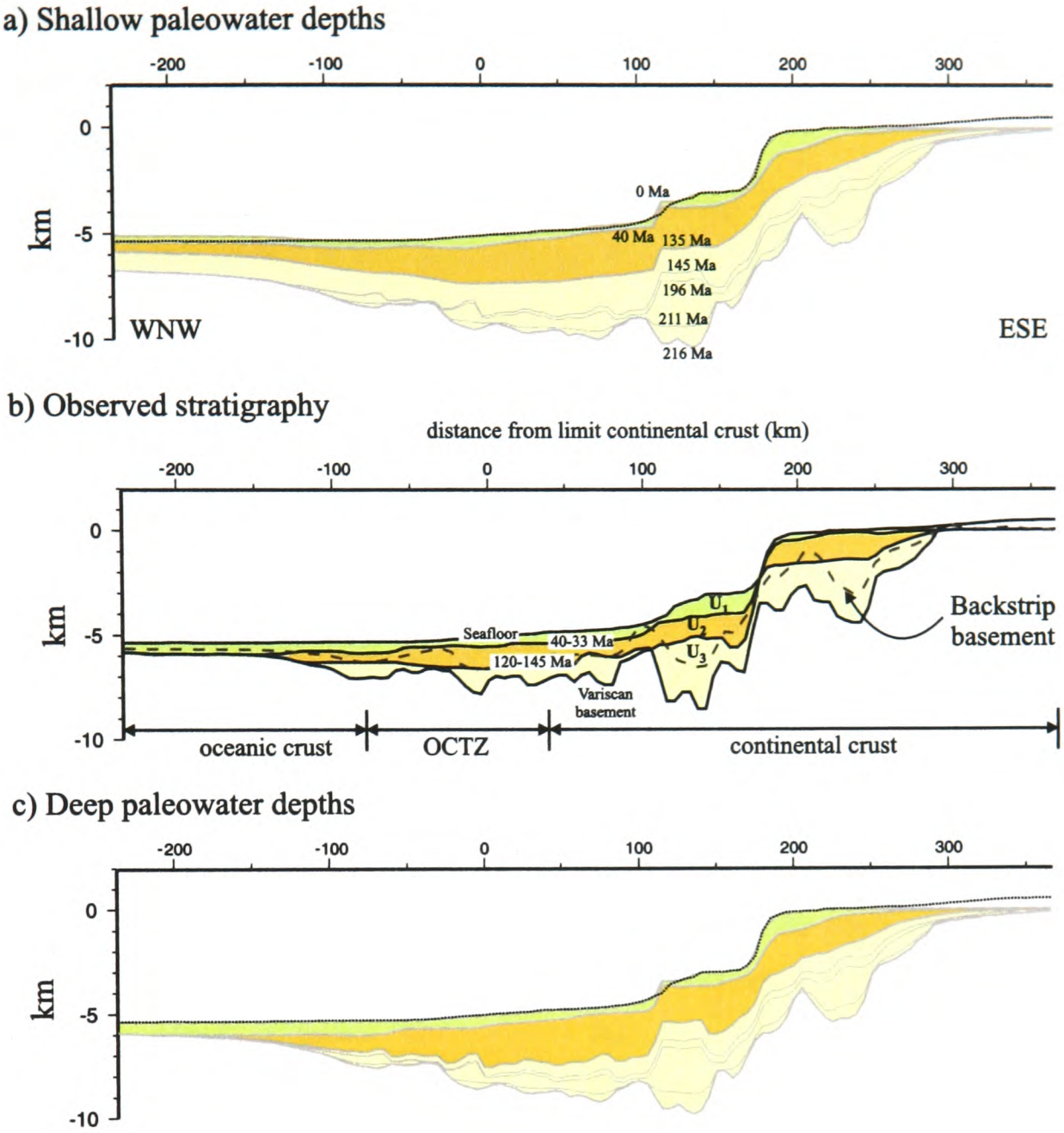

Figure 6.8: Effects of varying the paleowater depths on the predicted margin stratigraphy. The models represent inferred maximum variations in the estimated paleowater depths, which account for uncertainties in the age and duration of the rifting events (or age of the backstrip horizons) and/or the thickness of the backstripped sedimentary units (see text).

widespread normal faulting (e.g. Ebinger *et al.* [1989]; Spadini & Podladchikov [1996]), low friction coefficients along the fault planes (e.g. Lavier *et al.* [2000]), and anomalously high geothermal gradients (e.g. Watts *et al.* [1982]; Fowler & McKenzie [1989], the results from POGM presented in Chapter 5 suggest a T_e(rift) of 10 km along Profile 7.

As shown in Figure 6.4e, when the heat produced by the decay of radiogenic elements in the crust is not accounted for, the T_e's calculated by the thermo-mechanical rheological model over relatively unstretched crust are significantly greater. Consequently, the flexure associated with the sediment loading will be of smaller amplitude and broader wavelength, and the modelled sediment layers will become thinner over the main depocentres, as depicted in Figure 6.9d. This is particularly evident for sediment unit U_2,

even in relation to the model where the deeper range of estimated paleowater depths are used (Figure 6.9a). Despite this, large departures between the observed and modelled margin stratigraphy are still observed along most of the profile, both in terms of the thicknesses of the sediment units and the basement relief. Furthermore, the modelling results presented in Figure 6.4f and 6.4g suggest that changing the lower crust and mantle rheologies, and/or assuming a lower initial basement curvature, will not significantly affect the modelled margin stratigraphy.

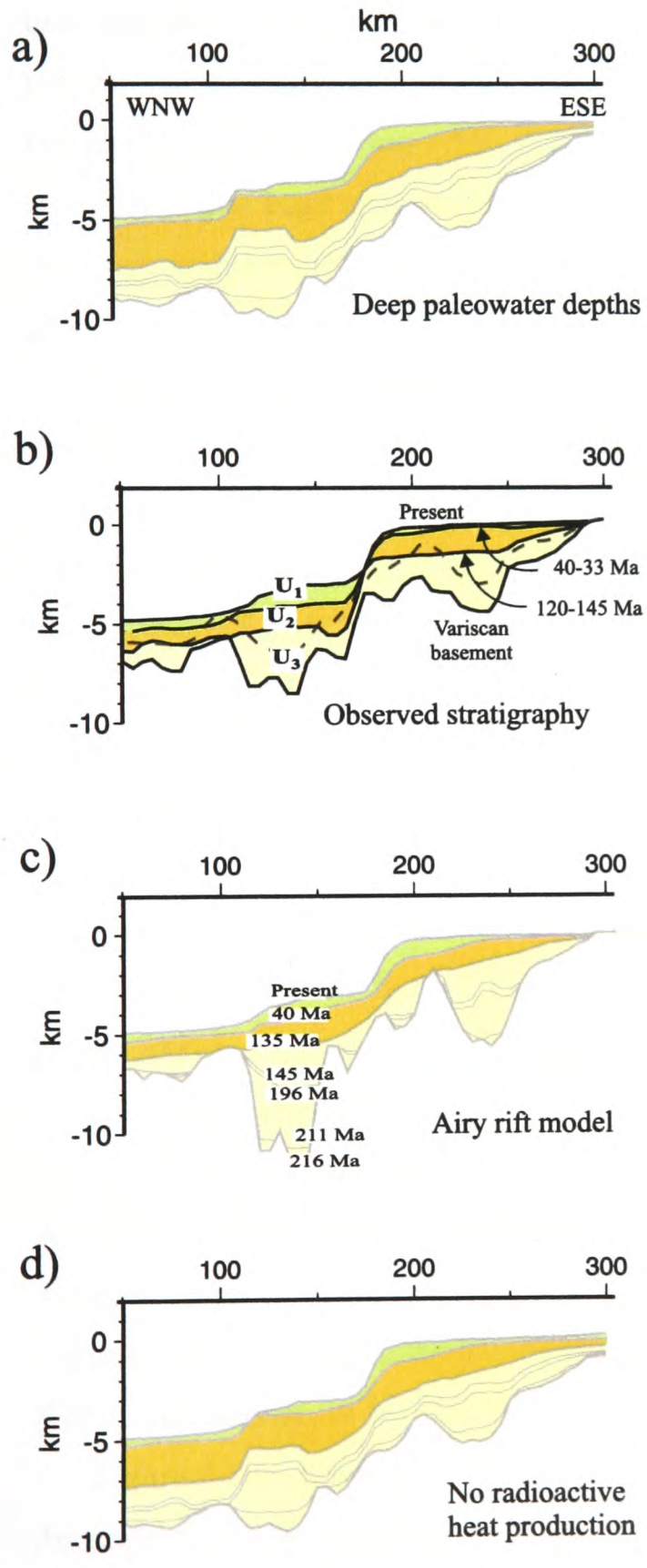

Figure 6.9: Tests on the computed margin stratigraphy for three different modelling scenarios: a) Deep top Jurassic-Paleogene water depths, as in Figure 6.8c; c) Zero lithospheric strength during rifting, i.e. $T_e(\text{rift}) = 0$ km (Airy model); d) No radiogenic heat production in the crust. The observed margin stratigraphy is shown in (b) for comparison. Results are plotted to the east of 50 km along Profile 7, i.e. over stretched continental crust (see Figure 6.7c).

The modelling results along Profile 7 discussed above are, in a way, paradoxal. On the one hand, the T_e's calculated analytically from the thermal structure of the margin and YSE considerations are considerably greater than those estimated from POGM,

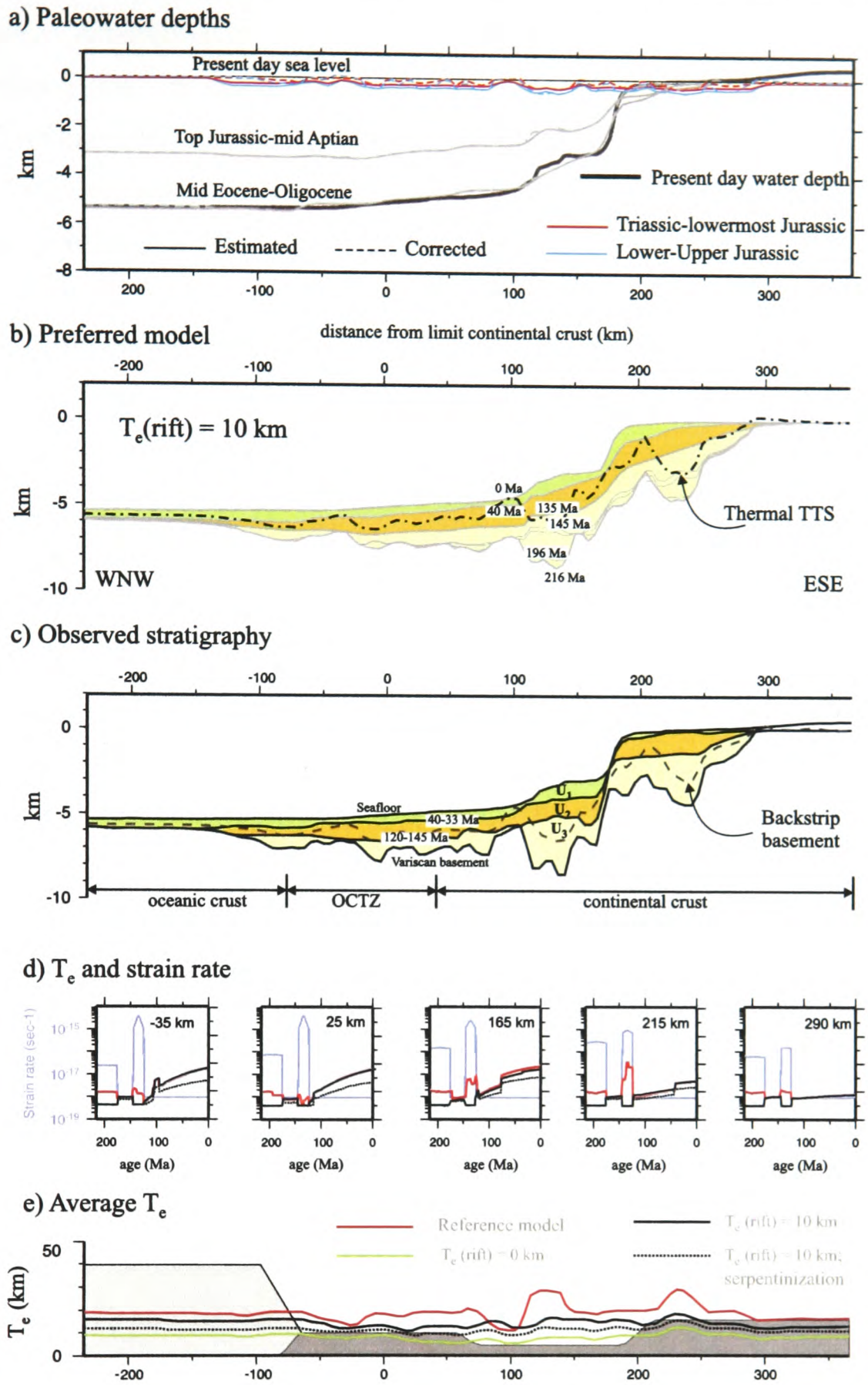

and 165 km along Profile 7, respectively). Over highly stretched continental crust and in the transitional domain (e.g. at -35 and 25 km of the profile) the effects of crustal and lithospheric thinning and associated high geothermal gradients become dominant.

A limitation of the models presented here, however, is that they treat the lithosphere as a continuous medium, where the bending stresses are laterally distributed. Consequently, the effects of widespread normal faulting, an essential mechanism which controls the development of rift basins, is not being accounted for. As shown by Ebinger *et al.* [1989], using combined flexural and gravity modelling techniques, and by Spadini & Podladchikov [1996], using dynamical models of rifting, the flexural strength of the

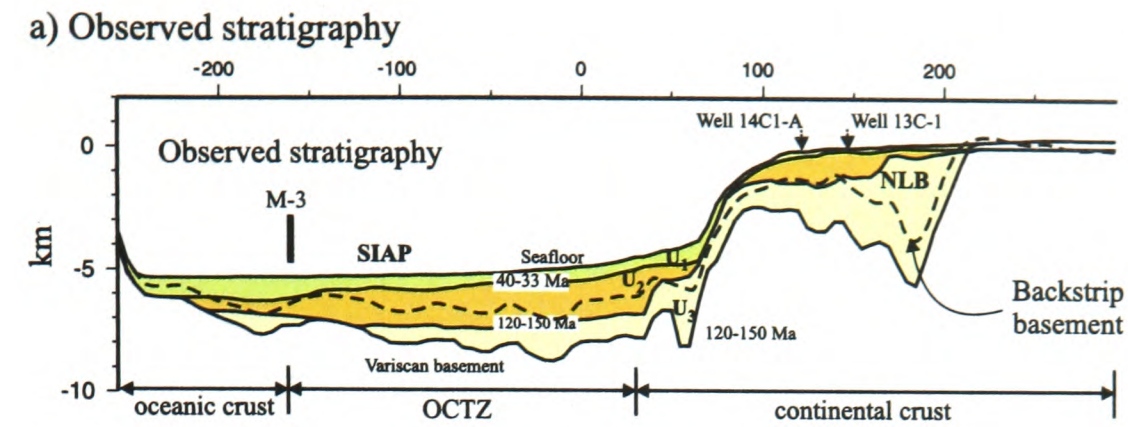
a) Observed stratigraphy
Observed stratigraphy
Well 14C1-A
Well 13C-1
NLB
M-3
SIAP
Seafloor
40-33 Ma
120-150 Ma
Variscan basement
Backstrip basement
oceanic crust
OCTZ
continental crust
km

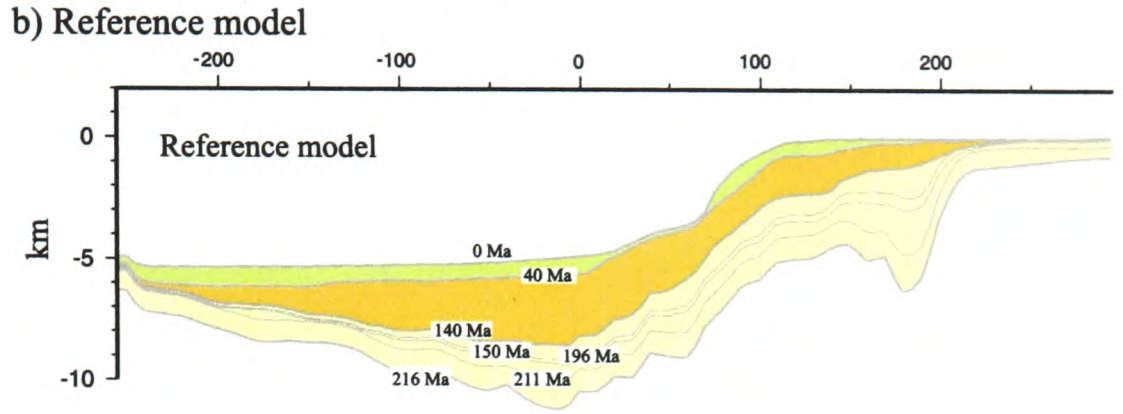
b) Reference model
Reference model
0 Ma
40 Ma
140 Ma
150 Ma
196 Ma
216 Ma
211 Ma
km

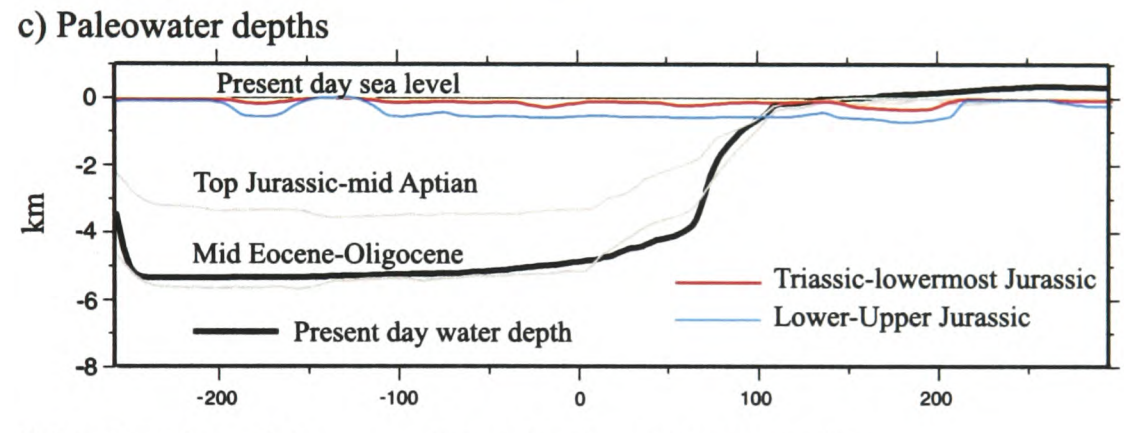
c) Paleowater depths
Present day sea level
Top Jurassic-mid Aptian
Mid Eocene-Oligocene
Present day water depth
Triassic-lowermost Jurassic
Lower-Upper Jurassic
km

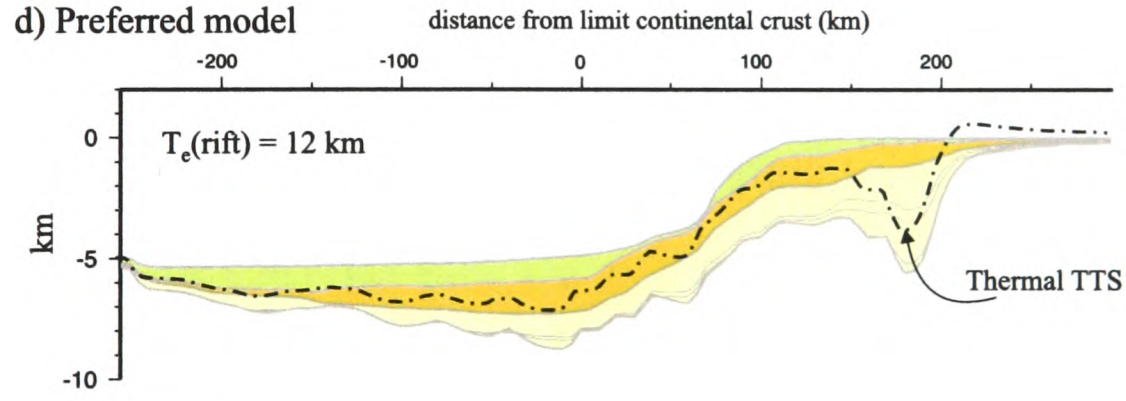
d) Preferred model
distance from limit continental crust (km)
Te(rift) = 12 km
Thermal TTS
km

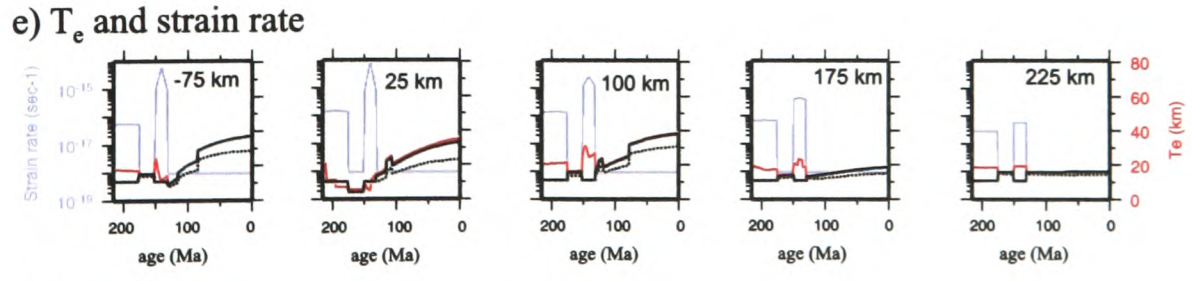
e) Te and strain rate
-75 km
25 km
100 km
175 km
225 km
Strain rate (sec-1)
age (Ma)
Te (km)

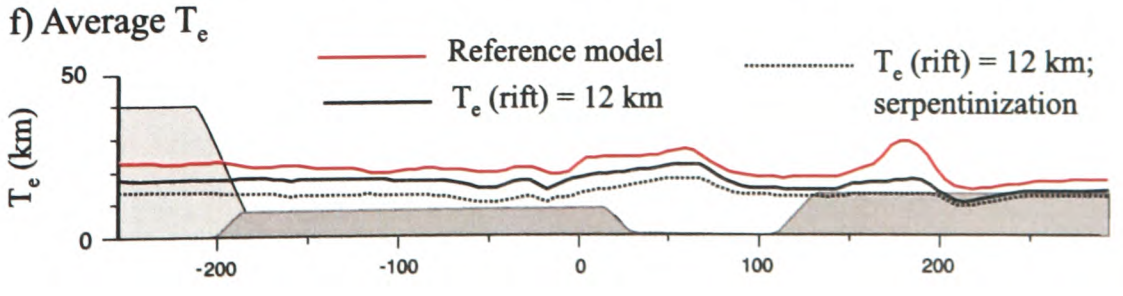
f) Average Te
Reference model
Te (rift) = 12 km
Te (rift) = 12 km; serpentinization
Te (km)

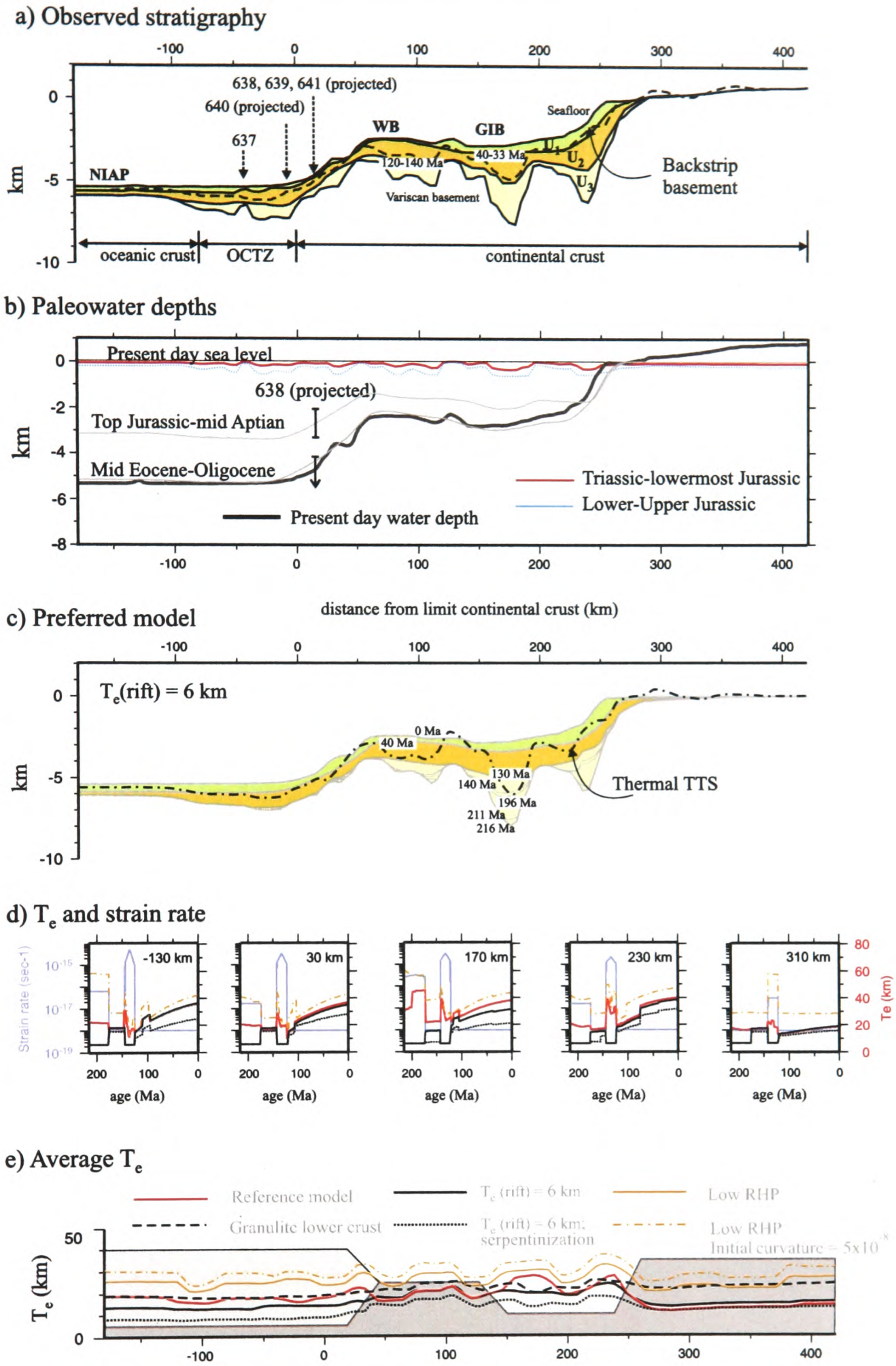

As shown in Figure 6.12f (dashed black line), even assuming such an extreme lower crust composition, the average T_e's computed with the thermal-mechanical rheological do not exceed 22 km over unthinned Variscan basement. Furthermore, the seismic data in the Central Iberian terrane does not support the existence of a mafic granulite lower crust at these latitudes (Téllez [1993]).

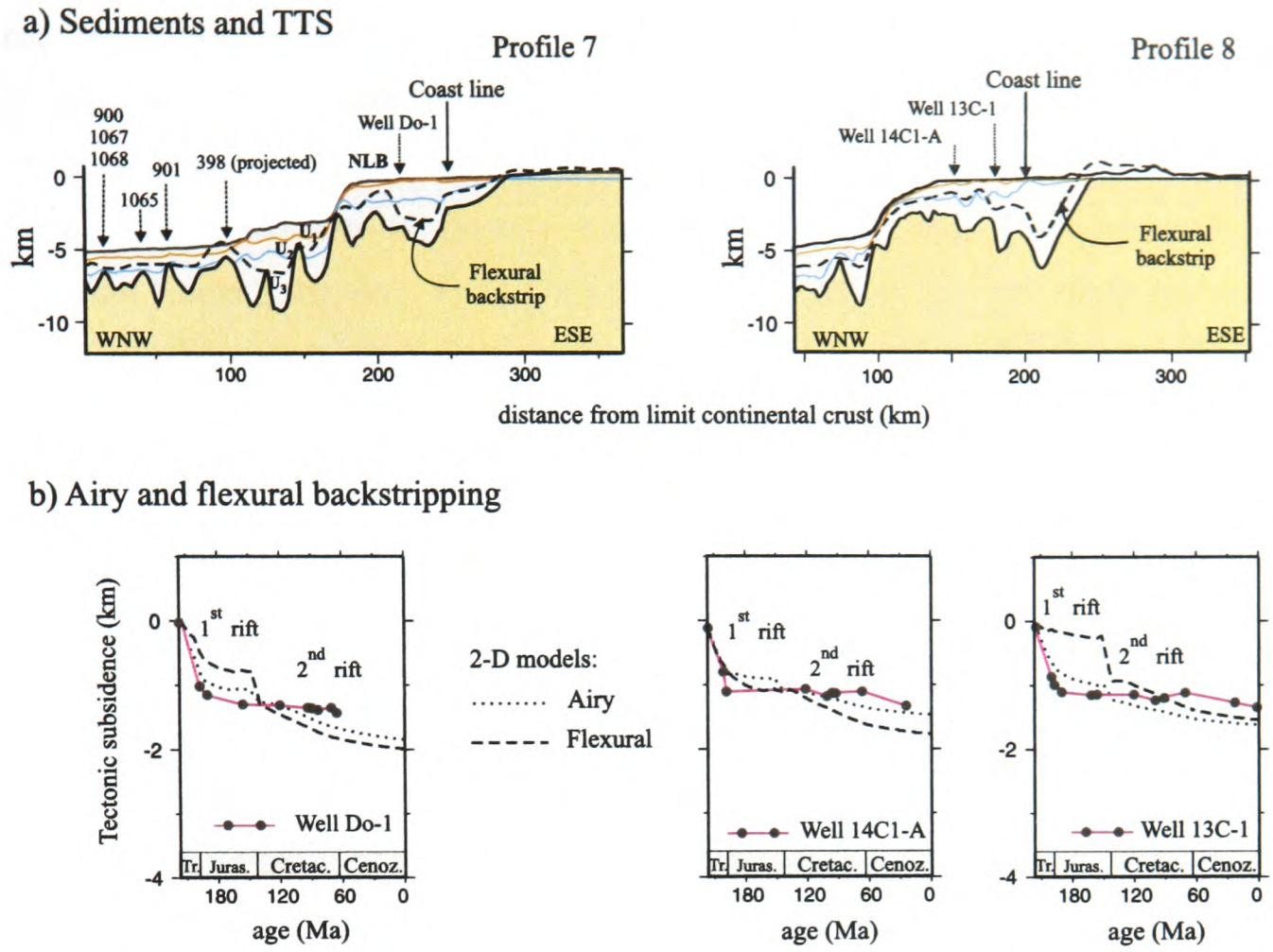

Figure 6.13: Comparison between the tectonic subsidence obtained from 1-D well backstripping and that predicted by the 2-D flexural models at the location of 3 wells along the Portuguese continental shelf. a) Basin configuration, backstrip basement (flexural; dashed line) and location of the wells along profiles 7 and 8 (see inset of Figure 6.1 for location). b) Comparison between the tectonic subsidence curves obtained from 1-D well backstripping (pink lines) and that predicted by the 2-D flexural models (black lines).

It appears, however, that along the continental shelf in the Intermediate and Central Portuguese segments of the WIM, the subsidence/uplift history predicted from the 2-D flexural models is inconsistent with that obtained from 1-D well backstripping. As depicted in Figure 6.13, this is especially noticed near the flanks of the main depocentres, in wells Do-1 and 13C-1 (Figure 6.13b). At these locations, most of the subsidence predicted by the flexural model occurs during the latest Jurassic-Early Cretaceous rifting event, instead of during the Late Triassic-earliest Jurassic, as suggested by the well data.

As described in Section 6.3.2, two sets of β profiles are given as input for the thermo-mechanical models. The first rift β's (Late Triassic-Late Jurassic) are obtained from the flexural backstrip of sediment unit U_3, and assuming an Airy model of stretching, and the second set of β's (latest Jurassic-Early Cretaceous rift event) from the ratio between the first rift β's and the total amount of extension constrained from POGM.

Since over 70% of the total sediment thickness in the main depocentres along the shelf and onshore are Late Triassic to Late Jurassic formations (Figure 6.13a), then the

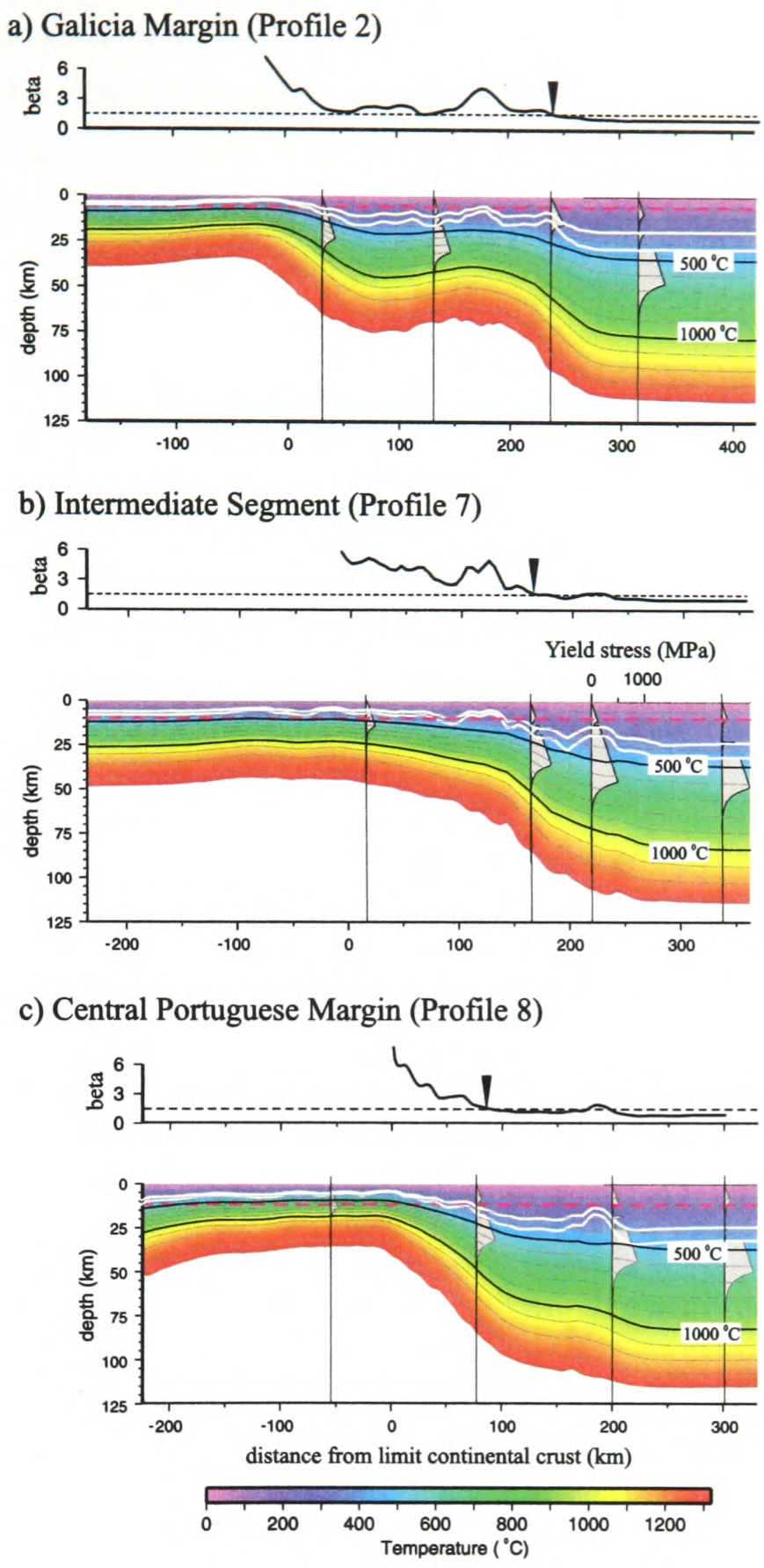

Figure 6.14: Thermal structure and YSE's at the end of the latest Jurassic-Early Cretaceous rifting event in the Galicia Margin (a), Intermediate Segment (b) and Central Portuguese Margin (c). Thermal contours are spaced of 100°C. The upper-middle/lower crust limit and the Moho depths are highlighted by the thin white lines. The dashed pink line show the necking depth inferred from POGM in each of the profiles (see Appendix C). Also shown along each transect are the corresponding β profiles. The black arrows indicate the location where Z_{neck} stabilizes at a certain depth, which according to Govers & Wortel [1999] corresponds to a β of 1.5 (see text).

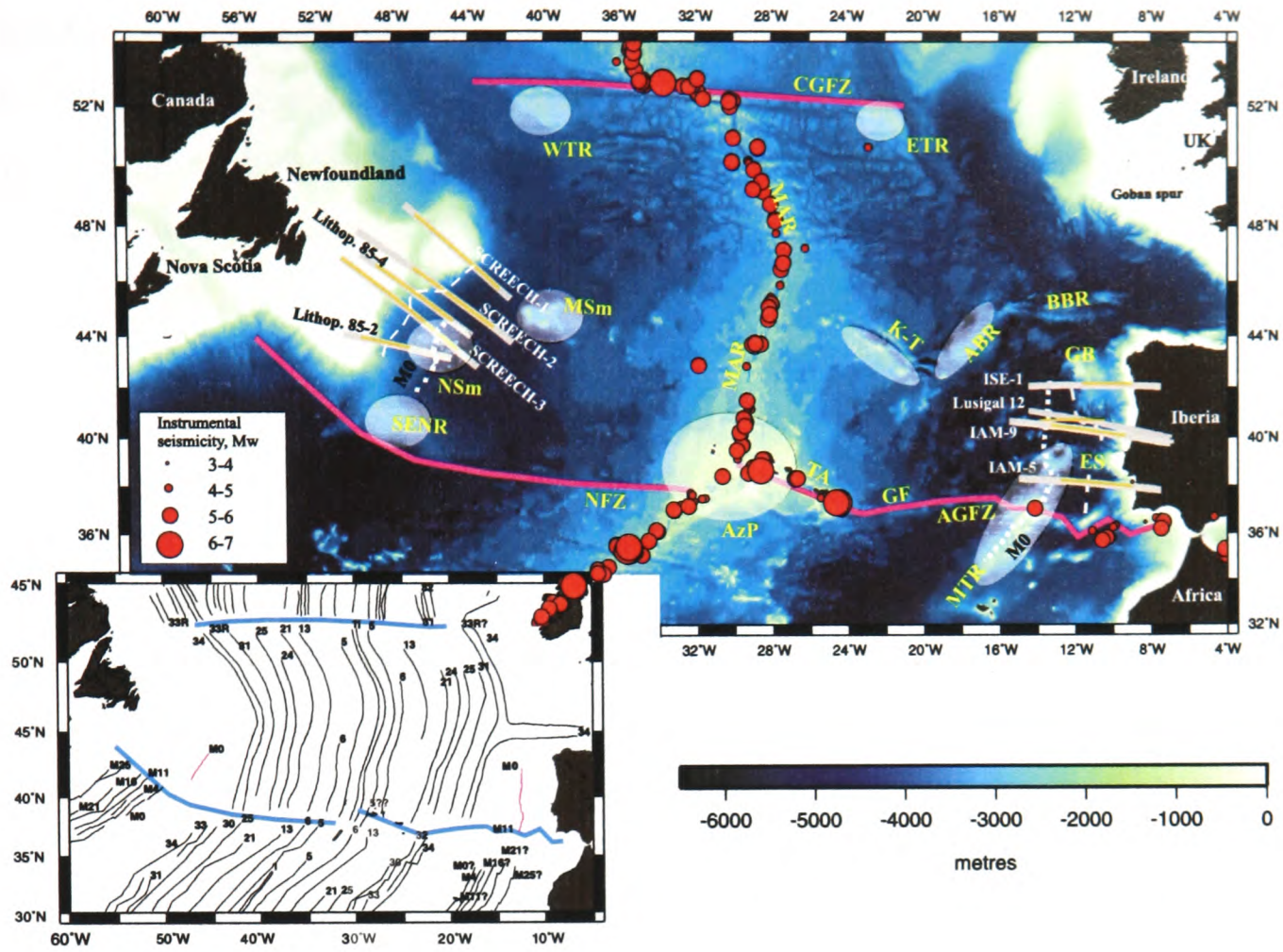

Figure 7.1: Bathymetric chart of the central North Atlantic, between the Charlie Gibbs (CGFZ), in the north, and the Newfoundland (NFZ) and Azores-Gibraltar (AGFZ) fracture zones in the south (thick pink lines). The map shows the location of the seismic datasets (yellow lines) which have been used to study the segmentation and style of rifting of the WI and NF margins. The thick grey lines show the profiles where POGM techniques have been applied. Also shown is the location of magnetic anomaly M0 (dotted white lines) and the interpreted limit of streched continental crust (dashed white lines) along the WI and NF margins. The shaded grey circles and ovals highlight areas of excess volcanism (see text). Red circles show the instrumental seismicity for Mw $\geq$ 3, recorded between 1977 and 2007 (extracted from the IRIS, network). Other acronyms in alphabetical order: ABR, Azores-Biscay Rise; AzP, Azores Plateau; BBR, Bay of Biscay Rise; ES, Estremadura Spur; ETR, Eastern Thulean Rises; GB, Galicia Bank; GF, Gloria Fault; K-T, Kings Trough; MAR, Mid-Atlantic Ridge; MSm, Milne Seamounts; MTR, Madeira-Tore Rise; NSm, Newfoundland Seamounts; SENR, Southeast Newfoundland Ridge; TA, Terceira axis; WTR, Western Thulean Rises. Inset in the bottom-left corner shows the seafloor spreading (SFS) magnetic lineations identified in this region of the North Atlantic Ocean.

Focal mechanism solutions indicate mainly NE-SW to NNE-SSW extension-transtension near the Azores, along the Terceira Axis (e.g. Madeira & Ribeiro [1990]; Lourenço *et al.* [1998] and references therein), changing to dextral strike-slip motion along the Gloria Fault segment of the Azores-Gibraltar Fracture Zone (AGFZ; Udias [1982]; Grimison & Chen [1986]). East of the Madeira-Tore Rise, the seismicity becomes more diffuse

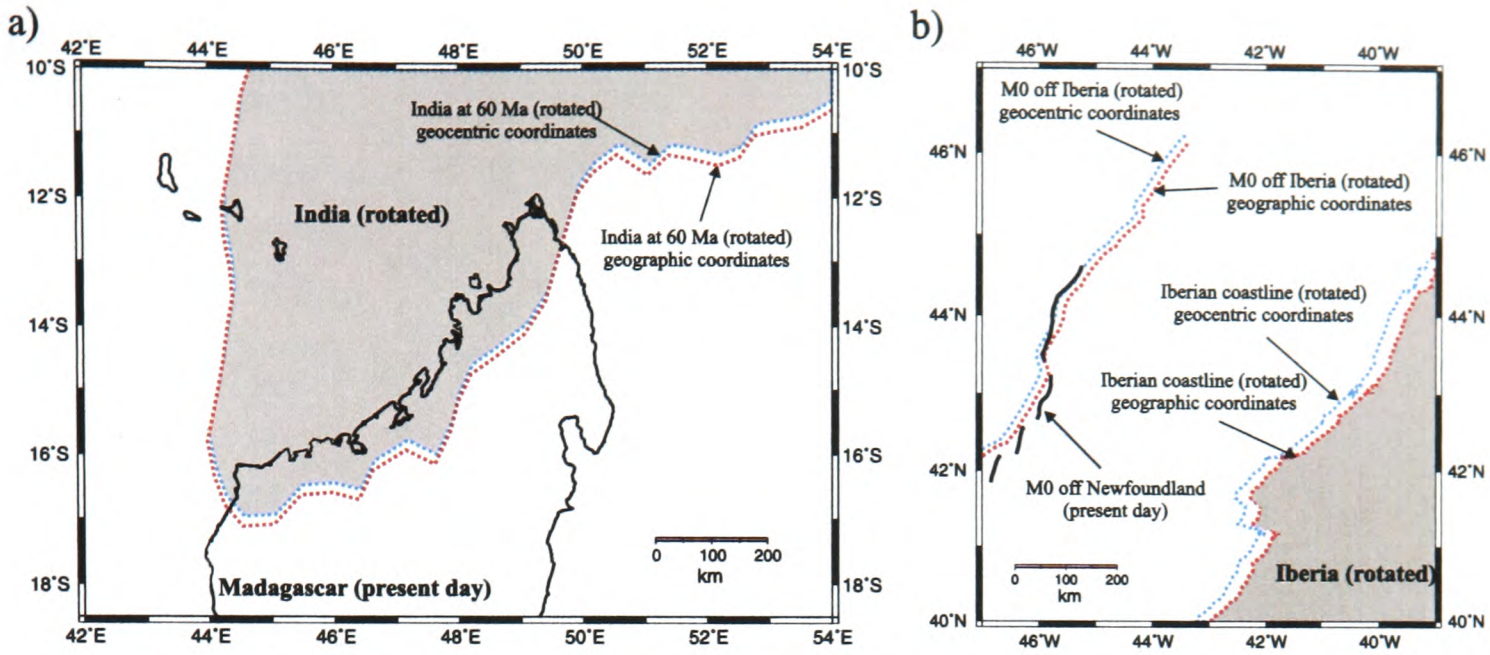

Figure 7.2: Geocentric versus geographic coordinates in plate reconstructions. Tests using the: (a) reconstructed Indian and African plates at Chron 25 (59 Ma); and (b) reconstructed Iberian and North American plates at Chron M0 (~ 125 Ma). All rotations are performed in relation to a fixed North American Plate. The figure shows that in both cases a difference of 10-30 km is obtained between rotations performed in the two distinct coordinate systems.

in the past (Bullard *et al.* [1965]; McKenzie & Parker [1967]; Harland [1972]).

There are different types of rotation poles that can be derived, which either describe a plate rotation over a finite period of time (i.e. finite-difference poles) in relation to a fixed framework (Bullard *et al.* [1965]; Pitman & Talwani [1972]), or give the relative motion between two plates at a given time (instantaneous poles or "poles of motion"; e.g. Klitgord & Schouten [1986]). In this work, only the reconstruction poles will be considered. These are the finite-difference poles which describe (latitude, longitude and angle of rotation) the rotation necessary to match synchronous magnetic lineations and fracture zones on opposite sides of the spreading centre at a given time, regardless of how the plates actually moved in detail. This is justified, since we are mainly interested in analysing conjugate segments of the West Iberian and Newfoundland margins to discuss the mechanisms of rifting, and not the details of the central North Atlantic plate kinematics.

Rotations in plate kinematics commonly assume geographic (or geodetic) coordinates. However, for tracking objects moving at the Earth's surface it is more accurate to use geocentric, instead of geodetic coordinates (Matias *et al.* [2005] and references therein). The difference is that in the geocentric coordinate system the latitude is measured at the centre of the Earth, whilst the geographic latitude is measured between the Zenith and the equatorial plane. Longitude is not affected by converting from geographic to

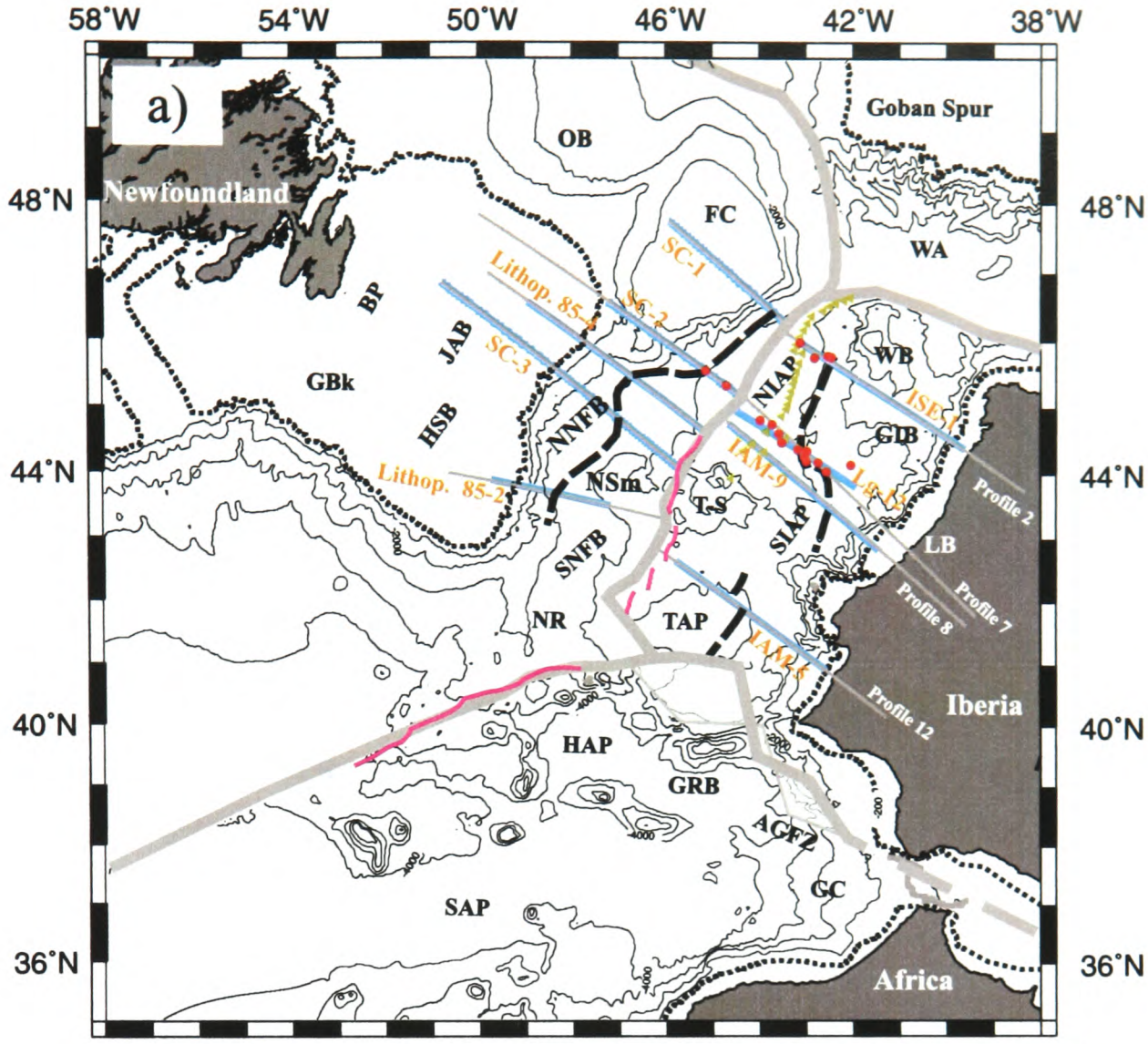
a)
b)
58°W
54°W
50°W
46°W
42°W
38°W
48°N
44°N
40°N
36°N
Newfoundland
Goban Spur
OB
FC
WA
BP
JAB
GBk
HSB
NNFB
NSm
SNFB
NR
T-S
TAP
NIAP
WB
GIB
SLAP
LB
HAP
GRB
AGFZ
GC
SAP
Africa
Iberia
SC-1
SC-2
SC-3
Lithop. 85-4
Lithop. 85-2
IAM-9
IAM-5
ISE-1
LG-12
Profile 2
Profile 7
Profile 8
Profile 12
M0 (Newfoundland)
Seismic data
Modelled profiles
Limit continental crust
200 m bathymetric
ODP / DSDP sites
Peridotite ridge

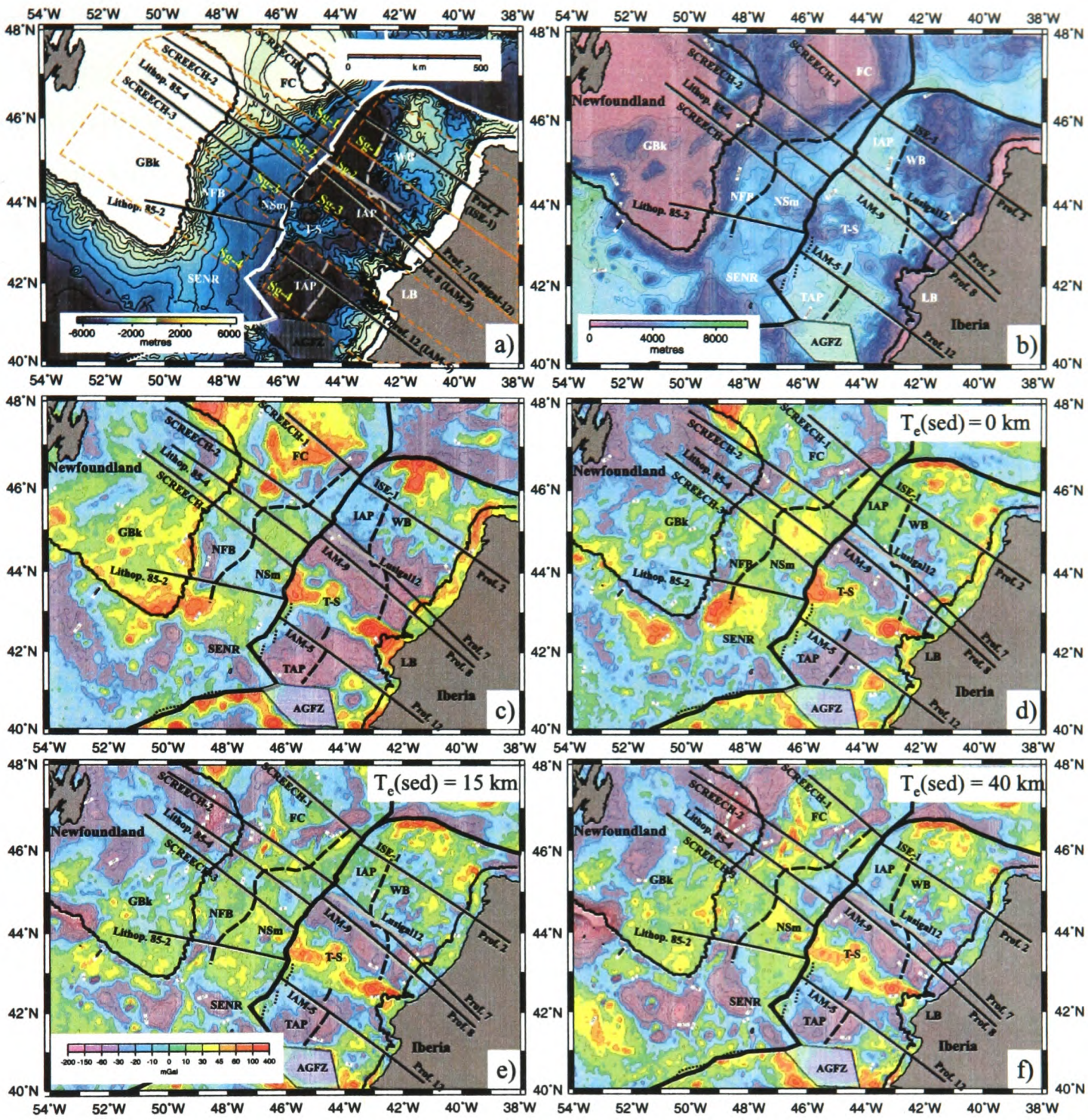

Figure 7.4: a) Bathymetry; b) Sediment corrected basement depth assuming an Airy compensation model for the sediment load, i.e. $T_e(\text{sed}) = 0$ km; c) Free-air gravity anomaly; d)-f) Isostatic anomalies (IA) for a uniform $T_e(\text{sed})$ of 0 km (d; Airy isostatic anomaly), 15 km (e) and 40 km (f). The maps show the West Iberian-Newfoundland rift reconstructed at the time of M0 (i.e. $\sim$ 125 Ma, early Aptian) assuming the rotation pole of Srivastava *et al.* [2000] (see Table 7.1). Also shown are the limits of the continental shelves (solid black lines), the limits of stretched continental crust (dashed black or grey lines) and the modelled transects (grey-black lines), where the grey highlights the segments where there is seismic control on the structure of the crust. In (a), the segments assumed for the analysis of the data across conjugate transects and discussion of the margins degree of symmetry are highlighted by the dashed orange lines (segments, Sg, 1 to 4). Acronyms as in figures 7.1 and 7.3.

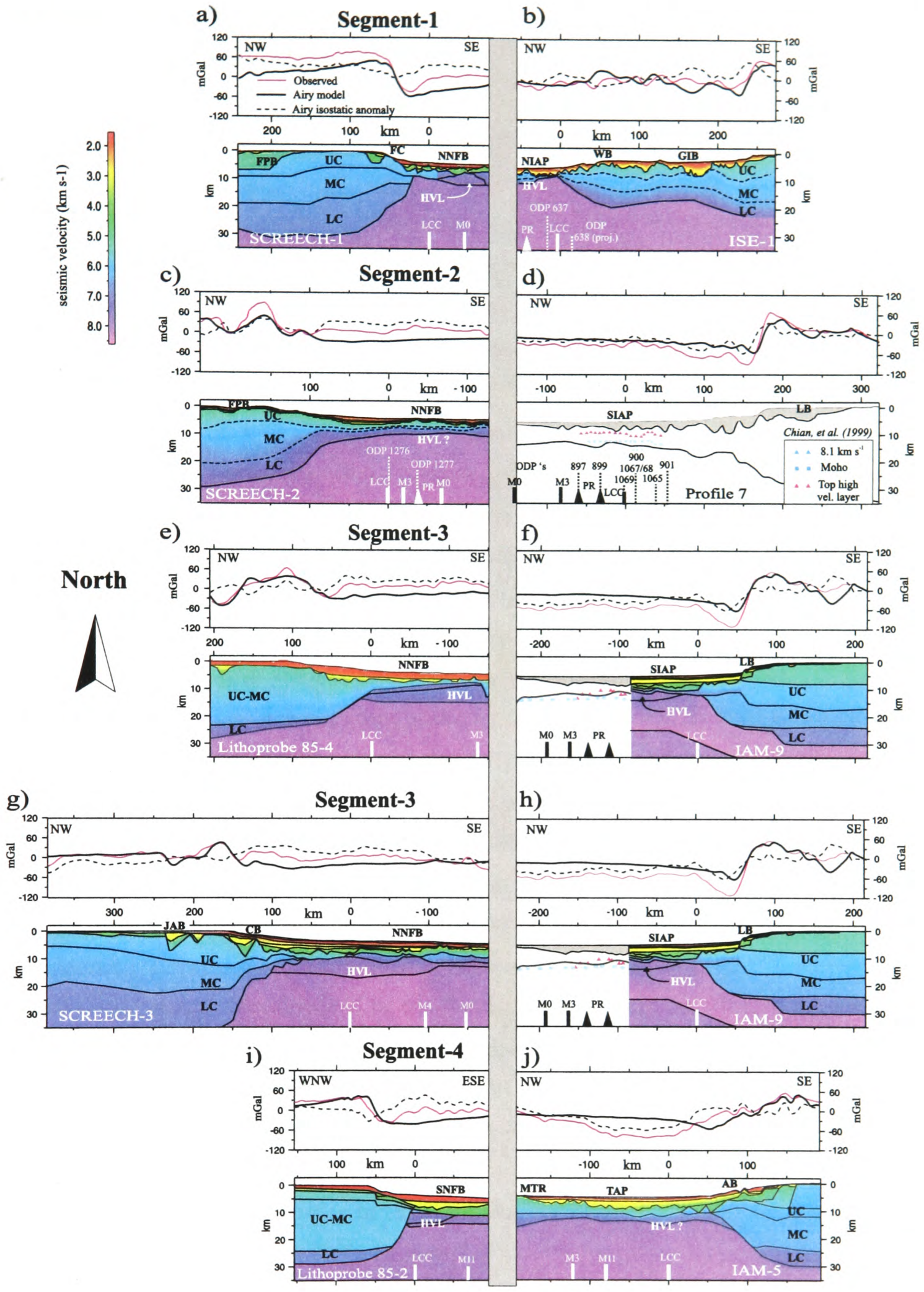

These authors suggest an ~ 30 km wide region of serpentinized upper mantle to the west of M3 (Figure 7.5c), exhumed at the surface along a dipping to the west detachment.

In the WIM, the limit of continental crust follows Whitmarsh *et al.* [2001b], and includes a region where lower crust and upper mantle lithologies have been cored in two

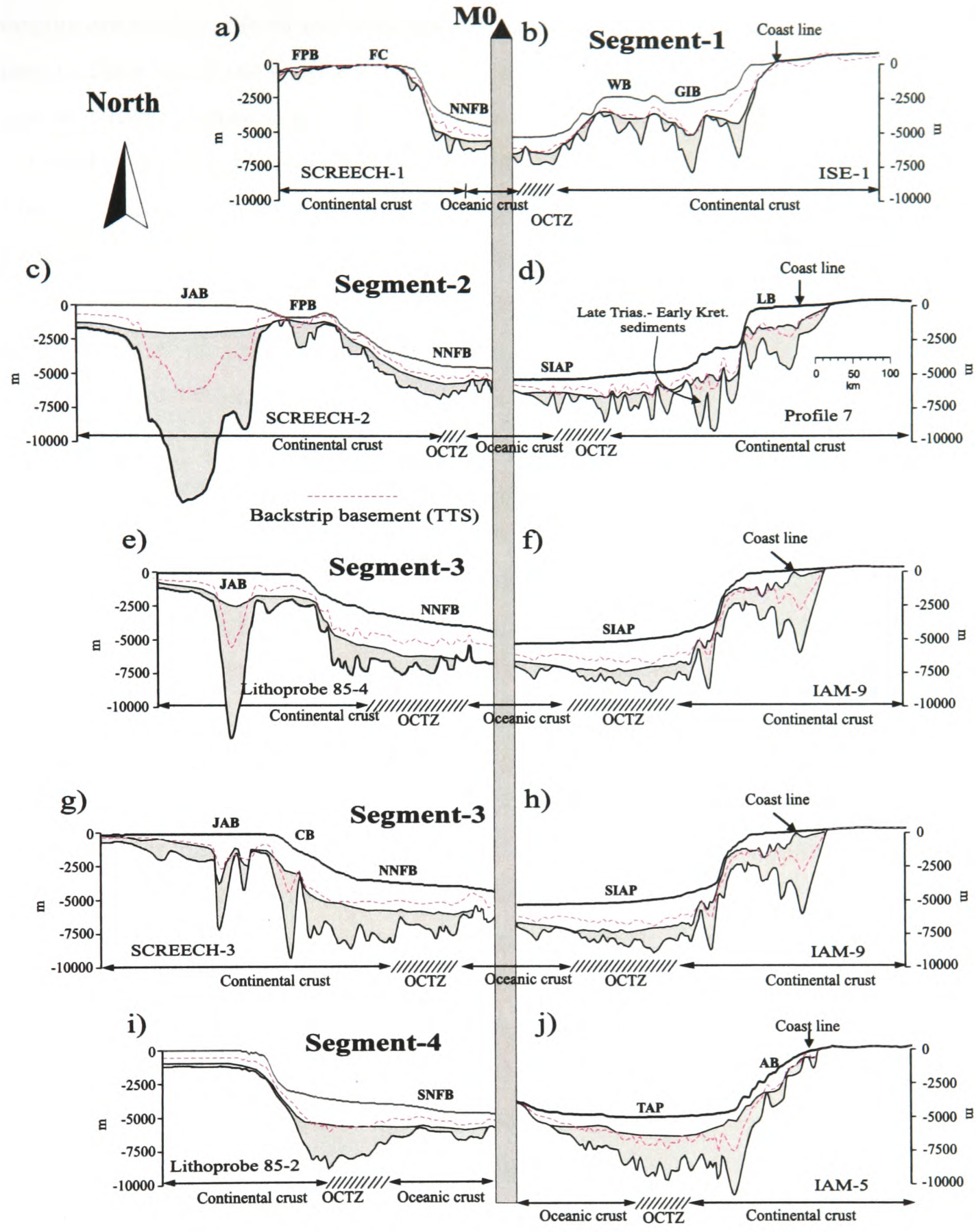

Figure 7.6: Basin profiles and total tectonic subsidence (TTS). The TTS (dashed pink lines) was obtained from the sediment backstripping, assuming that the sediments are Airy compensated, i.e. $T_e(\text{sed}) = 0$ km. The conjugate profiles are defined according to the rotation pole of Srivastava *et al.* [2000] at the time of magnetic anomaly M0 (see Figure 7.3a for location). The exception is the SCREECH-3/IAM9 conjugates, which are in better agreement with the reconstruction pole proposed by Olivet [1996] (see Figure 7.3b). The grey shaded areas highlight the sediment thicknesses accumulated between the Late Triassic and the Early Cretaceous. Regions acronyms are as in Figure 7.3.

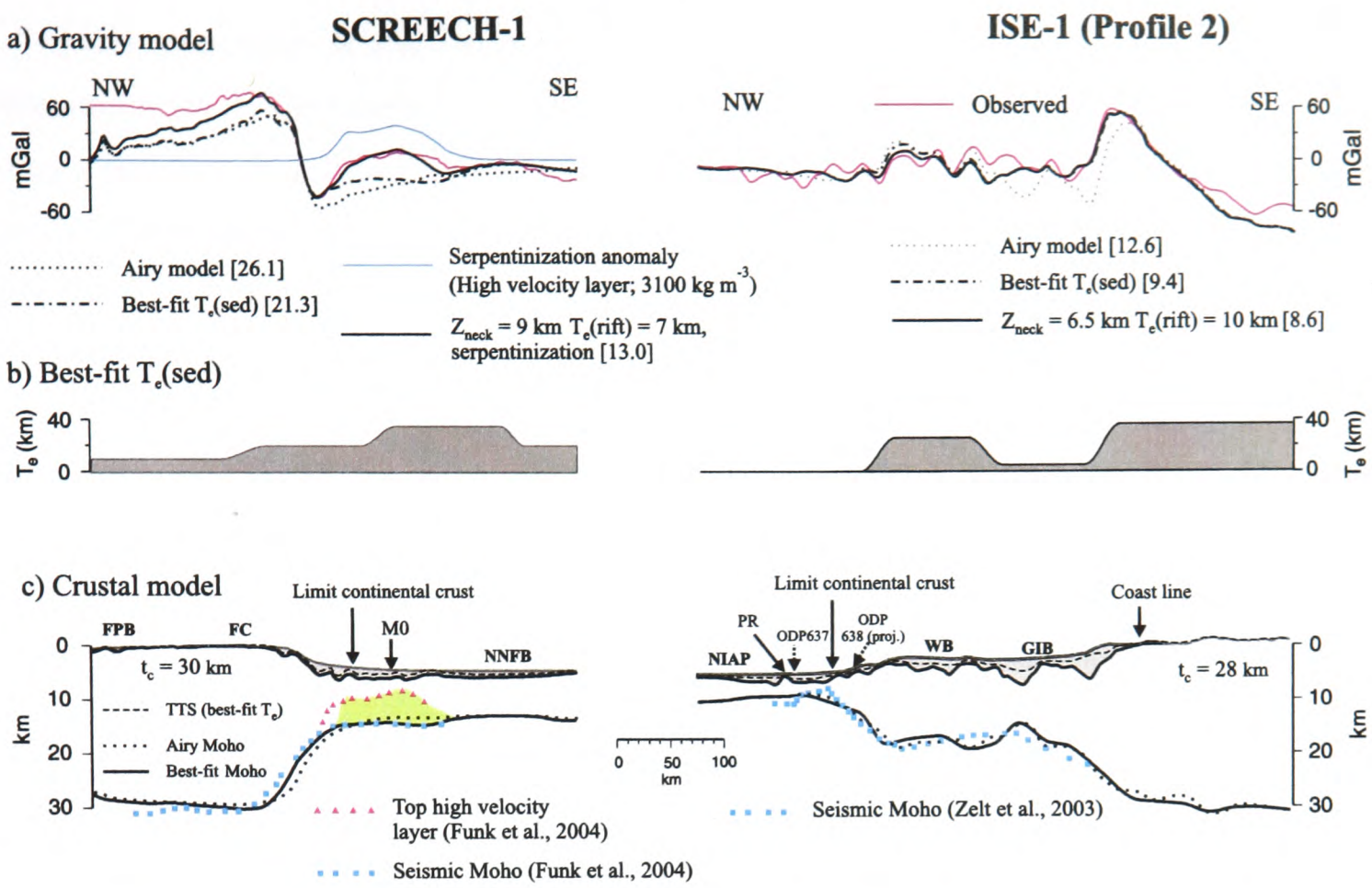

Figure 7.7: Results from POGM on conjugate profiles located in Segment 1 of the West Iberia and Newfoundland margins: Seismic lines SCREECH-1 and ISE-1 (see Figure 7.4a for location). a) Comparison between the observed (pink lines) and calculated gravity anomalies (black lines) for different models. These include the Airy model (i.e. T_e(sed) = T_e(rift) = 0 km), the best-fit, laterally varying T_e(sed) model, and the final gravity model. The later accounts for the effects of finite strength during rifting, T_e(rift), and depth of necking, Z_{neck}. The gravity anomaly associated with the high velocity layer in the OCTZ (see text) is depicted in blue. For each model the root mean square difference (RMS) between observed and calculated anomalies is indicated within brackets, in mGal. b) Best-fit T_e(sed). c) Crustal models implied by the Airy and final gravity models. The initial crustal thickness (t_c) assumed for the gravity models is indicated for each profile. The coloured triangles and squares show the locations where there is seismic control on the deep crustal structure. The green body in the NFM corresponds, approximately, to the high velocity layer in the velocity model of Funk *et al.* [2004]. Regions acronyms are as in Figure 7.3.

density body (3100 kg m^{-3}) replacing crust. This body is defined between the seismic and gravity predicted Mohos (Figure 7.7c, left) and corresponds, approximately, to the high velocity layer in the velocity model of Funk *et al.* [2004]; and (3) the sedimentary loads do not exceed 2-3 km in thickness along most of the profiles and, consequently, the calculated gravity anomalies are less sensitive to variations in the T_e(sed) than, for example, in the Galicia Interior Basin (Figure 7.7c, right).

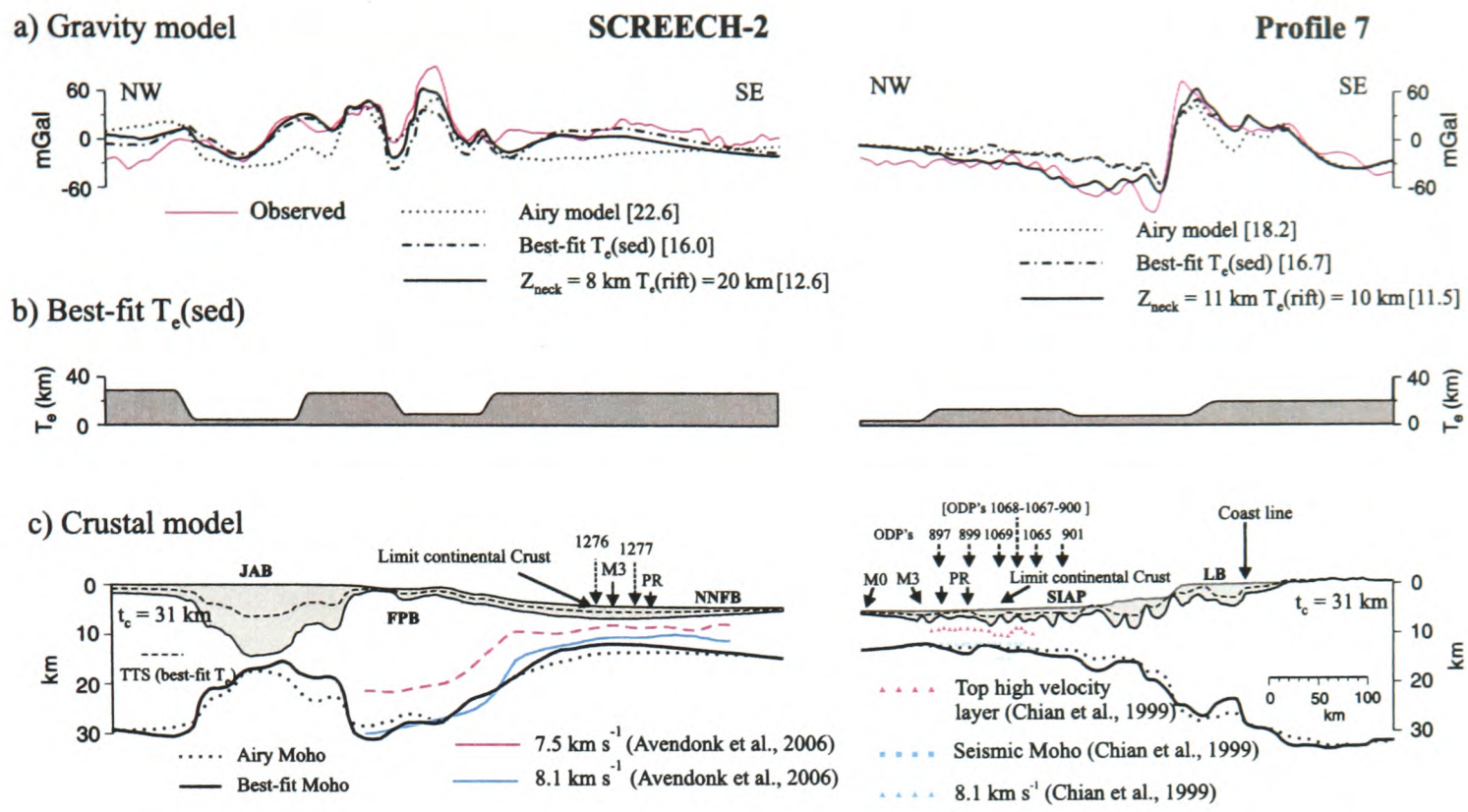

Figure 7.8: Results from POGM on conjugate profiles located in Segment 2 of the West Iberia and Newfoundland margins: Seismic line SCREECH-2 and Profile 7 (see Figure 7.4a for location). See Figure 7.7 for legend. Along the SCREECH-2 transect the 7.5 and 8.1 km s^{-1} velocity contours were extracted from the tomographic velocity model of van Avendonk *et al.* [2006].

have been constrained in several modelled transects along the Intermediate Segment (see Profiles 5-7 in Appendix C).

Although the final gravity models along the SCREECH-2 and Profile 7 transects do not fully recover the amplitude of the EEA's, they provide a good overall fit between observed and calculated gravity anomalies and explain the main features of the margins gravity field. Furthermore, they represent improvement in the calculated RMS of 34-45% in relation to the Airy models (Figure 7.8a).

Along Profile 7, a reasonable good agreement is also obtained between the gravity predicted and the seismic Moho (blue squares in Figure 7.8c, right), with maximum discrepancies of $\sim$ 2 km. In the NFM, the gravity Moho follows approximately the 8.1 km s^{-1} velocity contour of the tomographic velocity model of van Avendonk *et al.* [2006] between the continental shelf and the limit of stretched continental crust. Oceanwards, however, it appears that the gravity model overestimates the thickness of the crust in 2-3 km.

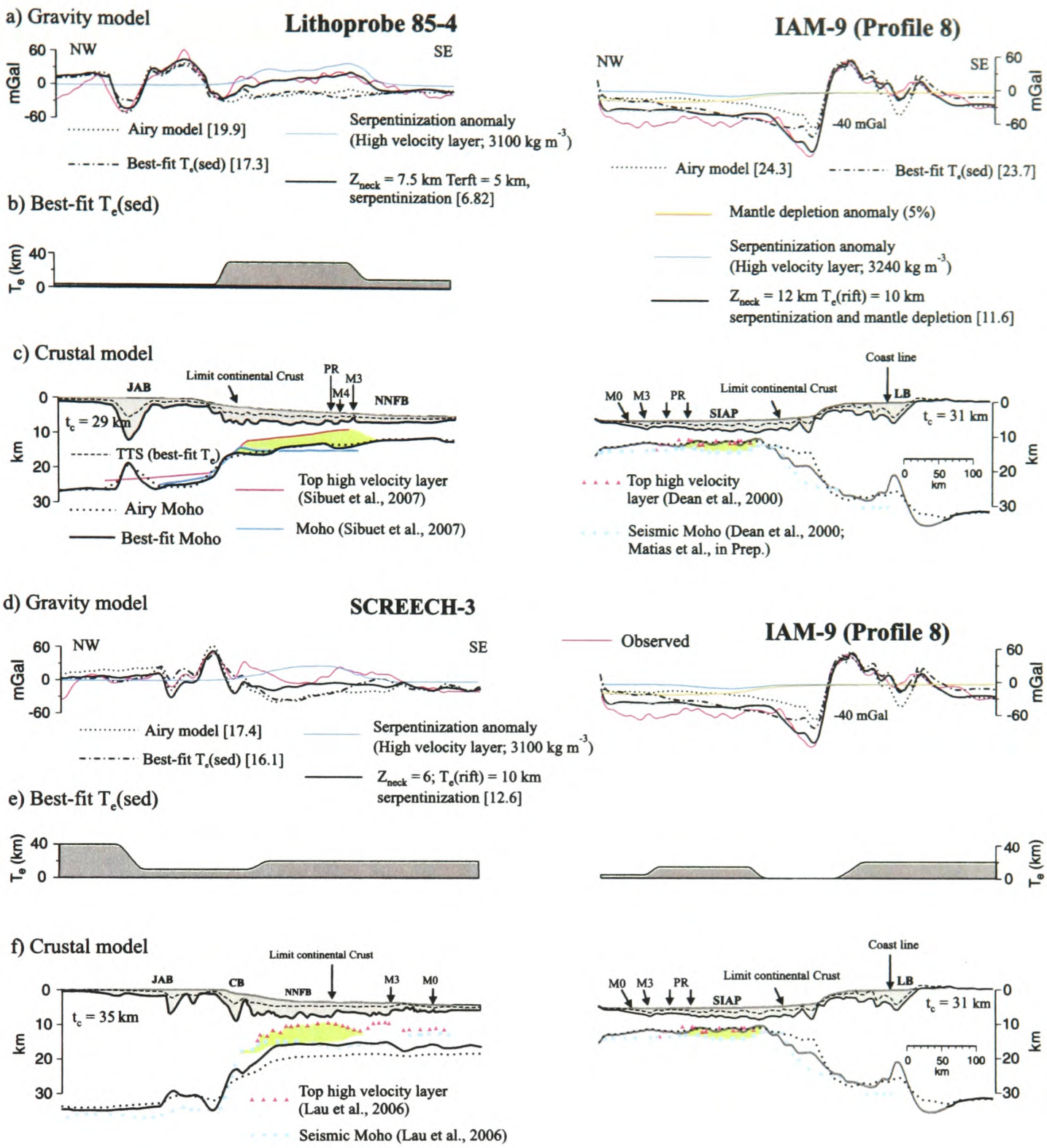

Figure 7.9: Results from POGM on conjugate profiles located in Segment 3 of the West Iberia and Newfoundland margins: Seismic lines Lithoprobe 85-4, SCREECH-3 and IAM-9 (see Figure 7.4a for location). See Figure 7.7 for legend. Along the Lithoprobe 85-4 transect the top of the high velocity layer and the seismic Moho were digitised from the crustal model proposed by Sibuet *et al.* [2007]. The SCREECH-3/IAM-9 conjugate transects shown in (d)-(f) assume the reconstruction of the WI and NF margins at the time of magnetic anomaly M0 according to the rotation pole of Olivet [1996] (see Figure 7.3b). The bodies coloured in green in (c) and (f) show the high velocity layers in the wide-angle velocity models, which in the Lithoprobe 85-4 and SCREECH-3 transects replace crust (positive gravity anomalies) and in the IAM-9 transect replaces mantle (negative gravity anomalies).

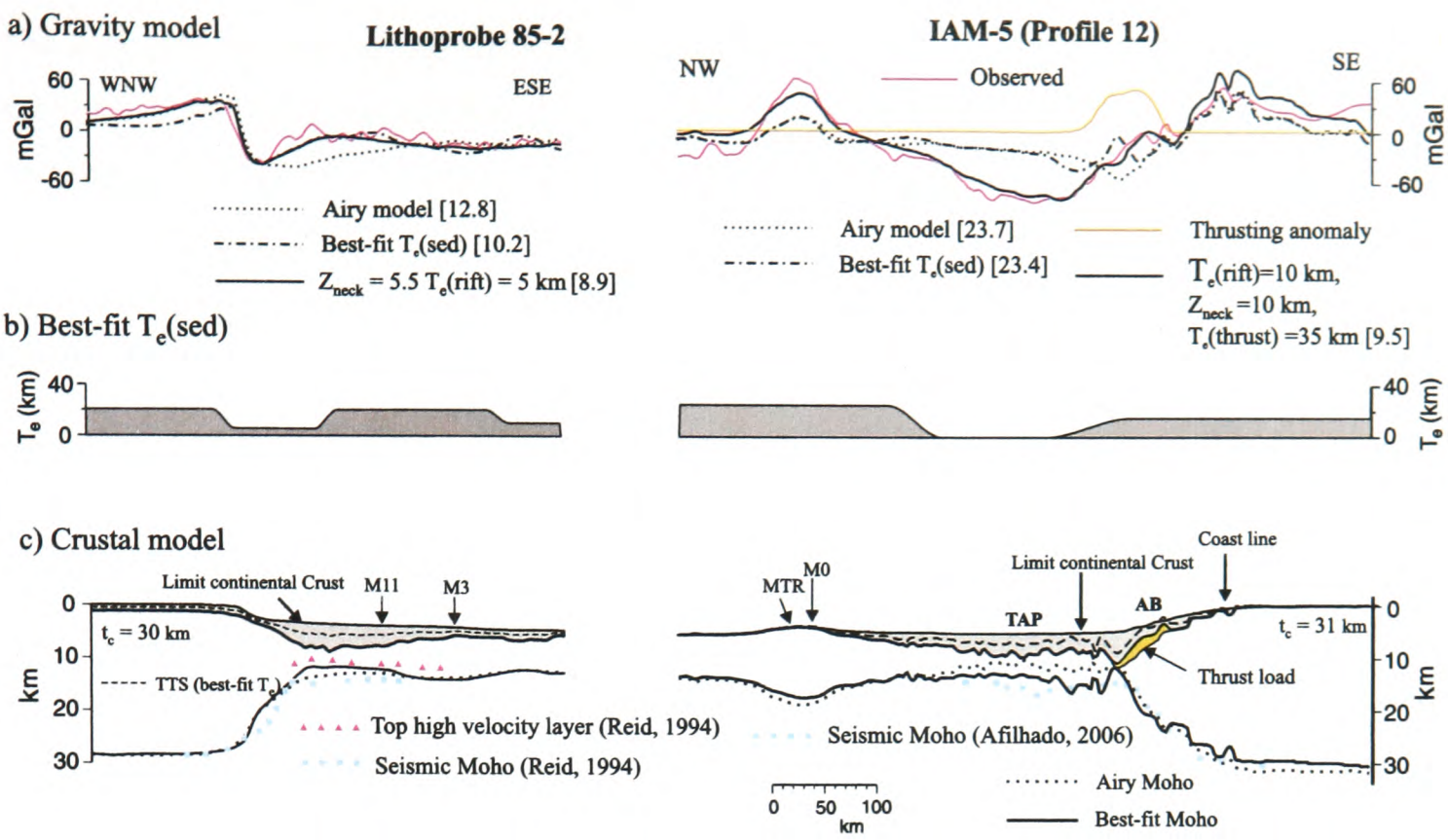

Figure 7.10: Results from POGM on conjugate profiles located in Segment 4 of the West Iberia and Newfoundland margins: Seismic lines Lithoprobe 85-2 and IAM-5 (see Figure 7.4a for location). See Figure 7.7 for legend.

transitional domains (T_e(sed) $\leq$ 20 km) along most of the length of the West Iberia and Newfoundland conjugate margins. Exceptional situations have been found along profiles SCREECH-1 and Lithoprobe 85-4, located in segments 1 and 3 of the Newfoundland Margin (NFM), respectively. In these, the best-fit gravity models suggest an increase in the T_e(sed) from $<$ 10 km over the continental shelf to $>$ 20 km in the distal margin (figures 7.7 and 7.9). It is important to note, however, that these profiles present some of the largest misfits between modelled and observed gravity anomalies in the region of the shelf, suggesting either a poorly constrained sediment thickness grid or important lateral contributions to the observed FAA, which have not been taken into account in the 2-D models. In the case of the Lithoprobe 85-4 transect, for example, large isostatic residuals remain unexplained even when combined 3-D backstripping and gravity modelling techniques are applied (Figure 7.4d-f).

Higher T_e(sed) values have, in general, been recovered along the NFM, both over the continental shelf and slope and in the distal margin. In the region of the shelf, the higher basement flexural rigidities may be related to a thicker lower crust (Figure 7.5), and/or to a more mafic composition of the crust (e.g. Burov & Watts [2006]). Over highly stretched continental and transitional basement, the lower T_e(sed) values obtained along the WIM are probably related to its more complex structural framework, characterized by widespread normal faulting and prominent low-angle detachment faults, and/or to

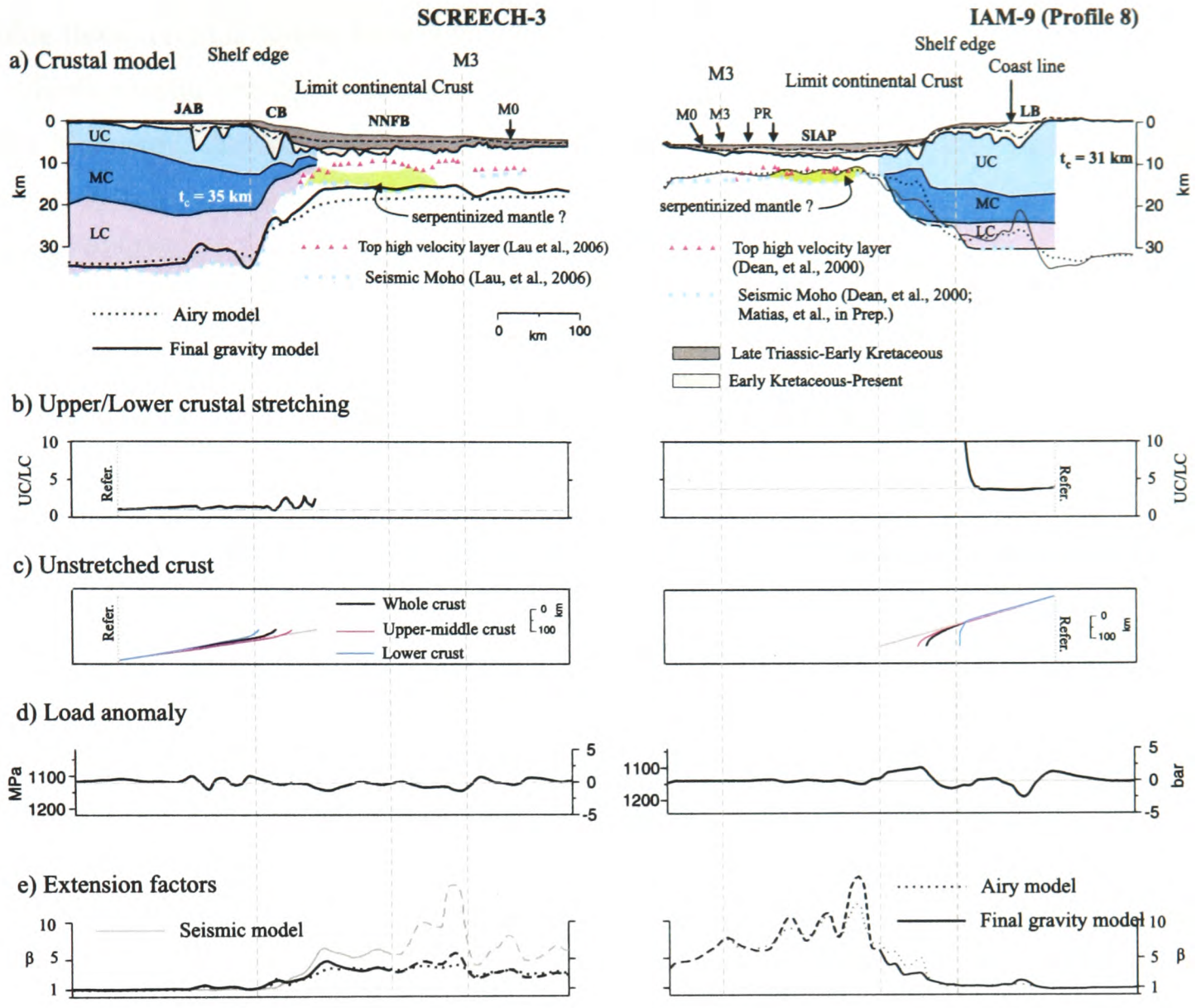

Figure 7.11: Rifting geometry, crustal extension and load anomalies along seismic transects SCREECH-3 and IAM-9 (see figures 7.1 and 7.3 for location). a) Comparison between the crustal structure inferred from POGM and that constrained from wide-angle and refraction seismic data. The Moho geometry implied by both the Airy and the best-fit gravity models are shown. The crustal velocity models are truncated at the continental rise. b) Ratio between the amount of upper-middle and lower crustal thinning, calculated from the stratification observed in the seismic velocity models, in relation to a fixed referential. c) Limit of the unstretched crustal layers calculated from the upper-middle, lower and whole crust stretching factors (see text). d) Load anomaly, calculated between the Airy and best-fit gravity models at a depth of 40 km. e) β's implied by the Airy (dotted) and best-fit (solid black) gravity models. Oceanwards of the limit of continental crust, the final gravity model β's are dashed. In line SCREECH-3, the β's calculated from the velocity model are also shown (grey line).

the pre-stretched crustal structure of the margins. By integrating the amount of stretching (β factors) observed in the distinct crustal layers along the profiles, and assuming that the mass is conserved during rifting, the oceanwards limit of the unstretched crust (black lines in Figure 7.11c) as well as that of the upper-middle (red lines) and lower

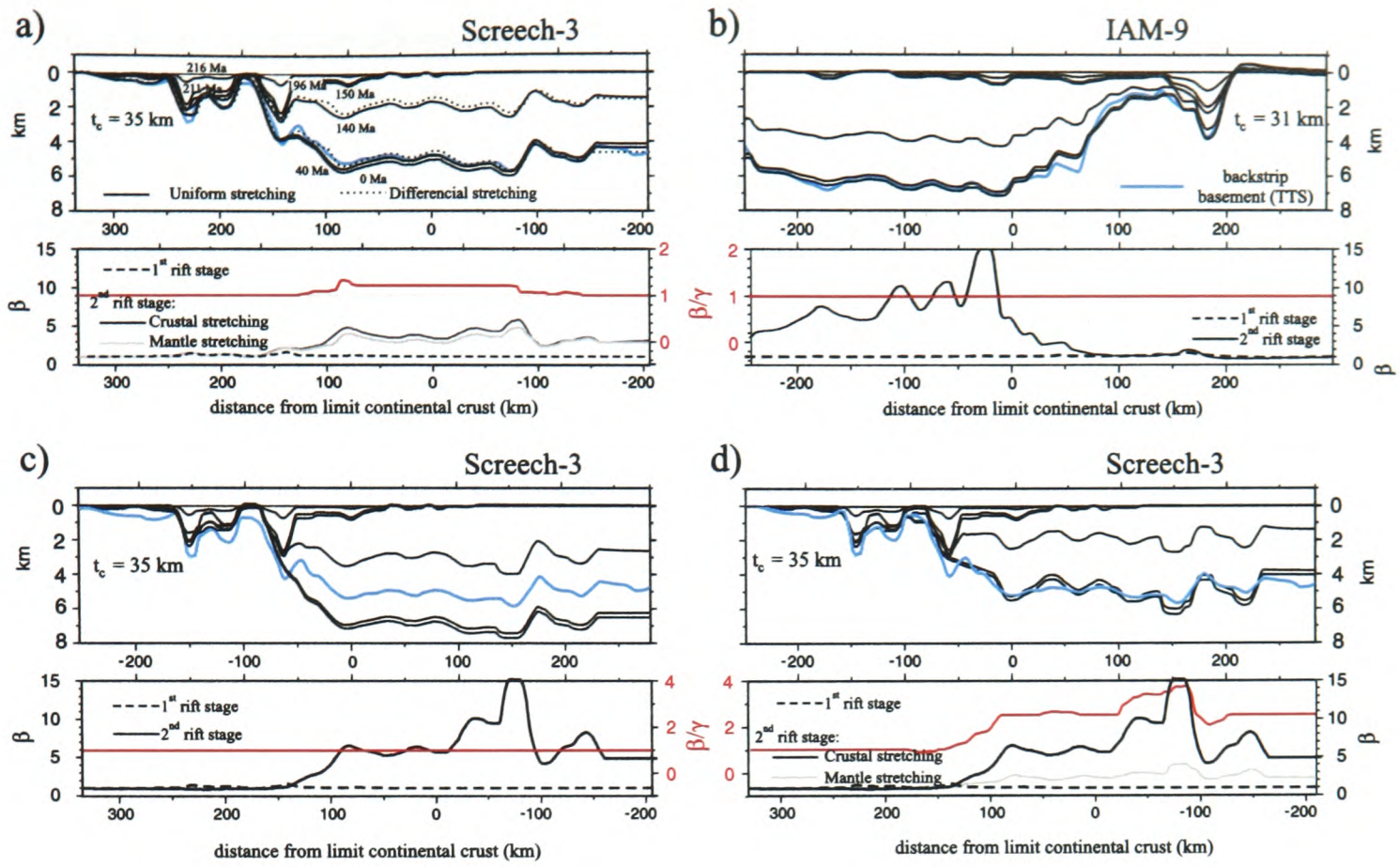

Figure 7.12: Comparison between the TTS inferred from sediment backstripping and that calculated from the β's and the thermal structure of the margins along the SCREECH-3 and IAM-9 transects. For each model the figure shows: TOP, the thermal model predicted subsidence (see Table 2.1 for modelling parameters) at different stages of the margin development (black lines; see legend in the graphics) and the backstrip basement (blue lines). All models assume two rifting events, with a first event starting at 216 Ma and lasting for 20 m.y. and a second event starting at 150 Ma and lasting for 10 m.y.; BOTTOM, the β's used to calculate the thermal structure and subsidence of the margins. The ratio between the amount of crustal and mantle stretching (β/γ) that best recovers the backstrip basement (see text) is shown in red. In (b) and (c) the models assume pure shear stretching, i.e. $\beta/\gamma = 1$. In (a) and (b), the utilized β's correspond to the best-fit gravity models along lines SCREECH-3 and IAM-9, respectively (solid black lines in Figure 7.11). In (c) and (d), the β's constrained from the wide-angle velocity model along profile SCREECH-3 were used, assuming either a depth-uniform (c) or depth-dependent lithospheric stretching model (d). The depth-uniform stretching model shows large discrepancies between the backstrip basement and the thermal predicted subsidence. These are recovered for a β/γ of $\sim$ 2.5 along most of the distal margin, as shown in (d).

the gravity predicted β's along the SCREECH-3 transect, oceanwards of the base of the continental slope, are significantly lower than those measured from the wide-angle velocity model of Lau *et al.* [2006a] (grey line).

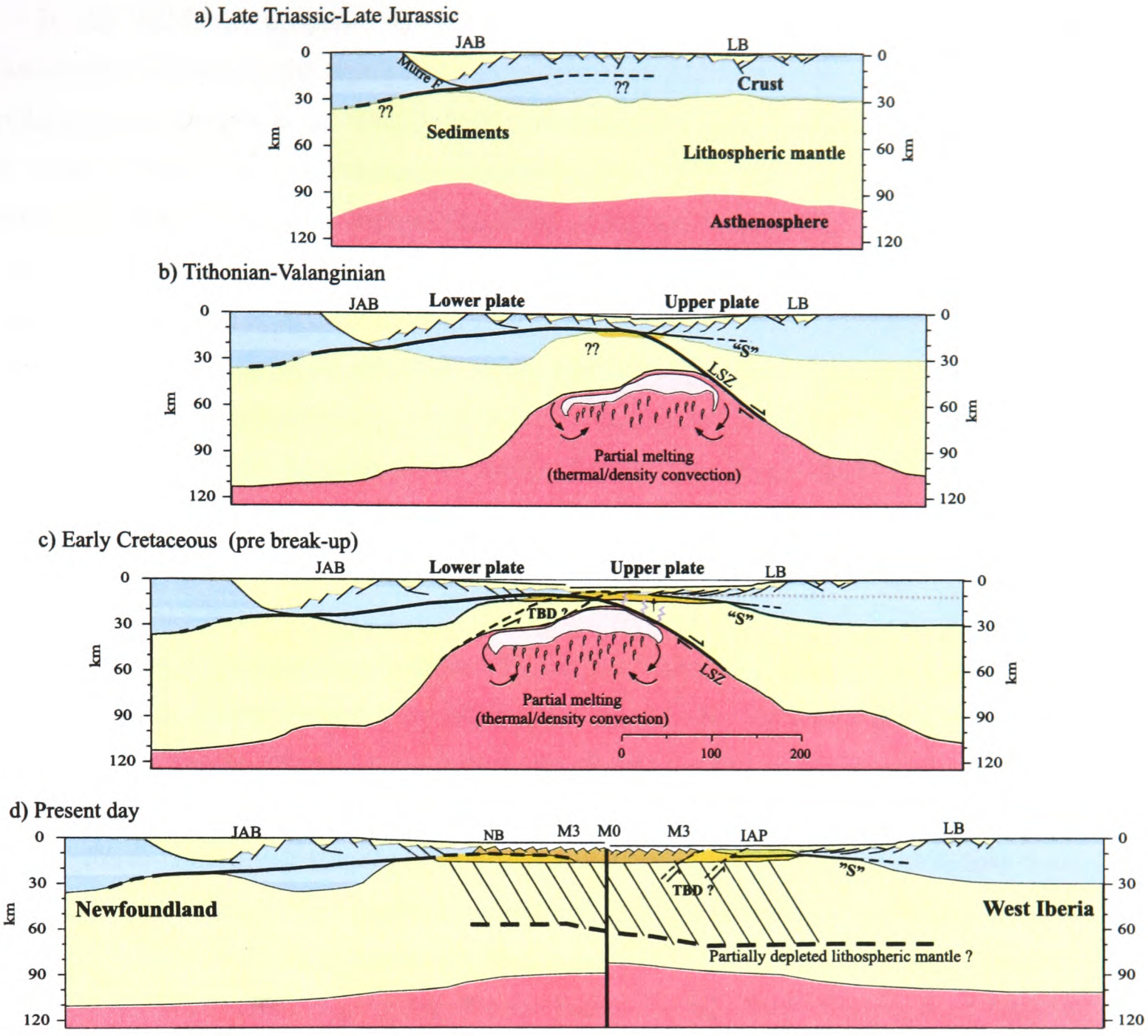

In the model proposed here, the differential crust and mantle stretching is accommodated along a dipping to the east lithospheric-scale detachment, or major shear zone, which probably propagated to the east from the décollement surface identified beneath the Grand Banks off Newfoundland (e.g. Tankard & Welsink [1987]) during the latest Jurassic-Early Cretaceous rifting event (Figure 7.13b and 7.13c). This model establishes a clear upper plate (WIM)-lower plate (NFM) conjugate margin pair and may explain a number of features in the WI and NF margins, as well as the lack of significant syn-rift magmatism, as it will discussed below.

In the Newfoundland Margin, the upwards doming of the main shear zone in the region of the continental slope and rise, as depicted in Figure 7.13b, could be related, for example, to the shallower Z_{neck}'s (5-9 km) and steeper Moho geometries observed in most of the modelled profiles, in relation to their conjugates in the WIM. A similar asymmetry in the calculated TTS, Z_{neck} and Moho geometries is also observed, for example, between the Southern Labrador and the Western Greenland conjugate margins (Chian *et al.* [1995]; Keen & Dehler [1997]).

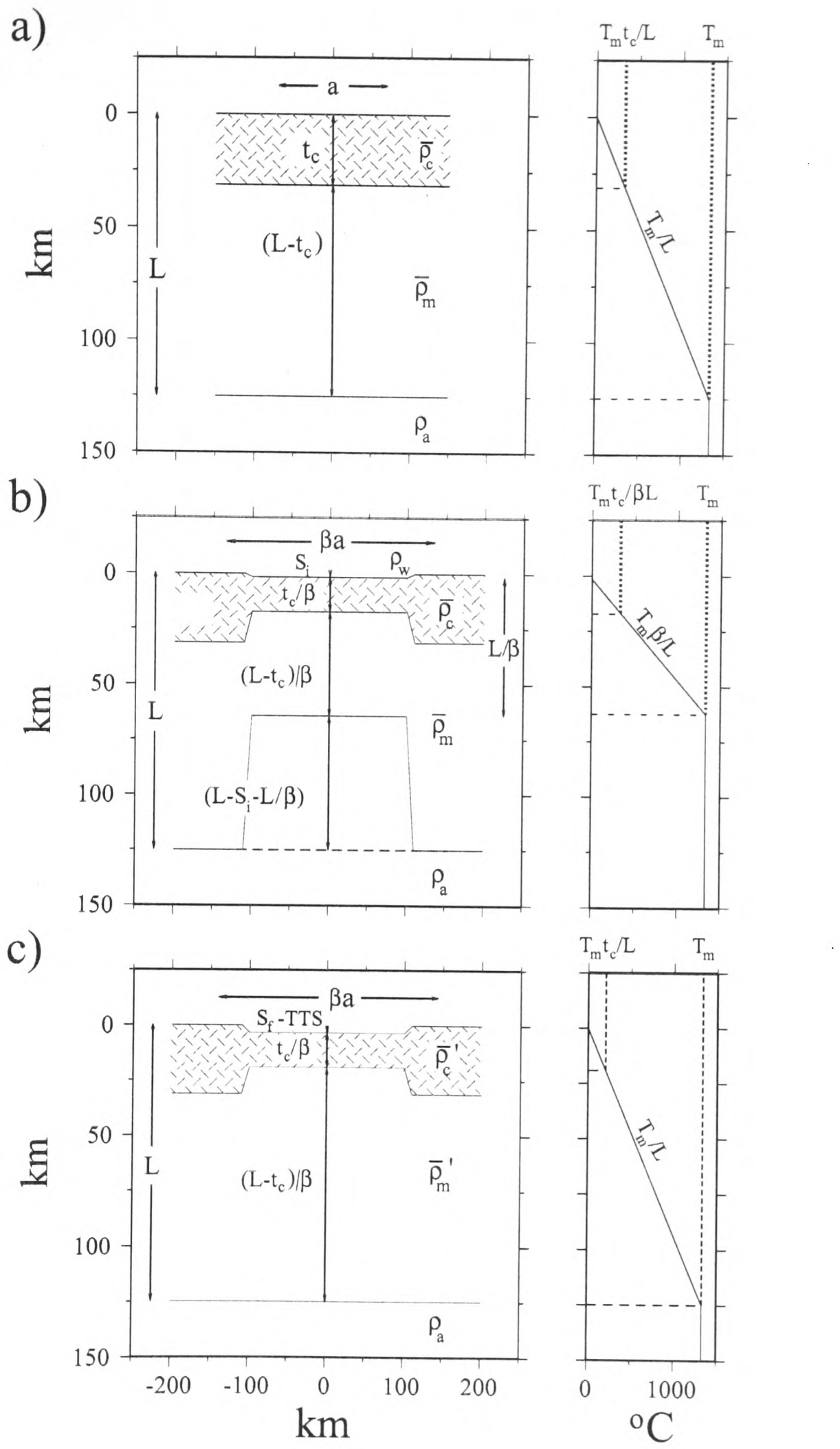

Figure A.1: Model proposed by McKenzie [1978] for the formation and evolution of rift type basins: Subsidence (left) and thermal structure of the lithosphere (right). The symbology is described in the text.

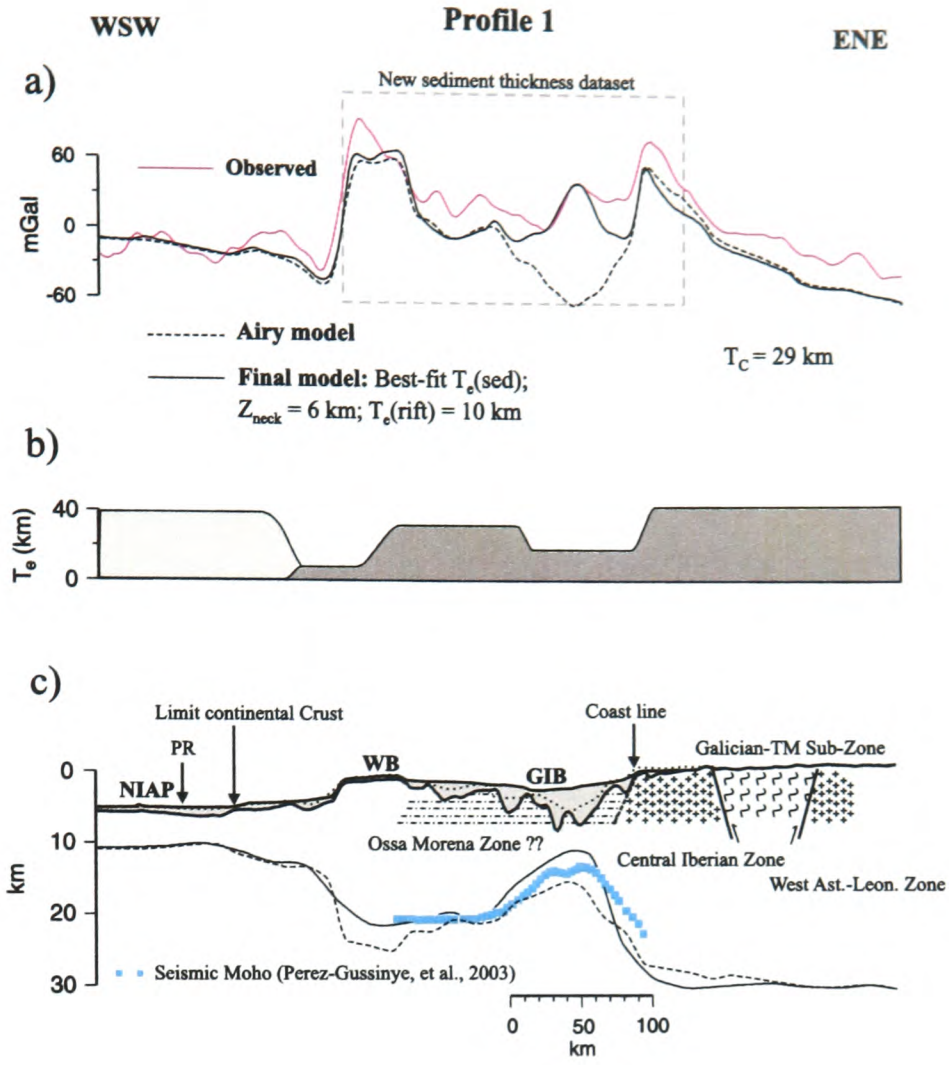

Figure C.1: Process-Oriented Gravity Modelling results along Profile 1.

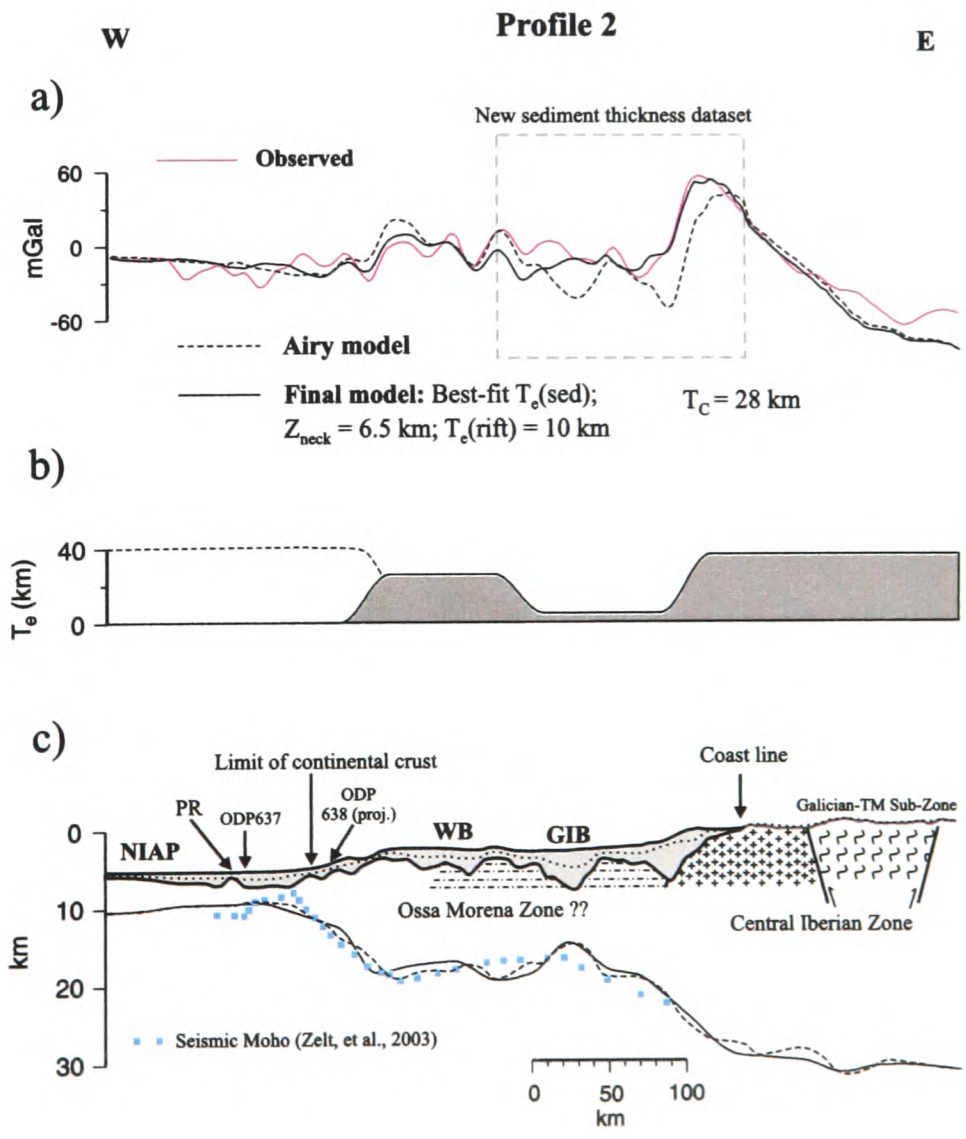

Figure C.2: Process-Oriented Gravity Modelling results along Profile 2.

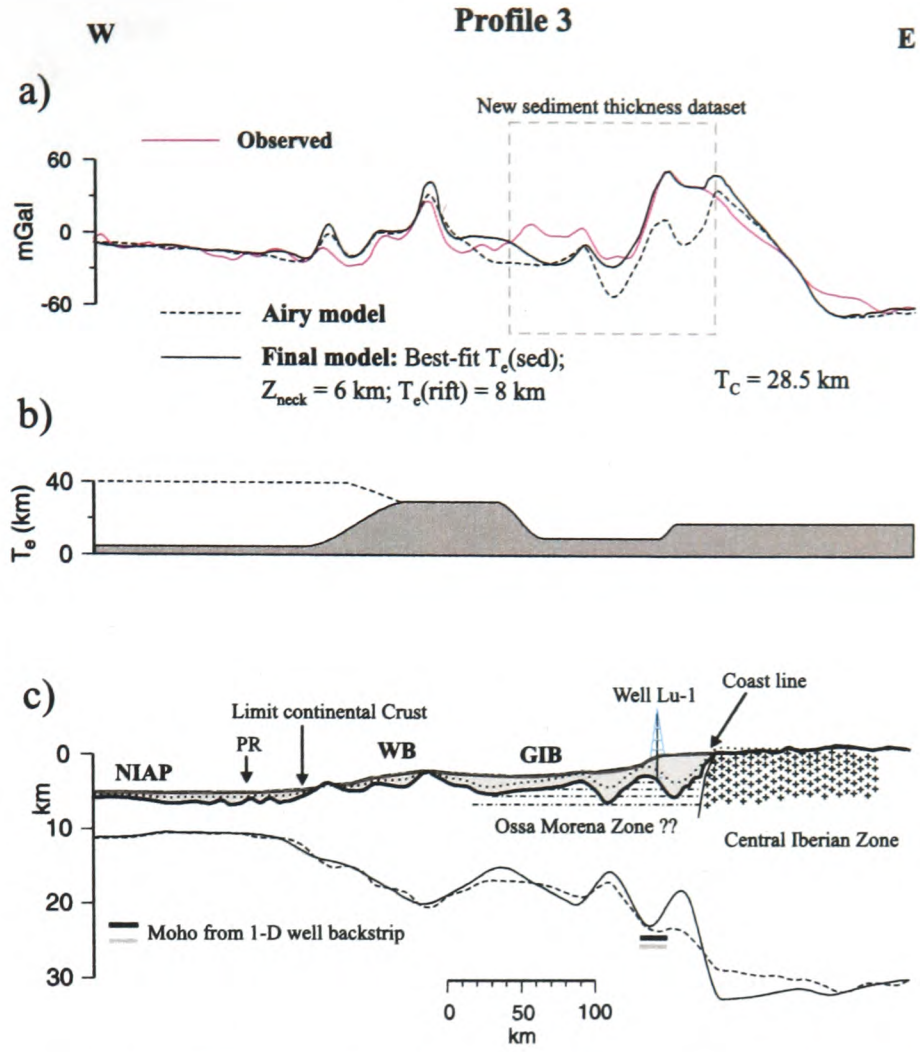

Figure C.3: Process-Oriented Gravity Modelling results along Profile 3.

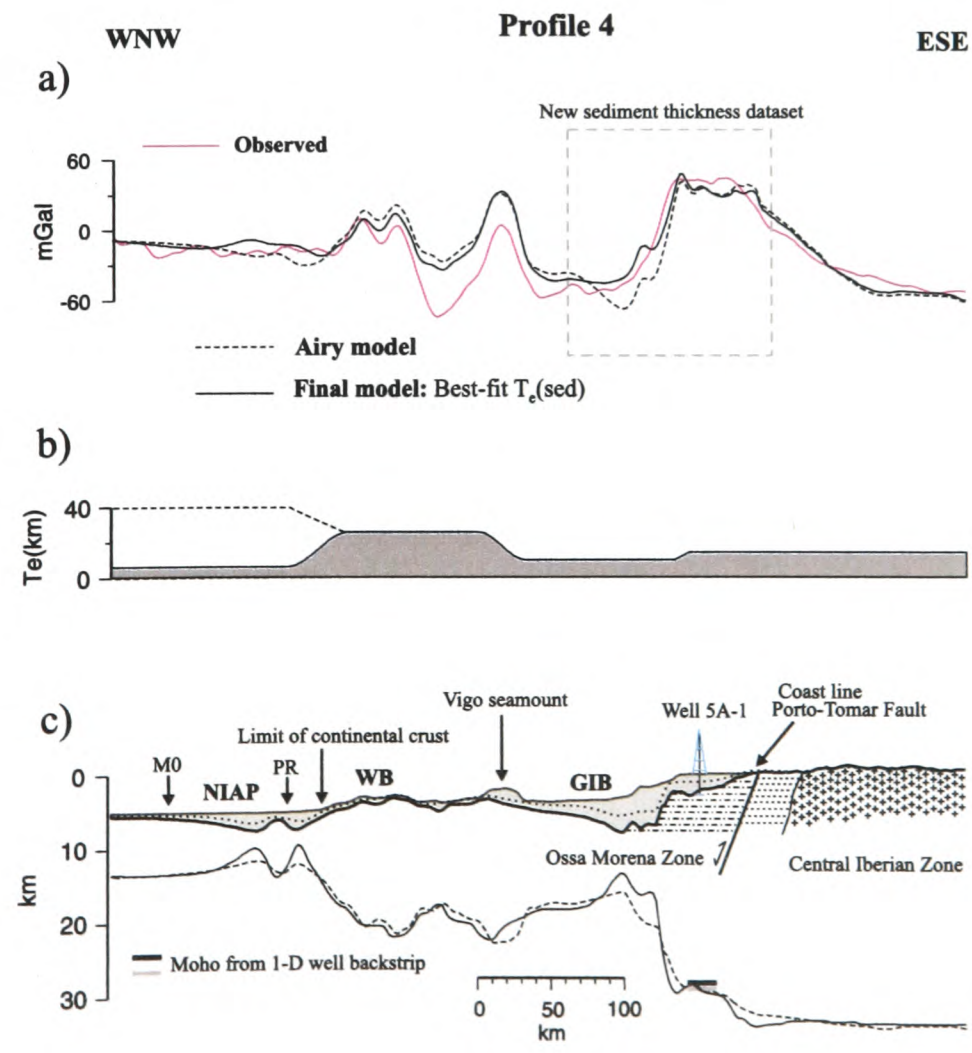

Figure C.4: Process-Oriented Gravity Modelling results along Profile 4.

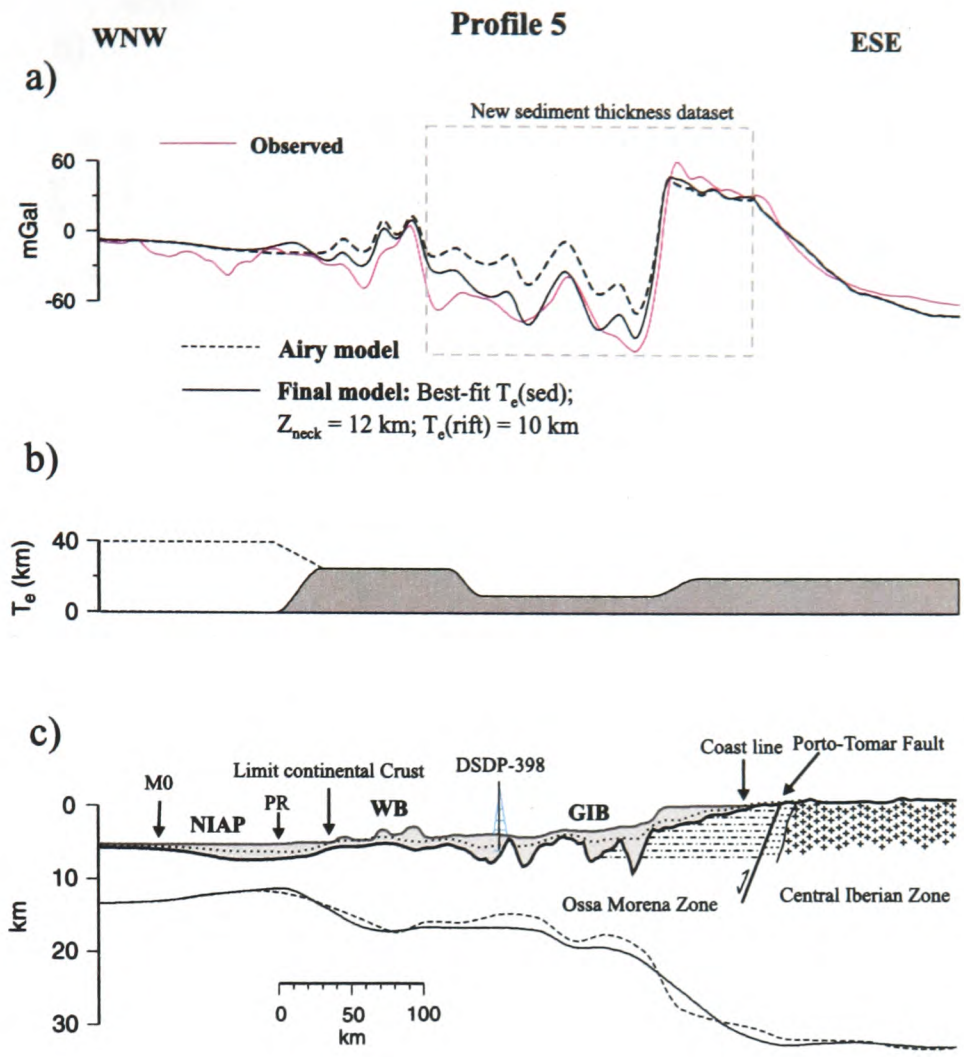

Figure C.5: Process-Oriented Gravity Modelling results along Profile 5.

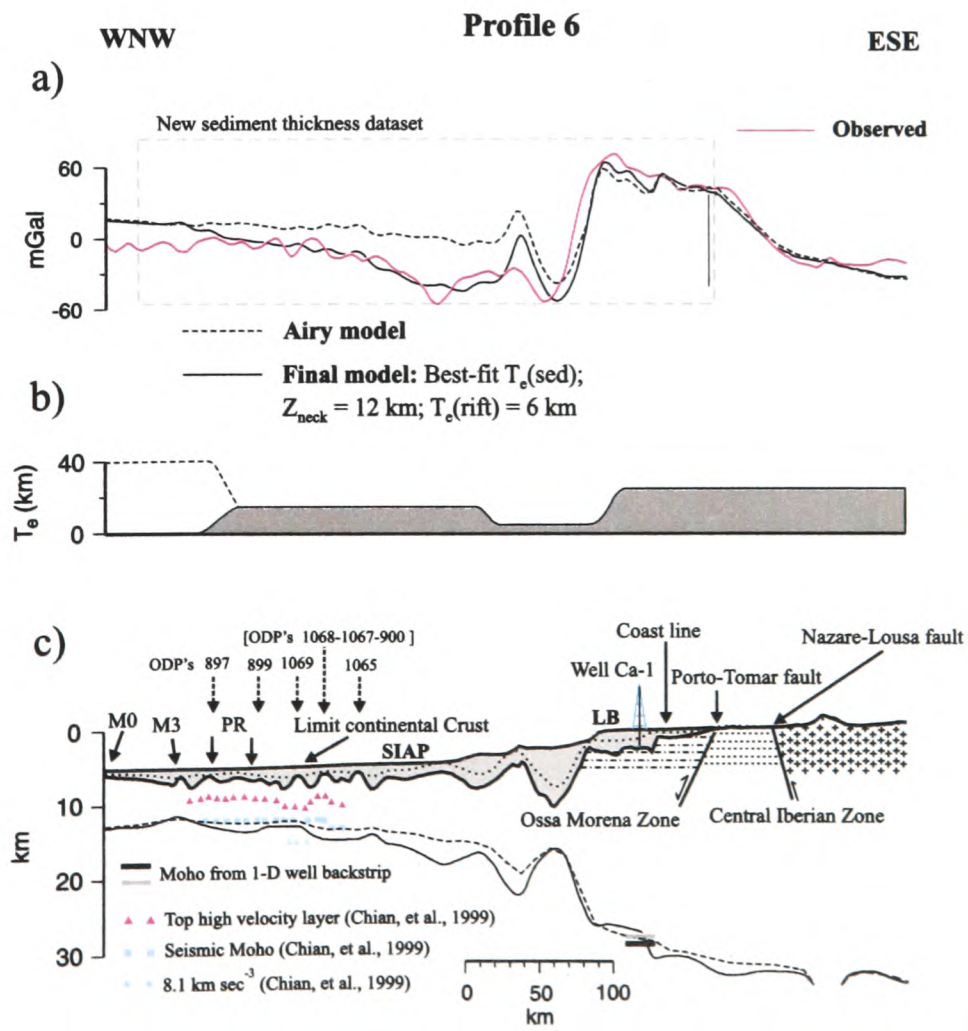

Figure C.6: Process-Oriented Gravity Modelling results along Profile 6.

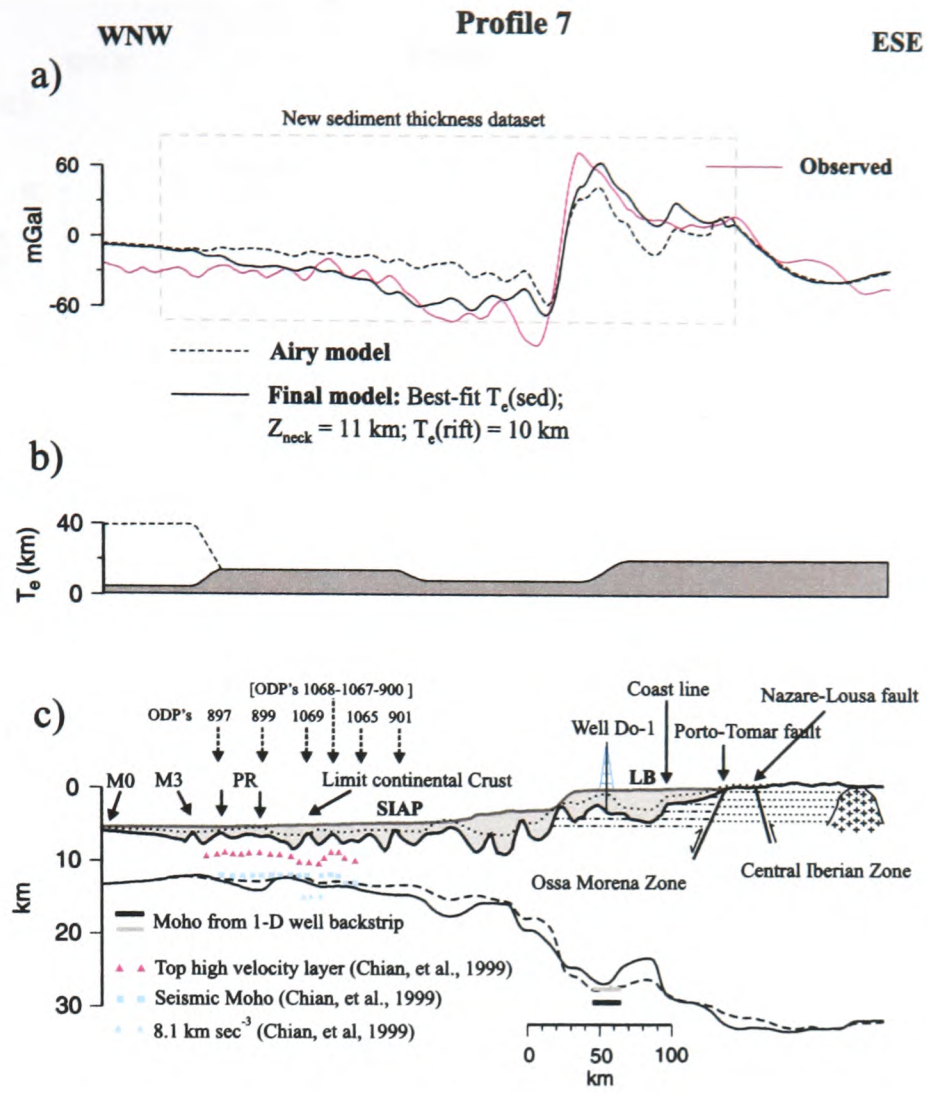

Figure C.7: Process-Oriented Gravity Modelling results along Profile 7.

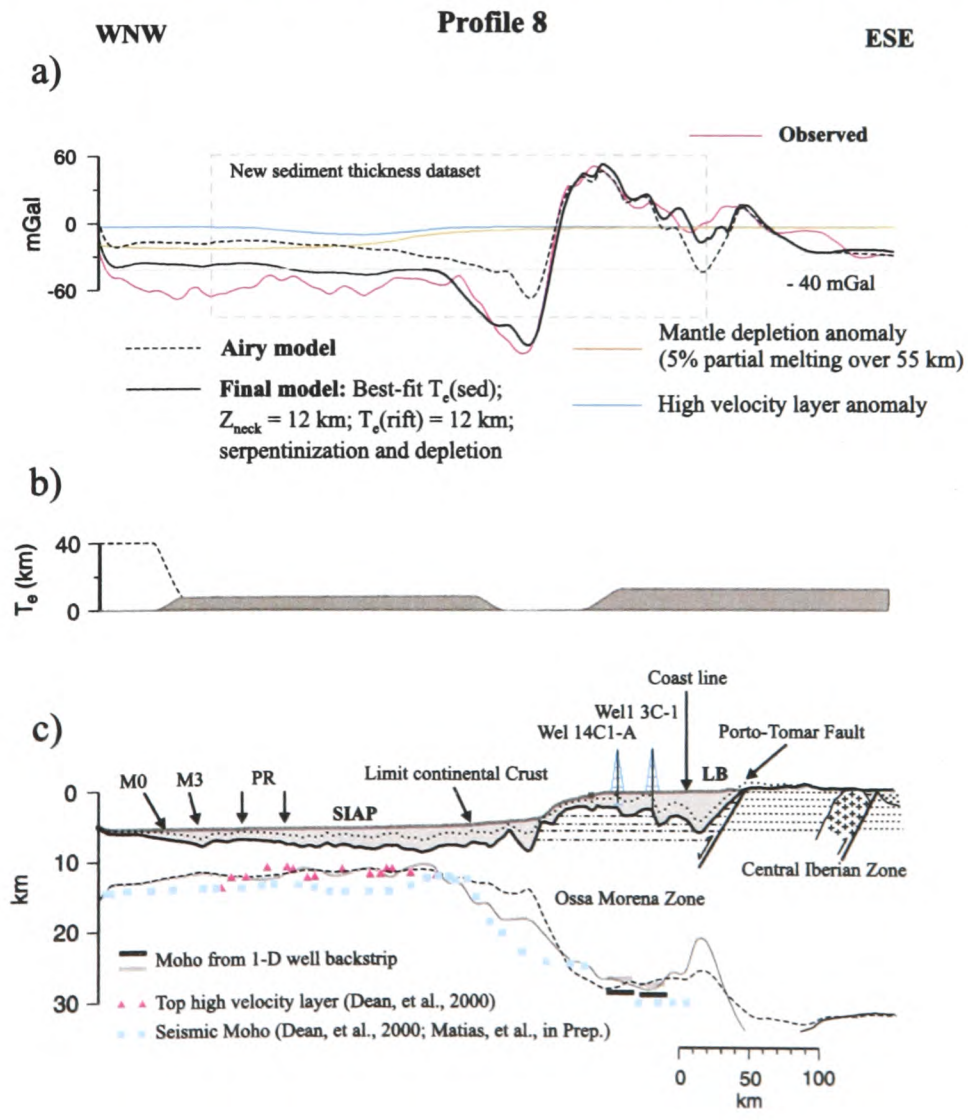

Figure C.8: Process-Oriented Gravity Modelling results along Profile 8.

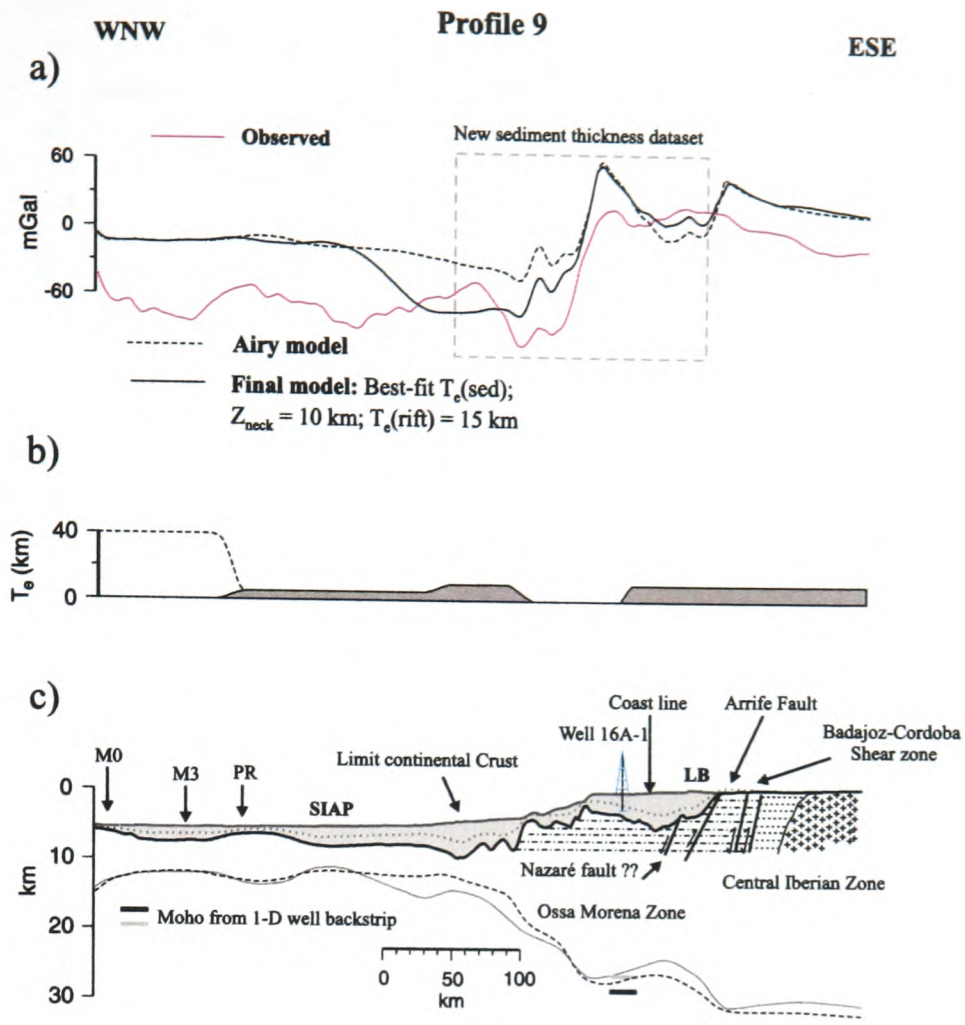

Figure C.9: Process-Oriented Gravity Modelling results along Profile 9.

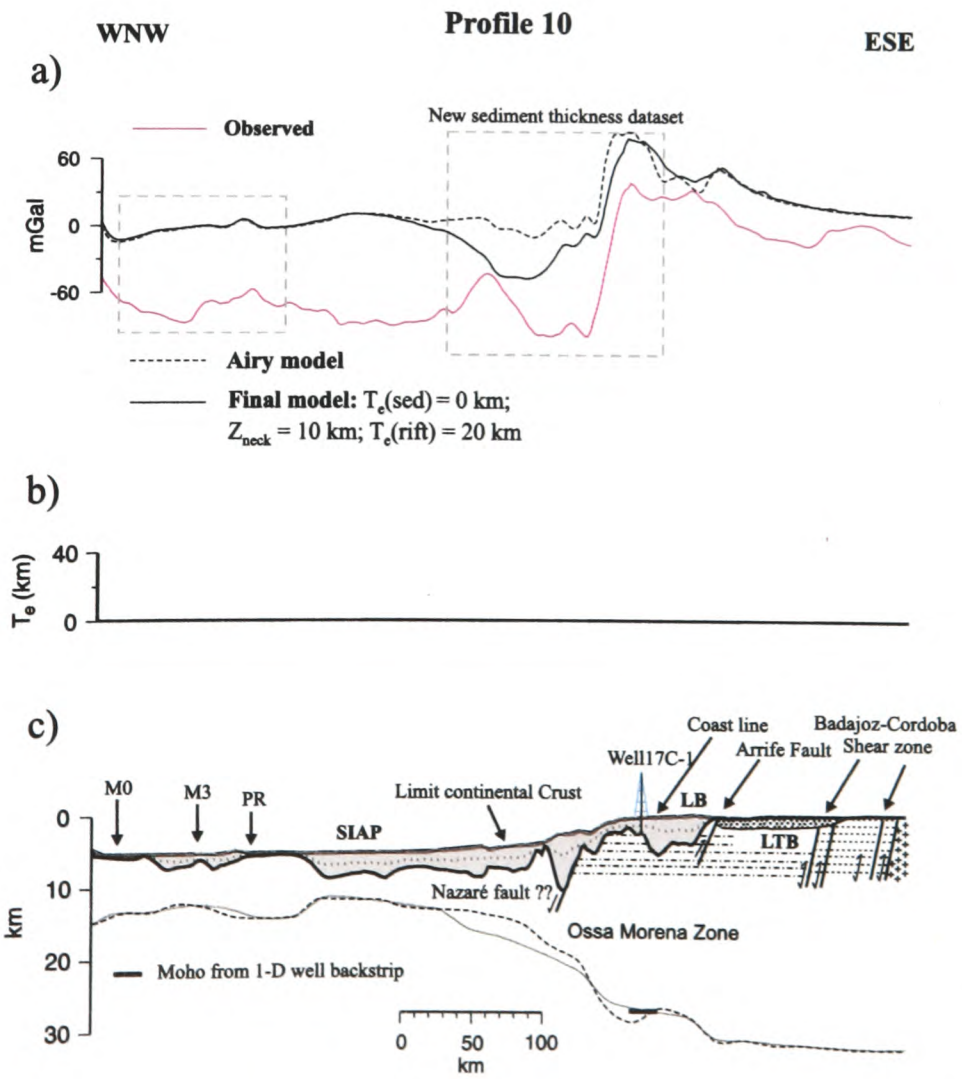

Figure C.10: Process-Oriented Gravity Modelling results along Profile 10.

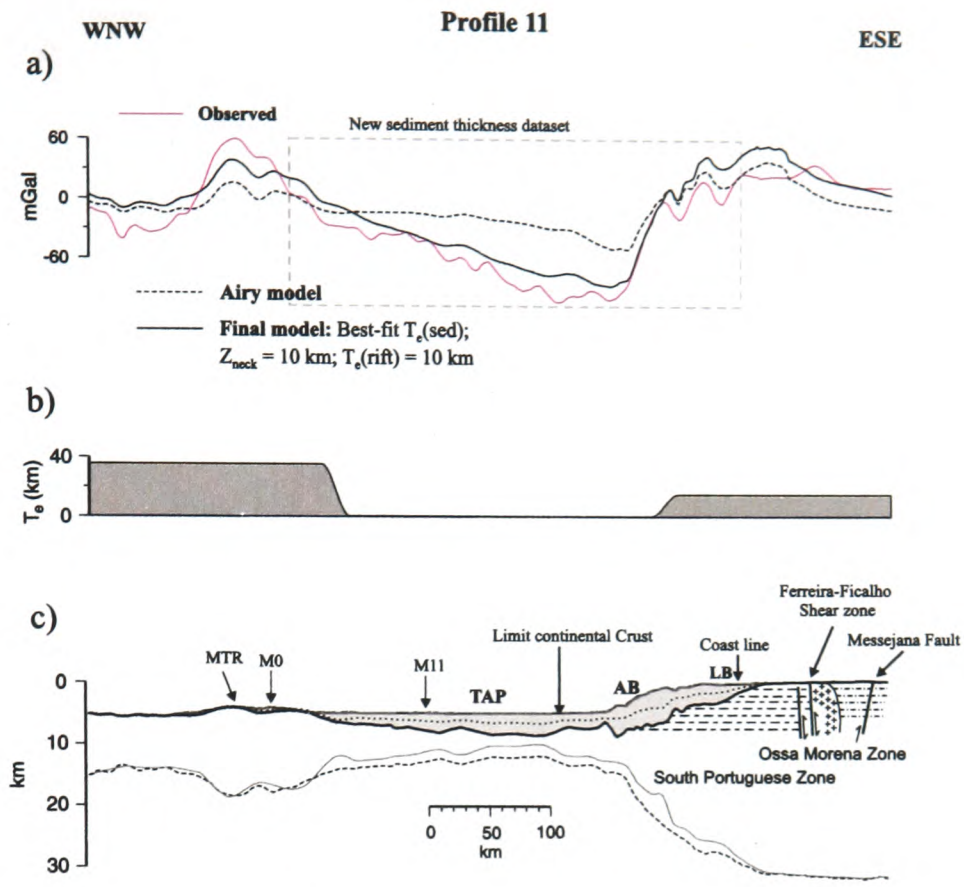

Figure C.11: Process-Oriented Gravity Modelling results along Profile 11.

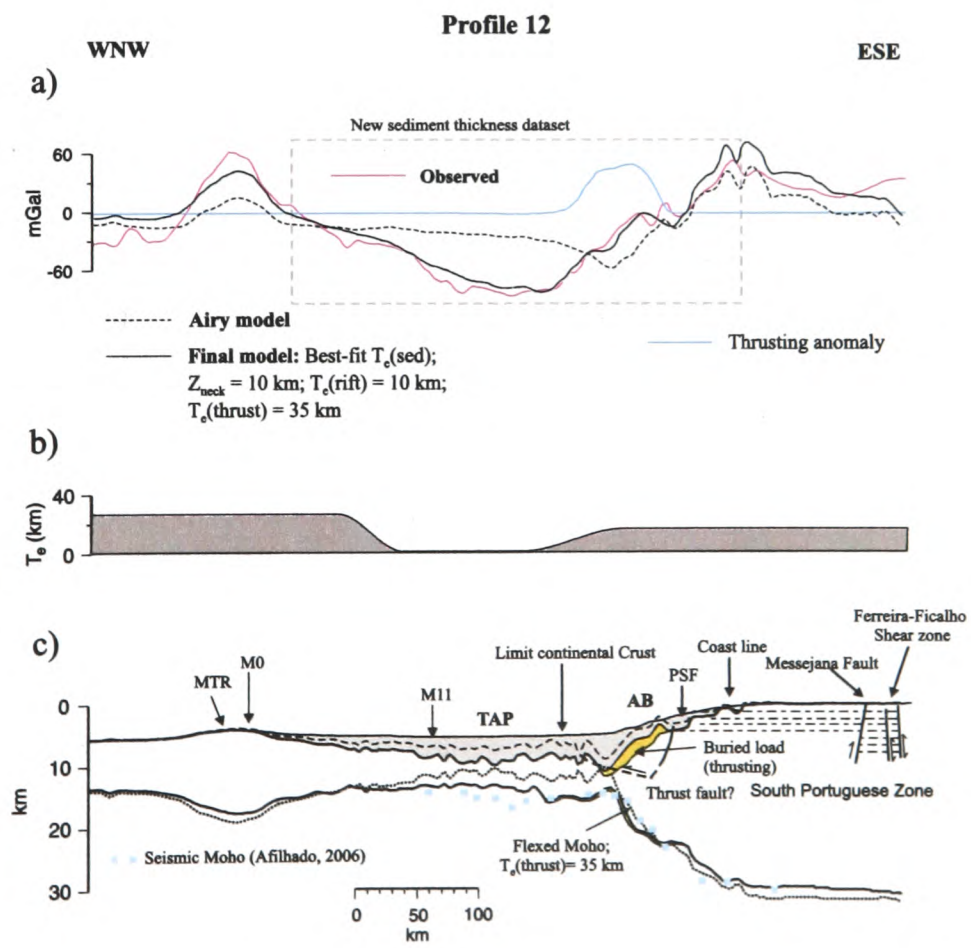

Figure C.12: Process-Oriented Gravity Modelling results along Profile 12.

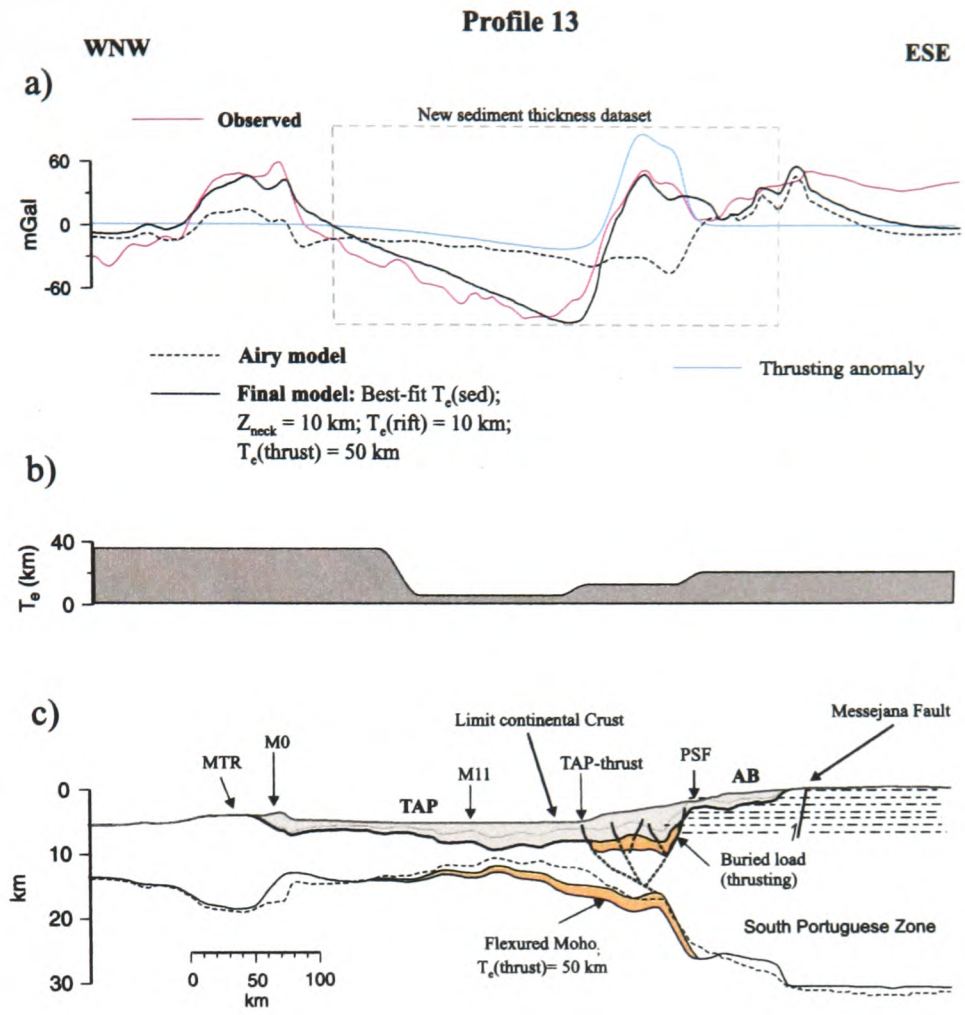

Figure C.13: Process-Oriented Gravity Modelling results along Profile 13.

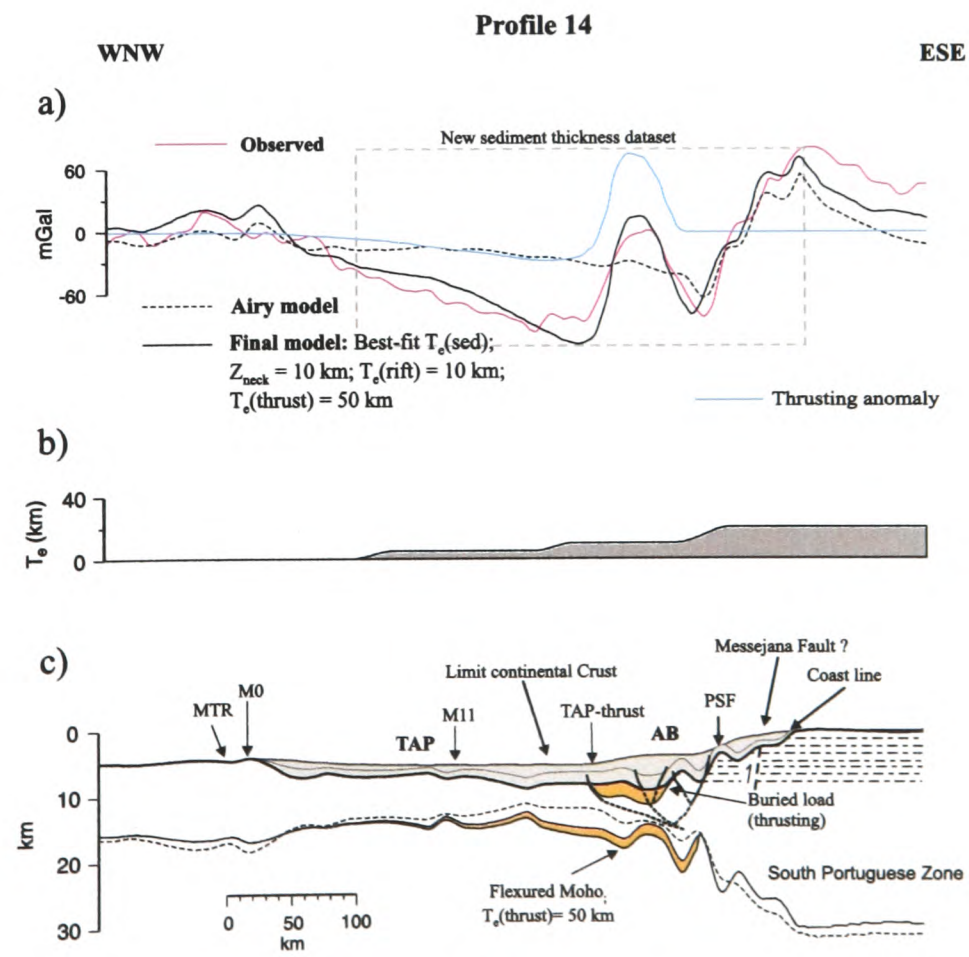

Figure C.14: Process-Oriented Gravity Modelling results along Profile 14.